

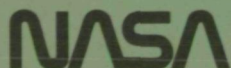
NASA Contractor Report 3343

Design of the Annular Suspension and Pointing System (ASPS)

(Including Design Addendum)

D. Cunningham, T. Gismondi, B. Hamilton,
J. Kendig, J. Kiedrowski, A. Vroman,
and G. Wilson

CONTRACT NAS1-14214
OCTOBER 1980



NASA Contractor Report 3343

Design of the Annular Suspension and Pointing System (ASPS)

(Including Design Addendum)

D. Cunningham, T. Gismondi, B. Hamilton,
J. Kendig, J. Kiedrowski, A. Vroman,
and G. Wilson
Sperry Flight Systems
Phoenix, Arizona

Prepared for
Langley Research Center
under Contract NAS1-14214



National Aeronautics
and Space Administration

Scientific and Technical
Information Branch

1980

TABLE OF CONTENTS

Preceding Page Blank

Section	Page
1.0 INTRODUCTION.....	1
2.0 SYSTEM DESIGN AND DESCRIPTION.....	5
2.1 General Description.....	5
2.2 Pointing Control System Description.....	13
2.3 Structural Flexibility.....	35
2.4 Magnetic Suspension Station Control System.....	38
3.0 SYSTEM PERFORMANCE.....	45
3.1 Pointing Control Design and Performance Analysis.....	45
3.2 System Parametric Performance Analysis.....	55
3.3 Performance Summary.....	74
4.0 ASPS MECHANICAL DESCRIPTION.....	81
4.1 Hardware Description.....	81
4.2 Mechanical Design.....	115
5.0 ELECTRONIC DESIGN.....	131
5.1 Payload Data Support.....	131
5.2 Payload Power Support.....	136
5.3 Information Panel.....	140
5.4 Control Electronics Assembly.....	140
5.5 Vernier Electronics Assembly (VEA).....	158
5.6 ASPS Power and Electronics Weight.....	158
6.0 ELECTROMAGNETIC COMPONENTS.....	169
6.1 Introduction.....	169
6.2 Roll Axis Torque Motor.....	170
6.3 Roll Axis Angular Position Sensor.....	181
6.4 Magnetic Bearing Assemblies (MBA).....	198
6.5 Position Sensors.....	215
6.6 Coarse Gimbal Components.....	222
7.0 ASPS THERMAL ANALYSIS.....	233
7.1 Model Description.....	233
7.2 Model Parameters.....	236
7.3 Thermal Control System Requirements and Approach.....	239
7.4 Simulation Results.....	241
7.5 Conclusion.....	252

TABLE OF CONTENTS (cont)

APPENDICES

Appendix		Page
A	ASPS Linear System Model.....	257
B	ASPS Digital System Simulation.....	263
C	Magnetic Actuator Linear and Nonlinear Dynamic Models and Prototype Test Results	287
D	Roll Torque Motor Model Test Report.....	309
E	Design Addendum.....	323

LIST OF ILLUSTRATIONS

Figure No.		Page No.
1	Annular Suspension and Pointing System (ASPS).....	6
2	ASPS/Experiment Control (Baseline Design).....	10
3	ASPS/Experiment Control (Spacelab No. 2 Design).....	11
4	ASPS/Experiment Control (OFT No. 4 Design).....	12
5	ASPS Control Servos.....	14
6	Elevation and Lateral Coarse Gimbal Configuration.....	16
7	Control Law for Coarse Gimbals.....	18
8	Torque and Actuator Sizing.....	19
9	Roll Torquer Cogging.....	21
10	Roll Servo Control System.....	23
11	Vernier Actuator Forces and Moments.....	25
12	Vernier Pointing/Isolation Control System.....	27
13	Vernier Actuator Decoupling.....	28
14	Coarse Gimbal Backup System.....	30
15	Simplified Structural Flexibility Dynamics - Elevation Near Zero.....	36
16	Magnetic Suspension Station Dynamics.....	40
17	Gap Compensation.....	42
18	Dynamic Compensation.....	43
19	ASPS Pointing Controllers.....	46
20	ASPS Pointing Controller Lead Lag Compensator (Closed Loop Frequency Response).....	47
21	ASPS Pointing Controller Proportional + Rate Feedback (Closed Loop Frequency Response)	48

LIST OF ILLUSTRATIONS (cont)

Figure No.		Page No.
22	ASPS Pointing Controller Integral Control (Closed Loop Frequency Response).....	49
23	Step Response of 1 Hz Pointing Servos.....	50
24	Worst-Case Shuttle VRCS Limit Cycle Transient.....	51
25	ASPS Pointing Controllers Pointing Error Response to Worst-Case Shuttle VRCS Transient, 1 Percent Decoupling Error (15 mm).....	52
26	Pointing Error from Sinusoidal Disturbance at VRCS Pitch Thrusters.....	56
27	MBA Gap Response to Worst-Case Shuttle VRCS Transient.....	57
28	Radial MBA Response to Worst-Case Shuttle VRCS Transient, Max Available Force = 14.2 Newtons.....	58
29	Axial MBA Response to Worst-Case Shuttle VRCS Transient, Max Available Force = 28.9 Newtons.....	59
30	Elevation Gimbal Angle Error Response to Worst-Case Shuttle VRCS Transient.....	60
31	Gimbal Torquer Response to Worst-Case Shuttle VRCS Transient.....	61
32	Peak Transient Pointing Error from VRCS Pitch Limit Cycle Versus Pointing Servo Bandwidth (1 Percent Decoupling Error, Proportional + Rate Feedback).....	63
33	Peak Pointing Error Versus Suspension Servo Bandwidth (During Worst-Case Shuttle VRCS Transient, 1 Percent Decoupling Error, 1 Hz Pointing Servo, Proportional + Rate Feedback).....	64
34	Pointing Error from Sinusoidal Disturbance at VRCS Pitch Thrusters (1 Percent Decoupling Calibration Error, 1 Hz Pointing Servos, Proportional + Rate Feedback, Varying Suspension Servo Bandwidth).....	65
35	Peak Suspension Gap Versus Suspension Servo Bandwidth (During Worst-Case VRCS Transient).....	66

LIST OF ILLUSTRATIONS (cont)

Figure No.		Page No.
36	Peak Pointing Error Versus CM Decoupling Error (During Worst-Case Shuttle VRCS Transient, 1 Hz Pointing Servo, Proportional + Rate Feedback).....	67
37	Peak Pointing Error Versus Radial Cable Stiffness During VRCS Transient.....	69
38	Peak Pointing Error Versus Gimbal Servo Bandwidth (During VRCS Transient, Vernier Latched).....	71
39	182 \hat{S} , 1 Hz Command Peak MBA Force and Gimbal Torque Versus Gimbal Servo Bandwidth.....	72
40	182 \hat{S} , 1 Hz Command Peak Gap Excursions Versus Gimbal Servo Bandwidth.....	73
41	Peak Suspension Gap Versus Suspension Servo Bandwidth.....	75
42	Peak Force and Torque Versus Suspension Servo Bandwidth.....	76
43	Peak Forces and Torque Required for ASPS Slewing.....	77
44	Slewing Performance.....	78
45	ASPS Component Breakdown.....	82
46	ASPS Outline Operating Position.....	83
47	ASPS Outline Caged Position.....	84
48	Orbiter Installation End View.....	85
49	Orbiter Installation Side View.....	86
50	Vernier Layout.....	89
51	Vernier Cross Section.....	90
52	Vernier - Flex Capsule Installation.....	93
53	Gimbal Cross Section.....	95
54	Typical Fixed/Floating Bearing Assemblies.....	97

LIST OF ILLUSTRATIONS (cont)

Figure No.		Page No.
55	ASPS Gimbal Stops.....	100
56	Backup Gimbal Position Sensing System.....	102
57	ASPS Flex Capsule Characteristics.....	103
58	Mounting/Jettison Assembly.....	106
59	Caging Schematic.....	108
60	Vernier Latch.....	109
61	Caging Latch.....	110
62	Linear Actuator (Typical Outline Drawing).....	111
63	Vernier - Flex Capsule Alternative Installation.....	113
64	Optical Coupler.....	114
65	Vernier Flex Capsule.....	116
66	Payload Plate Analysis.....	120
67	Reinforced Plate Analysis.....	121
68	Ribs.....	122
69a	Caging Annulus.....	123
69b	Caging Annulus.....	124
70	Liftoff Random Vibration Spectrums Input to Pallet Mounted Equipment.....	126
71	Aeronoise Random Vibration Spectrums Input to Pallet Mounted Equipment.....	127
72	Environmental Model.....	128
73	ASPS Optical Data Coupler.....	132
74	Variable Definitions in Spot Size Calculation.....	133
75	Variable Definitions in Spot Motion Calculations.....	135

LIST OF ILLUSTRATIONS (cont)

Figure No.		Page No.
76	Beam Receiver Electronics.....	137
77	Battery Charging Characteristics.....	139
78	ASPS Information Panel.....	141
79	ASPS Control Electronics Assembly.....	142
80	ASPS Control Electronics Assembly Connectors.....	143
81	ASPS Control Electronics Assembly Side View.....	144
82	CDMS Interface.....	146
83	ASPS Wiring Harness Layout.....	147
84	ASPS Hybrid Packages.....	149
85	Power Driver Hybrid.....	150
86	Modulator Hybrid.....	151
87	Dual Demodulator Hybrid.....	152
88	ASPS Control Electronics Assembly Module and Cards.....	153
89	Coarse Gimbal Driver Module.....	154
90	Roll Fixed Coil Drive Module (A).....	155
91	Roll Control Coil Drive Module (B).....	156
92	MBA Driver Module.....	157
93	Vernier Control Matrix Module.....	159
94	Serial Command Format.....	160
95	Command Interface Module.....	161
96	Telemetry Interface Module.....	162
97	Payload Services Module.....	163
98	Vernier Assembly Electronics Modules.....	164

LIST OF ILLUSTRATIONS (cont)

Figure No.		Page No.
99	ASPS Vernier Electronics Assembly.....	165
100	ASPS Control Electronics Power Dissipation.....	166
101	ASPS Control Electronics Weight.....	167
102	Roll Axis Torquer Requirements.....	171
103	Roll Axis Torque Motor Candidates.....	172
104	Roll Axis Torquer Concept Comparison.....	173
105	Roll Axis Torque Motor Design Description.....	176
106	Equivalent Circuit per Phase.....	178
107	Motor Configuration.....	179
108	Resolver and Synchro Schematic Diagrams.....	183
109	Basic System - Photoelectric Shaft Position Encoder.....	184
110	Rotary Inductosyn.....	186
111	Production of Output Voltage.....	187
112	ASPS - Roll Axis Angular Senso.....	191
113	Use as a Transmitter and Control Transformer with Rotary Transformer for Power Transfer.....	194
114	Roll Axis Angular Sensor Model Accuracy Test Data.....	197
115	Magnetic Suspension Station Control Law.....	200
116a	MBA Configurations Considered.....	202
116b	MBA Configurations Considered.....	203
117	Magnetic Bearing Assemblies Electrical Descriptions.....	205
118	Radial Magnetic Bearing with Sensor (Full Station).....	206
119	Axial MBA with Sensor (Half Station).....	207

LIST OF ILLUSTRATIONS (cont)

Figure No.		Page No.
120	MBA Model Test Data, Stator: Low Carbon Steel, Rotor: Low Carbon Steel.....	208
121	MBA Model Test Data, Stator: 50 Percent Ni-Steel, Rotor: 50 Percent Ni-Steel.....	209
122	MBA Model Test Data, Stator: 50 Percent Ni-Steel Rotor: Low Carbon Steel.....	210
123a	Rotor Flux Options.....	212
123b	Hysteresis Versus Rotor Flux Polarities.....	213
124	Rotor-Material Trade-off.....	214
125	Position Sensor Classifications.....	216
126	Photoconductive Potentiometer.....	216
127	Photoconductive Potentiometer Transducer System.....	217
128	Laser Interferometer System.....	217
129	Differential Capacitor Transducer.....	219
130	Inductive Transducer.....	220
131	Position Sensor Errors.....	223
132	Relative Sensor Output Capability for Various Rotor Materials.....	224
133	Coarse Torquer Redundancy.....	227
134	ASPS Orbital Thermal Environment.....	234
135	ASPS Thermal Mode Nodal Breakdown.....	235
136	ASPS Thermal Model.....	240
137	Hot Orbit Predicted Temperatures.....	242
138	Hot Orbit Energy Balance.....	244
139	Effect of Pallet Temperature on Hot Orbit Temperatures.....	245

LIST OF ILLUSTRATIONS (cont)

Figure No.		Page No.
140	Effect of Payload (α_S/ϵ) Ratio on Hot Orbit Temperatures.....	246
141	Effect of Payload Area on Hot Orbit Temperatures.....	247
142	Effect of Vernier Base Plate MLI Insulation on Hot Orbit Temperatures.....	248
143	Cold Orbit Predicted Temperatures ASPS Operational.....	249
144	Cold Orbit Predicted Temperatures ASPS Nonoperational.....	250
145	Cold Orbit Energy Balance.....	251
146	Effect of Pallet Temperature on Cold Orbit Temperatures (ASPS Nonoperating).....	253
147	Effect of Payload Emissivity ϵ on Cold Orbit Temperatures (Nonoperational).....	254
148	Effect of Payload Area on Cold Orbit Temperatures (Nonoperational).....	255
149	Effect of Vernier Base Plate MLI Insulation on Cold Orbit Temperatures (Nonoperational).....	256
150	ASPS Linear System Model.....	258
151	ASPS Linear System Model Block Diagram.....	261
152	ASPS Digital System Simulation.....	285
153	Magnetic Bearing Assembly Design Calculations.....	289
154	Electrical Analog of Magnetic Circuit.....	289
155	Station Model Calculation Results.....	291
156	Nonlinear Model Dynamics.....	292
157a	Nonlinear Dynamic Model Magnetic Bearing Assembly.....	293
157b	Nonlinear Dynamic Model Magnetic Bearing Assembly.....	294

LIST OF ILLUSTRATIONS (cont)

Figure No.		Page No.
158a	Linearized Model Magnetic Suspension System.....	295
158b	Linearized Model Magnetic Suspension System.....	296
159	Prototype MBA Showing Test Mass.....	297
160	Prototype MBA Showing Proximeter.....	298
161	Coil Force Versus Current Characteristics.....	300
162	Determination of MBA Constants from Static Coil Measurements.....	301
163	Determination of MBA Constants from Coil Input Impedance Measurements.....	302
164	Coil Current/Voltage Versus Frequency, Gap = 9.40 mm (.37 inch).....	303
165	Coil Current/Voltage Versus Frequency, Gap = 15 mm (.59 inch).....	304
166	Prototype MBA Gap Compensation.....	306
167	Closed-Loop Frequency Response, F/F_C	307
168	Closed-Loop Frequency Response, F/F_C	308
169	Mechanical Schematic of Roll Torque Motor Test Setup.....	310
170	Torquer Excitation Schematic.....	311
171	Low-Pass Filter.....	311
172	Low-Pass Filter-Response.....	311
173a	Roll Motor Test Charts 1, 2, and 3.....	313
173b	Roll Motor Test Charts 4, 5, and 6.....	314
173c	Roll Motor Test Chart 7.....	315

LIST OF ILLUSTRATIONS (cont)

Figure No.		Page No.
174	Fast Loop/Slow Loop Attitude Error Generator Simplified Single Loop Block Diagram.....	330
175	Maneuver Command Generator Block Diagram and Maneuver Euler Axis Rotation Acceleration and Rate Profiles.....	332
176	Search Raster Scan Pattern Command (Projection of Z Pointing Axis Unit Vector on the Initial X-Y Plane).....	334
177	Manual Pointing Command Processor Block Diagram.....	334

LIST OF TABLES

Table No.		Page No.
1	ASPS Characteristics.....	9
2	Elevation and Lateral Coarse Gimbal Requirements.....	13
3	Roll Axis Requirements.....	20
4	Vernier Pointing/Isolation Requirements.....	24
5	ASPS Servo Control Modes.....	31
6A	Typical ASPS Operating Modes.....	33
6B	Typical ASPS Operating Modes.....	34
7	Sensitivity of ASPS Dynamics to Structural Stiffnesses.....	37
8	Vernier Pointing Servo Design Data.....	53
9	Peak Pointing Error Due to MBA Mismatch.....	70
10	Pallet Structure Weight.....	87
11	ASPS Weight Projection.....	87
12	Payload Plate Module Weights.....	88
13	Vernier Module Weight Breakdown.....	94
14	Gimbal Bearing Characteristics.....	96
15	Kendall KG-80 Oil Characteristics.....	98
16	Gimbal Bearing and Lubrication.....	99
17	Gimbal Module Weight Breakdown.....	104
18	Mounting/Jettison Assembly Weight Breakdown.....	105
19	Caging System Weight Breakdown.....	107
20	Orbiter Acceleration Limit Load Factors (g's).....	118
21	Design Criteria.....	118
22	Payload/Vernier Plates Versus Supporting Payload Case 3 Stress and Deflection.....	125

LIST OF TABLES (cont)

Table No.		Page No.
23	Sinusoidal Vibration.....	129
24	Payload/Vernier Plates - Liftoff Random Response.....	130
25	Roll Axis Angular Sensor Requirements.....	182
26	Roll Axis Sensor Candidates and Concept Comparison.....	188
27	Roll Axis Angular Sensor Design Description.....	190
28	Rotary Transformer Description.....	193
29	Roll Axis Angular Sensor.....	195
30	Roll Axis Angular Sensor Model Accuracy Test Data Summary.....	196
31	MBA Station Requirements.....	199
32	Selected Sensor Description and Outline.....	221
33	Coarse Gimbal Torquer Preliminary Requirements.....	225
34	Coarse Torquer Candidates.....	228
35	Coarse Gimbal Torquer Description.....	229
36	Coarse Gimbal Position Resolver.....	230
37	Coarse Gimbal Commutating Resolver.....	231
38	Nominal Thermal Capacitances.....	237
39	Nominal Thermal Resistances.....	237
40	Nominal Radiation Constants.....	238
41	Internal Power Dissipation.....	238
42	Solar Heat Input.....	239

LIST OF TABLES (cont)

Table No.		Page No.
43	ASPS Component Temperature Limits.....	241
44	Comparison of Theoretical and Measured Model Parameters.....	299
45	Summary of Quaternion Integration Error Equations.....	327
46	Summary of Results ϵ 10 Hz Digital Control Loop Simulation.....	337

SECTION 1.0

INTRODUCTION

An Annular Suspension and Pointing System (ASPS) is being designed under contract to NASA Langley Research Center (NAS 1-14214). Purpose of the ASPS is to provide extremely precise 3-axis pointing of variety of shuttle payload experiments. The ASPS provides noncontacting magnetically suspended vernier pointing in three orthogonal axes, which are coarse pointed by an elevation/lateral gimbal pair. The arrangement allows for isolation of small carrier motion from the payload, and a decoupling control law minimizes transient response of the payload due to translational centering forces. Payload power and data support are included in the ASPS.

The ASPS concept was developed at Langley Research Center to meet the needs of solar, stellar, and earth viewing experiments planned for the 1980s. The concept is a derivative of the Annular Momentum Control Device (AMCD) which was also developed at Langley Research Center and is described in Reference 1. A description of the ASPS concept and its expected performance are presented in Reference 2.

Initial design of the ASPS has been completed and a Final Design Review held. This report is organized around the design review presentation. Section 2 provides an overall description of the ASPS and discusses the control system configuration and general operation. System performance as predicted by simulation and analysis is given in Section 3. A description of the electronics, mechanical, and electromagnetics designs are presented in Sections 4, 5, and 6, respectively. A thermal analysis of the ASPS is given in Section 7.

Use of trade names or names of manufacturers in this report does not constitute an official endorsement of such products or manufacturers, either expressed or implied, by the National Aeronautics and Space Administration.

ABBREVIATIONS AND SYMBOLS

ACS	Attitude Control System
AGC	Automatic Gain Control
ASPS	Annular Suspension and Pointing System
CCW	Counterclockwise
CDMS	Command and Data Management System
CM	Center of Mass
CEA	Control Electronics Assembly
CGA	Coarse Gimbal Assemblies
CW	Clockwise
DDU	Data Display Unit
EMI	Electromechanical Interference
EPDB	Electrical Power Distribution Box
GPC	General Purpose Computer
HRM	High-Rate Multiplexer
I/S	Interconnect Station
LED	Light Emitting Diode
MBA	Magnetic Bearing Assembly
MBPS	Megabits Per Second
MJA	Mounting and Jettison Assembly
MLI	Multilayer Insulation
mmf	Magnetomotive force
MPC	Manual Pointing Control
MS	Margin of Safety
PEA	Payload Electronics Assembly
PPA	Payload Plate Assembly
RAU	Remote Acquisition Unit
RC	Transformer

RF	Radio Frequency
RX	Resolver Transmitter
UTC	Universal Time Clock
VCMM	Vernier Control Matrix Module
VEA	Vernier Electronics Assembly
VPA	Vernier Pointing Assembly
VRCS	Vernier Reaction Control System

Page Intentionally Left Blank

SECTION 2.0

SYSTEM DESIGN AND DESCRIPTION

This section presents an overview of the ASPS configuration and its characteristics, and discusses the system design of each of the major control servos: coarse gimbal, roll, and vernier pointing/isolation. Structural flexibility is assessed, and the subsystem used to control the magnetic suspension stations is presented.

2.1 GENERAL DESCRIPTION

The Annular Suspension and Pointing System (ASPS) shown in Figure 1 is a precision payload pointing system designed for use on the Space Shuttle. Experiments of virtually any size may be accommodated by overhanging the one meter diameter payload mounting plate. Actuators in the ASPS are sized to accept payloads weighing up to 600 kg with CM (Center of Mass) offsets up to one and a half meters; however, larger experiments may be used if lower accelerations are acceptable.

The ASPS consists of a Vernier Pointing Assembly, two Coarse Gimbal Assemblies, a Mounting and Jettison Assembly, a Control Electronics Assembly, and assorted connecting hardware. Two identical Coarse Gimbal Assemblies (CGAs) are stacked to form an elevation and a lateral gimbal pair. Design of the Gimbal Mounting Bracket and the Gimbal Mounting Structure is such as to provide a mechanically limited travel of ± 100 degrees (from vertical) along the lower elevation gimbal axis, and ± 60 degrees about the upper lateral gimbal axis. The Vernier Pointing Assembly (VPA) contains the roll axis drive which provides unlimited rotation about the payload longitudinal axis and a vernier rotation of $\pm .75$ degrees about any axis in the plane normal to the payload roll axis. The Payload Mounting Plate forms a removable base plate for mounting and aligning experiments prior to installation on the ASPS. For missions not requiring roll freedom or very high pointing stability, the Payload Mounting Plate may be attached directly to the upper Gimbal Mounting Bracket. ASPS electronics are contained within a separate electronics package which is mounted to a pallet cold plate near the bottom of the Mounting and Jettison Assembly.

Magnetic Suspension is utilized in the VPA to provide noncontacting isolation and vernier positioning of the payload. Three-axial Magnetic Bearing Assemblies (MBAs) provide axial translation and vernier pointing about the transverse axes. Proximometers associated with each MBA are used to linearize the force/displacement characteristics of each actuator. The proximeter outputs are also combined electronically to compute the axial displacement and the tilt of the payload about the two axes normal to the payload line-of-sight. Axial displacement is always required for centering of the axial isolation servo, while the tilt angle is used only for modes where rotational centering is required (e.g., during coarse gimbal slews).

The axial MBAs react against the horizontal surface of an L-shaped soft iron rotor which runs circumferentially under the payload plate mounting surface at a radial distance of .362 meter. The vertical surface of this rotor is

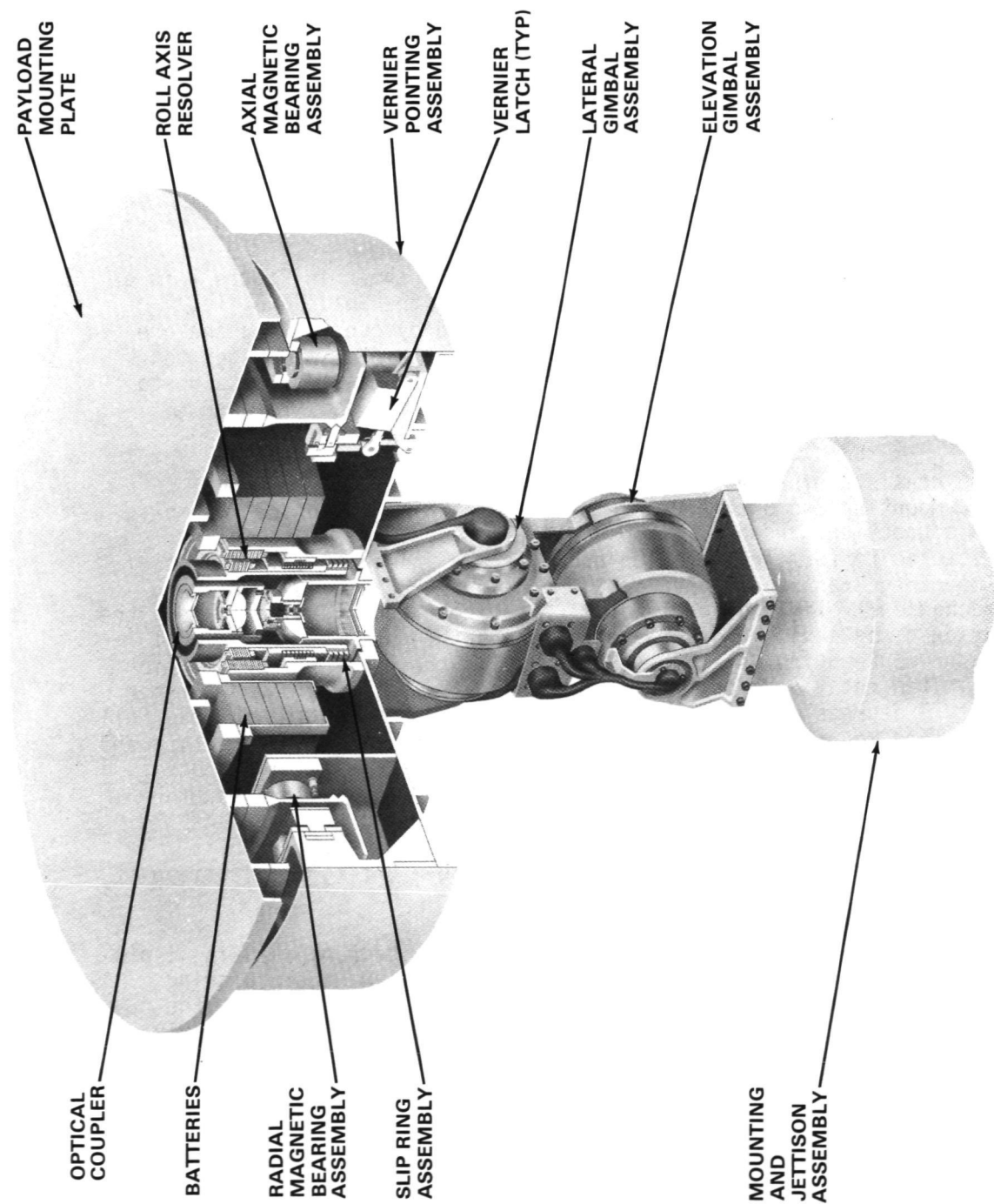


Figure 1
Annular Suspension and Pointing System (ASPS)

utilized by the two radial MBAs and the single Roll Torquer Assembly. The radial MBAs are spaced 90 degrees apart and provide radial centering of the payload mounting plate. Each radial MBA contains a proximeter for magnetic gap compensation and for centering.

A segmented two-phase solid iron rotor ac induction motor controls the roll (about line-of-sight) position of the payload. This motor also contains a proximeter to compensate the radial attractive force associated with the two motor segments. Roll angular position is sensed by a single-speed wound rotor resolver located near the center of the VPA. Resolver rotor signals are ac coupled to the stationary side of the assembly through a rotary transformer.

In addition to the 6 degree of freedom positioning and readout provided by the VPA, power, control, and data transfer support to the payload experiment is also supplied. Twenty-five nickel-cadmium cells are mounted below the rotating top plate to supply 300 watt hours of energy to the experiment. The selected cells are NASA Standard and the configuration chosen provides a nominal 28 V dc with peak power output of 300 watts. A fast recharge circuit is included to allow the use of the experiment at a one hour, 300 watts discharge, followed by a one hour (temperature limited) recharge duty cycle. To recharge the batteries, the VPA is caged by energizing five solenoid actuated vernier latches. A solenoid operated brush block assembly is engaged with the vernier slip rings to connect power and battery charge signals directly to the payload plate. The vernier latch mechanism permits the use of the ASPS in a coarse gimbal only mode for comparison with the vernier system or as a backup. Additionally, the latch design is such that a failure within the magnetic suspension causes the suspended assembly to touch down on the retracted latches. Contact occurs between the latch pins and the mating surface on the rotor. These are designed to accommodate the touchdown loads and, thereby, protect the MBAs, proximeters, etc.

Experiment control and data signals are transferred across the vernier gap using an optical coupling technique. Three serial data channels are provided. One uplink and one downlink are used to extend the (1 MBPS) Spacelab Experiment Data Bus to a standard Remote Acquisition Unit (RAU) located on the payload mounting plate. A single high-speed (5 MBPS) downlink is also provided to couple wide band experiment data to the high rate multiplexer for mass storage or downlink.

Two identical CGAs provide elevation and lateral pointing of the ASPS. A permanent magnet, two-phase brushless dc torque motor generates up to 33.9 N m (25 ft-lbs) of shaft torque. The motor contains samarium cobalt magnets for high efficiency and to ensure against a single point failure of the rotor. (With conventional magnets, an electronics failure can create a high stator current which might demagnetize the torquer's permanent magnets.) A separate pair of windings is brought out from the torquer stator for use in a backup caging mode. In this mode, hard wired control signals switch the backup power bus alternately between the backup sine and cosine windings to cause the torquer to step clockwise or counterclockwise to the caged position for latching. A backup optical readout is contained in the CGA to indicate whether the drive is positioned clockwise or counterclockwise from the caged position.

Commutation of the torquer is accomplished using a multispeed wound rotor resolver. Since the torquer contains 24 poles, the resolver must be a 12-speed device to provide sine and cosine phase currents to the torquer drive electronics which are synchronized with the torquer electrical angle.

A single-speed wound rotor resolver is included in the CGA for position readout and control of the gimbal angle. Since both elevation and lateral gimbals have a limited rotational freedom, the electrical connection to the rotating resolver windings occurs through a flex capsule. The flex capsule contains a band of flat flex wire cable which is looped between concentric cylinders in the center of each CGA. These cables are sized to support all of the coarse and vernier signal and power requirements as well as high-speed payload data and battery recharge power.

Two duplex gimbal bearing pairs are used in a fixed/floating cartridge arrangement. The cartridges permit the bearing preload to be set by tolerances within the cartridge itself; dimensional changes which result from temperature variations cause the sliding cartridge to move axially without inducing mechanical stresses or upsetting the bearing preloads.

The Mounting and Jettison Assembly supports the Coarse Gimbals and also contains pyrotechnics to Jettison the ASPS (and payload) in the event of a multiple failure which prevents stowage in orbit. This assembly is a simple rigid tubular structure which can be varied for different missions depending on the pallet layout. It may also be replaced by an extensible telescoping column for experiments requiring extreme view angles. During jettison, two pin pullers are actuated by pyrotechnics which release a pretensioned separation band. The band normally retains the gimbal interface to the mounting pedestal by a clamping action between parallel raised lips. The jettison system does not impart a velocity to the ASPS; consequently, the orbiter Remote Manipulator System or Orbiter flyaway is required to physically jettison the unit. Electrical connections are broken by pyrotechnic actuated cable cutters which are located inside the mounting column.

Overall characteristics of the ASPS are listed in Table 1. The peak power of 997 watts is a worst-case combination of maximum force and torque by all actuators simultaneously.

Information flow, for several alternate ASPS installations, is shown in Figures 2, 3, and 4. The baseline design (Figure 2) utilizes the Spacelab Experiment Computer for processing of experiment pointing errors to form the ASPS pointing commands. The primary user interface is the Spacelab Keyboard and Data Display Unit. An Information Panel may be used for manual hardwired backup control and caging of the ASPS in the event of a primary system failure. An alternative arrangement, shown in Figure 3, uses a dedicated miniprocessor to relieve the computational load on the experiment computer and the data bus. Attitude determination and pointing command computations are performed within this processor. An Orbital Flight Test application of the ASPS is illustrated in Figure 4. Here, none of the Spacelab equipment is available, and the Orbiter computer cannot be used except for experiment initiation and status monitoring. A simple analog compensation network connecting the experiment pointing error sensor and the ASPS magnetic bearing actuators is provided within the ASPS electronics.

TABLE 1
ASPS CHARACTERISTICS

Power		
Standby		75 Watts
Peak (Worst Case)		997 Watts
Heaters (Peak)		210 Watts
Weight		
Mechanical	239.04 kg (527 lbs)	
Control Electronics	12.7 kg (28 lbs)	
Caging and Mounting Structure	104.33 kg (230 lbs)	
Size		
Vernier System Height	.241 m (9.5 in.)	
Overall Height	1.174 m (46.25 in.)	
Payload Plate Diameter	.965 m (38 in.)	
Payload Accommodation		
Size	1 Meter Dia End Mount (may overhang)	
CG Offset		1.5 Meters
Weight		600 kg
Power (28 V dc Levitated)		300 Watts
Energy (28 V dc Levitated)		300 Watt - Hrs
CDMS Interface	RAU to Spacelab Data Bus	
Wideband Data Interface		5 MBPS to HRM

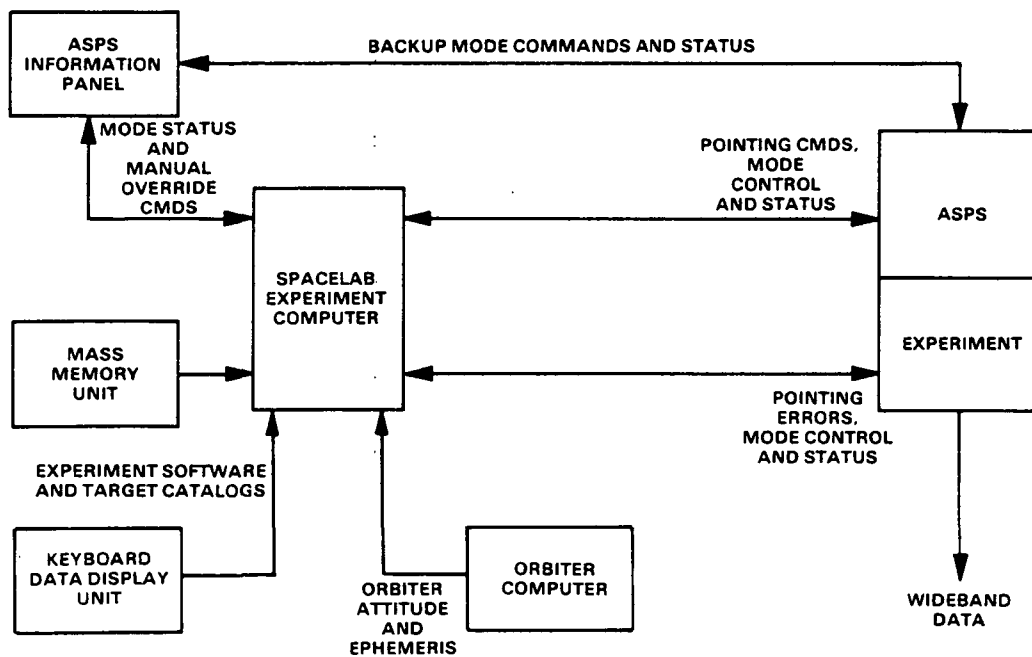


Figure 2
ASPS/Experiment Control (Baseline Design)

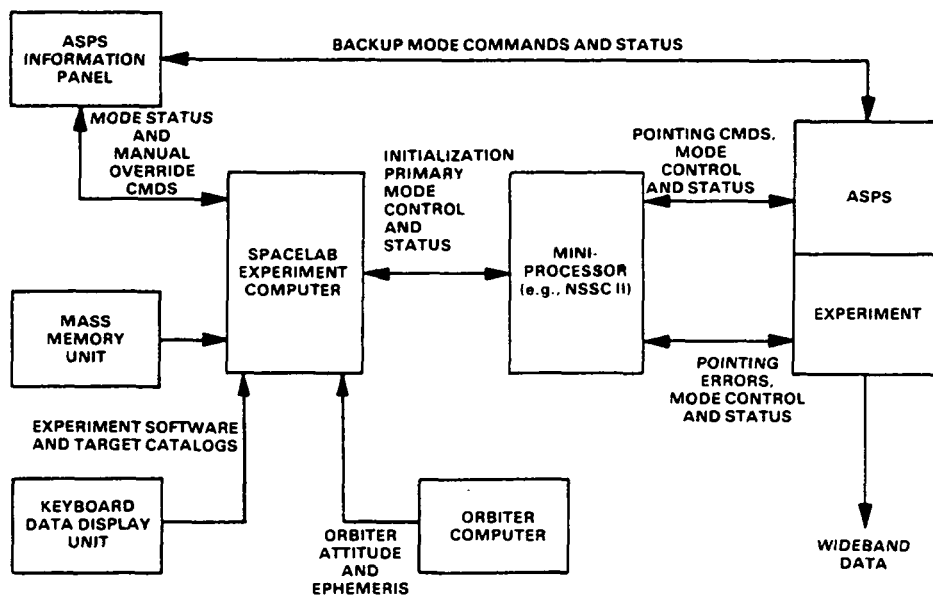


Figure 3
ASPS/Experiment Control (Spacelab No. 2 Design)

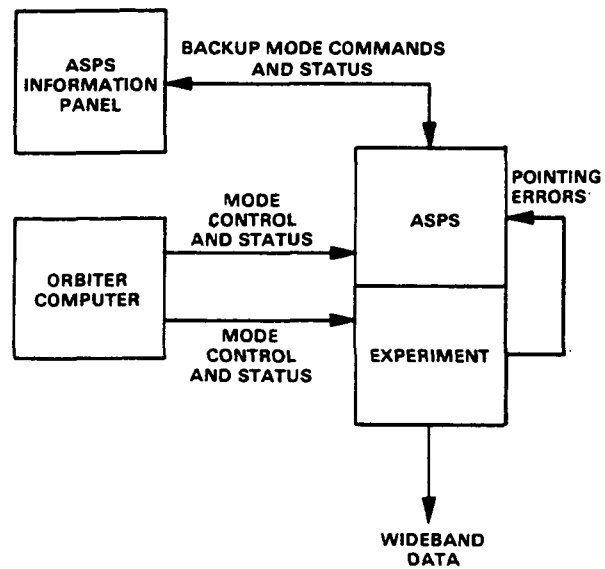


Figure 4
ASPS/Experiment Control (OFT No. 4 Design)

2.2 POINTING CONTROL SYSTEM DESCRIPTION

The ASPS contains eight control servos: six for vernier positioning and two for coarse gimbal pointing. Figure 5 identifies the nomenclature for the controlled axes and the operational range of each. Each of these servos operates in several different modes depending on what payload error sensors are available and the mission operational mode (raster, slew, track, etc). Control law compensation and bandwidth are also selectable depending on the operational mode.

The ASPS control servos may be functionally grouped into coarse, roll, and vernier pointing/isolation. Each of these are discussed in the following subsections.

2.2.1 Elevation and Lateral ("Coarse") Gimbal Servos

The principal requirements for the coarse gimbal servos are listed in Table 2.

TABLE 2
ELEVATION AND LATERAL COARSE GIMBAL REQUIREMENTS

Direct Drive Torquers and Angle Sensors
Elevation Range = ± 100 degrees
Lateral Range = ± 60 degrees
Max Rate = ± 3 deg/sec
Max Acceleration = ± 2000 arc sec/sec ²
Position Accuracy = ± 6 arc minutes*
Rate Accuracy = ± 0.03 deg/sec*
Standby Electronics Power (Lateral and Elevation Gimbals) = 5 watts maximum
*(Internal Sensor)

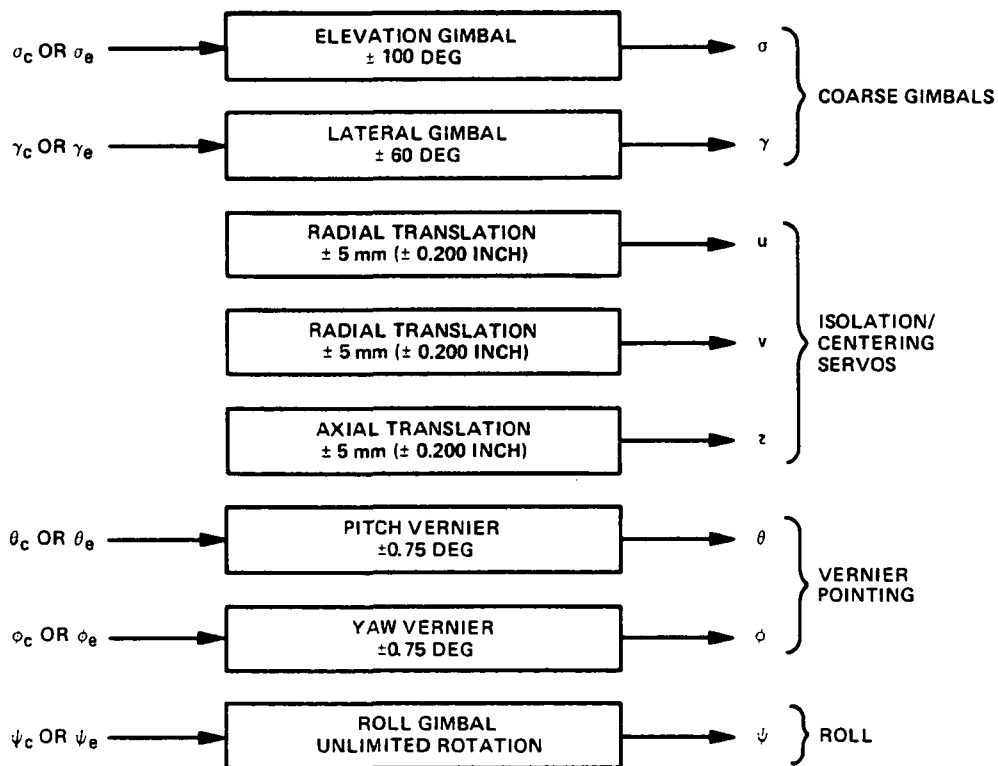


Figure 5
ASPS Control Servos

Figure 6 is a block diagram of the control system used in both coarse gimbals. A permanent magnet brushless dc torque motor with 24 poles and two phases is used to drive each gimbal. The motor is continuously commutated by a 12-speed wound rotor resolver. A peak torque capacity of 33.9 N m (25 ft-lbs) is provided by the coarse torquers to achieve the required slew accelerations.

Current control loops are used in each phase for low offsets, good linearity, and high bandwidth response. A single-speed wound rotor resolver is used to measure the gimbal angle for readout or control. This resolver is connected in one of two different configurations depending on the command mode.

When an external angular error signal is provided, the resolver rotor is excited with a constant amplitude ac voltage and the sine and cosine outputs are synchronously demodulated to provide sine and cosine readouts. If internal loop closure is desired, the resolver stator windings are excited by ac signals proportional to the sine and cosine of the commanded angle. The voltage induced in the rotor is proportional to the component of each stator winding voltage times the cosine of the angle between rotor and stator windings.

$$\begin{aligned} E_R &= kE_{S1} \cos \sigma - kE_{S2} \sin \sigma \\ &= V \sin \sigma_C \cos \sigma - V \cos \sigma_C \sin \sigma \\ &= V \sin (\sigma_C - \sigma) \end{aligned} \tag{1}$$

where

E_R = Rotor Voltage

E_{S1}, E_{S2} = Stator Voltages

k = Transformation Ratio

V = Input Voltage Scale Factor

σ = Gimbal Angle

σ_C = Commanded Gimbal Angle

The resolver output is demodulated to form a feedback signal which is equal (at small error) to the difference between commanded and actual gimbal angle. Linear compensation in the form of a lead/lag is used in the forward path to create a torque to the motor. The gain and time constants of this compensator are switched depending on the ASPS mode. For vernier fine pointing, the coarse gimbal servos are stiffened to have approximately 10 Hz bandwidth, while during slew maneuvers, the gains are reduced to about .1 Hz bandwidth. A proportional plus integral filter is included in the forward loop of these control systems to provide steady state torque rejection and to minimize drift due to electrical offsets.

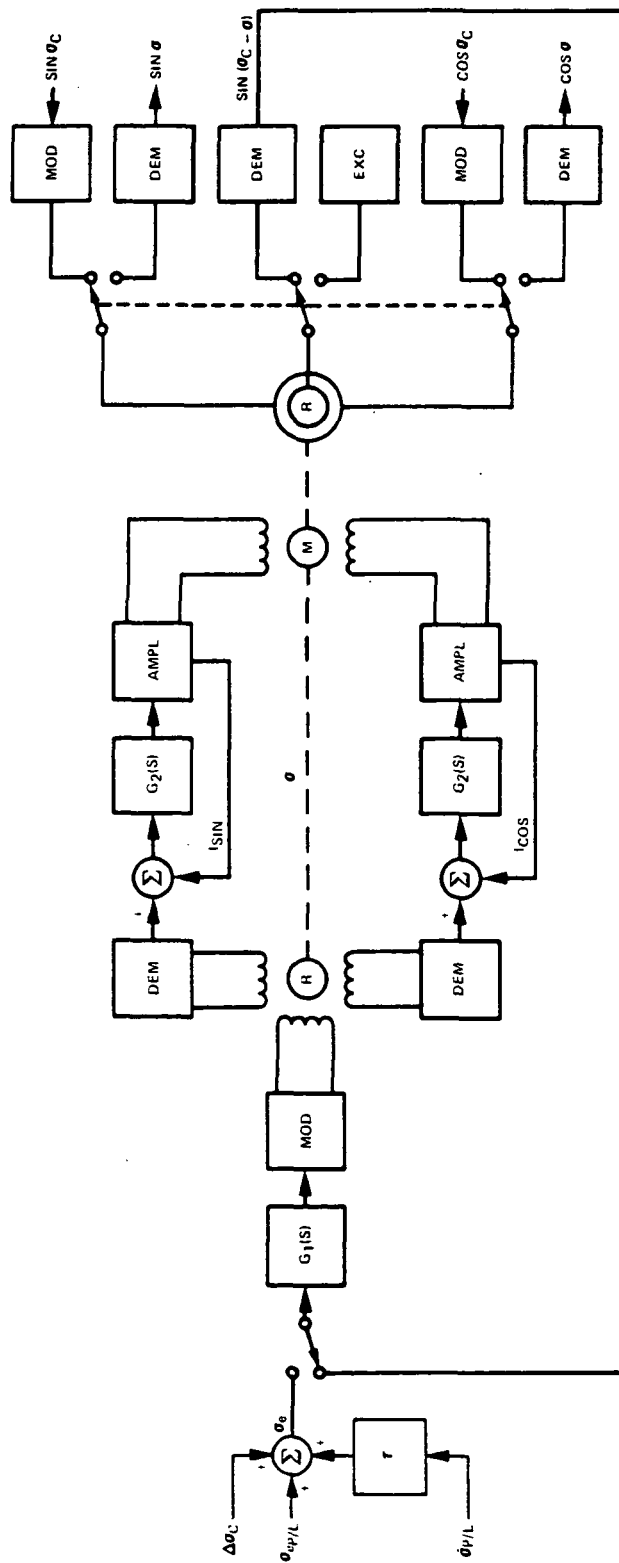


Figure 6
Elevation and Lateral Coarse Gimbal Configuration

Figure 7 is an open loop Bode plot which illustrates the design procedure used to initially select the compensation gains and time constants. The lead/lag breaks are located such that the open-loop crossover occurs at the geometric mean between them. This tends to maximize the phase margin for a fixed high frequency gain. The integrator gain is well below this frequency to avoid degrading this phase margin.

When an external pointing error is available for the coarse gimbals (for example, when the vernier system is mechanically latched), the gimbal resolver is conventionally connected, and the motor torque command is generated from

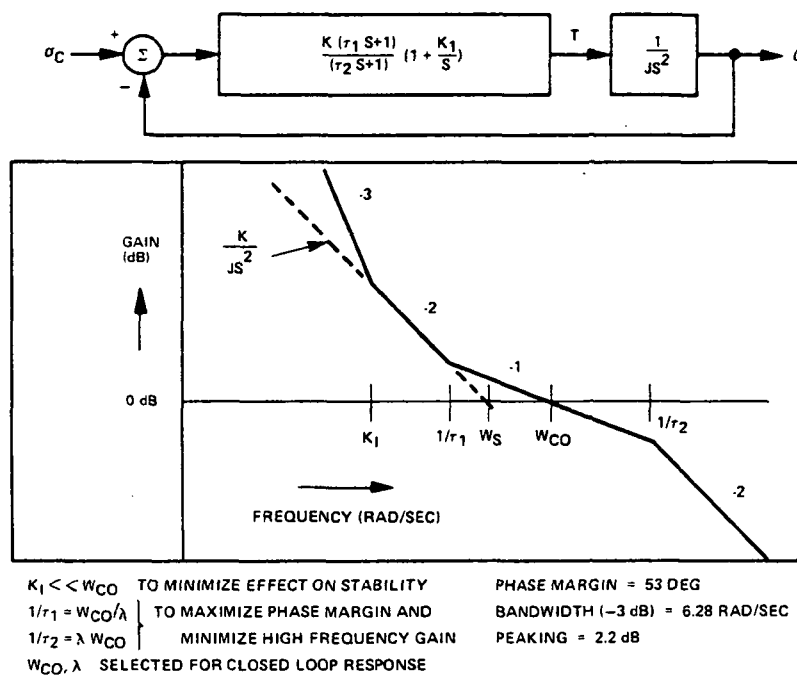
$$T_{cmd} = [\sigma_{ep/L} + \Delta\sigma_C + \tau \dot{\sigma}_{p/L}] G_1(s) \quad (2)$$

where $\sigma_{ep/L}$ is the pointing error measured by or computed from a payload angular error sensor, $\Delta\sigma_C$ is an offset pointing command, and $\dot{\sigma}_{p/L}$ is the angular rate of the payload, and τ is the rate to displacement gain ratio. $G_1(s)$ is of the same form as with internal feedback - proportional plus integral with lead/lag filtering; the parameters values are changed however to be consistent with scaling and bandwidth characteristics of the payload error sensors. The offset pointing command and the payload rate terms are optional signals which can be accommodated if available.

Sizing of the coarse gimbal torquers as well as the vernier assembly magnetic actuators is based on the acceleration requirement of 2000 arc second/second². Figure 8 summarizes the sizing tradeoff using a free-body representation of the coarse gimbal/fixed vernier and the payload/suspended vernier assemblies. The axial separation between the gimbal axis and the plane containing the magnetic actuators (Z_G) is important in sizing the torquer and actuators. This distance was minimized by selecting a small OD torquer and designing compact bracketry and mounting structure. The selected motor and actuator sizes shown on Figure 8 provide a margin of approximately 20 percent above the values required for an elevation (lower) gimbal slew.

2.2.2 Roll Servos

Table 3 lists the requirements for the ASPS roll control system. The most severe requirement is the pointing stability of one arc second per second which is to apply at rates up to the maximum of 1.5 degrees per second. This corresponds to a rate ripple of .0185 percent and applies to the roll control system when commanded by an ideal roll error sensor. Allowable cogging and torque ripple anomalies in the roll motor are determined by this requirement to be less than 1.36×10^{-4} N m (10^{-4} ft-lbs) and .02 percent respectively. Figure 9 summarizes the analysis used to compute the maximum anomaly torque from the specified roll rate ripple (stability) requirement. The selected roll motor is a two-phase, segmented, solid iron rotor, ac induction motor which can provide peak torques of ± 6.78 N m (± 5 ft-lb). This motor was selected specifically to meet these low anomaly torque requirements.



- σ_c = GIMBAL ANGLE COMMAND (RADIAN)
- σ = GIMBAL ANGLE (RADIAN)
- J = EQUIVALENT GIMBAL INERTIA (kg - M²)
- T = GIMBAL TORQUE (N - M)
- K = PROPORTIONAL GAIN (N - M/RADIAN)
- K_1 = INTEGRAL GAIN (N - M/RADIAN-SEC)
- τ_1, τ_2 = CONTROL LAW TIME CONSTANTS (SECONDS)
- W_S = OPEN LOOP INTERCEPT FREQUENCY (RAD/SEC)
- W_{CO} = OPEN LOOP Crossover FREQUENCY (RAD/SEC)
- λ = LEAD/LAG SEPARATION RATIO

Figure 7
Control Law for Coarse Gimbals

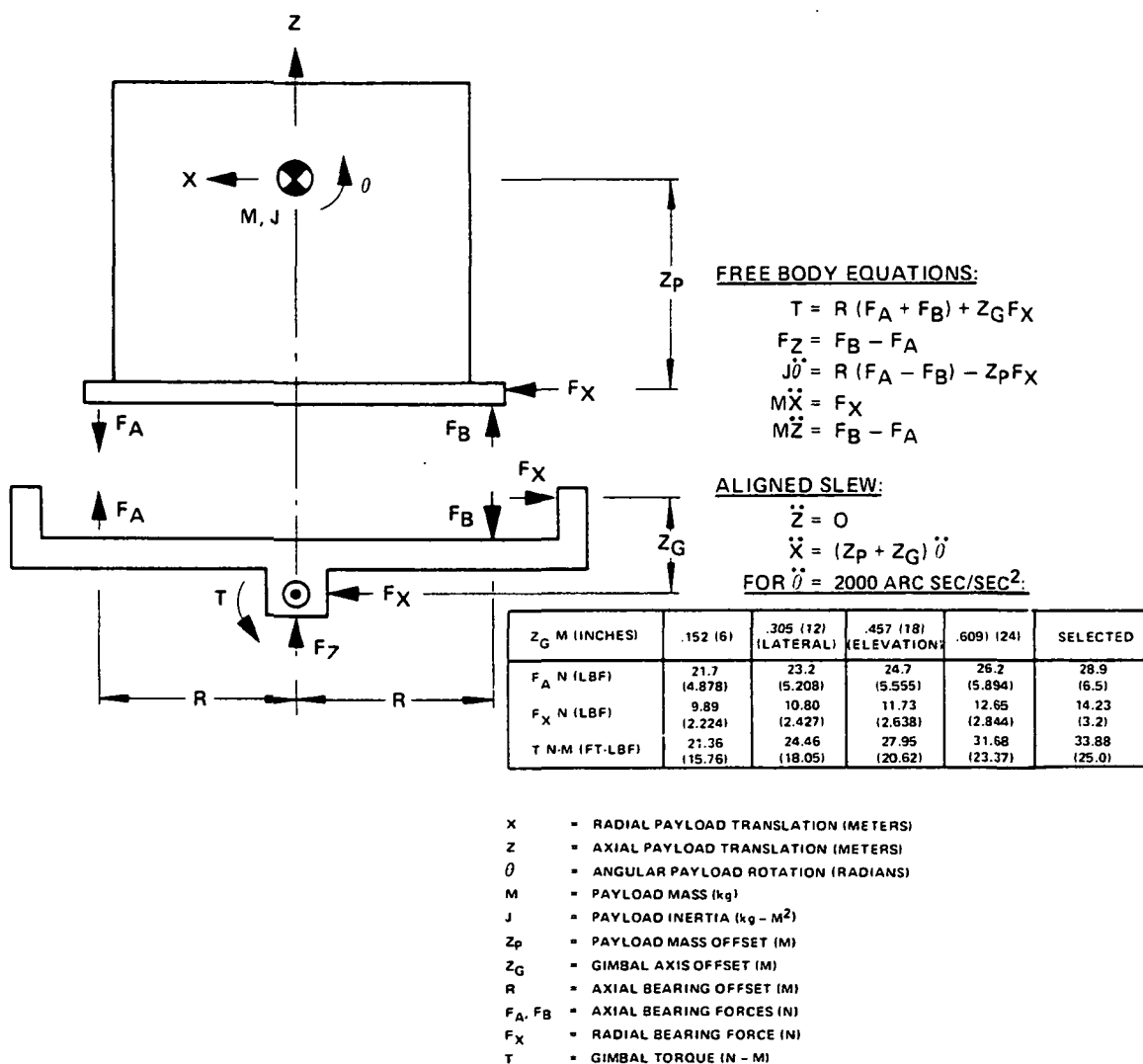


Figure 8
Torquer and Actuator Sizing

TABLE 3
ROLL AXIS REQUIREMENTS

Torquer

Acceleration: $\pm 0.06 \text{ deg/sec}^2$ at 10 to 100 kg-m^2 Payload Inertia
(7.38 to 73.8 sl-ft^2)

Rate: $\pm 1.5 \text{ deg/sec}$

Pointing Accuracy: 1 arc second

Pointing Stability: 1 arc second/second

Noncontacting

Accommodate Rotor/Stator Misalignments from Disturbances

Minimum Side Force

Stall Power < 100 Watts

Average Power < 5 Watts

Sensors

Noncontacting,

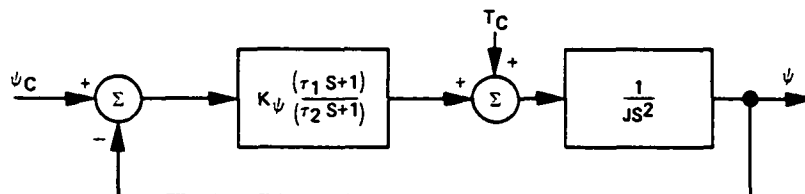
Accuracy*: 1 arc minute

System

Accuracy*: 6 arc minutes (internal sensor)

Bandwidth: 1 Hz at 90 degrees phase with 30 arc second amplitude

*Rim Centered

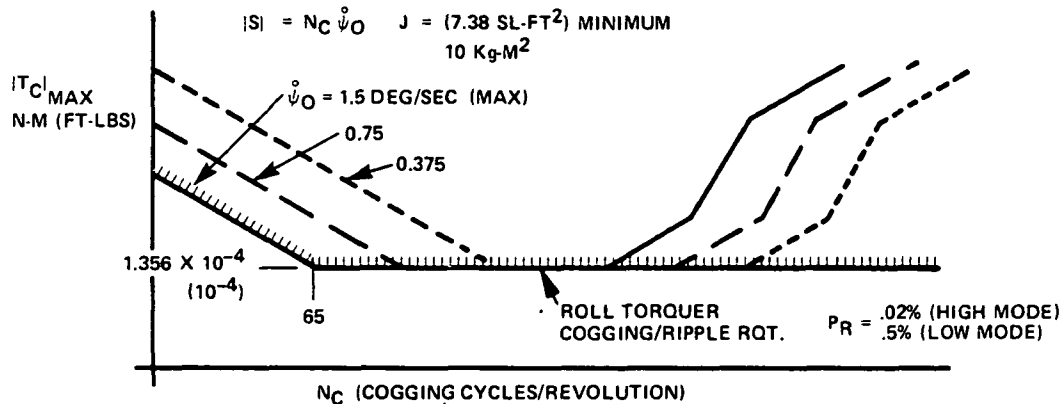


SELECTING K_ψ , τ_1 AND τ_2 FOR 1 Hz BANDWIDTH, 20% OVERSHOOT:

$$\frac{\dot{\psi}}{T_C} = \frac{\frac{S}{4.385J} \left(\frac{S}{15.5} + 1 \right)}{\left(\frac{S}{1.717} + 1 \right) \left(\frac{S}{4.083} + 1 \right) \left(\frac{S}{9.695} + 1 \right)}$$

$$\dot{\psi}_{MAX} = 1 \text{ SEC/SEC} = .000278 \text{ RAD/SEC}$$

$$|S| = N_C \dot{\psi}_O \quad J = (7.38 \text{ SL-FT}^2) \text{ MINIMUM} \\ 10 \text{ Kg-M}^2$$



- ψ = ROLL ROTATION (RADIAN)
- ψ_C = ROLL COMMAND (RADIAN)
- J = ROLL INERTIA ($\text{kg} - \text{M}^2$)
- T_C = ROLL MOTOR COGGING TORQUE (N - M)
- K_ψ = ROLL GAIN (N - M/RADIAN)
- τ_1, τ_2 = CONTROL LAW TIME CONSTANTS (SEC)
- N_C = NUMBER OF COGS PER REVOLUTION
- P_R = PERCENT RIPPLE
- $\dot{\psi}_O$ = CONSTANT ROLL RATE (RADIAN/SEC)

Figure 9
Roll Torquer Cogging

Figure 10 shows the control system employed for the roll axis. A single-speed wound resolver is used in either the control or readout modes to provide internal roll angle error feedback or external roll angle output information as described previously for the coarse gimbal resolver. A rotary transformer is used to transfer the resolver rotor signal across the vernier gap.

External payload roll error, offset roll angle command, and roll error rate signals may be used in place of the internally generated roll angular error for control. Compensation of these signals is the same as described for the coarse gimbals.

The ac induction motor is connected as a servo motor with constant fixed field excitation and a control field excitation which is proportional to the roll torque command, $T_{\psi C}$. The fixed field excitation can be switched to a high or low level to conserve power and to minimize radial unbalance forces. In the high mode, peak output torque is $\pm 6.78 \text{ N m}$ ($\pm 5 \text{ ft-lb}$) while only $\pm 0.271 \text{ N m}$ ($\pm 0.2 \text{ ft-lb}$) are available in the low mode.

The roll motor contains two curved stator segments which are nominally equidistant from the solid iron rotor. One of these segments reacts against the rotor's inside concave surface while the other segment is outside the rotor and directly opposite the inside segment. Each segment contains a fixed and a control field winding. Both fixed and variable field excitations are current controlled using active current control loops. The use of current rather than voltage control is required to effect minimum radial unbalance force from the roll actuators over the full range of radial gap variation $\pm 5.08 \text{ mm}$ ($\pm 0.200 \text{ in.}$). Since the roll motor segments act like magnetic actuators in the radial direction, it is necessary to modulate both the fixed and variable field currents proportional to the distance between the rotor and each stator segment. This distance is computed from the sensed gap measured by proximeters which are integrally mounted in the outside roll actuator segment. Since the radial attractive force is proportional to current squared and is inversely proportional to gap squared, a force balance can be achieved by causing each stator winding current to vary linearly with its respective gap. The same technique is used in both radial and axial magnetic actuators.

The highest ASPS radial control bandwidth is approximately 10 Hz, and the roll magnetic actuator current loops are therefore designed for 50 Hz bandwidth in order to compensate dynamically for radial motion. The roll motor is excited by a 200 Hz carrier in order to minimize power. Ripple from demodulating the sensed current will contain frequencies which are multiples of 400 Hz, and a second order filter located at approximately 100 Hz provides the required smoothing of this ripple without adding excessive phase lag to the roll current loop.

2.2.3 Vernier Pointing and Isolation System

Vernier payload pointing and isolation from shuttle disturbances are provided by a system of five magnetic actuator assemblies located under the payload mounting plate. Table 4 lists the key requirements of this subsystem. The pointing accuracy and stability goals of ± 1 and ± 0.1 arc seconds respectively are based on the use of an ideal payload error sensor. Since the ASPS

TABLE 4
VERNIER POINTING/ISOLATION REQUIREMENTS

Magnetic Actuators

Noncontacting, No Permanent Magnets

Centering During Slew, Translational Isolation During Pointing

Angular Range: ± 75 degrees

Pointing Accuracy: ± 1 arc seconds

Pointing Stability: ± 0.01 arc seconds

System

Bandwidth: 1 Hz at 90 degrees phase with 182.6 arc seconds amplitude
600 kg payload, inertia 50 to 500 kg-m²

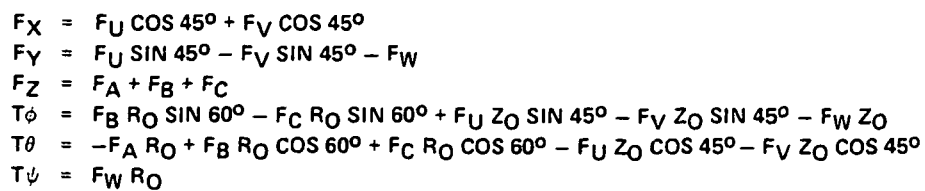
Decoupling of Radial Centering Forces into Payload Torques with 0 to 1.5
Meter CM (Center of Mass) Offset

Electronics Standby Power: 5 Watts

is an end-mounted system, shuttle motion from vernier reaction jet firing and man motion will introduce a disturbance torque about the payload center of mass. If not compensated, this disturbance torque will introduce a transient pointing error in excess of the stability requirement for any reasonable control loop bandwidth.

Unlike conventional mechanical isolation systems, the ASPS magnetic actuators can be adjusted to provide extremely low isolation frequencies and, in addition, the axial actuators can be used differentially to produce a torque on the payload which cancels the moment due to the radial actuator force applied through the CM offset. This decoupling of the radial centering forces is a key to achieving the required pointing stability, and it depends on having linear and gain-matched magnetic actuator assemblies. Decoupling provides the ASPS with the advantages of a CM mount with the flexibility of an end mounted system.

Figure 11 shows the location of the various magnetic actuators and the nomenclature used. The three axial actuators are designated A, B, and C and are spaced at radius R_0 , 120 degrees apart. The radial actuators are U and V and are located ± 45 degrees from the A actuator. Roll torque is produced by a force at point W which is diametrically opposite A. The payload CM is located at distance Z_0 directly above the center of the vernier actuator plane, and forms the origin of the payload fixed coordinate system, X, Y, Z.



25

The six forces and torques acting on the payload are listed in terms of the individual actuator forces at the bottom of Figure 11. While there are a total of 6 actuators (including roll) and 6 degrees of freedom, the end mount geometry creates significant coupling. This coupling is indicated on the block diagram of Figure 13 by the summing junction on the right side. The matrix products shown represent the geometrical layout of the actuators in the plane of the payload rim and are not related to the end mount cg offset. Decoupling is accomplished by crossfeeding electrical signals proportional to the commanded actuator forces in the control circuitry on the left-hand side of the diagram. Knowledge of the actual cg location is necessary to provide accurate decoupling since the crossfeed gains are proportional to Z_0 , the estimated offset distance.

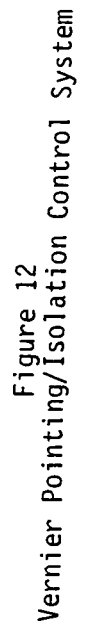
Under the assumption of ideal decoupling, all of Figure 13 can be condensed to the blocks shown as "decoupled vernier dynamics" on Figure 12. This figure also shows the control loops used to provide translational isolation and vernier pointing. (The roll crossfeed has been omitted for clarity.) Matrix products are indicated in Figure 12 to obtain the translational gap motions at each actuator which are sensed by the integral proximeters. The terms ϕ_G , θ_G , Z_G , U_G , and V_G represent angular and translational motion of the coarse gimbal side of the vernier assembly; i.e., motion of the proximeters themselves.

The axial proximeter signals \hat{g}_A , \hat{g}_B , and \hat{g}_C are combined electronically to compute the relative axial motion of the payload \hat{Z}_R , and the relative tilt of the payload, $\hat{\phi}_R$ and $\hat{\theta}_R$. Relative translations \hat{Z}_R , \hat{U}_R , and \hat{V}_R are used at all times to provide centering of the payload plate relative to the coarse gimbal side of the VPA. The bandwidth of these centering loops switches from a low value (typically .1 Hz) used for fine pointing to a high value (typically 10 Hz) during slew. The minimum bandwidth is selected to prevent gap touchdown during worst-case shuttle limit cycle motion.

The vernier pointing axes (ϕ and θ) are centered for zero relative tilt during slew by closing the pointing servo loops on $\hat{\phi}_R$ and $\hat{\theta}_R$. During vernier pointing, external payload pointing signals are accepted. As in the case of the coarse gimbals and the roll servo, these externally provided signals represent payload angular error, payload angular rate and an offset pointing command.

2.2.4 Backup Caging and Latches

During launch and reentry, the ASPS is held by a system of latching mechanisms to the pallet integration structure. Caging latches are located under the vernier assembly bottom plate, and for larger payloads in the plane of the payload cg. Vernier latches are located inside the vernier assembly and are used to connect the suspended and fixed sides of the vernier structure. To minimize loading on the coarse gimbal bearings and components inside the vernier pointing assembly, the fine vernier latches are engaged and the base of vernier assembly is rigidly caged by three additional latches to the caging support structure. Location of the latches within the vernier assembly ensures that the launch and landing loads are supported by the caging system and are not transmitted through the coarse gimbal bearings. One of each type of latch may fail without preventing the retention of the ASPS during reentry.



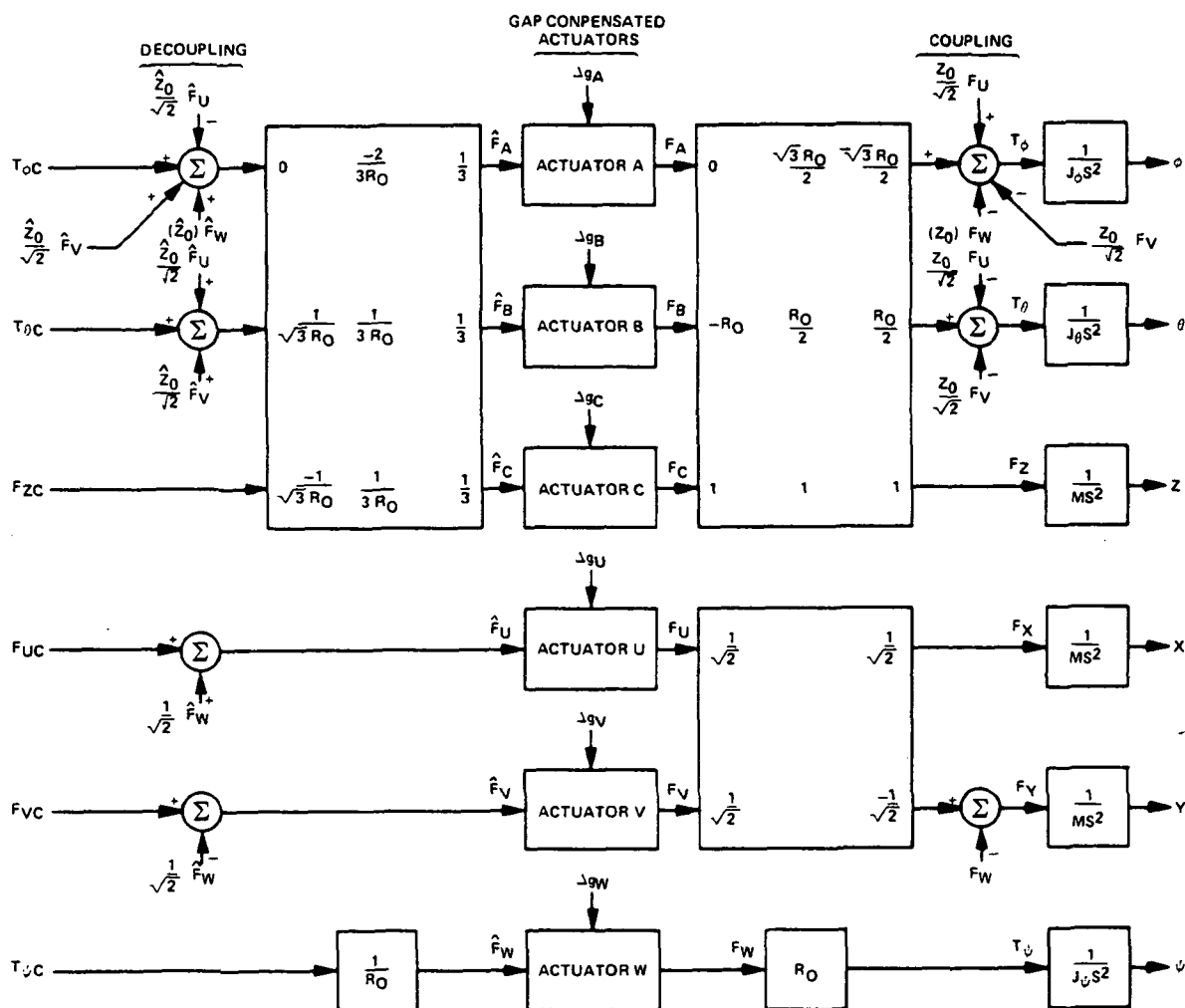


Figure 13
Vernier Actuator Decoupling

A coarse gimbal backup system is provided for caging the ASPS following a failure of the lateral or elevation gimbal control systems (no roll orientation is required for caging); Figure 14 illustrates the technique used. Each coarse gimbal torquer contains samarium cobalt permanent magnets which cannot be demagnetized by the stator currents, even with full bus voltage applied across a winding. This prevents the torquer magnets from becoming a single point failure. Redundant sine and cosine phase windings are switched sequentially to the backup 28 V dc bus by relays which are hard wired to control circuitry on the ASPS information panel. This provides discrete commutation of the torquer and allows it to be used as a permanent magnet stepping motor. To determine whether the gimbal angle is clockwise or counterclockwise from the caged position, an independent optical sensor is included on each gimbal. This is also brought back to the information panel via hardwired connections. The step size is determined by the number of poles (24) and phases (2) in the torquer and is $360/(24)(2) = 7.5$ degrees. An interlock is provided on the information panel to prevent moving the elevation gimbal in this mode until the lateral gimbal is first positioned within one step of its null.

2.2.5 Operational Modes

Each ASPS control servo is arranged to provide maximum flexibility of operation in terms of mission pointing profiles, payload mass and inertia properties, and available payload error sensing. For a given mission, prior analysis of these requirements will determine the gains, time constants, position, and/or rate inputs which are combined to form the torque commands for each control servo.

Control modes which may be selected for each control servo are listed in Table 5. While the parameters necessary to provide required performance for each of these modes are determined before launch, any of these modes may be selected unless logically prohibited by the Spacelab ASPS software.

Feedback for the axial and radial translation servos is always derived from the internal proximeters. However, either internal or external angular errors may be used for feedback on the coarse, roll, and vernier pointing servos. The coarse gimbal servos utilize their internal resolvers for feedback in all modes except for coarse pointing with the vernier latched. In the latter case, external feedback is selected and the attitude error from the payload is compensated to form the gimbal torque command. If payload rate is available, it is summed with the attitude error also. An offset pointing command is subtracted from the payload attitude error when external feedback is used.

In the vernier pointing axes (pitch and yaw), the command may be either angle or rate. Rate commands are integrated by the ASPS electronics to form a smooth raster command without taxing the data handling capabilities of the Spacelab Command and Data Management System (CDMS). All of the rotational and translational servos have a high and low bandwidth mode. Normally the coarse gimbals are used in the high mode for fine pointing, rastering, etc, while the vernier servos are in a low bandwidth mode. If a coarse gimbal slew is required or if the coarse gimbals are to be used for payload pointing (vernier system fixed), the suspension servos are stiffened and the coarse bandwidth reduced to handle the much larger effective payload inertia.

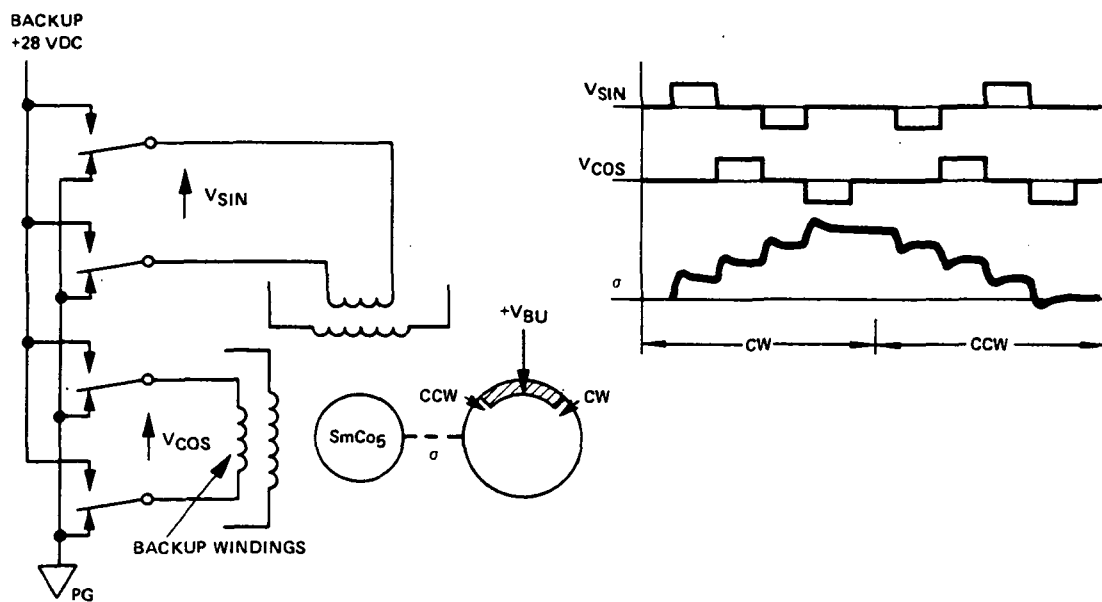


Figure 14
Coarse Gimbal Backup System

TABLE 5
ASPS SERVO CONTROL MODES

Servo	Control Modes Available
Elevation	Elevation Feedback (Internal or External) Elevation Bandwidth (High or Low)
Lateral	Lateral Feedback (Internal or External) Lateral Bandwidth (High or Low)
Roll	Roll Feedback (Internal or External) Roll Bandwidth (High or Low) Torque Mode (High or Low)
Pitch	Pitch Feedback (Internal or External) Pitch Bandwidth (High or Low) Pitch Command (Angle or Rate)
Yaw	Yaw Feedback (Internal or External) Yaw Bandwidth (High or Low) Yaw Command (Angle or Rate)
Axial	Axial Bandwidth (High or Low)
Radial - U	Radial U Bandwidth (High or Low)
Radial - V	Radial V Bandwidth (High or Low)

Table 6 lists five typical operational modes which are formed by combining the control modes in Table 5. The terminology used in this table requires some explanation as follows:

- σ_c , γ_c , ψ_c , θ_c , and ϕ_c represents angular commands to the elevation, lateral, roll, pitch, and yaw servos, respectively.
- Δ prefix denotes an offset pointing command
- $(\dot{})$ represents a rate command
- "e" subscript means an error output
- "R" subscript represents the relative error between vernier and coarse gimbal surfaces as measured by the proximeters
- CST denotes a constant value of the command
- 0 a zero value
- $\int \theta_R$ or $\int \phi_R$ indicates that the command is proportional to the integrated relative tilt
- SLW stands for slew profile
- PRX for proximeter
- RES for resolver
- P/L for payload

The bandwidths shown in Table 6 are preliminary values which have been selected from representative mission simulation studies. The actual bandwidths, command inputs, and feedbacks selected would be optimized for a particular payload configuration and mission.

As an example of the use of this table, consider the coarse gimbal follow-up mode (second line). The lateral and elevation servo loops are closed on their respective resolvers with a high bandwidth. This provides a stiff base under the 1 Hz vernier pointing servos. The angular command to the coarse gimbals is derived by integrating the tilt between the vernier and coarse gimbals. A low integrator gain is used such that the coarse gimbal receives a nearly constant input command which changes slowly to "follow-up" on a steady state or low frequency error between coarse and fine pointing systems. Both radial and axial suspension servos are placed in the low bandwidth mode for maximum isolation from shuttle disturbances.

TABLE 6A
TYPICAL ASPS OPERATING MODES

OPERATIONAL MODE (P/L SENSING)	ELEVATION			LATERAL			ROLL		
	COMMAND	FEEDBACK	B.W.	COMMAND	FEEDBACK	B.W.	COMMAND	FEEDBACK	B.W.
FINE POINTING (3-AXIS P/L ATTITUDE AND RATE SENSOR)	$\sin a_C$ $\cos a_C$ $a_C = \text{CST}$	σ (RES)	10 Hz	$\sin \gamma_C$ $\cos \gamma$ $\gamma_C = \text{CST}$	γ (RES)	10 Hz	$\Delta \psi_C$	$\dot{\psi}_\theta$ (P/L) $\dot{\psi}$ (P/L)	1 Hz
FINE POINTING WITH COARSE GIMBAL FOLLOWUP (2-AXIS P/L ATTITUDE)	$\sin a_C$ $\cos a_C$ $a_C = \int \theta_R$	σ (RES)	10 Hz	$\sin \gamma_C$ $\cos \gamma_C$ $\gamma_C = \int \phi_R$	γ (RES)	10 Hz	$\sin \psi_C$ $\cos \psi_C$ $\psi_C = \text{CST}$	ψ (RES)	1 Hz
PITCH/YAW RASTER (NO P/L SENSING)	$\sin a_C$ $\cos a_C$ $a_C = \text{CST}$	σ (RES)	10 Hz	$\sin \gamma_C$ $\cos \gamma_C$ $\gamma_C = \text{CST}$	γ (RES)	10 Hz	$\sin \psi_C$ $\cos \psi_C$ $\psi_C = \text{CST}$	ψ (RES)	1 Hz
COARSE POINTING (2-AXIS P/L ATTITUDE AND RATE)	Δa_C	θ_θ (P/L) $\dot{\theta}$ (P/L)	1 Hz	$\Delta \gamma_C$	ϕ_θ (P/L) $\dot{\phi}$ (P/L)	1 Hz 1 Hz	-	-	-
COARSE SLEW (NO P/L SENSING)	$\sin a_C$ $\cos a_C$ $a_C = \text{SLW}$	σ (RES)	.1 Hz	$\sin \gamma_C$ $\cos \gamma_C$ $\gamma_C = \text{SLW}$	γ (RES)	.1 Hz	$\sin \psi_C$ $\cos \psi_C$ $\psi_C = \text{CST}$	ψ (RES)	1 Hz

TABLE 6B
TYPICAL ASPS OPERATING MODES (cont)

OPERATIONAL MODE (P/L SENSING)	PITCH VERNIER			YAW VERNIER			AXIAL B.W.	RADIAL-U B.W.	RADIAL-V B.W.	VERNIER LATCH
	COMMAND	FEEDBACK	B.W.	COMMAND	FEEDBACK	B.W.				
FINE POINTING (3-AXIS P/L ATTITUDE AND RATE SENSOR)	$\Delta\theta_C$	θ_e (P/L) $\dot{\theta}$ (P/L)	1 Hz	$\Delta\phi_C$	ϕ_e (P/L) $\dot{\phi}$ (P/L)	1 Hz	.04 Hz	.04 Hz	.04 Hz	UNLATCHED
FINE POINTING WITH COARSE GIMBAL FOLLOW UP (2 AXIS P/L ATTITUDE)	$\Delta\theta_C$	θ_e (P/L)	1 Hz	$\Delta\phi_C$	ϕ_e (P/L)	1 Hz	.04 Hz	.04 Hz	.04 Hz	UNLATCHED
PITCH/YAW RASTER (NO P/L SENSING)	$\Delta\theta_C$	θ_R (PRX)	1 Hz	$\Delta\phi_C$	ϕ_R (PRX)	1 Hz	.04 Hz	.04 Hz	.04 Hz	UNLATCHED
COARSE POINTING (2-AXIS P/L ATTITUDE AND RATE)	-	-	-	-	-	-	-	-	-	LATCHED
COARSE SLEW (NO P/L SENSING)	$\Delta\theta_C = 0$	θ_R (PRX)	10 Hz	$\Delta\phi_C = 0$	ϕ_R (PRX)	10 Hz	1 Hz	1 Hz	1 Hz	UNLATCHED

2.3 STRUCTURAL FLEXIBILITY

Initial mechanical design of the ASPS was based on a highly conservative criteria for structural stiffness. The assumption was made that all control servos were rigid (infinite stiffness), and that the maximum payload mass, inertia, and cg offsets existed. Component brackets, plates, shafts, etc were selected so as to provide a minimum natural frequency of 100 Hz operating independently and 10 Hz minimum using composite stiffnesses. In reality, the control loops have low stiffness in comparison to the structure, thereby separating the system into a number of weakly coupled spring-mass assemblies.

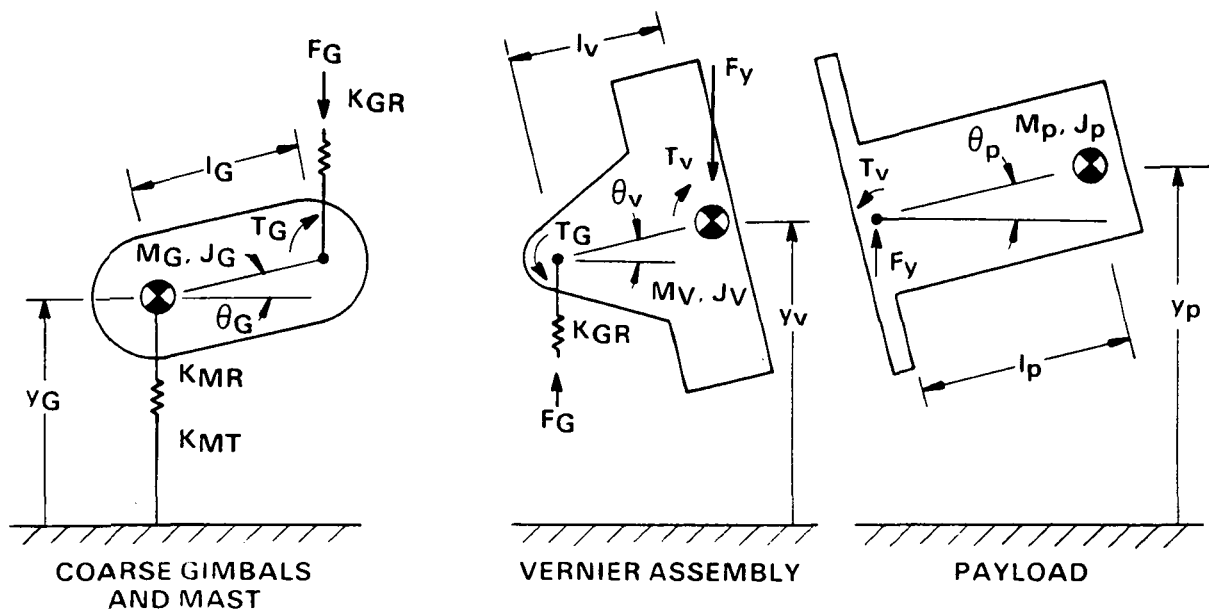
The worst case (most compliant structure with highest cantilevered mass) occurs when the elevation angle is close to its caged position and consists of both torsional and translational motion. Figure 15 illustrates the free body dynamics considered. The dynamic equations of motion for this system, in matrix form are:

$$\begin{bmatrix} (M_G S^2 + K_{MR}) & 0 & 0 & 0 & 0 & 0 & +1 & 0 & 0 & 0 & Y_G \\ 0 & (J_G S^2 + K) & 0 & 0 & 0 & 0 & +1G & +1 & 0 & 0 & \theta_G \\ 0 & 0 & M_V S^2 & 0 & 0 & 0 & -1 & 0 & +1 & 0 & Y_V \\ 0 & 0 & 0 & J_V S^2 & 0 & 0 & +1V & -1 & 0 & +1 & \theta_V \\ 0 & 0 & 0 & 0 & M_P S^2 & 0 & 0 & 0 & -1 & 0 & Y_P \\ 0 & 0 & 0 & 0 & 0 & J_P S^2 & 0 & 0 & +1P & -1 & \theta_P \\ -K_{GR} & -1G K_{GR} & +K_{GR} & -1V K_{GR} & 0 & 0 & +1 & 0 & 0 & 0 & F_G \\ 0 & -K_G(\tau_{1G} S + 1) & 0 & K_G(\tau_{1G} S + 1) & 0 & 0 & 0 & (\tau_{2G} S + 1) & 0 & 0 & T_G \\ 0 & 0 & -K_Y(\tau_{1Y} S + 1) & 0 & K_Y(\tau_{1Y} S + 1) & -K_Y 1P(\tau_{1Y} S + 1) & 0 & 0 & (\tau_{2G} S + 1) & 0 & F_Y \\ 0 & 0 & 0 & -K_V(\tau_{1V} S + 1) & 0 & K_V(\tau_{1V} S + 1) & 0 & 0 & -1P(\tau_{2V} S + 1) & (\tau_{2V} S + 1) & T_V \end{bmatrix} \begin{bmatrix} 0 \\ 0 \\ 0 \\ 0 \\ 0 \\ 0 \\ 0 \\ 0 \\ 0 \\ 0 \\ 0 \end{bmatrix} \quad (3)$$

K_G = GIMBAL SERVO STIFFNESS (N-M/RADIAN)
 τ_{1G}, τ_{2G} = GIMBAL SERVO TIME CONSTANTS (SEC)
 K_Y = RADIAL CENTERING SERVO STIFFNESS (N/M)
 τ_{1Y}, τ_{2Y} = RADIAL CENTERING SERVO TIME CONSTANTS (SEC)
 K_V = VERNIER POINTING SERVO STIFFNESS (N-M/RADIAN)
 τ_{1V}, τ_{2V} = VERNIER POINTING SERVO TIME CONSTANTS (SEC)
 OTHER SYMBOLS ARE DEFINED ON FIGURE 15

Roots of the characteristic equation of this system are listed in Table 7. A relatively wide frequency separation exists between the servo roots and the structural mode roots. Also, as each of the structural stiffnesses was varied, the control system poles were not significantly affected. One exception occurs when the mast radial stiffness is reduced by a factor of five causing the mast radial translation mode frequency to overlap the roots associated with the vernier pointing servo.

The conclusion to be drawn from this preliminary assessment of flexibility is that the current design provides a wide separation between the control and structural modes with little dynamic coupling.



M_P = PAYLOAD MASS (kg)
 J_P = PAYLOAD INERTIA (kg-M^2)
 θ_P = PAYLOAD ROTATION (RADIAN)
 y_P = PAYLOAD TRANSLATION (M)
 l_P = PAYLOAD OFFSET (M)
 F_V = VERNIER RADIAL FORCE (N)
 T_V = VERNIER TORQUE (N-M)
 y_V = VERNIER TRANSLATION (M)
 M_V = VERNIER MASS (kg)
 J_V = VERNIER INERTIA (kg-M^2)
 θ_V = VERNIER ROTATION (RADIAN)

l_V = VERNIER OFFSET (M)
 T_G = GIMBAL TORQUE (N-M)
 F_G = GIMBAL RADIAL FORCE (N)
 K_{GR} = GIMBAL RADIAL STIFFNESS (N/M)
 I_G = GIMBAL AXIS OFFSET (M)
 M_G = GIMBAL MASS (kg)
 J_G = GIMBAL INERTIA (kg-M^2)
 θ_G = GIMBAL ROTATION (RADIAN)
 Y_G = GIMBAL TRANSLATION (M)
 K_{MR} = MAST RADIAL STIFFNESS (N/M)
 K_{MT} = MAST TORSIONAL STIFFNESS (N-M/RADIAN)

Figure 15
Simplified Structural Flexibility Dynamics - Elevation Near Zero

TABLE 7
SENSITIVITY OF ASPS DYNAMICS TO STRUCTURAL STIFFNESSES

ASPS – ROOTS OF CHARACTERISTIC EQUATION SLEW MODE 90° ELEVATION ANGLE	NOMINAL STIFFNESSES	MAST TORSIONAL STIFFNESS		MAST RADIAL STIFFNESS		GIMBAL RADIAL STIFFNESS	
		X 1/5	X 5	X 1/5	X 5	X 1/5	X 5
COARSE GIMBAL SERVO	$\xi = .76$ } $\omega = .247$ } $\omega = .613$	$\xi = .76$ } $\omega = .247$ } $\omega = .613$	$\xi = .76$ } $\omega = .247$ } $\omega = .613$	$\xi = .76$ } $\omega = .247$ } $\omega = .613$	$\xi = .76$ } $\omega = .247$ } $\omega = .613$	$\xi = .76$ } $\omega = .247$ } $\omega = .613$	$\xi = .76$ } $\omega = .247$ } $\omega = .613$
RADIAL CENTERING SERVO	$\xi = .29$ } $\omega = 4.91$ } $\omega = 1.61$	$\xi = .29$ } $\omega = 4.91$ } $\omega = 1.61$	$\xi = .29$ } $\omega = 4.91$ } $\omega = 1.61$	$\xi = .29$ } $\omega = 4.89$ } $\omega = 1.61$	$\xi = .29$ } $\omega = 4.91$ } $\omega = 1.61$	$\xi = .29$ } $\omega = 4.91$ } $\omega = 1.61$	$\xi = .29$ } $\omega = 4.91$ } $\omega = 1.61$
VERNIER POINTING SERVO	$\xi = .23$ } $\omega = 45.9$ } $\omega = 98.5$	$\xi = .23$ } $\omega = 45.8$ } $\omega = 98.9$	$\xi = .23$ } $\omega = 45.8$ } $\omega = 99.0$	$\xi = .22$ } $\omega = 47.9$ } $\omega = 94.7$	$\xi = .24$ } $\omega = 45.5$ } $\omega = 101.$	$\xi = .23$ } $\omega = 46.1$ } $\omega = 97.1$	$\xi = .23$ } $\omega = 45.7$ } $\omega = 99.4$
MAST RADIAL MODE	$\xi = .01$ } $\omega = 177.$ }	$\xi = .01$ } $\omega = 176.$ }	$\xi = .01$ } $\omega = 178.$ }	$\xi = .05$ } $\omega = 79.5$ }	$\xi = 0$ } $\omega = 387.$ }	$\xi = .02$ } $\omega = 161.$ }	$\xi = .01$ } $\omega = 181.$ }
GIMBAL RADIAL MODE (DUMBBELL)	$\xi = 0$ } $\omega = 799.$ }	$\xi = 0$ } $\omega = 701.$ }	$\xi = 0$ } $\omega = 822.$ }	$\xi = 0$ } $\omega = 787.$ }	$\xi = 0$ } $\omega = 924.$ }	$\xi = 0$ } $\omega = 406.$ }	$\xi = 0$ } $\omega = 1645.$ }
MAST TORSIONAL MODE	$\xi = 0$ } $\omega = 2897.$ }	$\xi = 0$ } $\omega = 1492.$ }	$\xi = 0$ } $\omega = 7143.$ }	$\xi = 0$ } $\omega = 2897.$ }	$\xi = 0$ } $\omega = 2897.$ }	$\xi = 0$ } $\omega = 2827.$ }	$\xi = 0$ } $\omega = 3506.$ }

ξ = DAMPING FACTOR OF ROOT
 ω = NATURAL FREQUENCY OF ROOT

2.4 MAGNETIC SUSPENSION STATION CONTROL SYSTEM

The magnetic actuators used for radial and axial suspension are inherently nonlinear devices which require a unique compensation in this application. Figure 16 shows the geometry associated with each dual coil actuator. The soft iron rotor is attracted to solenoids 1 and 2 by forces F_1 and F_2 , respectively.

The net force can be found from the coenergy associated with the flux linkage between stator and rotor.

$$\begin{aligned} F &= \frac{1}{2} \frac{d}{dg} \left[\frac{L_G I_1^2}{(1 - \Delta g/g_0)} + \frac{L_G I_2^2}{(1 + \Delta g/g_0)} \right] \\ &= \frac{K}{g_0^2} \left[\frac{I_1^2}{(1 - \Delta g/g_0)^2} - \frac{I_2^2}{(1 + \Delta g/g_0)^2} \right] \end{aligned} \quad (4)$$

where the actuator constant is:

$$K \triangleq \frac{L_G g_0}{2}$$

(A derivation of the actuator dynamics and force equations is given in Appendix C.)

Note that the force is proportional to the square of the coil currents and is inversely proportional to the square of the distance to each coil. To remove the current-squared nonlinearity, a bias current technique is used. This consists of adding a bias current to one coil and subtracting the same bias current from the opposite coil.

To compensate for the inverse-gap-squared relationship, the total (bias and command) currents to each coil are multiplied by signals proportional to the measured gap of that coil.

$$I_{1C} = (1 - \Delta g/g_0) \left[I_0 + \left(\frac{g_0^2}{4K I_0} \right) F_C \right] \quad (5)$$

$$I_{2C} = (1 + \Delta g/g_0) \left[I_0 - \left(\frac{g_0^2}{4K I_0} \right) F_C \right] \quad (6)$$

where

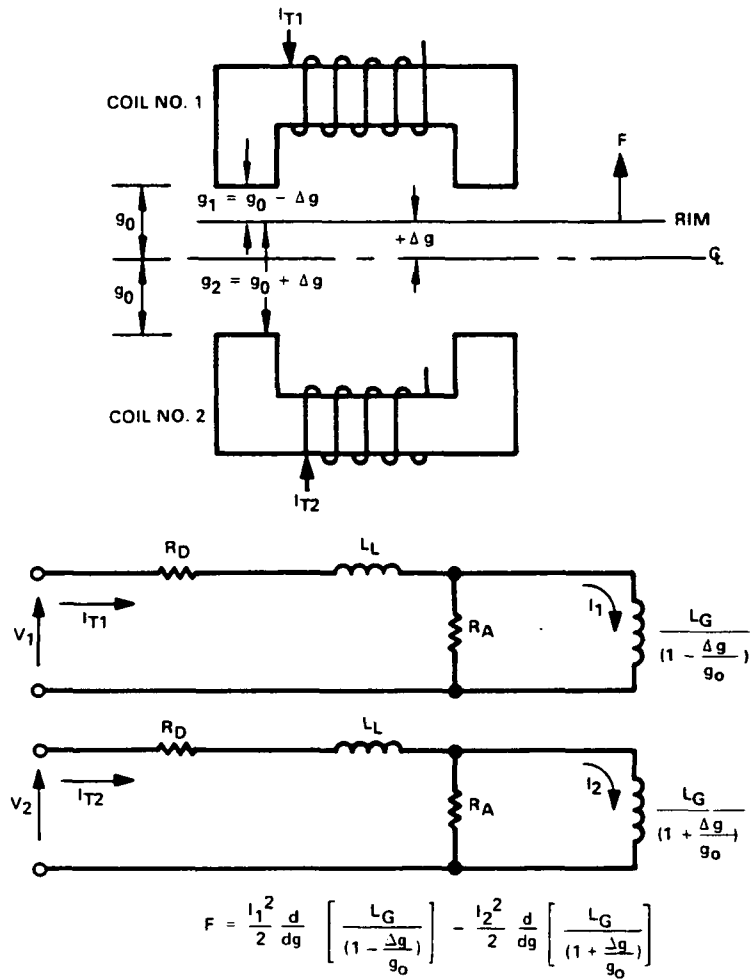
I_0 = Bias current (amperes)

I_C = Command current (amperes)

F_C = Command force (W)

and other symbols are as defined in Figure 16.

The magnitude of the bias current determines the scale factor between the current and force; it also affects the power dissipated in the actuator. On ASPS, the bias current was selected to minimize the peak power.



- g_0 = NOMINAL GAP (M)
- Δg = CHANGE IN GAP (M)
- 1, 2 = (SUBSCRIPTS) IDENTIFY PARAMETERS ASSOCIATED WITH COILS 1 AND 2
- F = FORCE (N)
- V = APPLIED COIL VOLTAGE (VOLTS)
- I_T = COIL CURRENT (AMPERES)
- I = MAGNITIZING CURRENT (AMPERES)
- L_G = MAGNITIZING INDUCTANCE (HENRIES)
- L_L = LEAKAGE INDUCTANCE (HENRIES)
- R_D = DC RESISTANCE (OHMS)
- R_A = AC RESISTANCE (OHMS)

Figure 16
Magnetic Suspension Station Dynamics

$$I_0 = \frac{g_0}{2} \sqrt{\frac{F_{MAX}}{K}} \quad (7)$$

where F_{max} is the maximum force output of the actuator.

This choice has the property that the net current through one coil doubles as the force command increases from zero to maximum, while the current through the opposite coil drops to zero under the same condition. This permits the MBAs to be driven from power amplifiers which do not have to provide bidirectional current outputs.

Figure 17 illustrates in block diagram form the nonlinear force equation given on Figure 16. The bias current linearization technique is included in the diagram. To compensate for the inverse-gap-squared relationship, indicated by the dividers, a signal proportional to the gap is used to multiply each coil current. The current-squared characteristic of the magnetics itself is used to generate a gap-squared gain characteristic which cancels the inverse gap-squared relationship. Through block diagram reduction, the electronic gap compensation can be implemented using a single four-quadrant multiplier as indicated in the lower half of Figure 17.

A significant advantage in the use of an all active (nonpermanent magnet) actuator in this application lies in the large variation in operating gap. Permanent magnets could be added to the magnetic circuit which, at a given gap, produce a bias flux indistinguishable from that produced by a bias current through the coils. The permanent magnet bias flux varies inversely with the gap resulting in the familiar static instability associated with positioning a piece of soft iron between two permanent magnets. As the iron moves from the equilibrium position at the center, the attractive force increases with the inverse-square of distance to the magnets pole pieces. By sensing this distance and actively controlling the current through the MBA coils, this instability could be controlled. The servo gain required must exceed the incremental gain of the static instability, which may be modeled as a negative spring constant. Since this spring constant is proportional to the inverse of the gap, the servo gain must be made large enough to overcome the instability at minimum gap. This requires a relatively high gain (high bandwidth) servo loop, since the permanent magnet must be sized to provide sufficient flux at the maximum gap to linearize the maximum force command. Permanent magnets are used to linearize magnetic actuators in applications where the gap variation is small compared to the total gap. On the ASPS, large gap motion is needed to provide low frequency translational isolation. For example, the axial gap varies by ± 5.59 mm ($\pm .22$ inch). If the nominal gap is sized so that the gap variation is a small fraction of the total gap, the actuator size would be impractical. When the bias flux is generated electronically, as in ASPS, it may be compensated by using a multiplier to eliminate the large nonlinearity due to the gap variation.

A simple current loop is used to provide a high bandwidth control of the actuator coil currents. Figure 18 summarizes the design procedure used to select the forward loop compensation. The assumption of low gap rate and high ac resistance, low eddy current losses, are good for the ASPS actuators. Closed loop bandwidth of the current loop, and therefore the overall actuator, is that of a 100 Hz first order lag.

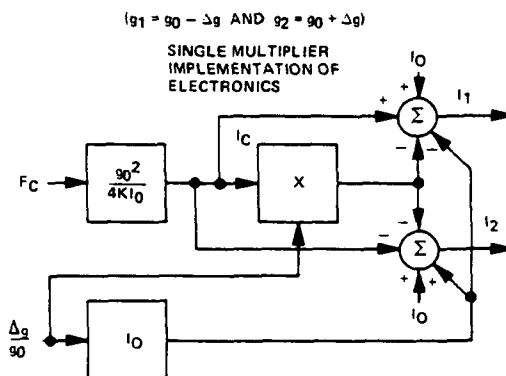
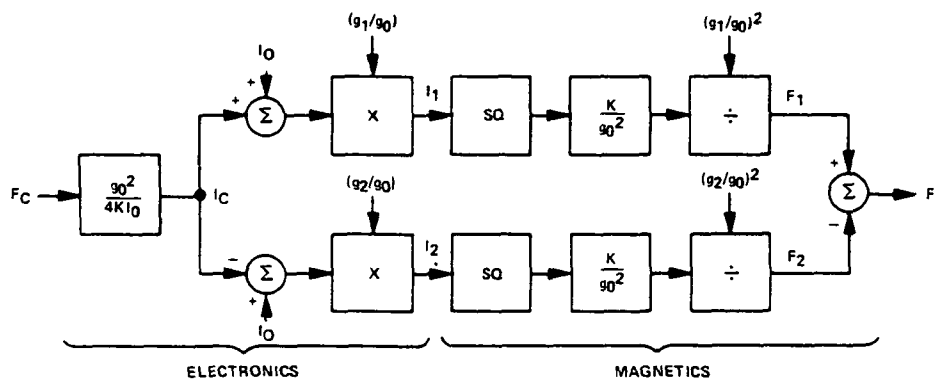
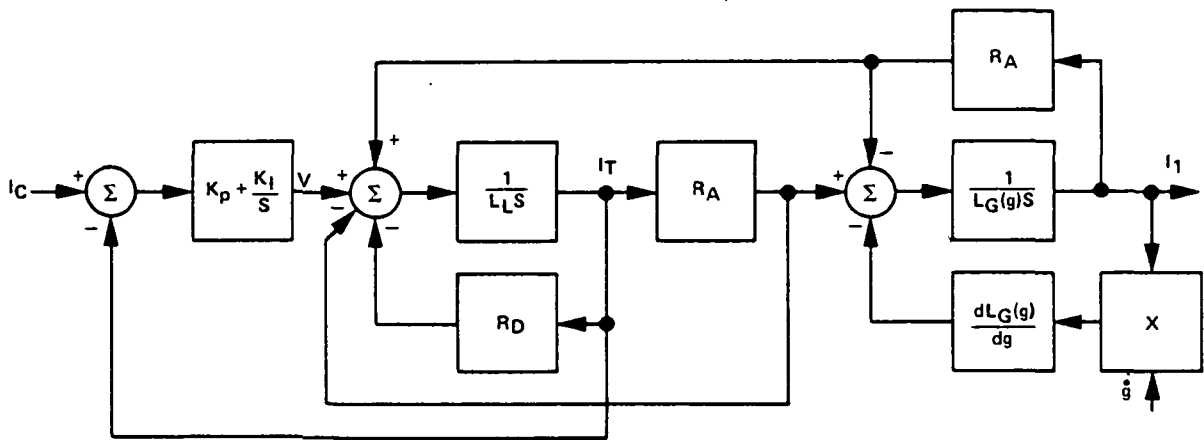


Figure 17
Gap Compensation



FOR $\dot{\theta} = 0$ AND $g = 90$ AND $R_A \gg R_D$

$$\frac{I_T}{V} = \frac{L_G S + R_A}{L_L L_G S^2 + R_A (L_L + L_G) S + R_A R_D} \approx \frac{1}{(L_L + L_G) S + R_D} \approx \frac{I_1}{V}$$

$K_P =$ PROPORTIONAL GAIN (VOLTS/AMP)

$K_I =$ INTEGRAL GAIN (VOLTS/AMP-SEC)

AND OTHER SYMBOLS ARE AS DEFINED ON FIGURE 16

CONTROL LAW:

$$K_P + \frac{K_I}{S} = \frac{K_C}{S} \{ (L_L + L_G) S + R_D \}$$

CLOSED LOOP:

$$\frac{I_1}{I_c} \approx \frac{K_C}{S + K_C}$$

Figure 18
Dynamic Compensation

Page Intentionally Left Blank

SECTION 3.0

SYSTEM PERFORMANCE

Performance analysis has primarily consisted of optimizing and evaluating fine pointing performance in the presence of Shuttle disturbances. Several types of pointing controllers have been evaluated and the effect of bandwidth on the pointing, suspension, and gimbal servos has been evaluated. The effect of most potential error sources such as: CM decoupling errors, actuator mismatch, gimbal friction, and payload cable effects have also been evaluated.

Other areas of ASPS performance analysis covered in this study include: latched vernier pointing performance and some preliminary raster and slewing performance studies. The simulations utilized in these studies are described in Appendices A and B.

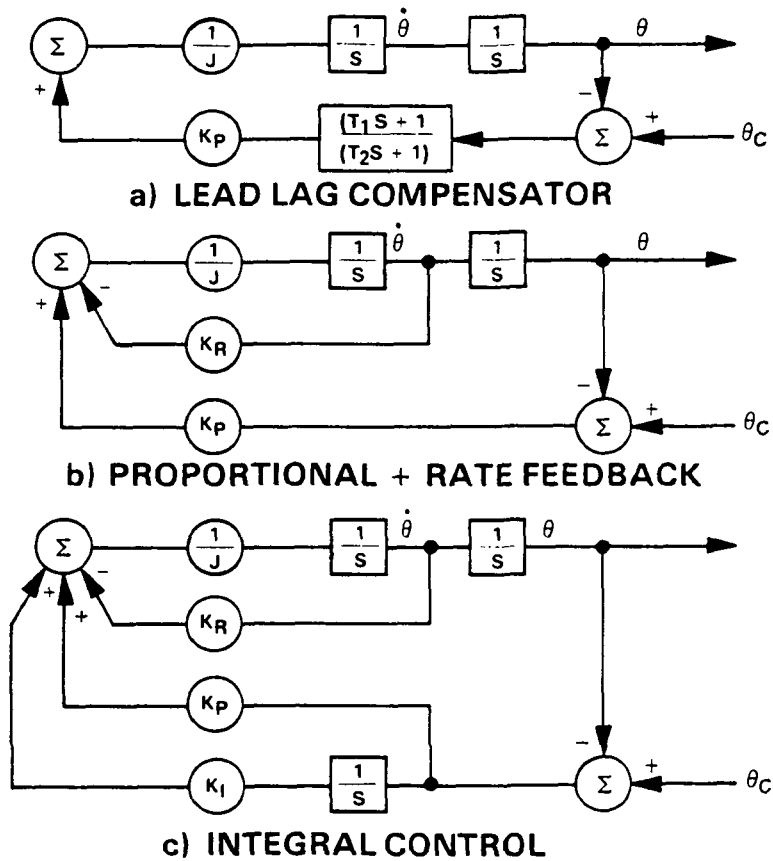
3.1 POINTING CONTROLLER DESIGN AND PERFORMANCE ANALYSIS

Three pointing servo types, as illustrated in Figure 19, have been considered in this study. The three types illustrated are:

1. Attitude error feedback with lead/lag compensation.
2. Attitude error and attitude rate feedback.
3. Attitude error and rate feedback plus integral of attitude error feedback.

Closed loop bandwidth of the vernier pointing servos is specified at one hertz which has been defined, in this study, as 3 dB gain and 85 degrees phase lag at one hertz on the pointing servo closed loop frequency response. Gains and time constants for the three one hertz servo designs are shown in Table 8. Closed loop frequency response of the three servos is illustrated in Figures 20, 21, and 22. This data has been obtained from the linearized ASPS model which is described in Appendix A. It is seen that each servo has been adjusted to approximately -3 dB gain and 85 degrees phase lag at one hertz. The step response of the three servos to a 100 arc second step command is shown in Figure 23. These plots have been obtained from the full scale ASPS simulation described in Appendix B.

Response of the three controller types, set at approximately equal bandwidth, to Shuttle transient disturbances has been studied. The characteristics of a Shuttle pitch transient defined as a worst-case Vernier Reaction Control System (VRCS) limit cycle transient is illustrated in Figure 24. The Shuttle is assumed to be drifting at $.76 \times 10^{-4}$ rad/sec in pitch when the aft pitch vernier thrusters (numbers 3 and 5) are turned on for .5 second. This results in a 224 newton positive Z axis force and a 2500 newton meter negative Y torque excitation to the Shuttle causing it to reverse its pitch rate direction to approximately $-.76 \times 10^{-4}$ radian per second. The initial payload attitude is assumed to be 30 degrees from vertical during the maneuver in this study. The pointing error of each of the three controller types to the disturbance described above is shown in Figure 25. The very significant performance



- θ = PAYLOAD ATTITUDE (RADIAN)
- θ_C = COMMANDED PAYLOAD ATTITUDE (RADIAN)
- J = PAYLOAD INERTIA (kg-M²)
- K_P = PROPORTIONAL GAIN (N-M/RADIAN)
- K_R = RATE GAIN (N-M-SEC/RADIAN)
- K_I = INTEGRAL GAIN (N-M/RADIAN-SEC)

Figure 19
ASPS Pointing Controllers

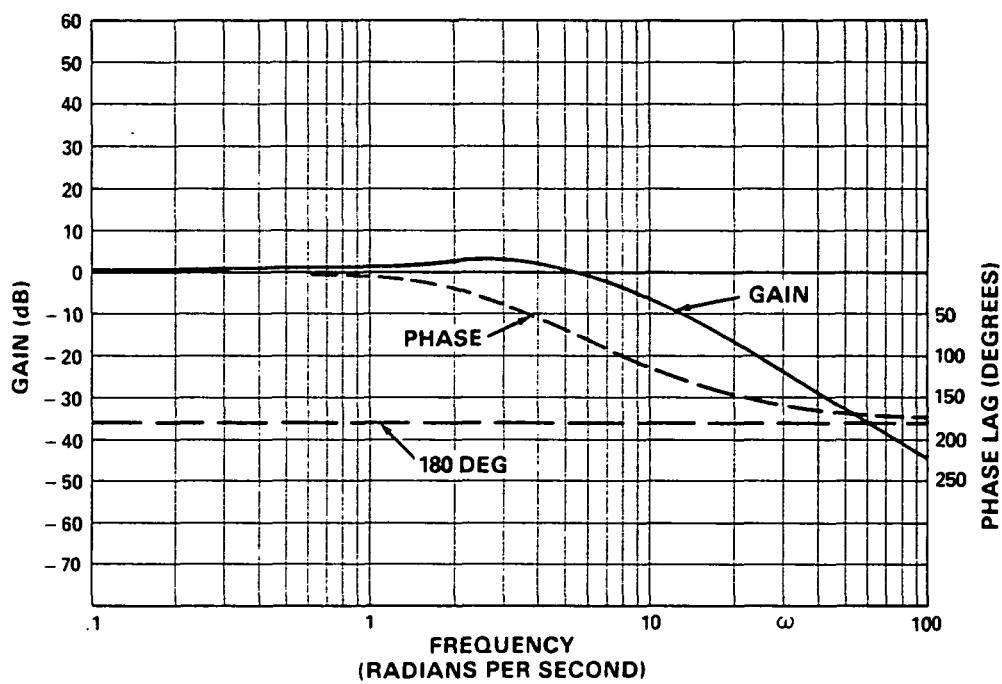


Figure 20
ASPS Pointing Controller Lead Lag Compensator
(Closed Loop Frequency Response)

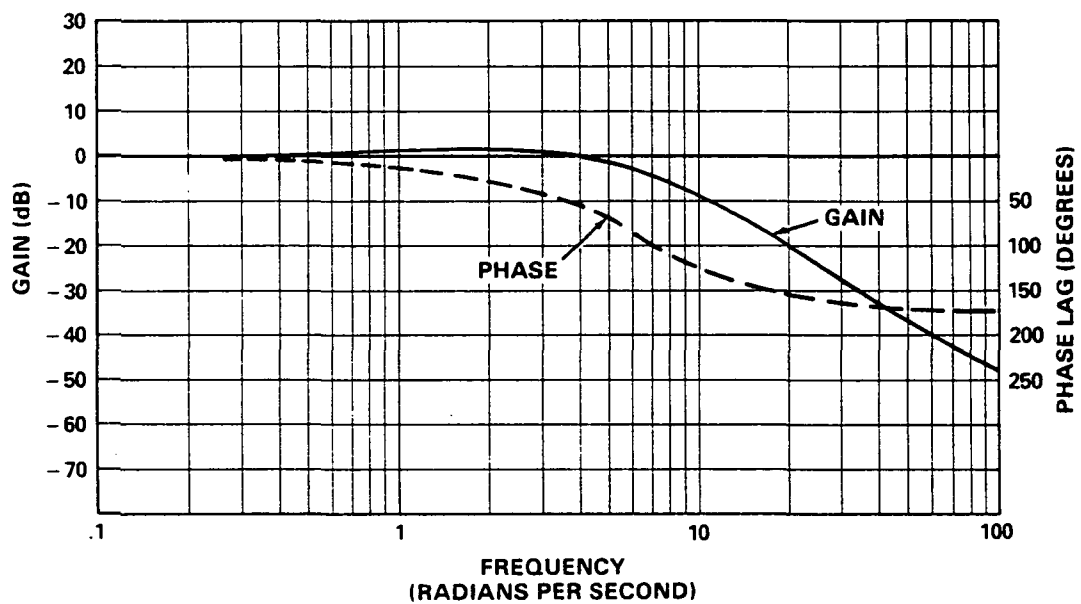


Figure 21
ASPS Pointing Controller Proportional + Rate Feedback
(Closed Loop Frequency Response)

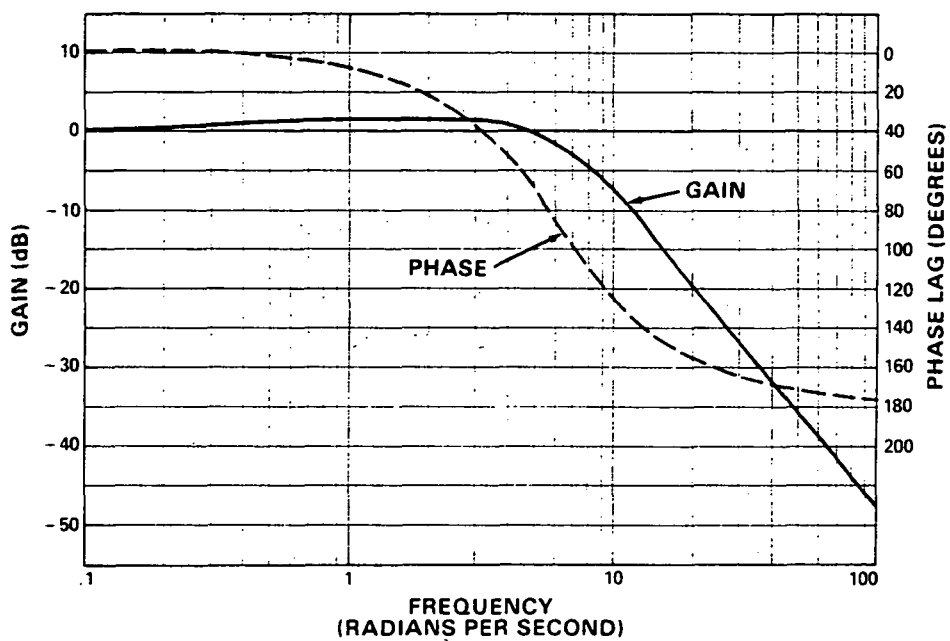


Figure 22
ASPS Pointing Controller Integral Control
(Closed Loop Frequency Response)

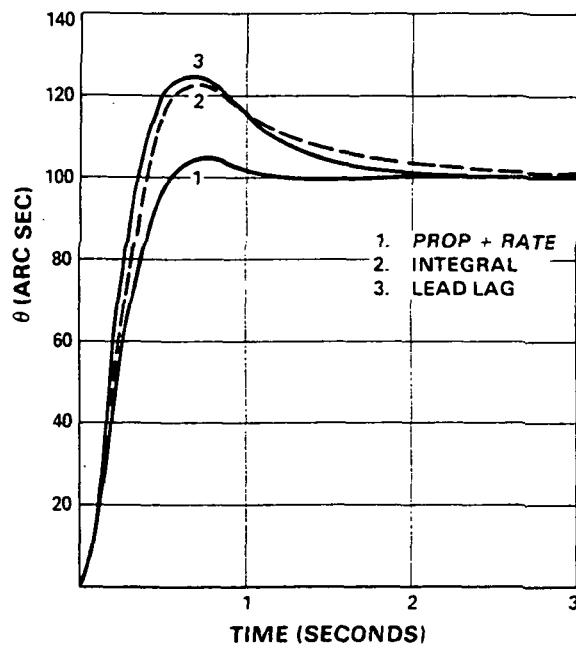


Figure 23
Step Response of 1 Hz
Pointing Servos

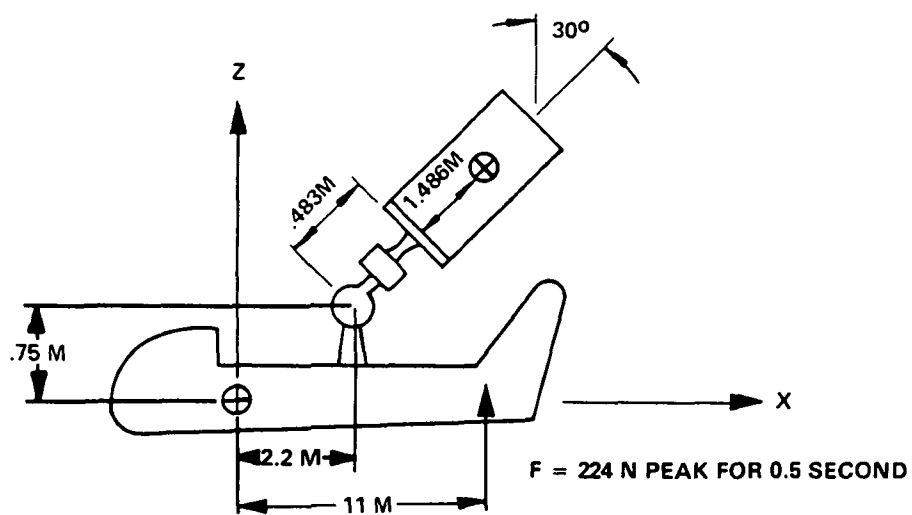


Figure 24
Worst-Case Shuttle VRCS Limit cycle Transient

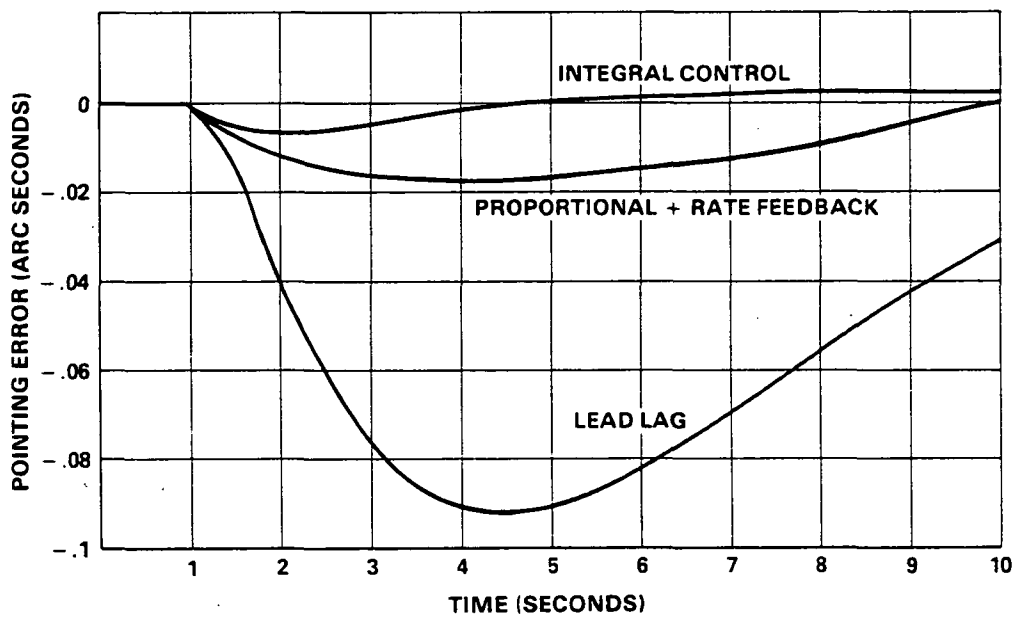


Figure 25
ASPS Pointing Controllers Pointing Error Response
To Worst-Case Shuttle VRCS Transient
1 Percent Decoupling Error (15 mm)

improvement resulting from integral control is obvious. Both the instantaneous peak error and the time integral of error are greatly reduced. It is also seen that the lead/lag type design exhibits considerably greater error to this disturbance. It should be noted that a one percent calibration error has been introduced in the decoupling compensation of the ASPS for these runs as there would be no pointing error from this type disturbance if the decoupling compensation were perfect. The suspension servo bandwidth is set at .3 radian per second for these runs and is of the proportional gain type with lead lag compensation.

TABLE 8
VERNIER POINTING SERVO DESIGN DATA

Payload Inertia = 503. kg

Lead Lag Servo

$$K_p = 3644. \text{ N m/Rad}$$

$$T_1 = .6435 \text{ sec}$$

$$T_2 = .0715 \text{ sec}$$

Proportional Plus Rate Feedback Servo

$$K_p = 19838. \text{ N m/Rad}$$

$$K_R = 4424. \text{ N m/Rad/Sec}$$

Proportional Plus Rate Plus Integral Feedback Servo

$$K_p = 22500 \text{ N m/Rad}$$

$$K_R = 5000 \text{ N m/Rad/Sec}$$

$$K_I = 22000 \text{ N m/Rad-Sec}$$

To gain an insight into the disturbance response behavior of the three controllers, the transfer function from a torque disturbance input to pointing angle output for each of the systems illustrated in Figure 19 is listed below:

a) Lead-Lag Compensator

$$\frac{\theta}{T_d}(s) = \frac{(T_2 s + 1)/K_p}{\frac{J T_2}{K_p} s^3 + \frac{J}{K_p} s^2 + T_1 s + 1} \quad (8)$$

b) Proportional plus Rate Feedback

$$\frac{\theta}{T_d}(s) = \frac{1/K_p}{\frac{J}{K_p} s^2 + \frac{K_R}{K_p} s + 1} \quad (9)$$

c) Integral Control

$$\frac{\theta}{T_d}(s) = \frac{s/K_I}{\frac{J}{K_I} s^3 + \frac{K_R}{K_I} s^2 + \frac{K_p}{K_I} s + 1} \quad (10)$$

The steady state gain at low frequencies is inversely proportional to K_p for the first two cases and inversely proportional to K_I for the integral control case. The constants K_p and K_I are listed in Table 8 for all three servos where applicable. The lead/lag servo K_p is 3644 and the proportional plus rate controller K_p is 19 838. For the integral control case, K_I is 22 000. Although K_p in the lead/lag case can be increased, it cannot be made equal to 19 838 and still maintain the nominal one Hz bandwidth except, perhaps, with elaborate higher order compensation.

The preceeding analyses is based on the simple models of Figure 19. In the actual system, the disturbance is applied to the Shuttle and transmitted through the gimbal and magnetic suspension dynamics of the ASPS. A similar analysis has also been conducted utilizing the linearized ASPS model described in Appendix A. The frequency response of the transfer function from a disturbance at the pitch thruster location to the ASPS pointing error is shown in Figure 25 for the three servo types. These results are very similar to those obtained with the simpler models. The response of the proportional plus rate servo is about 14.7 dB below the lead/lag servo at low frequencies. This

corresponds to the ratio of their respective displacement gains. Frequency response results with two values of K_I are illustrated in Figure 26, and shows the effect of integral gain on disturbance response. It is clear, from Figure 26, that disturbances in the frequency range below one radian per second are very effectively isolated by added integral control. All three controller types exhibit similar disturbance isolation characteristics at frequencies above one radian per second. The transient response of other critical system variables to the worst-case shuttle VRCS disturbance is illustrated in Figures 27 through 31 using the proportional plus rate pointing controller. Figure 27 shows that the peak axial gap excursion is just below the 5.6 mm gap limit indicating that the .3 radian per second suspension bandwidth is a practical lower limit for this disturbance environment.

Force output, during the transient, of the radial and axial MBAs are shown in Figures 28 and 29, indicating rather small peak force levels are required.

The elevation gimbal error and gimbal torque are shown in Figures 30 and 31. Peak gimbal angle error in 21.8 arc seconds and peak gimbal torque is .216 newton meter.

3.2 SYSTEM PARAMETRIC PERFORMANCE ANALYSIS

Most of the parametric studies described here pertain to optimizing pointing performance in the face of the worst-case Shuttle VRCS transient described above. Nominal values of ASPS operating parameters, unless otherwise noted, are:

Pointing Servo Bandwidth = 1 Hz

Gimbal Servo Bandwidth = 7.5 Hz

Suspension Servo Bandwidth = .3 radian per second

All data, except frequency response data, has been obtained from the digital nonlinear ASPS simulation described in Appendix B. A nonlinear model of the radial and axial magnetic bearings is included in the simulation for fine pointing performance evaluation. Gimbal friction is included in all runs with the parameters:

Friction stiffness coefficient = -474.5 newton meters per radian

Friction limit = -.68 newton

Frequency response data has been obtained using the linear ASPS simulation described in Appendix A.

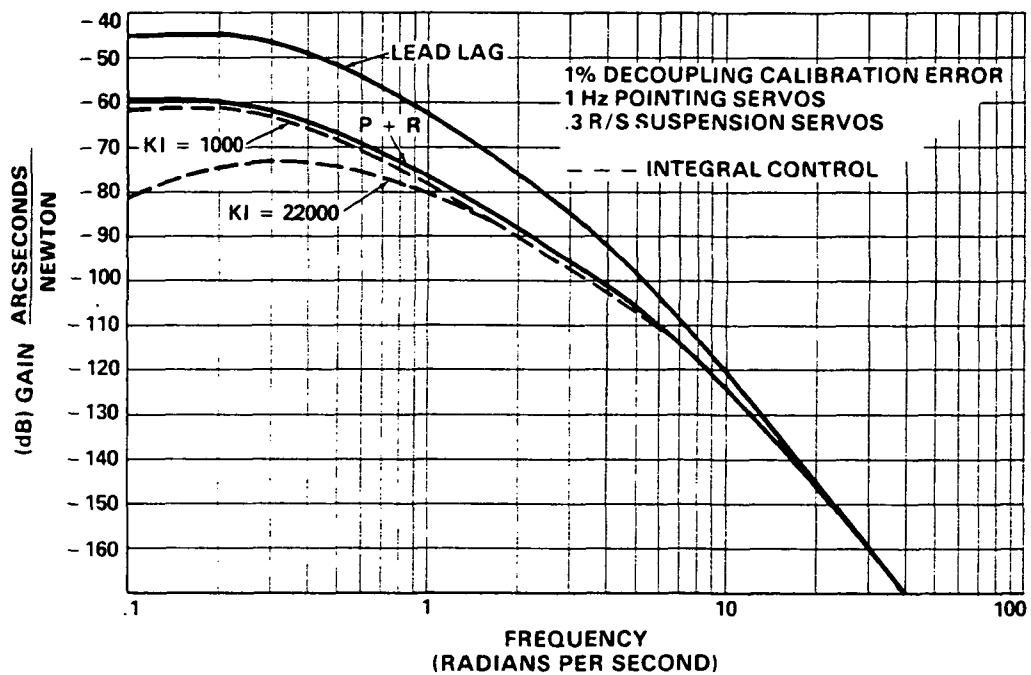


Figure 26
Pointing Error from Sinusoidal
Disturbance at VRCS Pitch Thrusters

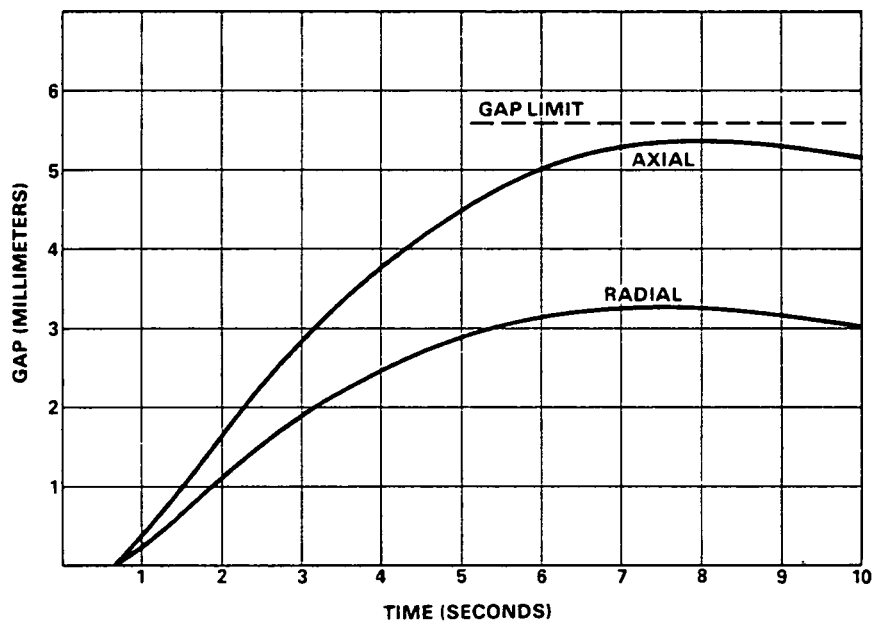


Figure 27
MBA Gap Response to Worst-Case Shuttle VRCS Transient

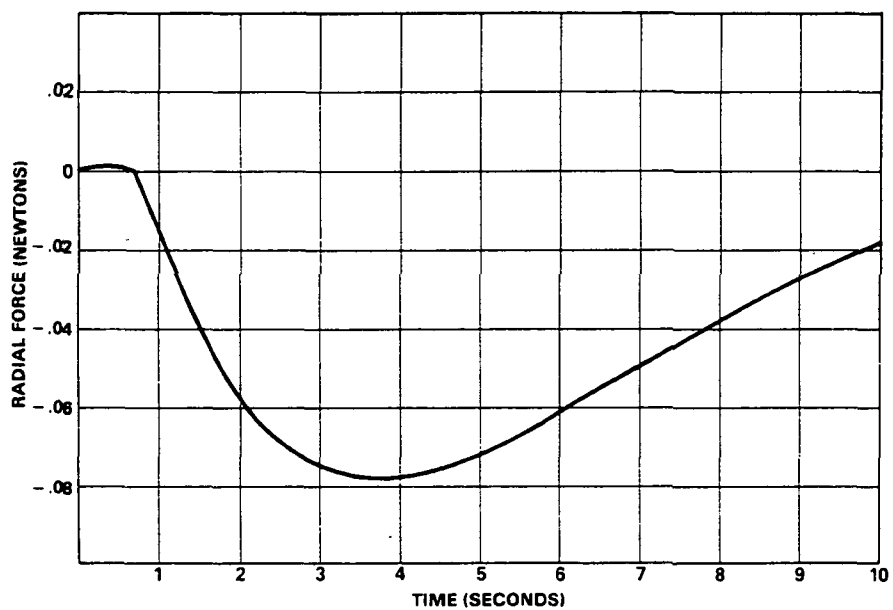


Figure 28
Radial MBA Response to Worst-Case Shuttle VRCS
Transient, Max Available Force = 14.2 Newtons

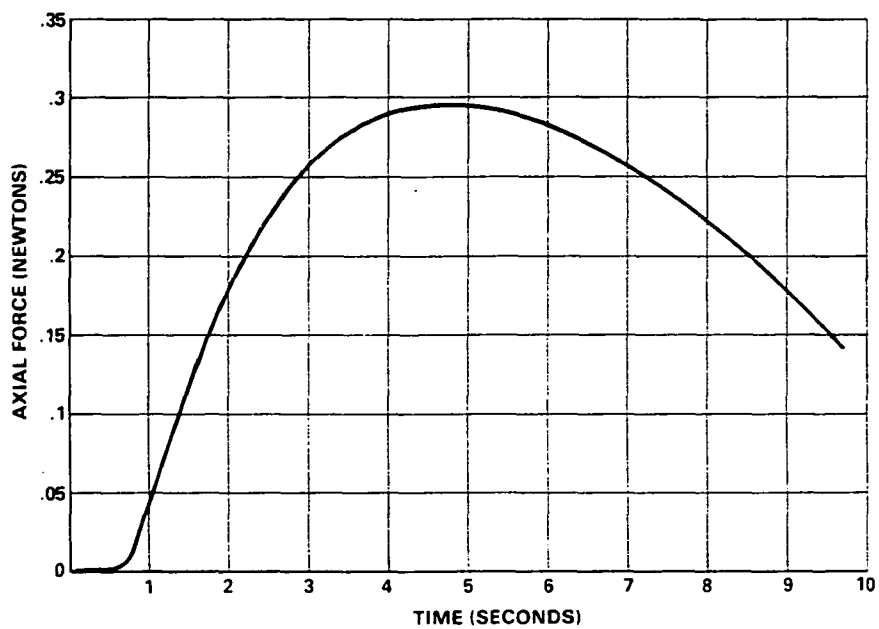


Figure 29
Axial MBA Response to Worst-Case Shuttle VRCS
Transients, Max Available Force = 28.9 Newtons

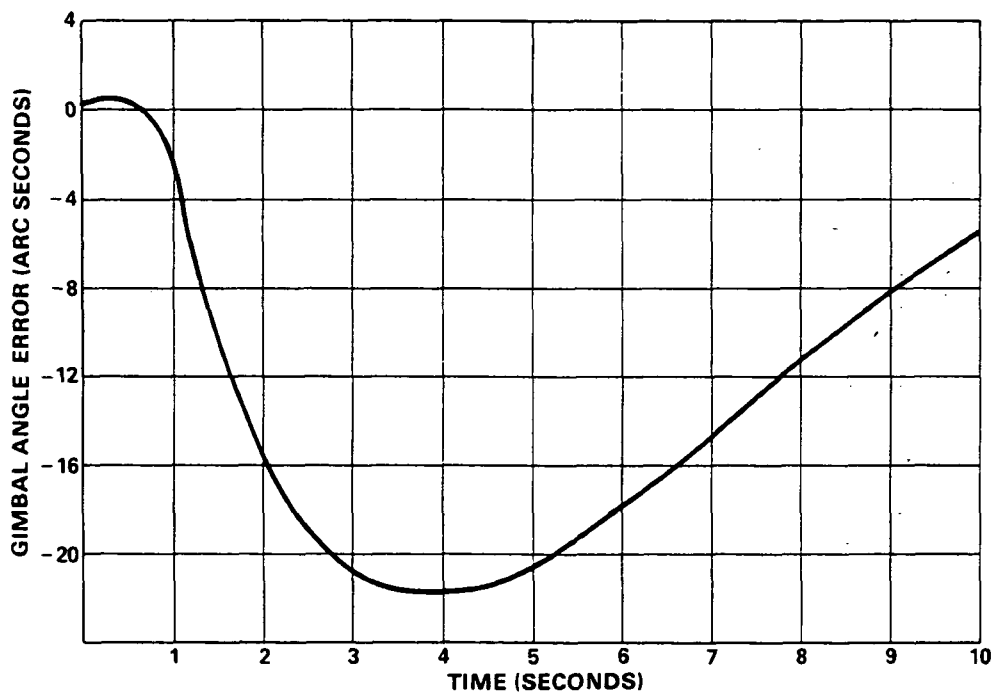


Figure 30
Elevation Gimbal Angle Error Response to
Worst-Case Shuttle VRCS Transient

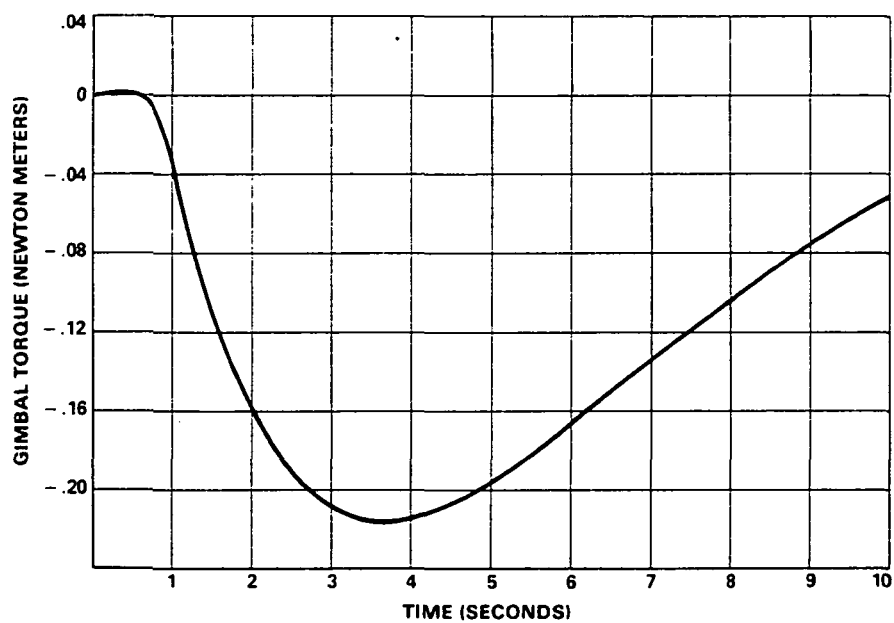


Figure 31
Gimbal Torquer Response to Worst-Case
Shuttle VRCS Transient

3.2.1 Pointing Controller Bandwidth Effect on System Performance

Figure 32 illustrates the variation of peak pointing error with pointing controller bandwidth. The peak error is inversely proportional to the square of the pointing controller bandwidth. The controller type is proportional plus rate feedback and the suspension servo bandwidth is set at .3 radian per second. Note that a one percent decoupling error is deliberately introduced for this study. Although a nominal one hertz pointing controller bandwidth has been assumed in this study, it is very likely that a higher operating bandwidth is possible with careful design. The results in Figure 32 indicate that any effort expended to achieve a higher operating bandwidth is well rewarded.

3.2.2 Suspension Servo Bandwidth Effect on System Performance

The payload isolation from Shuttle disturbance improves as the suspension servo bandwidths are lowered. This is illustrated in Figure 33 where peak error to the worst-case VRCS transient vs suspension servo bandwidth is plotted. The effect of suspension servo bandwidth on disturbance isolation as a function of disturbance frequency is shown in Figure 34. In this case, a sinusoidal disturbance is assumed at the pitch thruster location. The plots show the transfer function from disturbance input to pointing error output for several suspension servo bandwidths. Comparing Figure 34 with Figure 26 shows that the suspension servo bandwidth determines the high frequency error response to Shuttle disturbances while the pointing servo characteristics determine the low frequency response.

Although isolation from Shuttle disturbances is enhanced by low suspension frequencies, the payload excursions in the magnetic bearing gaps become larger as suspension servo bandwidth is lowered. This effect is illustrated in Figure 35. Since the axial gap operating limit is 5.6 mm, .3 radian per second is the lowest practical suspension bandwidth in the disturbance environment considered here.

3.2.3 Center of Mass Decoupling Errors

The ASPS control circuitry incorporates a provision to compensate for payload center of mass offsets in the axial direction. If this CM decoupling circuitry is perfect, which also implies that the payload CM is known precisely, then the payload is completely isolated from Shuttle disturbances. Hence, in most of the parametric studies performed, an error in the decoupling law is deliberately introduced. Figure 36 shows, parametrically, the effect of a CM decoupling error on pointing error at various suspension servo bandwidths. A worst-case payload offset in the Z direction is 1.5 meters and a one percent CM decoupling error is interpreted to be equivalent to a 15 mm error.

The same pointing error results if there is an error in the decoupling circuitry or an equivalent error in the actual payload CM location.

Decoupling errors in the X and Y directions result in errors of approximately the same magnitude as those in Figure 36.

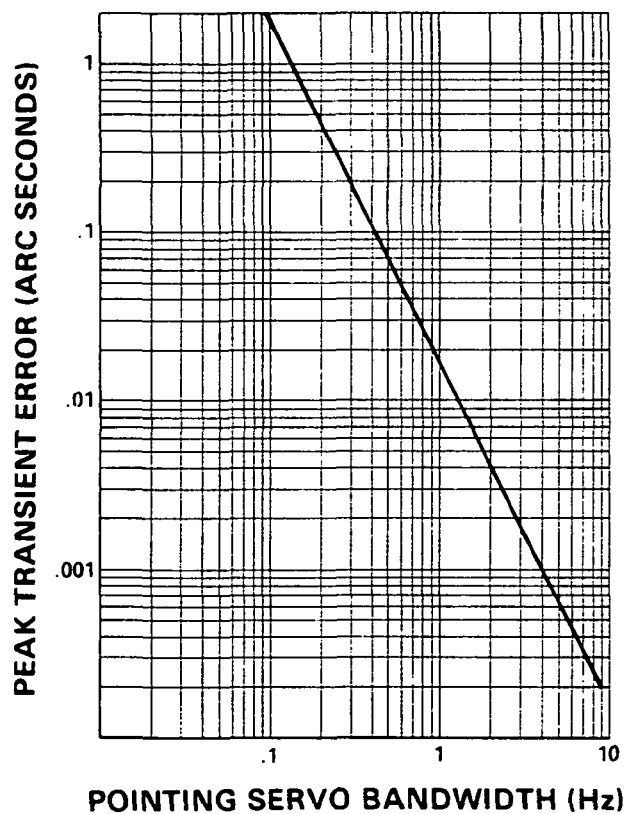


Figure 32
 Peak Transient Pointing Error from VRCS Pitch Limit Cycle
 Versus
 Pointing Servo Bandwidth
 (1 Percent Decoupling Error Proportional + Rate Feedback)

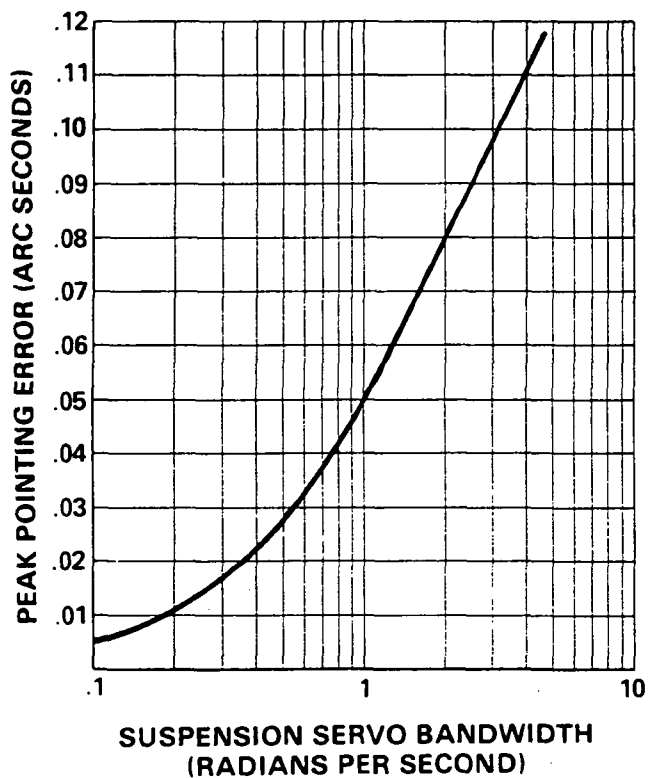


Figure 33
Peak Pointing Error
Versus
Suspension Servo Bandwidth
(During Worst-Case Shuttle VRCS Transient, 1 Percent
Decoupling Error, 1 Hz Pointing Servo, Proportional + Rate Feedback)

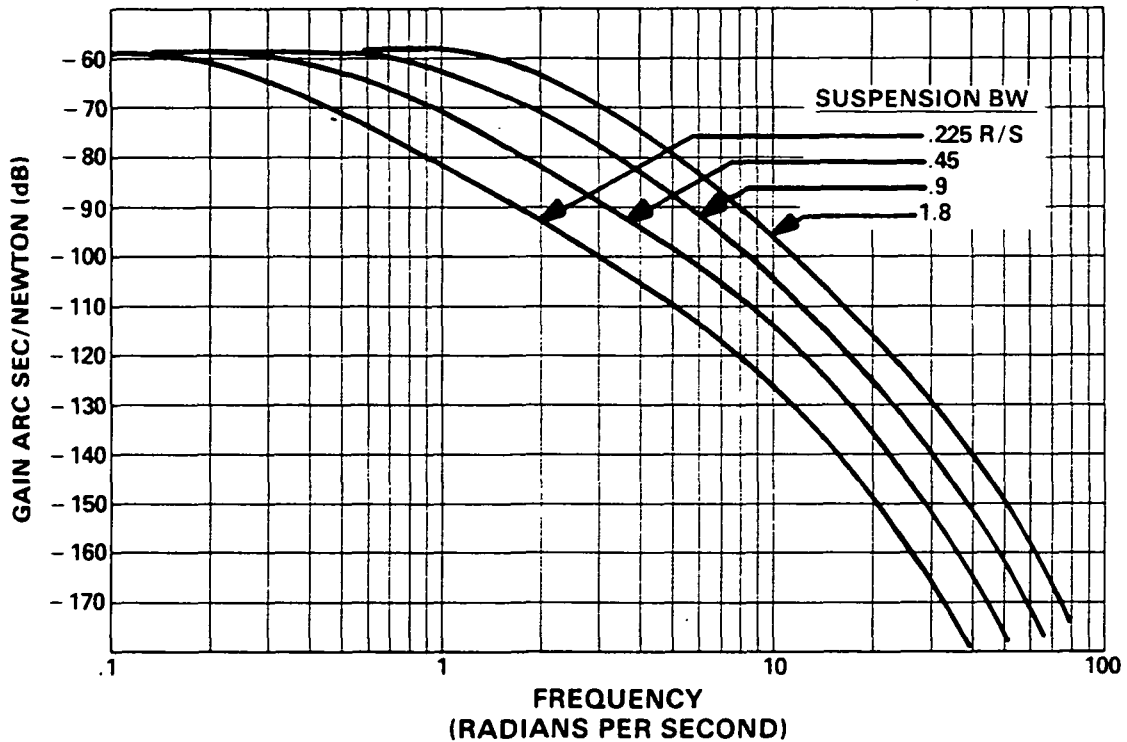


Figure 34
 Pointing Error From Sinusoidal Disturbance
 at VRCS Pitch Thrusters
 (1 Percent Decoupling Calibration Error
 1 Hz Pointing Servos
 Proportional + Rate Feedback
 Varying Suspension Servo Bandwidth)

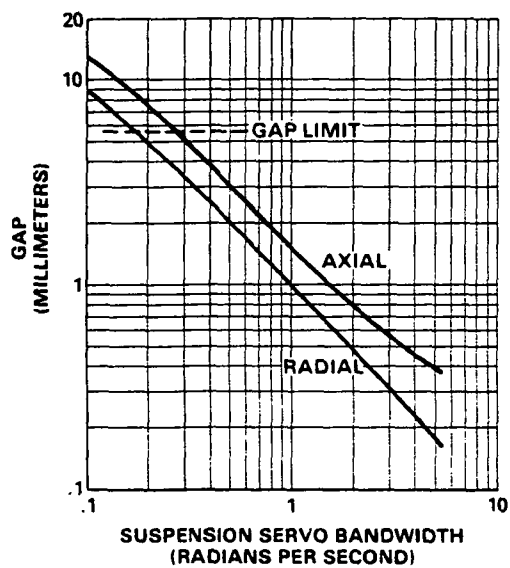


Figure 35
Peak Suspension Gap
Versus
Suspension Servo Bandwidth
(During Worst-Case VRCS Transient)

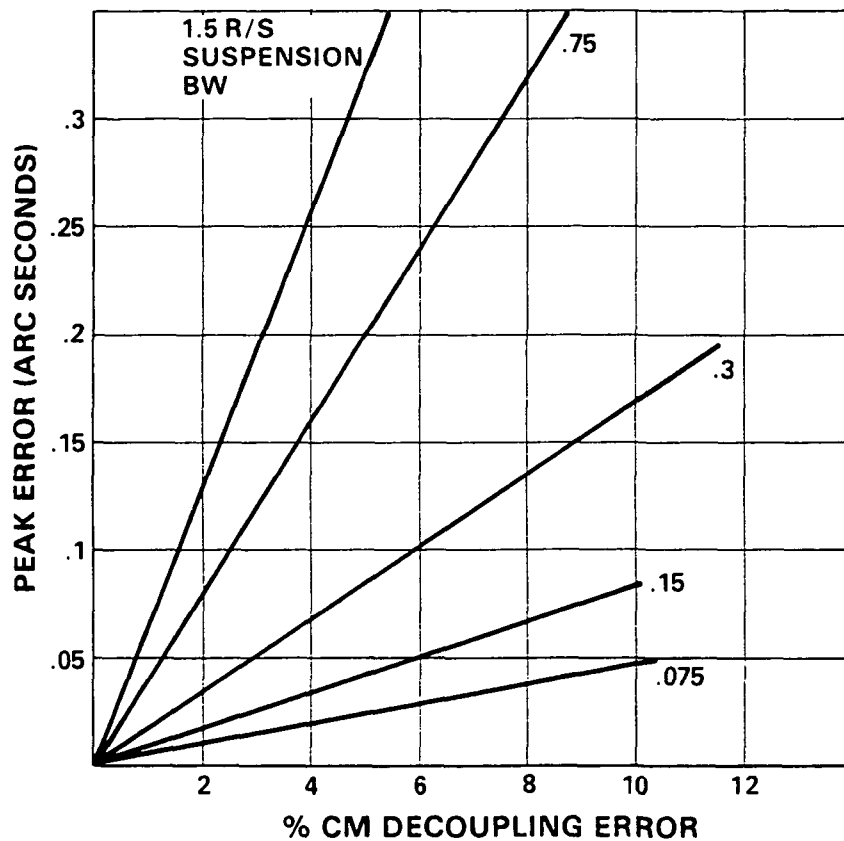


Figure 36
 Peak Pointing Error
 Versus
 CM Decoupling Error
 (During Worst-Case Shuttle VRCS Transient, 1 Hz Pointing
 Servo, Proportional + Rate Feedback)

3.2.4 Magnetic Bearing Assembly Gain Errors

As a rough method to estimate the effect of various MBA anomalies such as hysteresis, granularity, dead space and gain calibration error, deliberate gain mismatch between axial and radial actuator sets was introduced. Errors in each of the three pointing axes were noted as shown in Table 9. It is seen that gain mismatch of the radial actuators causes the largest errors, and error is directly proportional to mismatch.

Since pointing stability of .01 arc second is required, gain mismatch between radial actuators must be below one percent.

3.2.5 Payload Cable Effects

An alternative ASPS configuration consists of replacing the optical data link and payload battery complement with a cable to provide both power and communications with the payload. The intended cable is a modified flex capsule mounted in place of the optical coupler. The capsule is designed to have six degrees of freedom, but motions are assumed to be very small except about the roll axis.

The cable effects were modeled as six-linear spring forces and torques between lateral gimbal and payload. In a series of runs, the cable stiffness was increased in one axis at a time and it was determined that the radial translation cable stiffness had the most significant effect on pointing error. Figure 37 illustrates the effect on pointing error of radial cable stiffness in the range .8 to 200 newtons per meter. A preliminary estimate by a potential vendor of the flex capsule radial stiffness is 35 to 55 newtons per meter which corresponds to approximately 1.5 arc seconds pointing error.

3.2.6 Latched Vernier Performance

By increasing all cable stiffness factors to very large values, the payload becomes essentially latched to the lateral gimbal. Figure 38 illustrates pointing performance in this mode as a function of gimbal servo bandwidth. At a gimbal servo bandwidth of 6.28 rad/sec (1 Hz) the pointing error is 15 arc seconds. Comparing this performance with anticipated performance of the cable configuration in Paragraph 3.2.5, it is seen that a suspended ASPS configuration with a cable across the payload/gimbal interface will exhibit considerably better pointing performance than a hard mounted configuration.

3.2.7 1 Hz Raster Performance

In these tests, the payload command is a 182 arc second peak magnitude sine wave at 1 Hz. The gimbal angle is commanded to a constant 30 degrees attitude and no disturbances are applied. The pointing controller is the proportional plus rate configuration set at 1 Hz bandwidth. Since the command is at the control bandwidth, the payload follows with approximately 85 degrees phase lag. Peak MBA forces and gimbal torque are plotted against gimbal servo bandwidth in Figure 39 indicating adequate system capability. The MBA gaps and MBA gap angle between payload and lateral gimbal plate are plotted against gimbal servo bandwidth in Figure 40. Minimum gimbal servo bandwidth is about 6 Hz because of the 5.6 mm gap limits.

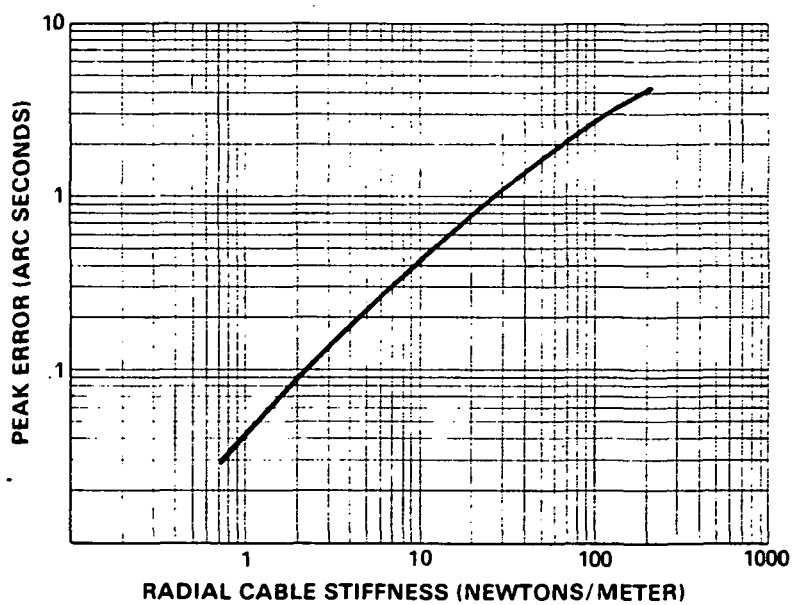


Figure 37
Peak Pointing Error
Versus
Radial Cable Stiffness During VRCS Transient

TABLE 9
PEAK POINTING ERROR
DUE TO MBA MISMATCH

	AXIAL		RADIAL	
% Mismatch	1%	5%	1%	5%
Lateral Pointing Error (arc Seconds)	.0034	.018	.0085	.043
Elevation Pointing Error (arc Seconds)	.0021	.0103	.0084	.043
Roll Pointing Error (arc Seconds)	.00029	.0015	.0007	.0035

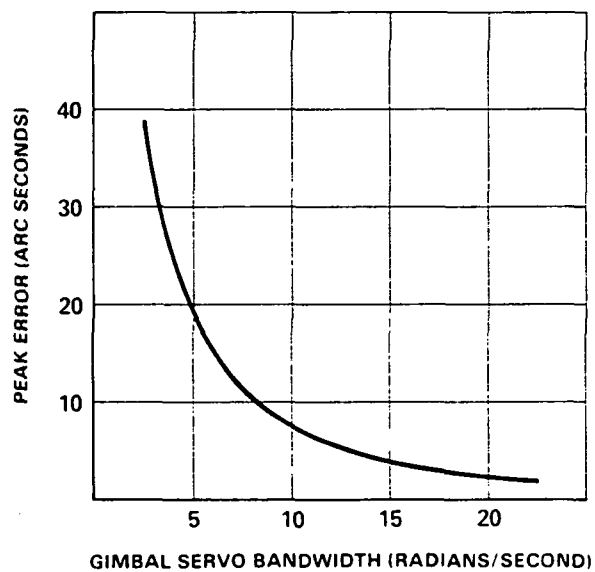


Figure 38
Peak Pointing Error
Versus
Gimbal Servo Bandwidth
(During VRCS Transient, Vernier Latched)

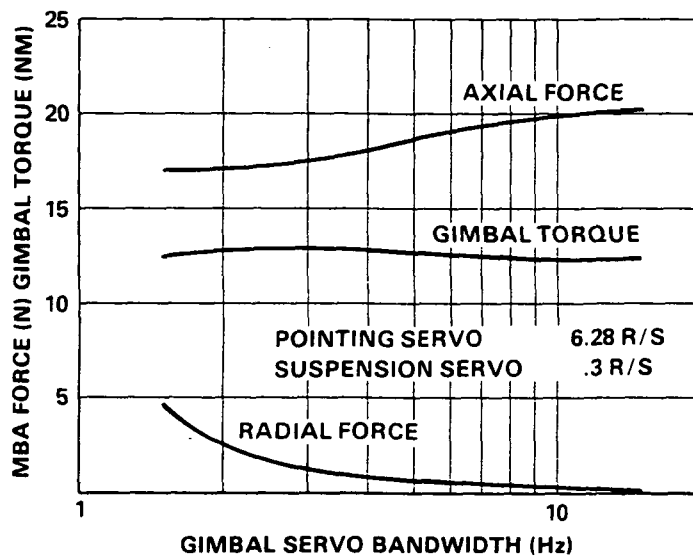


Figure 39
 $182\hat{S}$, 1 Hz Command Peak MBA Force and Gimbal Torque
 Versus
 Gimbal Servo Bandwidth

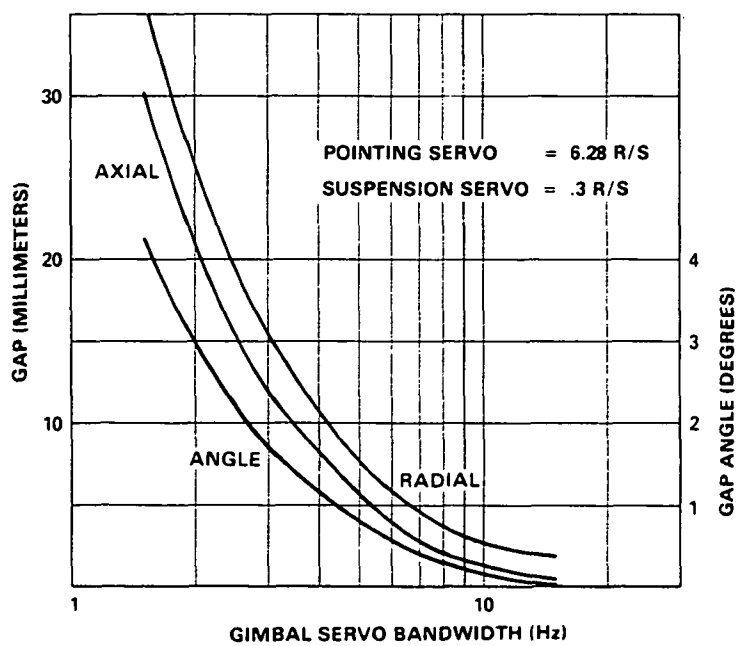


Figure 40
182S, 1 Hz command Peak Gap Excursions
Versus
Gimbal Servo Bandwidth

In Figures 41 and 42, the peak MBA gaps, MBA forces, and the coarse gimbal torques are plotted against suspension servo bandwidth. It is significant to note that when the suspension frequency approaches the command frequency, a region occurs in which minimum gap excursions result. By taking advantage of this, large raster patterns might be accommodated without exceeding gap limits.

3.2.8 Slewing Performance

ASPS slewing performance has been studied very briefly to obtain preliminary knowledge of satisfactory servo bandwidths for slew maneuvers. Actual mission slewing and tracking trajectories are likely to require several minutes, and in order to reduce computer time expenses, a compact slew maneuver shown in Figure 43 has been devised. The slew maneuver is a cosine command which has zero initial rate and attains a peak angular rate of 2 degrees per second after 9.2 seconds. The initial command acceleration is .006 radian per second².

In Figure 43, the peak MBA forces and gimbal torque are plotted against gimbal servo bandwidth. The pointing and suspension servos have been set at the same bandwidth which is varied from 6 to 20 radians per second. The peak available MBA forces are 28.9 newtons axial, 14.2 newtons radial and peak available gimbal torque is 34 newton meters. These force and torque levels are adequate over the range of bandwidths shown in Figure 43.

In Figure 44 the peak gimbal angle error versus gimbal servo bandwidth is plotted for the same slewing maneuver. The gimbal resolver accuracy is at least .1 degree and, in addition, a slewing maneuver must bring the payload to some "window," defined by fine sensor characteristics, in a predictable manner. These constraints dictate that the gimbal servo bandwidth be above 2 radians per second.

The peak MBA gap versus the pointing and suspension servo bandwidths is also plotted in Figure 44. Maximum operating gap is 5.6 mm and the suspension and centering servo bandwidths should be above 6 radians per second.

3.3 PERFORMANCE SUMMARY

Results and analysis to date indicate that .01 arc second pointing stability is attainable with the present ASPS design and ideal sensors. Since addition of integral of pointing error feedback into the pointing controller offers a 2.5 to 1 performance improvement over proportional plus rate feedback, it will be incorporated in the final ASPS design.

Pointing error from Shuttle transients has three sources:

1. Uncertainty of the payload CM
2. CM decoupling circuit errors
3. MBA mismatch/alignment error

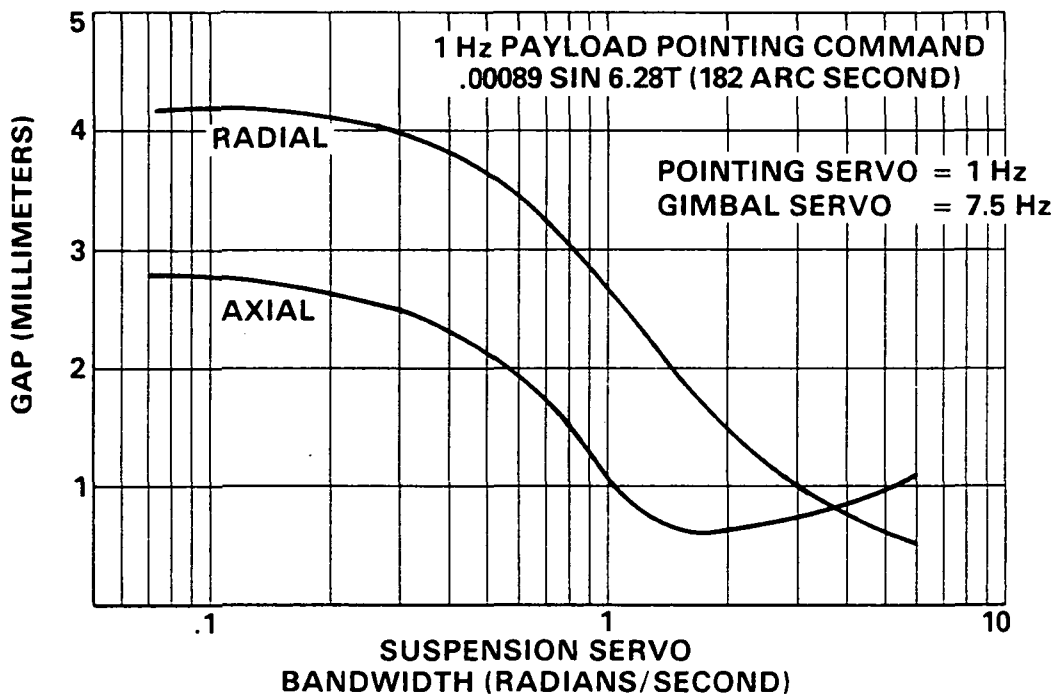


Figure 41
 Peak Suspension Gap
 Versus
 Suspension Servo Bandwidth

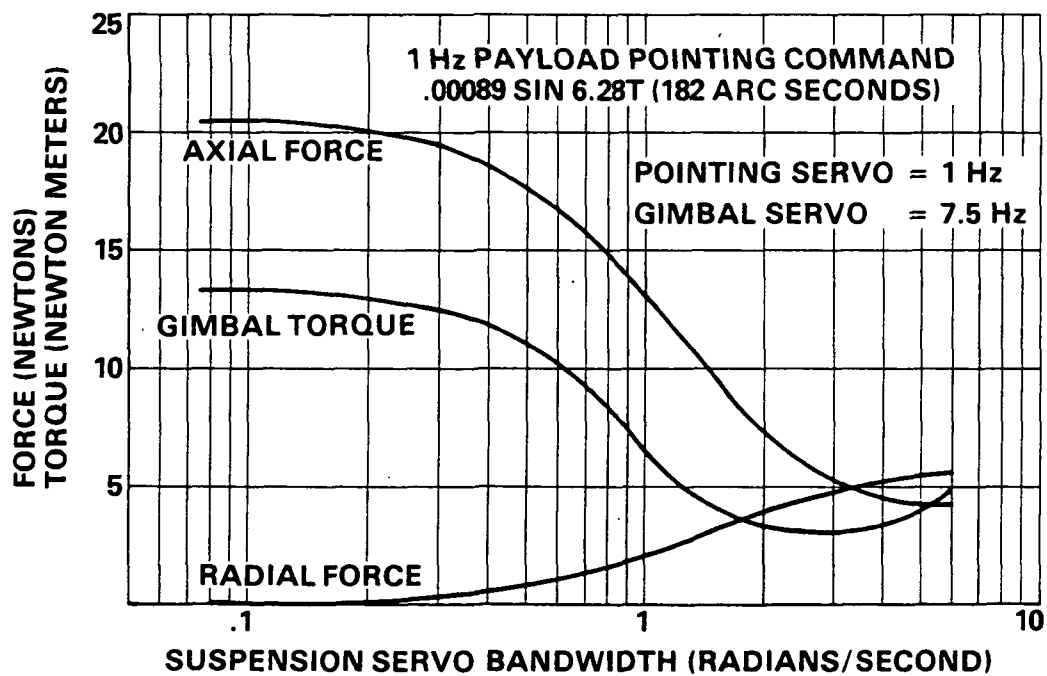


Figure 42
 Peak Force and Torque
 Versus
 Suspension Servo Bandwidth

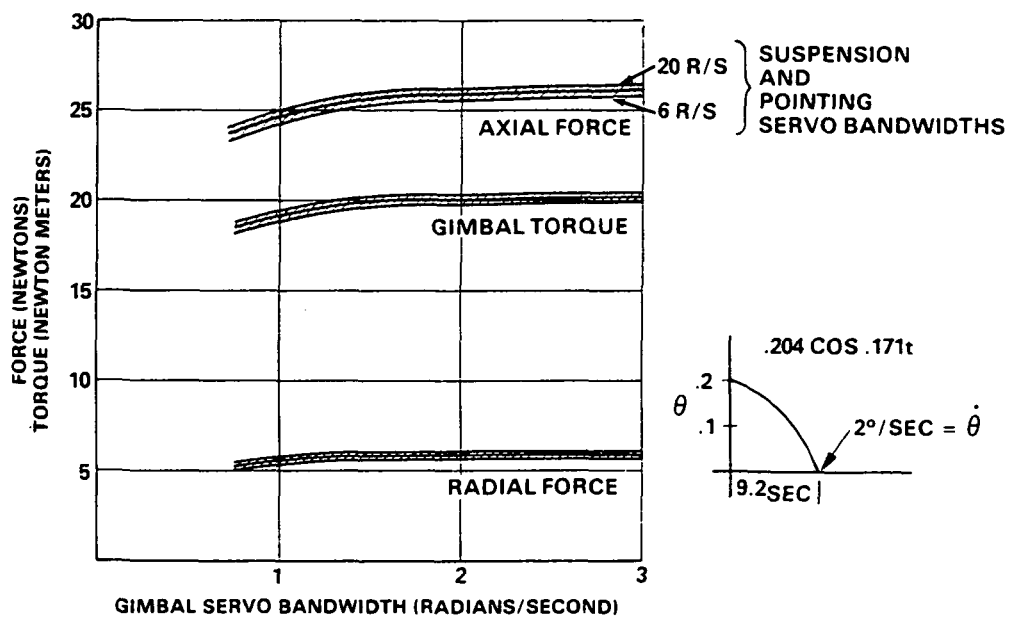
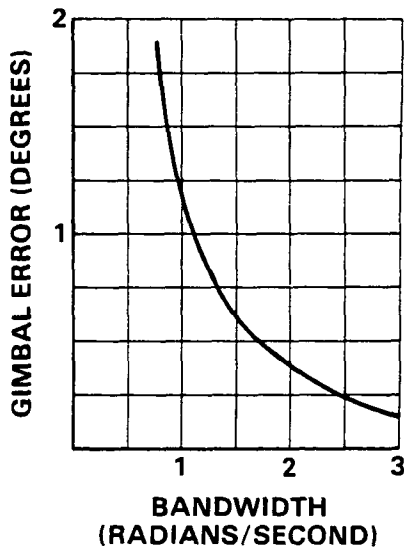


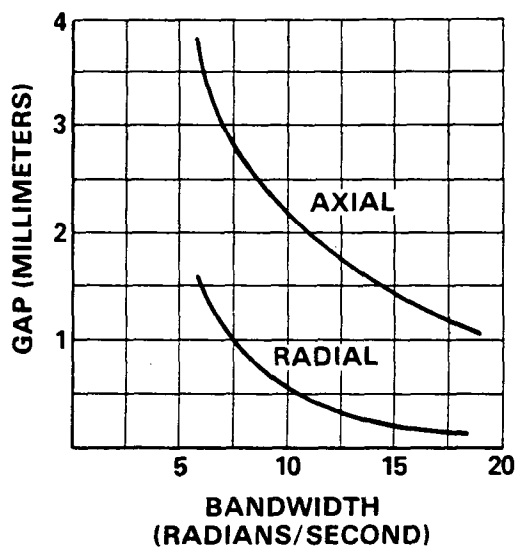
Figure 43
Peak Forces and Torque Required for ASPS Slewing

SLEWING PERFORMANCE

**PEAK GIMBAL ERROR
VERSUS
GIMBAL SERVO BANDWIDTH**
(POINTING AND SUSPENSION SERVO
BANDWIDTHS = 10 RAD/SEC)



**PEAK GAP VERSUS
POINTING AND SUSPENSION
SERVO BANDWIDTH**
(GIMBAL SERVO BANDWIDTH = 2 RAD/SEC)



Peak Gimbal Error while Slewing
Versus
Gimbal Servo Bandwidth
(Pointing and Suspension Servo
Bandwidths = 10 Radians/Second)

Peak Gap while Slewing
Versus
Pointing and Suspension
Servo Bandwidth
(Gimbal Servo Bandwidth =
2 Radians/Second)

Figure 44
Slewing Performance

Assuming integral control, a one percent CM decoupling error produces .006 arc second transient pointing error. If a one percent radial MBA mismatch error exists, it corresponds to .0085 arc second pointing error. The resultant root mean square total pointing error is $(.006^2 + .0085^2)^{1/2} = .010$ arc second.

The MBA mismatch/alignment error can come from more than one source and is not yet entirely budgeted. The CM decoupling error and payload CM uncertainty errors can, however, be largely calibrated out against each other via a ground or flight calibration sequence. Additionally, error can be reduced significantly by just a modest increase in bandwidth. The discussion above assumes, of course, perfect sensors, computation, and data transfers; i.e., no sampling errors.

ASPS servo bandwidth constraints determined in the preceeding performance analysis are:

	Fine Pointing	Slewing
pointing	1 Hz	≥ 1 Hz
gimbal	> 6 Hz	> 2. rad/sec
suspension	>.3 rad/sec	> 6. rad/sec

ASPS performance with a cable at the lateral gimbal/payload interface, although considerably worse than a freely suspended ASPS, is still significantly better than can be expected with a hard mounted payload.

Page Intentionally Left Blank

SECTION 4.0

ASPS MECHANICAL DESCRIPTION

The Annular Suspension and Pointing System (ASPS) is a precision payload pointing system which is designed to accommodate a wide range of Space Shuttle experiments. To achieve a high degree of standardization throughout a broad range of mission and payload requirements, the ASPS is designed in a modular fashion.

4.1 HARDWARE DESCRIPTION

The modules which comprise the ASPS are the VPA, CGAs, a Mounting and Jettison Assembly (MJA) and the Payload Plate Module. Figure 45 describes the position of each of these units within the ASPS, as well as illustrating the connecting hardware.

The Payload Mounting Plate forms a removable base plate for mounting and aligning experiments prior to installation on the ASPS. For missions not requiring roll freedom or very high pointing stability, the Payload Mounting Plate may be attached directly to the CGAs.

The VPA contains the roll axis drive which provides unlimited rotation about the payload longitudinal axis and a vernier rotation of ± 7.5 degree about any axis in the plane normal to the payload roll axis.

Two identical CGAs are stacked to form an elevation and a lateral gimbal pair. Design of the gimbal mounts is such as to provide a mechanically limited travel of ± 100 degrees (from vertical) along the lower elevation gimbal axis, and ± 60 degrees about the upper lateral gimbal axis. The MJA provides the connection between the pallet mount and the coarse gimbals and includes hardware for ASPS jettison.

Figure 46 is a composite illustration of the ASPS assembly which provides overall outline dimensions. This figure shows the ASPS in a normal (payload vertical) operational mode. Figure 47 shows the ASPS in a stowed configuration with outline dimensions. To obtain a better perspective of the ASPS in relation to the Orbiter, Figures 48 and 49 show the ASPS installed on a typical pallet assembly.

The total weight of the ASPS alone is projected to be 239 kg (527 lb). Complete with the pallet interface structure, listed in Table 10, and other flight equipment this is increased to 356 kg (785 lb). Table 11 provides a general breakdown of these weights, based upon major assemblies.

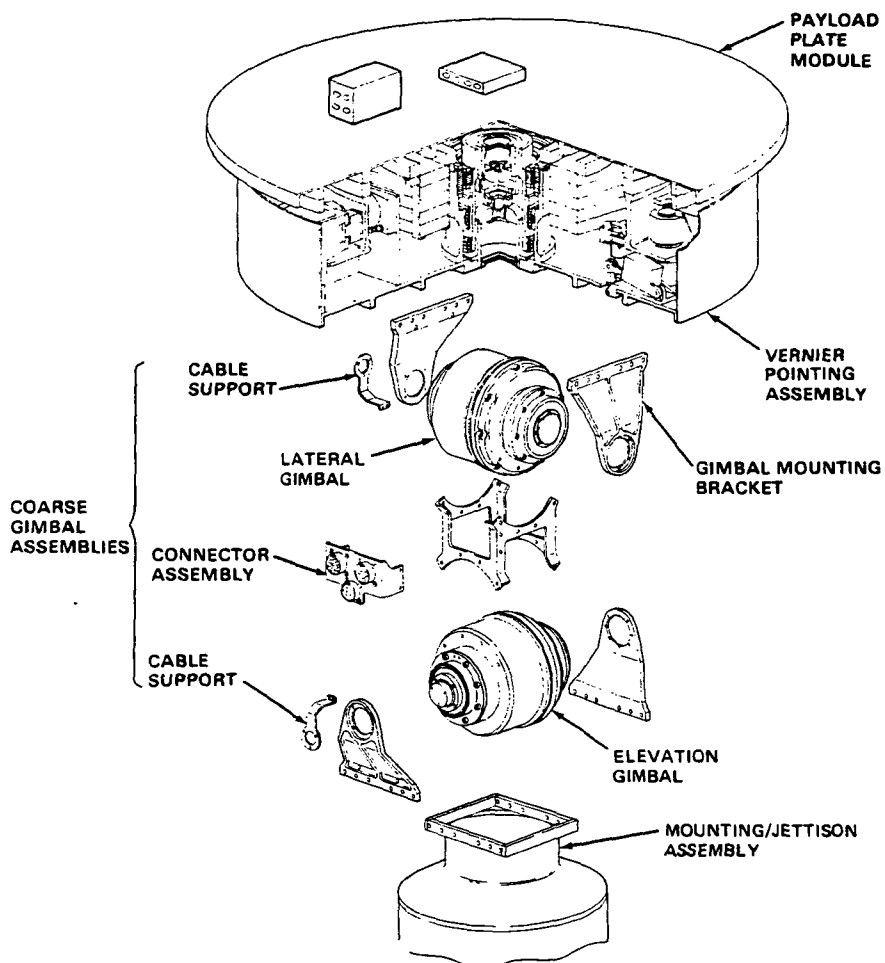


Figure 45
ASPS Component Breakdown

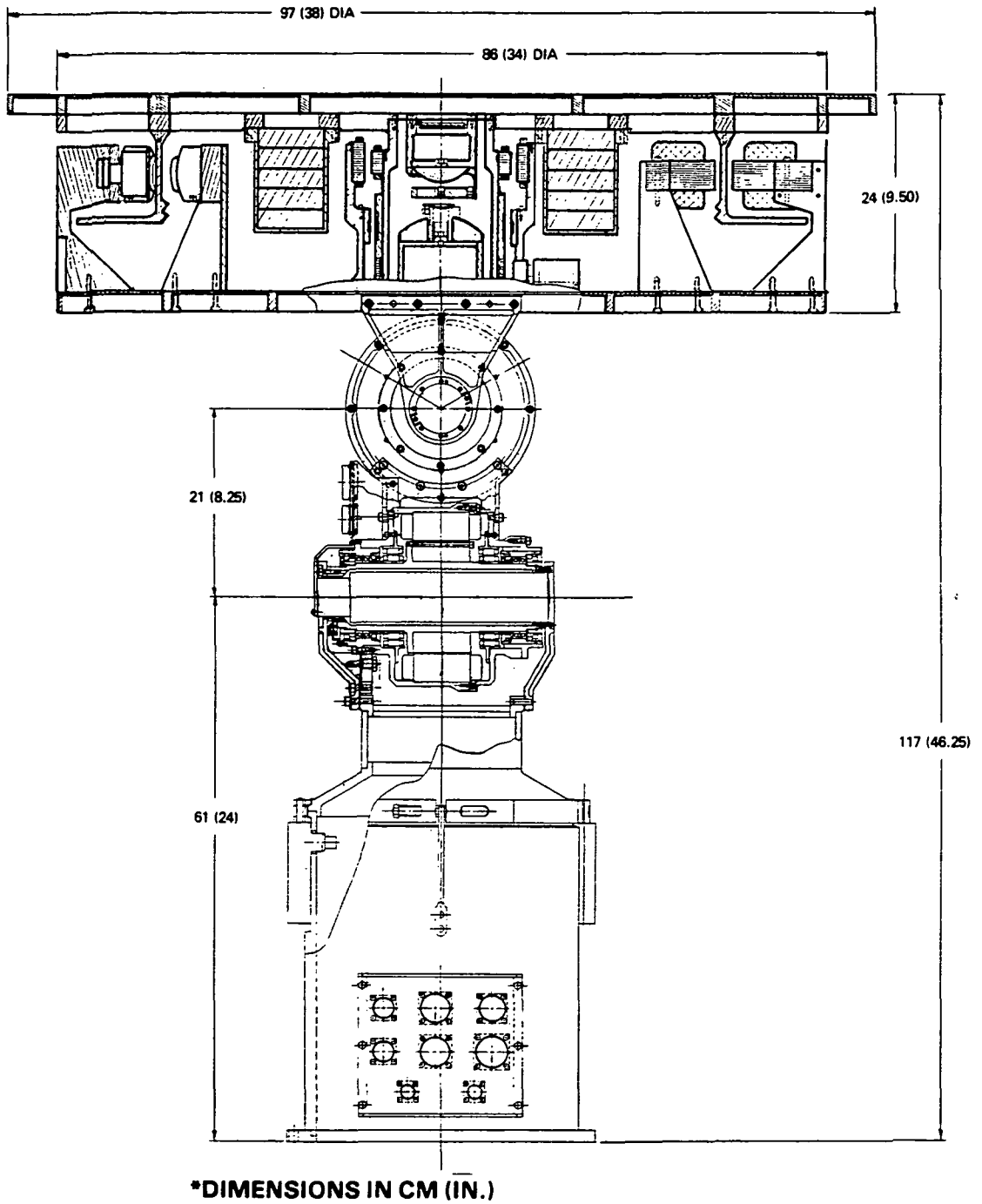
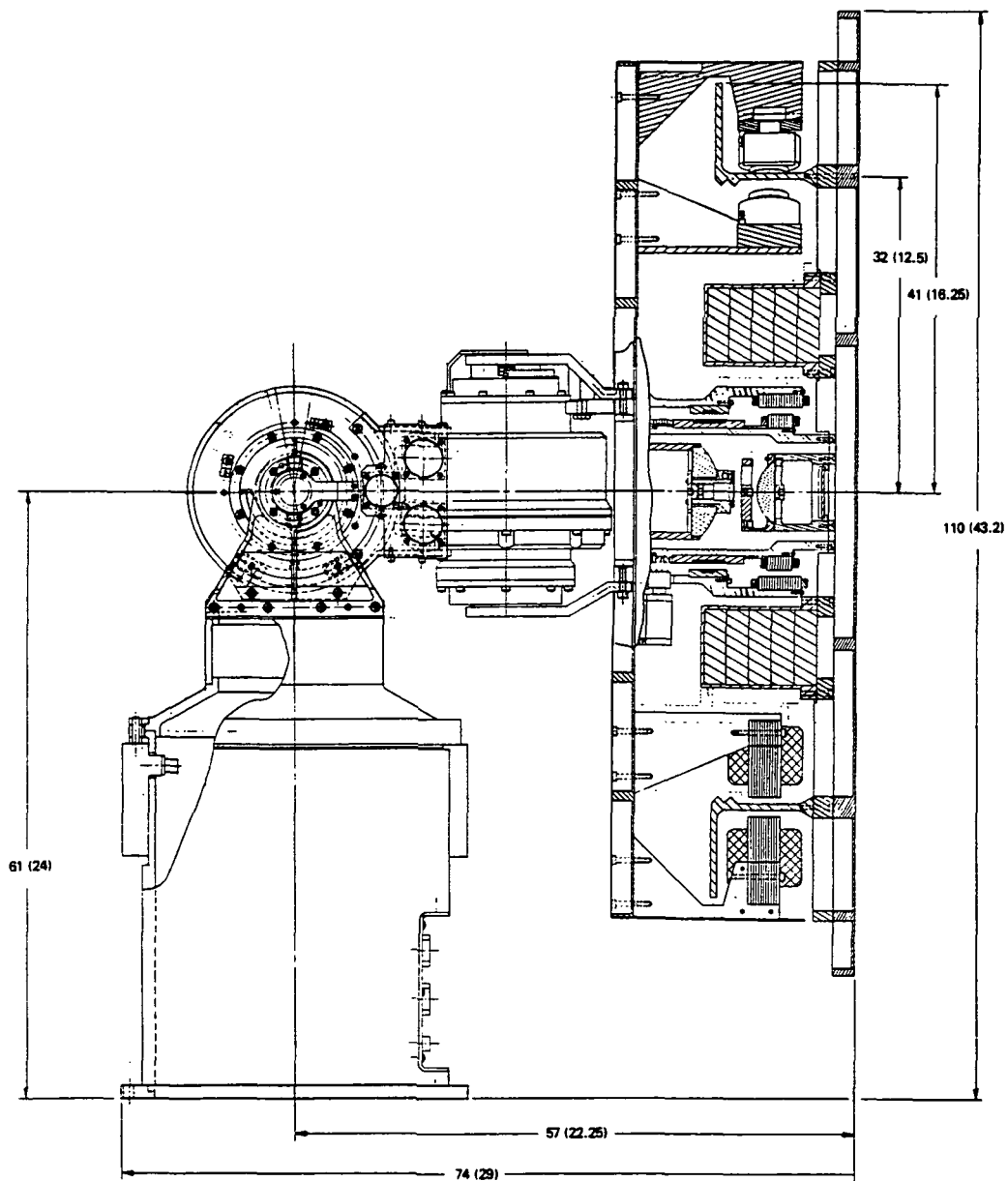


Figure 46
ASPS Outline Operating Position



***DIMENSIONS IN CM (IN.)**

Figure 47
ASPS Outline Caged Position

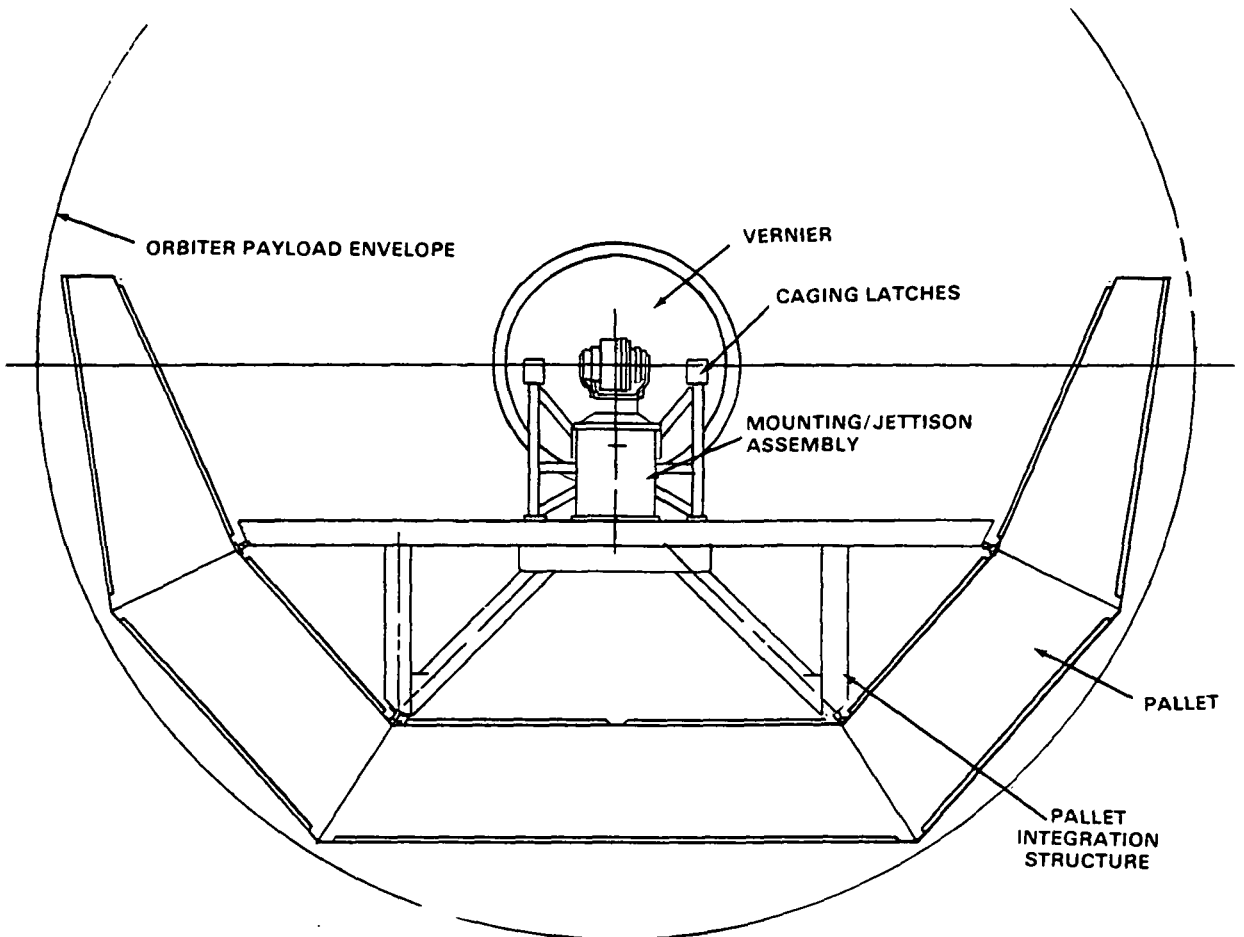


Figure 48
Orbiter Installation End View

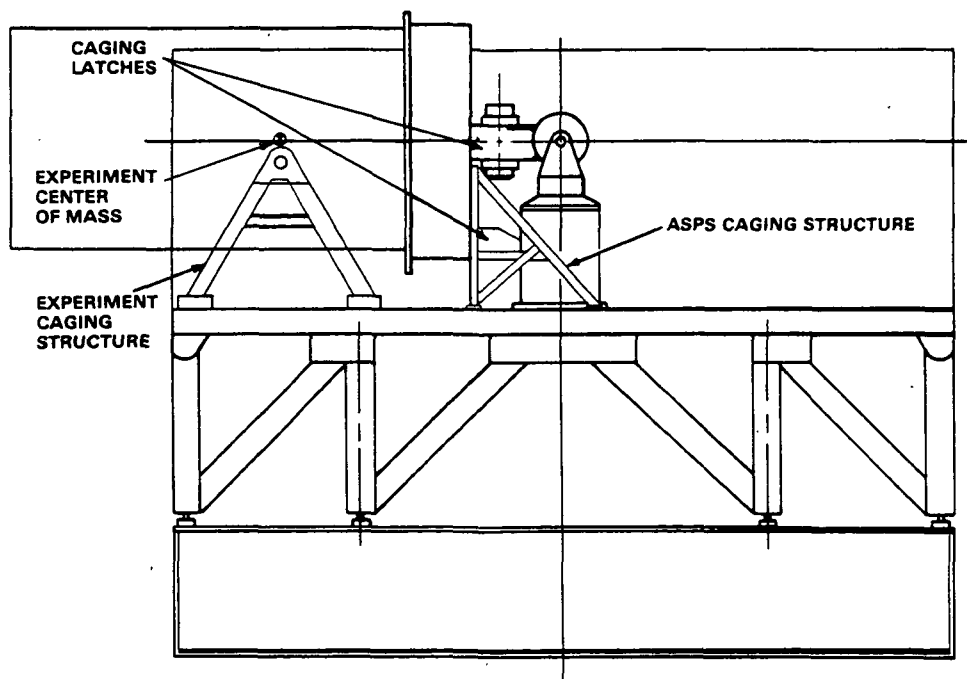


Figure 49
Orbiter Installation Side View

TABLE 10
PALLET STRUCTURE WEIGHT

Component	Material	Quantity	Weight, kg (lb)	
Frame	Al	1	90.70	(200.00)
			Total	90.70 (200.00)

TABLE 11
ASPS WEIGHT PROJECTION

	Weights			
	ASPS kg (lb)		Launch kg (lb)	
Payload Plate Module	12.47	(27.50)	12.47	(27.50)
Vernier Module	152.82	(336.97)	152.82	(336.97)
Gimbal Modules	53.71	(118.42)	53.71	(118.42)
Mast/Mtg Module	20.20	(44.54)	20.20	(44.54)
Caging System	_____		13.49	(29.75)
Pallet Interface	_____		90.70	(200.00)
Electronics (CEA)	_____		12.53	(27.63)
Total	239.20	(527.43)	355.92	(784.81)

4.1.1 Payload Plate Module

The experiment attaches directly to the removable Payload Plate Module as described in Paragraph 4.2.1. The Payload Plate Module consists of the payload plate and the Payload Electronics Assembly (PEA), which is discussed in Section 5.

The payload plate is a .965 m (38 in.) diameter aluminum reinforced plate which attaches directly to the ASPS Vernier Assembly. The basic construction is a one piece machining which has a 2.39 mm (.094 in.) face sheet over the entire upper surface. Below this is a series of radial and circumferential reinforcing ribs which provide structural stiffness and integrity. Rib functions not only include stiffening and payload mounting but also are designed to enable direct attachment to the gimbal mounting brackets in the event the coarse gimbal pointing accuracy is sufficient to meet the mission requirements and the vernier system can therefore be omitted. Under this mode of operation, provision is also made to accommodate the caging assembly which must be mounted in order to cage the ASPS and payload for the launch and land mission phases.

The weight estimate for the Payload Plate Module is shown in Table 12.

TABLE 12
PAYLOAD PLATE MODULE WEIGHTS

Payload	Material	Quantity	Weight, kg (lb)
P/L Plate	Al-Alloy	1	12.02 (26.50)
PEA (Electronics)	-	1	.45 (1.00)
			Total 12.47 (27.50)

4.1.2 Vernier Pointing Assembly

The Vernier Pointing Assembly (VPA) provides the ASPS with its high resolution pointing capability. Overall assembly size is a cylinder .863 m (34 in.) diameter by .219 m (8.625 in.) in height. Figures 50 and 51 show cross sections through the VPA. The various components of this unit are mounted to one of two plates which form the top and bottom of the module. The top plate is attached to an L-shaped soft iron rotor which runs circumferentially below it. The iron rotor is levitated and controlled by the magnetic bearing assemblies mounted onto the lower, or fixed, portion of the vernier assembly.

The magnetic suspension system provides active control of all six degrees of freedom of the upper vernier portion, and hence the payload. Three axial MBAs control axial translation and angular rotation of the payload about two axes. These MBAs are spaced at 120° intervals about the vernier baseplate

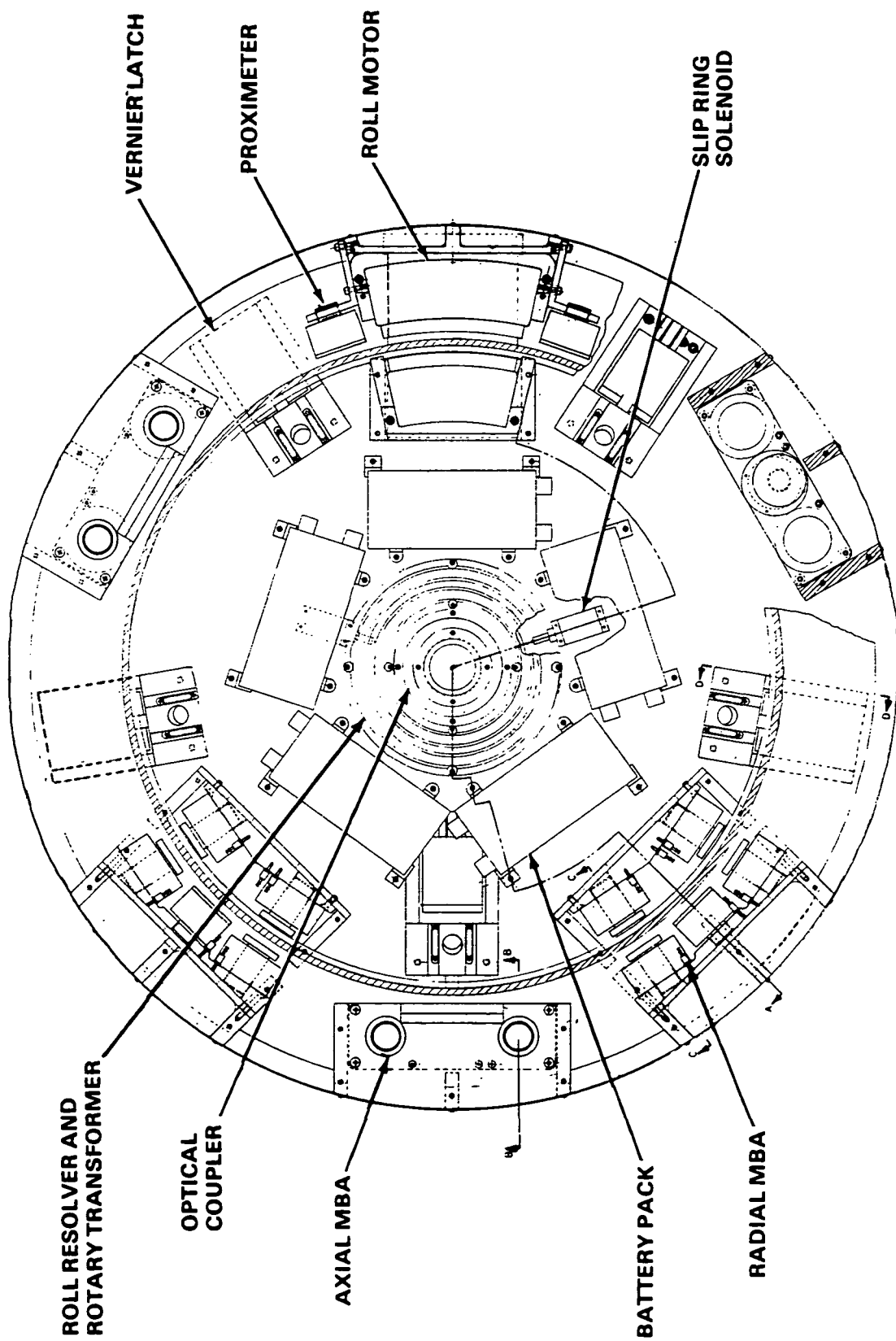
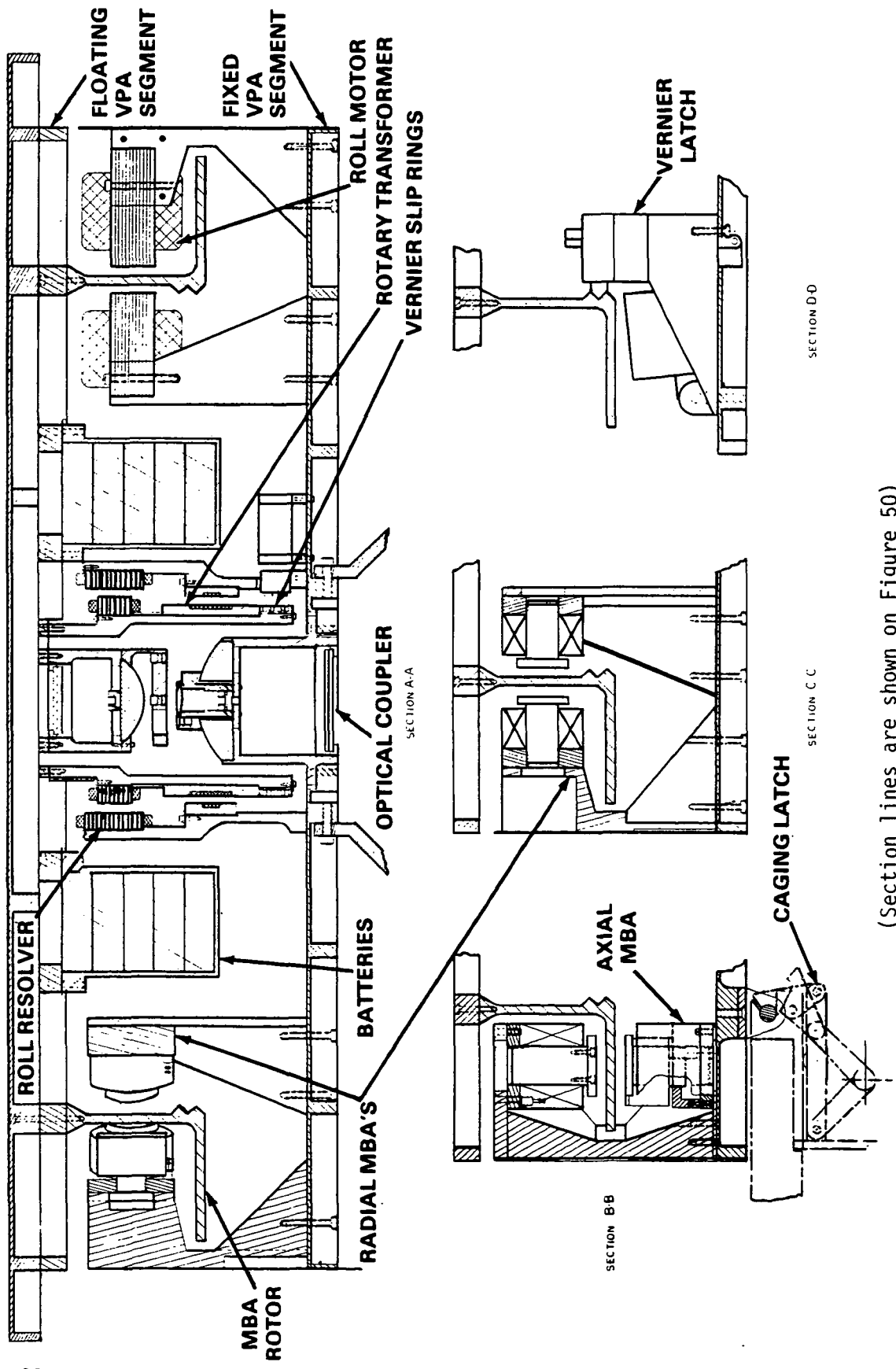


Figure 50
Vernier Layout



(Section lines are shown on Figure 50)

Figure 51
Vernier Cross Section

at a nominal .362 m (14.25 in.) radius. Lateral position is governed by two radial MBAs located orthogonal to each other and offset from the reference, or 'A', axial MBA by ± 45 degrees. The sixth degree of freedom, roll about the axis perpendicular to the payload plate, is controlled by the vernier roll motor which is located diagonally opposite the 'A' axial MBA. The mean centered radial position of the radial MBAs and the roll motor is .314 m (12.375 in.).

The L-shaped rotor is the component upon which the magnetic suspension system acts. The axial MBAs react against the horizontal flange of the rotor, which is 6.35 mm (.25 in.) thick and has an outer and inner radii of .406 m (16 in.) and .317 m (12.5 in.), respectively. The vertical surfaces of the L are used by the radial MBAs and by the roll motor. The vertical rotor segment is also 6.35 mm (.25 in.) thick with a mean radius of .314 m (12.375 in.) and the overall height is 101.6 mm (4 inches). All surfaces of the rotor which face the roll motor pole pieces and the radial MBA proximeter heads are plated with copper 1 mm (.040 in.) thick to provide a low rotor resistance for these components. Axial MBA rotor surfaces are similarly plated with .5 mm (.020 in.) copper.

Rotor displacement is sensed by proximeters, one of which is located in each of the MBA stations and two which are mounted on either side of the roll motor. These sense the rotor surface position relative to the MBA stators or motor segments and provide this information for use in the control system. The roll axis position is sensed by a roll resolver mounted in the central region of the vernier. Power to operate this resolver comes from a rotary transformer located in the same vicinity as the resolver.

Payload data is transferred between the suspended and fixed vernier portions by means of the optical coupler which is located at the center of the VPA and is discussed further in Paragraph 4.1.6. Payload power is supplied by twenty-five Ni-Cd battery cells which are supported by mounting brackets in five sets of five-cell groupings equally distributed angularly on the underside of the vernier top plate.

The Vernier Electronics Assembly (VEA) is housed in a separate enclosure which mounts beneath the roll motor and is accessible from the side of the VPA.

When the coarse gimbal pointing system is utilized in lieu of the vernier assembly, or when the vernier is rendered inactive for battery recharging, or when the vernier is caged for launch and landing operations, the suspended portion of the VPA is positioned and held centered in the magnetic gap by five vernier latches. Detailed descriptions of the latches are given in Paragraph 4.1.5. For battery recharging, the vernier latch assemblies clamp and center the rotor and the suspended portion of the VPA by means of a circumferential notch on the inboard rotor surface. Once firmly latched, direct electrical connections are possible to the batteries and payload. This is accomplished by means of a set of four conductor slip rings mounted below the rotary transformer on the suspended segment of the vernier assembly. The brush block is brought into contact with the slip ring by a solenoid mounted on the vernier baseplate. The brush block and slip rings are only functional at zero roll-speed and are engaged only while the suspended assembly is supported by the vernier latches.

Certain potential ASPS uses do not necessitate the extreme pointing accuracy possible with a totally noncontacting VPA. For these applications, an alternate VPA has been conceived. This system is portrayed in Figure 52 and shows a flex capsule replacing the noncontacting payload support components, which include the optical coupler, rotary transformer, and batteries. Further description of this configuration can be found in Paragraph 4.1.6.

Table 13 presents a detailed breakdown of the vernier components and their weights.

4.1.3 Coarse Gimbal Assemblies (CGA)

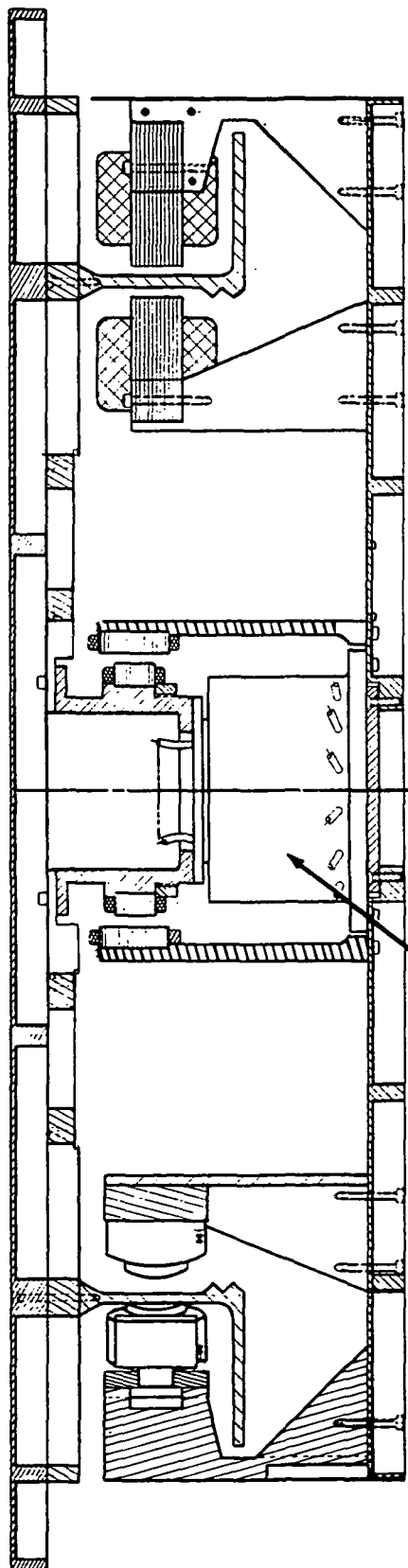
The gimbal module is a dual gimbal assembly which provides coarse pointing capabilities about two perpendicular axes. In this design two identical Coarse Gimbal Assemblies (CGAs) provide elevation and lateral pointing of the ASPS and payload. Configuration of these units is shown in Figure 53.

A permanent magnet, two-phase brushless dc torque motor delivers up to 33.9 N m (25 ft-lbs) of shaft torque. The motor contains Samarium Cobalt magnets for high efficiency and to ensure against a single-point failure of the rotor. With conventional magnets, and electronics failure can create a high stator current which could demagnetize the torquer's permanent magnets. A separate pair of windings is brought out from the torquer stator for use in a backup caging mode. In this mode, hard wired control signals switch the backup power bus alternately between the backup sine and cosine windings to cause the torquer to step clockwise or counterclockwise to the caged position for latching.

Commutation of the torquer is accomplished using a multispeed wound rotor resolver. Since the torquer contains 24 poles, the resolver must be a 12-speed device to provide sine and cosine phase currents to the torquer drive electronics which are synchronized with the torquer electrical angle.

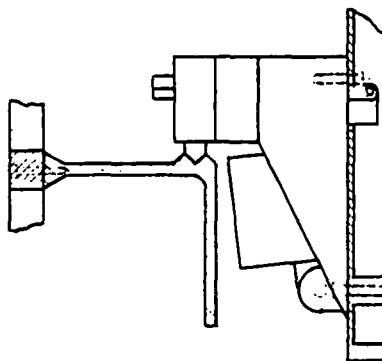
A single-speed wound rotor resolver is included in the CGA for position readout and control of the gimbal angle.

Outboard of the torque motor and resolvers are the gimbal bearings which are thin-line rolling element bearings mounted in bearing cartridges in a fixed/floating arrangement. Table 14 lists the characteristics of the selected gimbal bearings. Figure 54 presents pictorially the fixed/floating cartridge concept. Such a configuration allows very tight control of bearing preloads, since the preload is determined by the bearing geometry which is controlled by the bearing manufacturer and is only slightly affected by temperature differentials. The DF angular contact bearing pairs minimize bearing compliance while yielding increased radial load capacity and stiffness. Alignments can be maintained accurately by virtue of the through-the-bore-housing which requires no complex or involved machining or finishing operations. The fixed/floating installation allows for exact radial and axial positioning and is capable of accommodating axial expansion of the shaft or housing, such as caused by thermal expansion, without affecting the bearing preload or alignment. Although the floating cartridge provides this axial freedom, the fixed/floating cartridge combination is able to support radial or thrust loadings from any direction.

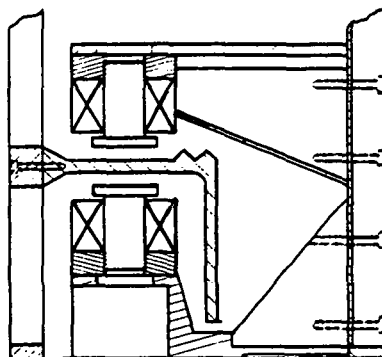


FLEX CAPSULE

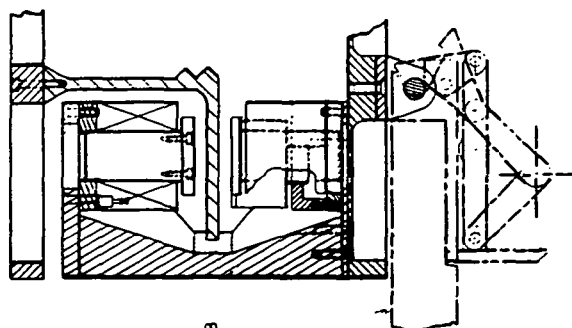
SECTION A-A



SECTION D-D



SECTION C-C



SECTION B-B

(Section lines are shown on Figure 50)

Figure 52
Vernier - Flex Capsule Installation

TABLE 13
VERNIER MODULE WEIGHT BREAKDOWN

Component	Material	Quantity	Weight, kg (lb)			
			Suspended	Fixed	Suspended	Fixed
Axial MBAs	-	3 sets	-	(36.00)	-	16.33
Radial MBAs	-	2 sets	-	(14.40)	-	6.53
Roll Motor	-	1 set	-	(20.50)	-	9.30
Roll Resolver	-	1	(4.33)	(8.67)	1.96	3.93
Rotary Transformer	-	1	(3.49)	(2.51)	1.58	1.14
Proximometers	-	7	-	(1.40)	-	.64
Batteries	-	25	(50.00)	-	22.68	-
Slip Ring Assembly	-	1	(1.00)	(0.25)	.45	.11
Rotor	Steel	1	(47.60)	-	21.59	-
Latch Ring	Steel	1	(8.12)	-	3.68	-
Facia	Al-Alloy	1	-	(1.69)	-	.77
Base Plate	Al-Machining	1	-	(21.07)	-	9.56
Top Plate	Al-Grid	1	(10.40)	-	4.72	-
Optical Coupler	Invar-Quartz	1	(1.97)	(4.17)	.89	1.89
Electronics	-	-	(1.00)	(3.45)	.45	1.56
AX MBA Brackets	Al-Alloy	3	-	(32.67)	-	14.82
RA MBA Brackets	Al-Alloy	2 sets	-	(16.46)	-	7.47
Roll Motor Brackets	Al-Alloy	1 set	-	(5.35)	-	2.43
Resolver Brackets	Al-Alloy	1	(2.92)	(7.04)	1.32	3.19
Battery Brackets	Al	5	(2.30)	-	1.04	-
Latch Mechanisms	Al-Alloy	5	-	(10.60)	-	4.81
Latch Actuators	-	5	-	(6.75)	-	3.06
Caging Bars	Steel	3	-	(3.36)	-	1.52
Slip Ring Solenoids	-	2	-	(1.00)	-	.45
Cabling, Connectors, etc	-	-	(2.50)	(4.00)	1.13	1.81
		Totals	(135.63)	(201.34)	61.49	91.32
		Total	(336.97)		152.82	

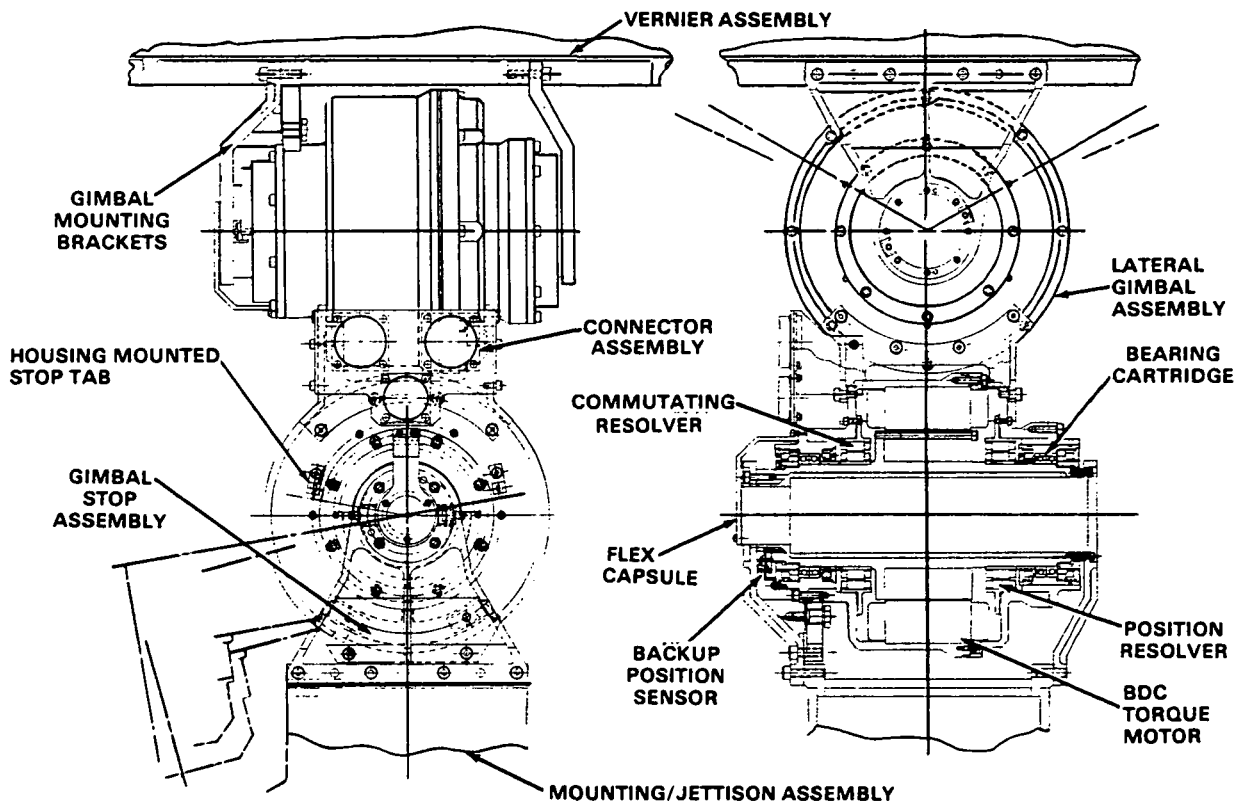


Figure 53
Gimbal Cross Section

TABLE 14
GIMBAL BEARING CHARACTERISTICS

Bearing Manufacturer	KAYDON
Manufacturer's Basic Part Number	KBO30ARD
Bore (ID)	76.2 mm (3.000 in.)
O.D.	92.1 mm (3.625 in.)
Width (per bearing)	7.94 mm (.3125 in.)
Ball Diameter	3.96 mm (.156 in.)
Ball Complement	44
Ball/Ring Material	52100/52100
Cage/Material	Full Halo/Phenolic
Preload	155.7 N (35 lb)
Axial Load Capacity (per bearing)	27135 N (6100 lb)
Radial Load Capacity (per bearing)	9431 N (2120 lb)

The use of the cartridge approach to gimbal bearing mounting simplifies the lubrication of the bearing elements because the lubricant supply and its sealing mechanism can be made an integral part of the cartridge assembly. In the ASPS gimbal bearings, the low bearing operating speeds require reliance upon boundary layer lubrication, as the elastohydrodynamic lubricant film will be virtually nonexistent. The bearing pairs are film lubricated with KG-80 oil which contains TCP as a normal constituent. TCP provides boundary layer lubrication enhancement. The tribological properties of KG-80 oil are listed in Table 15. Additional lubricant is available in porous reservoirs placed on either side of the bearing pair. The porous reservoirs are a nitrile acrylic copolymer (tradename, Microwell) which are capable of vacuum impregnation to 60 percent of the material volume. Oil availability tests conducted at Sperry in temperature/vacuum conditions have confirmed that virtually 100 percent of the impregnated lubricant is available for evaporation. The evaporation of the total lubricant supply provides a lubricant rich vapor within the bearing cartridges and thereby provides a constant lubricant supply to the rolling elements. Incorporated into the lubricant reservoirs are close tolerance labyrinth seals at either end of the bearing cartridge. Diametrical clearance of the labyrinth seals is $.127 \pm .005$ mm ($.005 \pm .0002$ in.). These seals limit lubricant loss to the space environment which is the prime source of lubricant loss and provide the mechanism by which vapor pressure is established and maintained within the cartridge.

By virtue of the fact that the gimbal bearing lubrication and sealing system is passive, there are virtually no failure modes because there are no active elements to fail. Excessive lubrication or starvation is prevented by the selected lubricant delivery system. Furthermore, because the principal

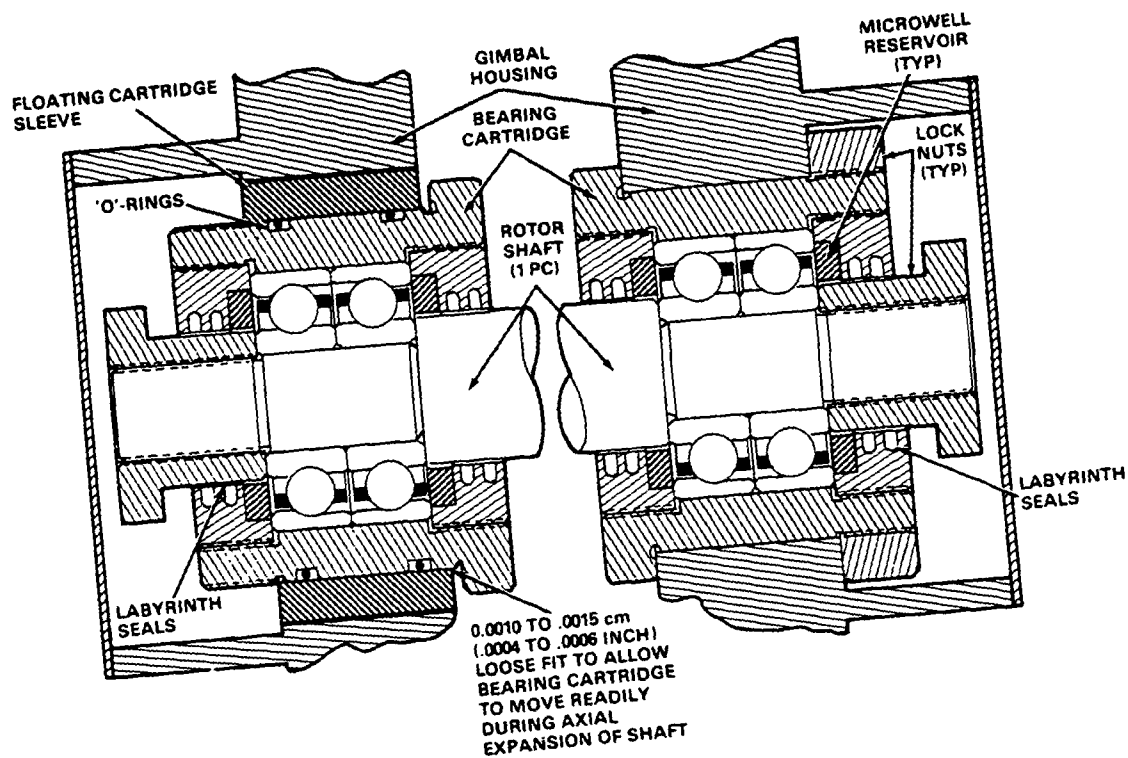


Figure 54
 Typical Fixed/Floating Bearing Assemblies

mode of lubricant loss is loss to space; the labyrinth seals allow for predictable oil supply depletion and a generous oil supply margin can be assured by reservoir sizing. This is illustrated in Table 16 which presents a conservative lubricant loss/life estimation for the ASPS based upon predicted worst-case thermal environments of the gimbal bearings and Sperry accelerated life test data.

Reliance upon the ASPS software provides the prime means of restricting gimbal movement. However, in the event of software or electronic failure, mechanical stops are mounted on the assembly to limit gimbal travel. Each gimbal assembly contains a stop unit mounted beneath the gimbal on one of the gimbal mounting brackets. Working in conjunction with the stop is a set of gimbal housing mounted tabs which function as the actuators for the stop mechanism. An enlarged view of the gimbal stop can be found in Figure 55. The basic stop unit consists of two aluminum pieces joined together by a 6.35 mm (.25 in.) layer of silicone rubber molding compound. Each of the metallic portions is attached to the gimbal bracket; one is rigidly fastened, the other is mounted by shoulder screws and is free to move relative to its attachment point. The housing mounted tabs are solid pieces mounted radially on the housing face and positioned angularly off of the centered gimbal position to allow the desired gimbal travel in each direction. These tabs, riding with the rotating gimbal housing, contact the tab in the center of the slot mounted aluminum piece and move the sliding portion relative to the fixed. The shearing action within the silicone rubber absorbs and dissipates the gimbal energy and brings it to a stop within three degrees of contact assuming a worst-case 600 kg payload rate of three degrees per second on impact. The shoulder screws provide a positive hard stop at the five degree position and ensures against a silicone failure.

TABLE 15
KENDALL KG-80 OIL CHARACTERISTICS

Vapor Pressure after initial 10 percent lubricant loss

Molecular Weight = 591 gm/gm-mole

Temperature (°C) (°F)		Pressure (mm of Hg)
51.7	(125)	8×10^{-8}
93.3	(200)	2.5×10^{-7}
121.1	(250)	3.5×10^{-6}

TABLE 16
GIMBAL BEARING AND LUBRICATION

Bearing	Life Test	ASPS	
		Hot Case	Cold Case
		DF, Preloaded Duplex, Thin Line	DF, Preloaded Duplex, Thin Line
Configuration	Fixed/Floating	Fixed/Floating	Fixed/Floating
Ball/Ring Material	52100/52100	52100/52100	52100/52100
Cage/Material	Full Halo/Phenolic	Full Halo/Phenolic	Full Halo/Phenolic
ID, cm (in.)	7.62 (3)	7.62 (3)	7.62 (3)
Ball Complement	44	44	44
Ball Diameter, cm (in.)	.396 (.156)	.396 (.156)	.396 (.156)
Relative Labyrinth Conductance	1	1	1
Lubricant	Film Oil KG-80 (TCP)	Film Oil KG-80 (TCP)	Film Oil KG-80 (TCP)
Reservoir/Lubricant	.920 gm/KG-80	.920 gm/KG-80	.920 gm/KG-80
Operating Temperature	32°C	54°C	28°C
Lubricant Supply			
1% Depletion	125 days	7.3 days	1.2 years
60% Depletion	20.5 years	1.2 years	72 years

Example Calculation:
$$\frac{\left(\frac{125 \text{ days}}{365 \text{ days/yr}} \right) \left(\frac{1}{1} \right) \left(\frac{.92}{.92} \right) \left(\frac{3.5 \times 10^{-8}}{6. \times 10^{-7}} \right)}{1} = 7.3 \text{ days}$$

\uparrow
Relative Conductance

\uparrow
Relative Oil Supply

\uparrow
Relative Vapor Pressure (Torr)

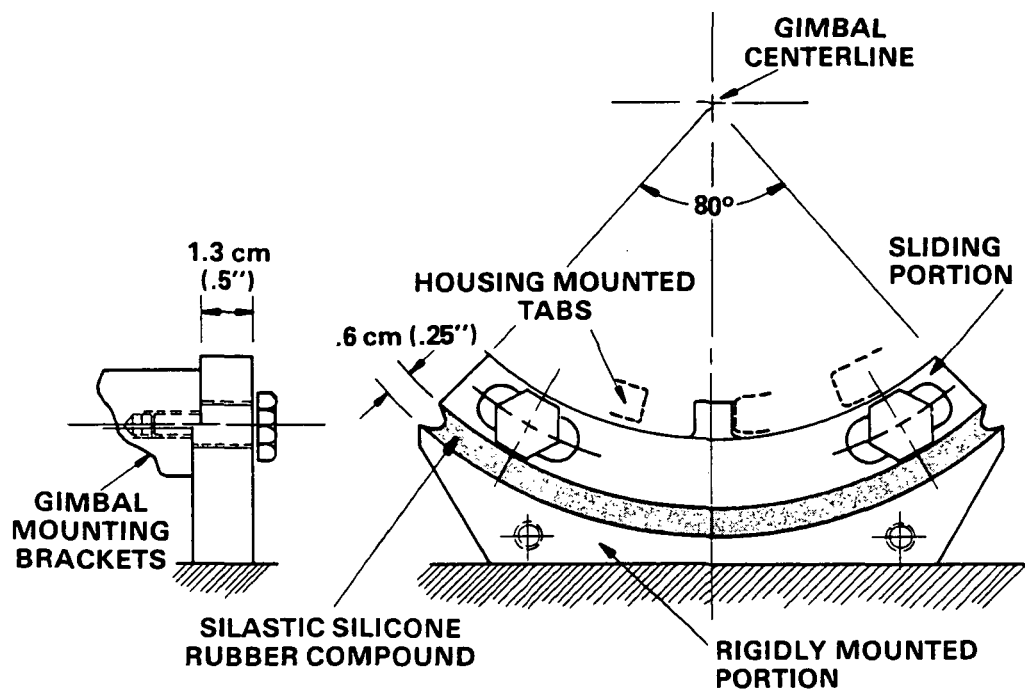


Figure 55
ASPS Gimbal Stops

In the event of a failure within the normal gimbal control system, a redundant position sensor is required for caging of the coarse gimbals during the backup torquing mode. This backup gimbal position sensing system is mounted at one end of the CGA as shown in Figure 53. The unit consists of two light emitter/sensor pairs which are hardmounted to the gimbal housing and a slotted disc attached to the CGA shaft. By sensing which detector(s) is not receiving light input, the gimbal position off of the centered location can be determined. If a particular location is desired additional emitter/sensor pairs can be added. Figure 56 depicts the operational concept of this system.

Although the CGAs are designed for coarse pointing of the ASPS, they have been designed to provide the most accurate pointing available with state-of-the-art, brushless direct drive technology. Frictional torque anomalies have therefore been minimized so as to provide fine pointing resolution using the CGAs. A significant source of these anomalies can be electrical cabling which can introduce variable reaction torques dependent upon temperature, flexure, twisting, etc. The limited rotational freedom of both the elevation and lateral gimbals allows this anomaly to be minimized by routing all electrical cabling through flex capsules. These devices, one mounted within each of the CGA shafts, consist of concentric sets of aluminum rotor and stator members connected by two counterwound flex print configured conductor tapes. This configuration minimizes torque deviations as a function of angular position. The conductor tapes within each flex capsule are designed to support all of the coarse gimbal and vernier signals, plus power requirements as well as the high rate payload data and battery recharge power. Figure 57 illustrates the flex capsule design and lists the conductor capacities supplied by the elevation and lateral CGA flex capsules. The flex capsules used in both CGAs are identical and are interchangeable.

All of the CGA components are housed within the gimbal housing which functions as a structural load carrying member of the gimbal module. The housing functions as the rotating member of the CGA while the CGA shaft performs the function of stator. Both ends of the shaft protrude beyond the volume defined by the CGA housing. This protrusion on each end allows the stator to be rigidly fastened to gimbal mounting brackets which, in turn, are mounted onto interface plates for attachment to the other ASPS modules. The fixed portion of the flex capsule is mounted to one of the gimbal mounting brackets whereas the floating or rotating portion passes through the other bracket and is attached to the gimbal housing by means of a cantilevered bracket.

The two CGA housings are rigidly tied together by the intergimbal support to form the basic gimbal module. On the rotating flex capsule side of the intergimbal support is a connector bracket which supports the cabling between the lateral and elevation gimbal flex capsules. On the opposite side of the intergimbal support is another connector bracket associated with harnessing to the rotating CGA components. Power for the stator portions of the CGAs is routed through connectors located on the VPA or the MJA.

A weight and component breakdown for the CGA is presented in Table 17.

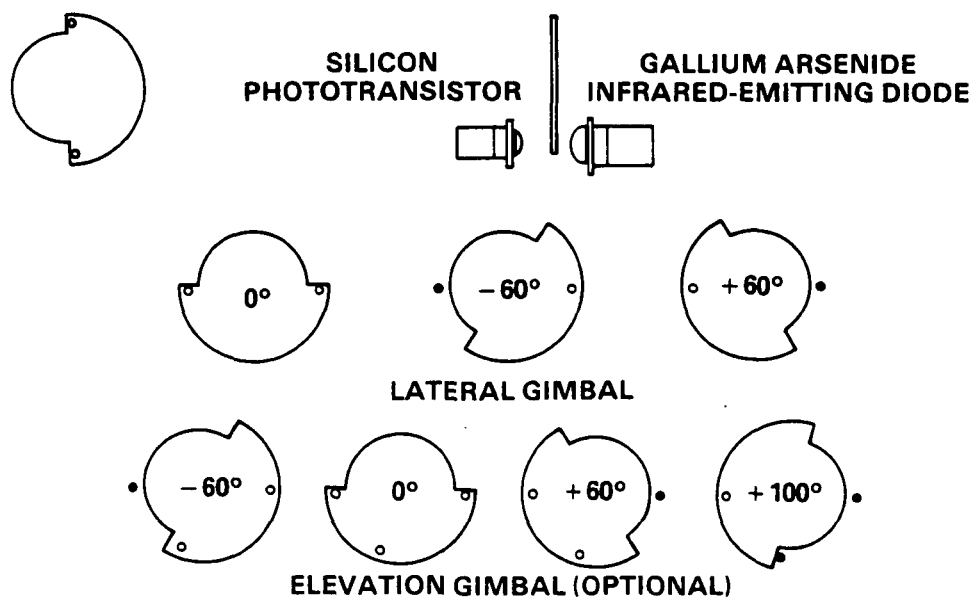
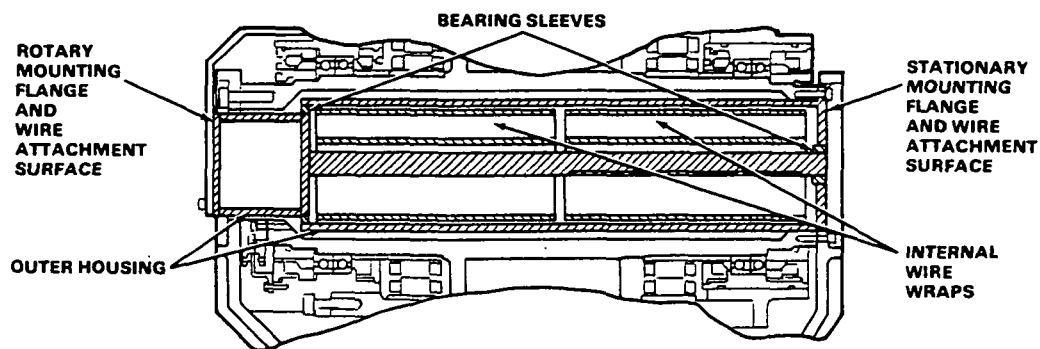


Figure 56
Backup Gimbal Position Sensing System



<u>WIRE GAGE</u>	<u>CURRENT CAPACITY, AMPS</u>	<u>ELE. GIMBAL</u>	<u>LAT. GIMBAL</u>	<u>VERNIER (OPTIONAL)</u>
16	20	8	8	—
16	10	16	16	8
18	5	8	8	8
22	4	15	15	—
22	2	48	48	14
22	SIGNAL	83	83	15
TWISTED	3 SIGNAL	18 TSP	18 TSP	18 TSP
SHIELDED PAIR (TSP)	CONDUCTORS EACH	TOTALS 232	TOTALS 232	TOTALS 91

Figure 57
ASPS Flex Capsule Characteristics

TABLE 17
GIMBAL MODULE WEIGHT BREAKDOWN

Gimbal Assembly				
Component	Material	Quantity	Weight (lb) (kg)	
DC Torque Motor	-	1	27.0	12.24
Resolver, Commutating	-	1	1.0	.45
Resolver, Position	-	1	1.0	.45
Bearings	ST-52100	4 pr	.80	.36
Shaft	Steel	1	6.82	3.09
Gimbal Housing	AL	1	4.09	1.86
Gimbal Cover	AL	1	5.43	2.46
Fixed Cartridge	Ti-6AL, 4V	1	1.14	.52
Floating Cartridge	Ti-6AL, 4V	1	.50	.23
Cartridge Sleeve	Ti-6AL, 4V	1	1.18	.54
Reservoir Cup	Ti-6AL, 4V	4	.48	.22
Cartridge Nuts	Ti-6AL, 4V	4	1.12	.51
Shaft Nut	Ti-6AL, 4V	2	.22	.10
Spacer	Ti-6AL, 4V	2	.12	.05
Flex Capsule	-	1	.8	.36
Thermostat	-	1	.05	.02
Thermistor	-	1	.01	.00
Heat Element	Kapton	2	.02	.01
Gimbal Stop System	-	1	.40	.18
Back-Up Position Sensor	-	1	.12	.05
Gimbal Bracket	AL	2	2.62	1.19
Cabling, Connectors, etc	-	-	4.5	2.04
		TOTAL	58.42	26.49
Gimbal Interface Bracket	AL	1	1.08	.49
Connector Brackets	AL	2	.50	.23
		TOTAL	1.58	.72
Elevation Gimbal	-	-	58.42	26.49
Lateral Gimbal	-	-	58.42	26.49
Interfacing	-	-	1.58	.72
		TOTAL	118.42	53.71

4.1.4 Mounting/Jettison Assembly

The Mounting/Jettison Assembly (MJA) provides the physical connection between the ASPS coarse gimbals and/or VPAs and the pallet structure. Its design can be tailored to provide the specific operational and structural characteristics required by a given mission, or category of missions. This might include an erectable mast assembly, a pallet mount, a simple mast, or a specially designed platform. In the case of the OFT-4 mission, the basic module is shown in Figure 58 and consists of a .3048 m (12 in.) diameter cylinder of .4826 m (19 in.) height which provides a mounting interface at the top to support the gimbal module and a mounting surface at the base for attachment to the pallet interface structure. This structure is comprised of three basic components: the mounting pedestal, the interface structure, and the pyrotechnic system.

The mounting pedestal is a simple straight walled hollow aluminum cylinder with a mounting flange on the base. A cutout near the base houses an electrical connector panel. The cabling runs inside this cylinder.

Atop the mounting pedestal is the interface structure which assembles to the pedestal by means of a locating flange on its base. It tapers to a smaller cylinder and square bracket at the top to which the gimbals are fastened.

Should the need arise, through a multiple failure, the ASPS can be separated and jettisoned from the Orbiter; Figure 58 shows the initial design of the jettison system. Three pyrotechnic devices are utilized for severing mechanical and electrical connections. The primary component in the separation system is a separation band which runs circumferentially about the MJA. During jettison, two pin pullers are actuated by pyrotechnics thereby releasing a pre-tensioned separation band; the band remains attached to the pedestal. The band normally retains the gimbal interface to the mounting pedestal by a clamping action between parallel raised lips. The jettison system does not impart a velocity to the ASPS; consequently, the Orbiter Remote Manipulator System or Orbiter flyaway is required to physically jettison the unit. Electrical connections are severed by a pyrotechnic actuated cable cutter located inside the mounting column.

Table 18 provides an estimate of the MJA weight by component.

TABLE 18
MOUNTING/JETTISON ASSEMBLY WEIGHT BREAKDOWN

Component	Material	Quantity	Weight, kg (lb)	
Mast	Al-Alloy	1	17.17	(37.86)
Jettison System	-	1	1.90	(4.18)
Cabling, Connectors, etc	-		1.13	(2.50)
		Total	20.20	(44.54)

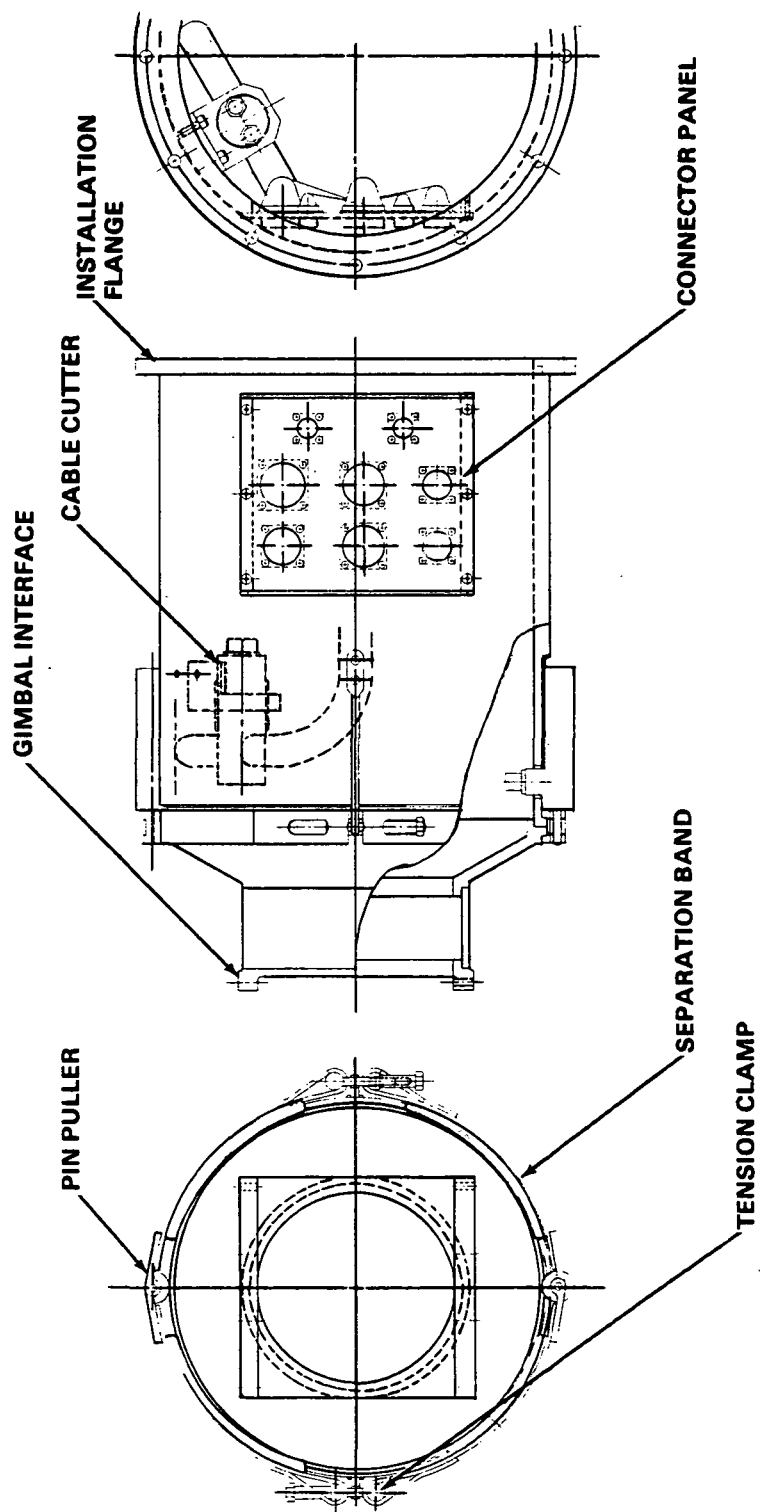


Figure 58
Mounting/Jettison Assembly

4.1.5 Caging and Latching

During launch and landing, the ASPS and the payload plate-mounted experiment are rigidly caged to the pallet integration structure as shown in Figures 48 and 49. Restraint of the ASPS in the event of an abnormal (crash) landing must also be provided. Under the present design, the restraint planes of the ASPS/Experiment system are located at the base of the vernier and through the payload CM, with additional latching planes as required. To minimize loading on the coarse gimbal bearings and components inside the vernier pointing assembly, the five vernier latches are engaged and the base of vernier assembly is rigidly caged by three additional latches to the caging support structure. Location of the latches within the vernier assembly ensures that the launch and landing loads are supported by the caging system, and are not transmitted through the coarse gimbal bearings. An idealization of this latching and caging system and how it relates to the ASPS is shown in Figure 59. It should be noted when referring to this illustration that in the actual ASPS the function of the caging annulus, which is to rigidly connect the vernier and caging latches, is performed by the baseplate of the VPA. A tabulation of the estimated weights of the caging and latching system components is given in Table 19.

TABLE 19
CAGING SYSTEM WEIGHT BREAKDOWN

Component	Material	Quantity	Weight, kg (lb)	
Latches	-	3	3.95	(8.70)
Actuators	-	3	1.84	(4.05)
Structure	Al	1	7.71	(17.00)
		Total	13.49	(29.75)

A vernier latch assembly is depicted in Figure 60, whereas a caging latch is shown in Figure 61. The basic actuator for both latch systems is illustrated in Figure 62. It can be noted that both devices are toggle type mechanisms.

The vernier latch assembly, shown in Figure 60, is based upon a slider-crank arrangement wherein the actuator drives a toggle joint connected to a slider. The slider is fabricated with a tapered lead which ramps up to a flat land. Riding against the slider, or latch pin driver, is the latch pin which is spring-loaded toward the retracted position and is constantly kept in contact with the slider. As the toggle moves the slider up and down, the latch pin by virtue of its contact with the ramp, is driven in and out of the vernier latch assembly housing. Placement of the latch pin on the slider land stops outward movement of the pin which is also limited from further movement by the retracting springs. Further motion of the slider does not change the pin

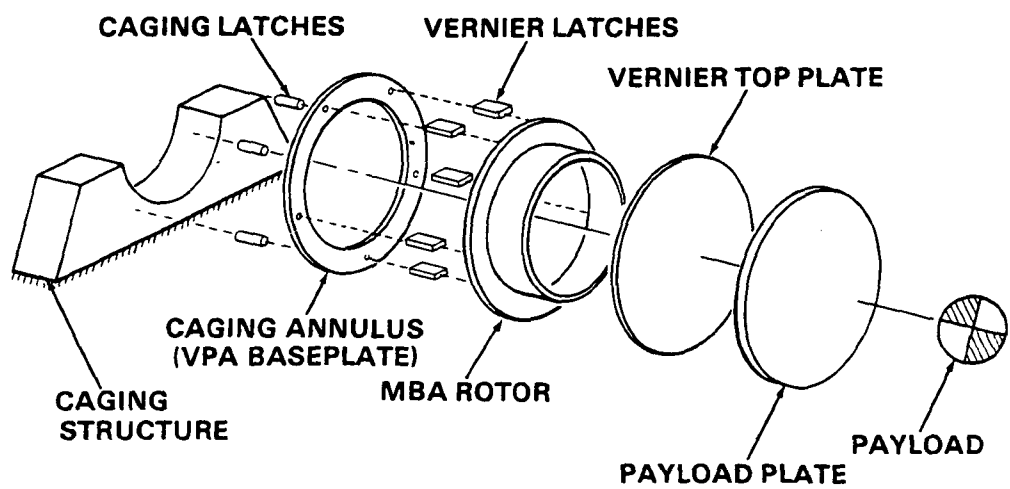


Figure 59
Caging Schematic

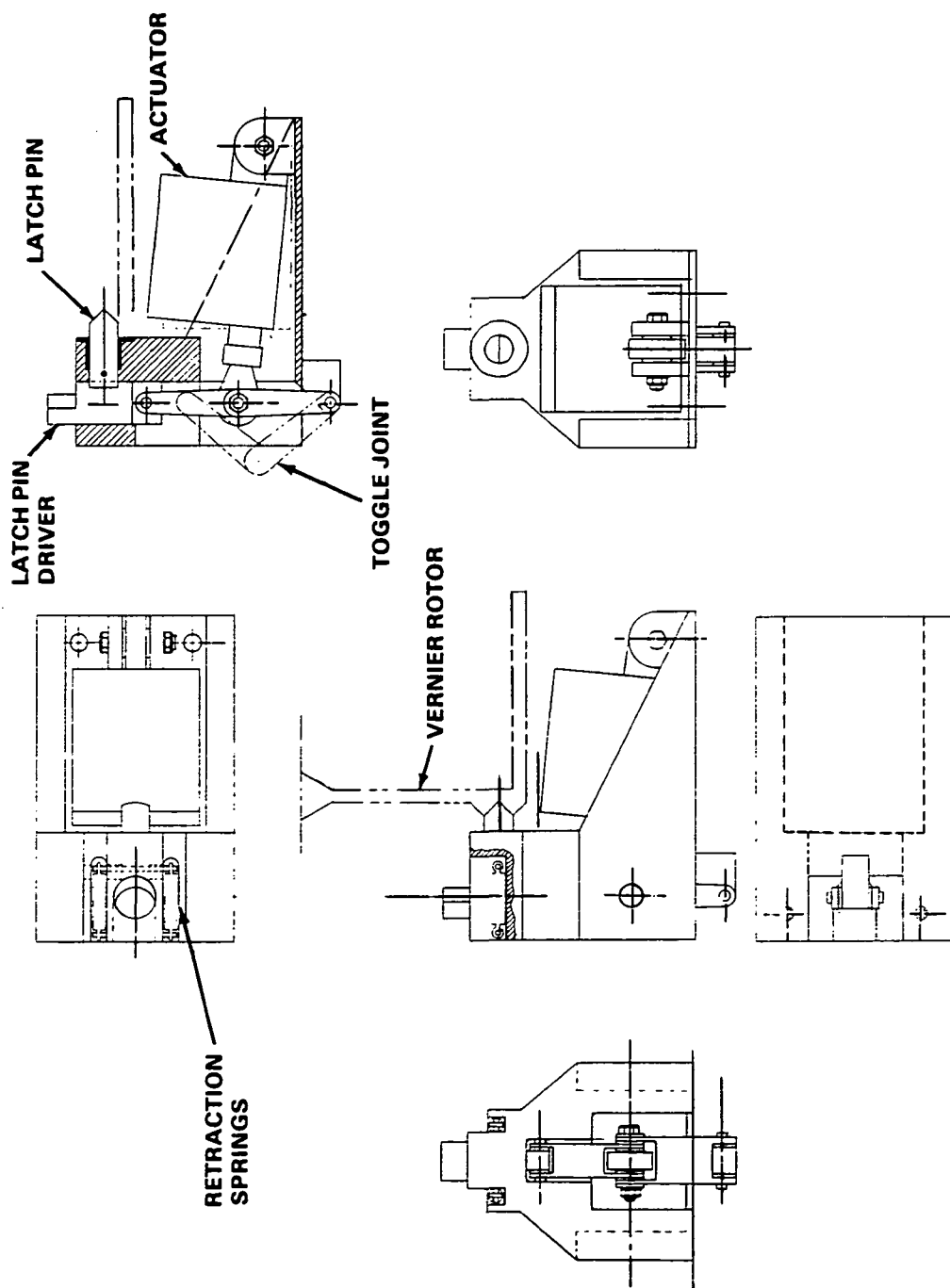


Figure 60
Vernier Latch

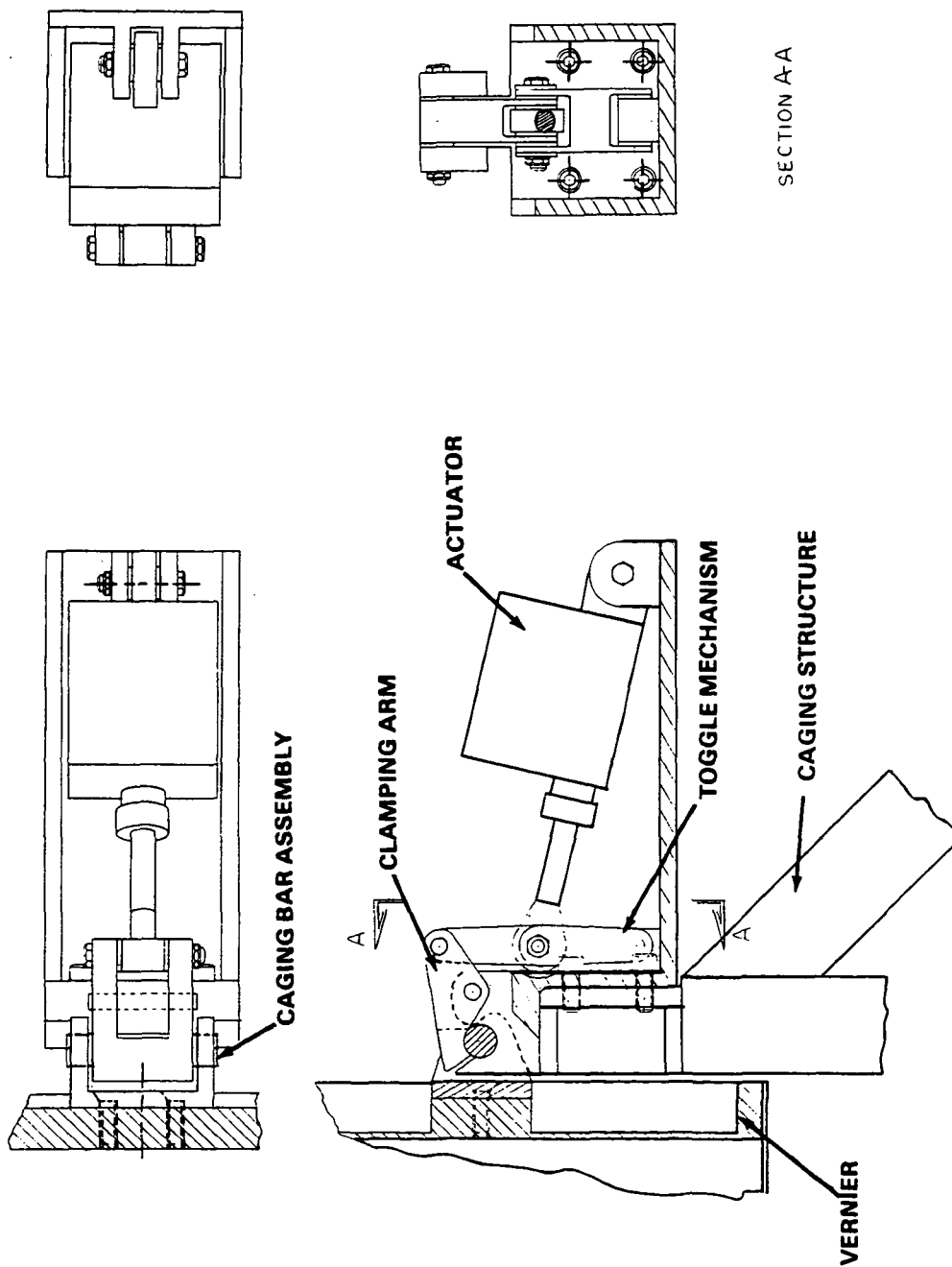
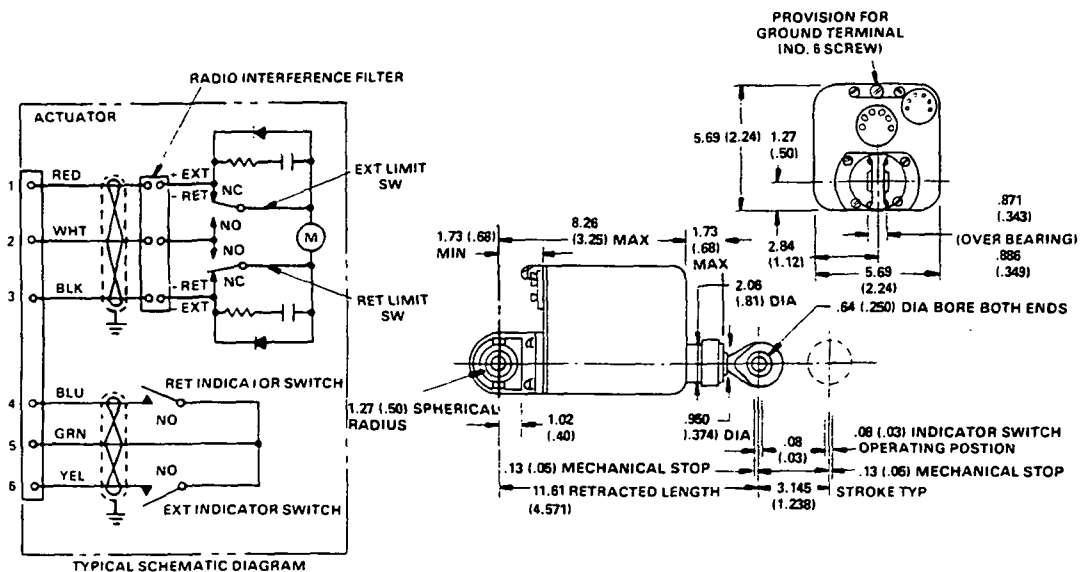


Figure 61
Caging Latch



DIMENSIONS IN cm (IN.)

Figure 62
Linear Actuator
(Typical Outline Drawing)

position once it is located on the land unless the slider ramp is brought into contact with the pin. The pin tip is tapered and mates with a groove on the MBA rotor to provide positive location and engagement of the rotor. The pin's tip is configured so as to bring the rotor into its centered position with respect to the MBAs as the pin is moved outward to the latched position. The simultaneous action of the five latches amplifies this action. In the fully retracted position, the pin floats in the rotor groove during normal rotor excursions, which never exceed 6.35 mm (.250 in.). Throughout this rotor movement, the rotor groove is captured by the set of five pins so that it is impossible for the rotor to become separated from the fixed portion of the VPA. The latch pins, therefore, function as a backup or touchdown bearing system for the VPA.

The caging latches, which are mounted on the caging frame attached to the pallet integration structure, act on a set of caging bars mounted on the underside of the VPA baseplate. Provision is also made to mount these bar assemblies on the undersurface of the payload plate in the event the VPA is not used. The caging bars are spaced at 90 degree intervals as shown in Figure 48.

The caging units themselves, shown in Figure 61, use a toggle to activate a bellcrank which captures, positions, and locks the VPA to the caging frame. The caging frame, to which the caging latches are mounted, is shown in Figures 48 and 49, and is a simple aluminum rectangular tubing weldment. As with the ASPS, the frame is located in an area on the pallet integration structure which is locally reinforced to provide the ASPS/Payload combination with as rigid a mount as practical.

4.1.6 Payload Command and Data Transfer

For transmission of data and control signals between the payload and the Orbiter, there are two options. For total separation of the payload, an optical coupler is available which provides three communications channels between the suspended and nonsuspended portions. For those applications in which extreme pointing stability is not necessary, a flexible cable unit is available. The optical coupler installation is shown in Figure 51. The flex capsule alternative appears in Figure 63.

A detailed layout of the optical coupler is contained in Figure 64. The larger of the two assemblies is attached to the fixed segment of the VPA while the smaller is a part of the suspended section. A detailed description of the theory of operation is to be found in Section 5.0 and will not be covered here, except as necessary to describe its mechanical features.

Each of the three communications channels consists of a light source that emits a beam which is corrected by a collimating lens from which the beam travels to an isolating lens. After passing through this lens, the light beam travels toward its focal point. On Channels 2 and 3, it is reflected by a mirror as it travels toward its detector. On Channel 1, the light travels directly from the isolating lens to the detector. These channels and their components can be located on Figure 64. The three channels are positioned coaxially, with Channel 1 on the inside, Channel 2 in the middle, and Channel 3 on the outside.

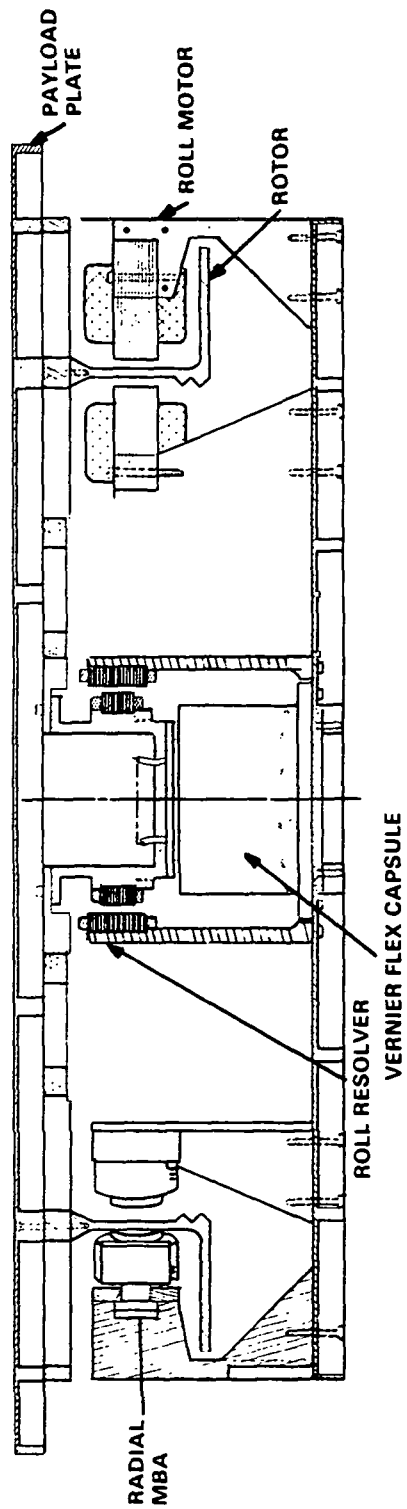


Figure 63
Vernier - Flex Capsule Alternative Installation

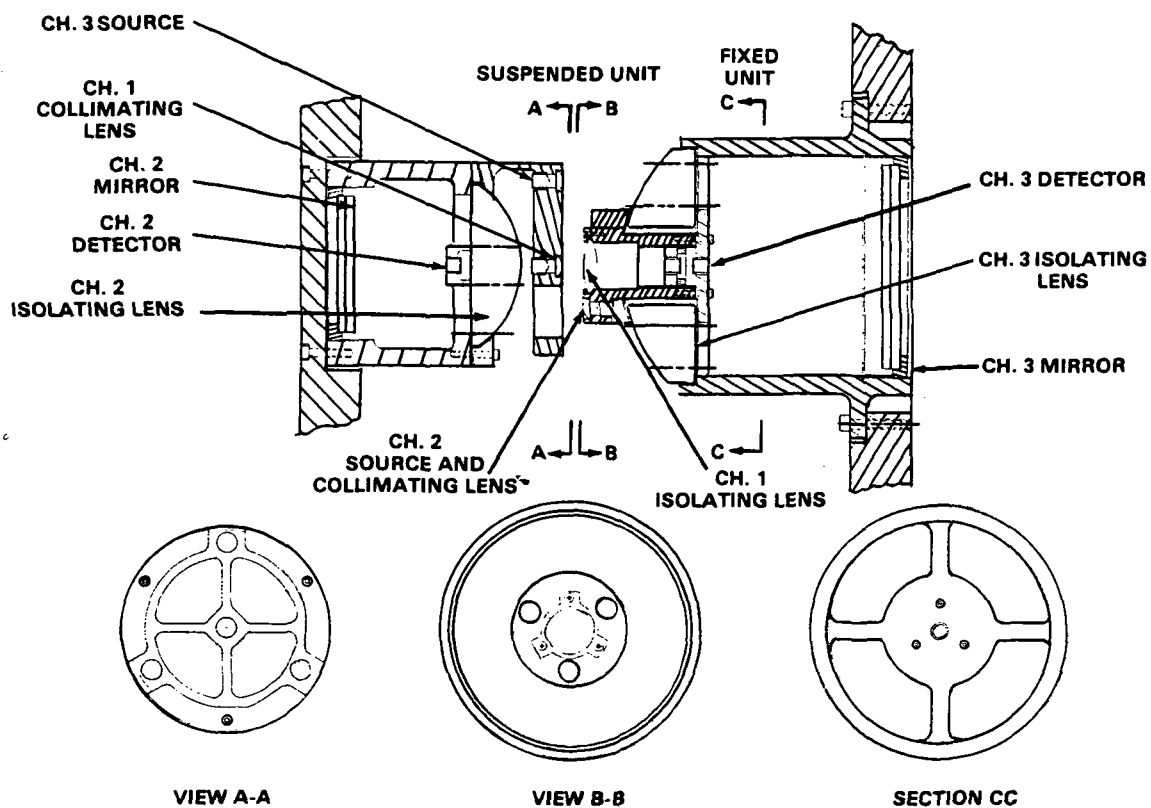


Figure 64
Optical Coupler

During assembly of the optical coupler, the emitting light source and detector are fastened into their mountings. The collimating lens is fixturized and adjusted until the proper beam characteristics are achieved and at that point is bonded in place. The isolating lens is clamped into position through resilient membranes to minimize shock yet still enable precise control of the optical positioning. The mirrors are then installed and adjusted until the desired beam detection levels are obtained and then bonded in place. Thermal effects are minimized by the use of good quality quartz lenses and INVAR housings. This allows for matching of the thermal characteristics so that the optical properties of the overall system are preserved.

A conceptual layout of the flex capsule alternative to the optical coupler is shown in Figure 65. The basic approach to this unit will be identical to that applied to the CGA flex capsules, except that accommodation for six degrees of freedom will be provided. Inclusion of the flex capsule allows deletion of the batteries, optical coupler, rotary transformer, and vernier slip rings. Figure 57 lists the available wire capacity of the vernier flex capsule alternative.

4.2 MECHANICAL DESIGN

4.2.1 Mechanical Interfaces

ASPS experiments are attached to a removable payload mounting plate. The payload plate is a .9652 m (38 in.) diameter, 22.2 mm (.875 in.) thick aluminum machined structure which normally mounts on top of the VPA.

Assembly of the payload plate to the upper vernier is provided by a series of twelve 1/4-20 fasteners spaced at 30 degree intervals around .628 m (24.75 in.) nominal diameter. Flathead screws pass through clearance holes in the payload plate and fasten into the vernier plate which is itself a machined aluminum grid 19.05 mm (.75 in.) thick. The boltheads attaching the payload plates to the vernier top plate do not protrude above the upper surface of the payload plate, thereby providing an obstacle-free surface for the payload integration.

Two electrical connectors are mounted to the vernier top plate, and a clearance hole in the payload plate provides access to these connectors from the payload. These connectors provide power and data connections for the experiment.

For those missions in which the VPA is not required, the payload plate is capable of being mounted directly to the lateral gimbal mounting brackets using eight 1/4-20 bolts and four 6.35 mm (.25 in.) locating pins. These fasteners attach the gimbal brackets to integral mounting ribs on the bottom surface of the payload plate or the vernier assembly bottom plate.

Mechanical integration of the payload to the ASPS payload plate is provided by a matrix of threaded inserts in the upper surface of the payload plate. Inserts selected are TAP-LOK type HM25028-5 (stainless steel). These embedded steel inserts provide for direct attachment to the plate reinforcing ribs and, by virtue of their being dispersed over the entire payload plate

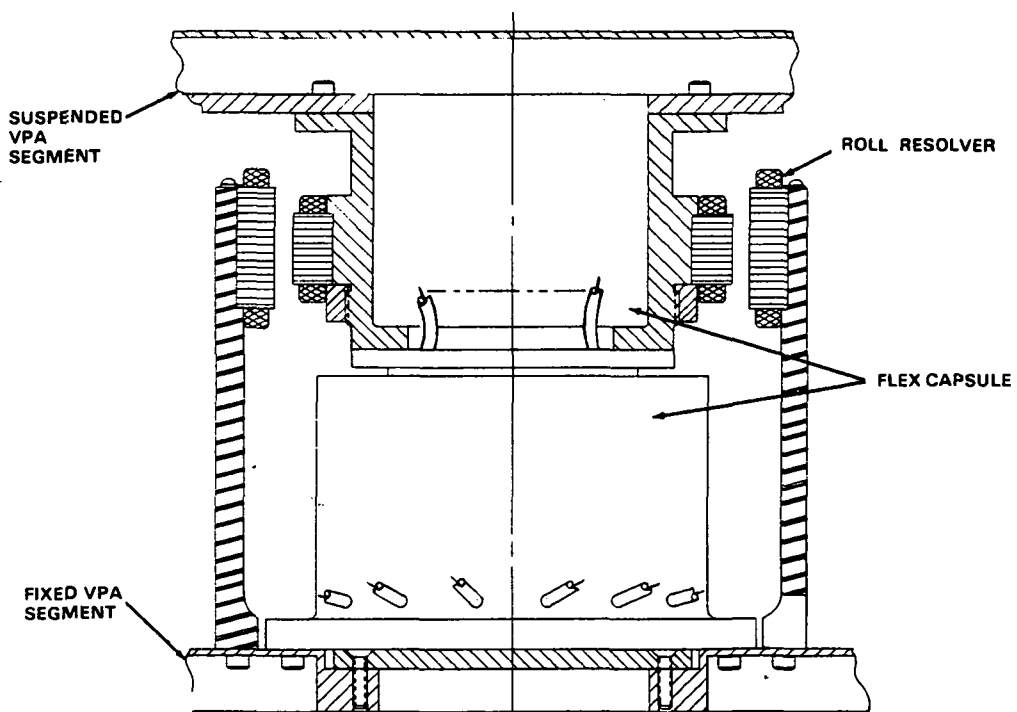


Figure 65
Vernier Flex Capsule

surface, allow for great freedom in payload attachment. In the event that this standard matrix is not sufficient for a particular application, additional attachment points can be added.

The MJA and interim mounting structure connect the CGA to the carrier pallet. The MJA contains the pyrotechnics required for ASPS jettison and is mission-dependent. It may consist of an erectable mast, a rigid mast, or a specially designed platform. In the case of the OFT-4 mission, the MJA is a 304.8 mm (12 in.) O.D. by 279.4 mm (11 in.) I.D. rigid cylinder of .4826 m (19 in.) height which provides a mounting surface at the top of the gimbal module and a mounting surface at the base for attachment to the pallet integration structure.

The platform must support the ASPS and payload loads during launch and landing including a one-time crash load. It also supports the caging assembly which retains the VPA and the payload mass. Figures 48 and 49 illustrate a typical mounting of the ASPS to the pallet using the general arrangement planned for OFT-4. The integration structure is braced and connected to the pallet hardpoints.

Alignment between the Orbiter Navigation Base and the ASPS will be in excess of two degrees due to alignment uncertainties in the Shuttle itself. Within the ASPS, mechanical tolerances and resolver alignments will add an additional .5 degree of fixed misalignment between the pallet interface and the payload mounting plate. Since the ASPS utilizes payload error for control, these initial misalignments may be calibrated in orbit. Resolver functional errors and mechanical instability due to thermal variations, gimbal axial non-orthogonality, etc, are controlled in the ASPS to provide repeatable coarse pointing within ± 1 degree relative to the calibrated alignment position.

4.2.2 Structural Considerations

The environments which comprise the mission can be categorized as quasi-static and dynamic. Quasi-static loads are those conditions which can be characterized by equivalent acceleration levels. These include Lift Off, High Q Boost, Max Boost, Entry and Descent, and Landing. Also, the abnormal mission case of crash landing is a quasi-static event. Dynamic Environments are those conditions which are of a frequency or time dependent nature and thereby impose dynamic loading on the structure. These include Sinusoidal, Random, Aeronoise and Acoustic Vibration.

4.2.2.1 Quasi-Static Events

The quasi-static events of primary concern are those of Lift Off, Orbiter Max Boost, Landing, and Crash. These loads are given in Table 20 which are taken from Reference 3. These values of the equivalent static loads are used to generate the limit loads which are defined as the maximum loads to which the structure will be subjected in operation. From the limit load the design load is derived. This is the limit load with the inclusion of a safety factor as explained in Table 21. The Margin of Safety (MS) is derived from the design load and is defined as follows:

$$\text{MARGIN OF SAFETY (MS)} = \frac{\text{ALLOWABLE LOAD (A)}}{\text{DESIGN LOAD (D)}} - 1.0 \geq 0.0.$$

TABLE 20
ORBITER ACCELERATION LIMIT LOAD FACTORS (G'S)
MAXIMUM ACCELERATION LEVELS, g's

Condition	\ddot{X}	\ddot{Y}	\ddot{Z}	Composite Magnitude	F.S.	Design Load
Lift-Off	-0.1 -2.9	± 1.0	± 1.5	3.4	1.65	5.6
Max Boost Orbiter Only	-2.7 -3.3	± 0.2	-0.75	3.4	1.65	5.6
Landing	+1.0 -0.8	± 0.5	+2.8 +2.2	3.0	1.65	5.0
Crash	+4.5 -1.5	± 1.5	+4.5 -2.0	6.5	1.00	6.5

TABLE 21
DESIGN CRITERIA

Design Loads		
Design = Factor of Safety (FS) x Limit Load (L)		
$D = FS \times L$		
Factors of Safety		
Environment	Factors of Safety For Primary Structure	Factors of Safety For Secondary Structure
Normal - Flight Events, Acceptance Test Prelaunch, Postlaunch	1.65 On Yield Strength	1.65 On Yield Strength
Shuttle Crash Event	< 1.0 On Yield Strength ≥ 1.0 On Ultimate Strength	< 1.0 On Yield Strength < 1.0 On Ultimate Strength

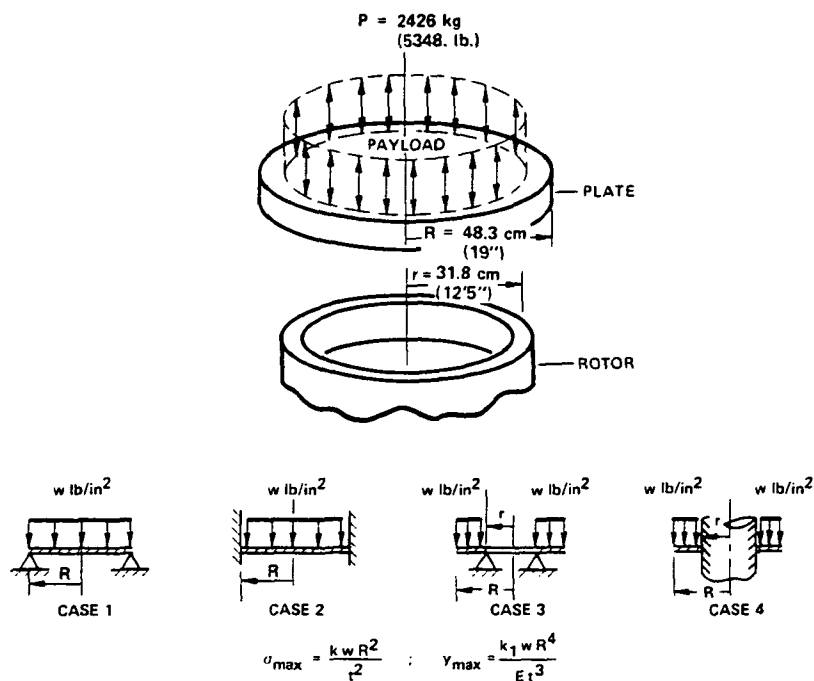
Reference to Table 20 shows that the crash load creates the maximum design load requirement. The load path of the caged ASPS/Payload system is directly from the payload plate/vernier plate, through the latches and caging assemblies, and into the pallet integration structure. The major compliant member is the payload plate and vernier top plate combination. The interface between the rotor and the vernier top plate as well as that between the payload plate and the vernier top plate is a bolted and pinned connection, and is neither a truly clamped nor a truly simply supported interface. However, the true interface will be somewhere between these two forms. Thus, both conditions may be analyzed and the worst case utilized for design. This approach is pictorially illustrated in Figure 66. In the analysis shown, the payload plate is acting alone as if the vernier module were not required. By considering this worst case, a minimum plate thickness can be generated which in turn can be used to generate the reinforcing rib and face thickness requirements of the machined grid-plates utilized in the payload and vernier base plates. This procedure is illustrated in Figures 67 and 68.

Another item which must be factored into the design of the plates is the structural element which functions as the caging restraint. An analysis can be performed if the plate being restrained by the caging latches is considered to be an annulus which is loaded, as shown in Figure 69a. From a structural standpoint, the worst case arises if the annulus is assumed to be built-in at the horizontal caging plane and is loaded by the vernier latches under the assumption that one or more vernier latches has failed; this is illustrated in Figure 69b. From this analysis, it can be seen that either the payload or vernier baseplate can function as the caging annulus if properly proportioned.

Having sized the payload plate, vernier top plate, and vernier bottom plate on the basis of their capacity to individually withstand the crash loads acting on the payload mass, it remains to verify the capacity of the combined payload plate/vernier top plate to support the combined mass of the payload and vernier rotor assembly under the same crash loading conditions. Table 22 shows the variation of stress and deflection of the assembly as a function of the percentage of 600 kg payload carried by the upper plate combination. (The remaining portion of the payload is assumed to be supported by the payload clamps.)

Under the assumption that the 600 kg payload is supported equally by payload cg clamps and the vernier caging clamps, the margin of safety can be calculated for each of the four loading cases. These values are 40.5, 67.6, 17.7, and 53.3 for the four loading cases, one to four, respectively.

The rotor connected to the top vernier plate ensures that the support condition represented in Figure 66 is valid. Outboard of the rotor attachment location, the rotor floats between the axial MBA clearances. Inboard, at the center of the vernier module, is the optical coupler which must also be protected from contact. Under the same conditions as analyzed previously, the deflections of the top plates are .23 mm (.009 in.), .05 mm (.002 in.), .89 mm (.035 in.), and .02 mm (.001 in.) for cases one through four, respectively.

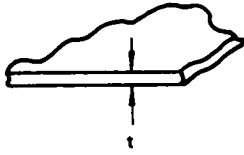


$t = 1.25 \text{ cm}$ $w = 33 \text{ kPa}$ $r = 31.8 \text{ cm}$ $R = 48.3 \text{ cm}$ $E = 69 \text{ GPa}$
 $(.494 \text{ in.})$ (4.72 lb/in.^2) (12.5 in.) (19 in.) $(10 \times 10^6 \text{ psi})$

CASE	1	2	3	4
γ_{\max}	.170cm (0.067 in.)	.041cm (0.016 in.)	.635cm (0.250 in.)	.023cm (0.009 in.)
σ_{\max}	24MPa (3447. psi)	16MPa (2267. psi)	57MPa (8309. psi)	20MPa (2863. psi)

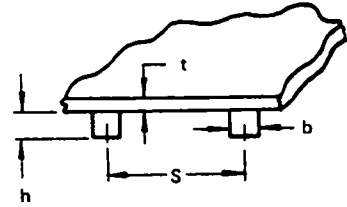
E = Young's Modulus, GPa (psi)
 k = Stress Correction Factor
 k_1 = Deflection Correction Factor
 P = Load, kg (lb)
 r = Inner Radius, cm (in.)
 R = Outer Radius, cm (in.)
 t = Plate Thickness, cm (in.)
 w = Distributed Load, GPa (psi)
 γ = Deflection, cm (in.)
 σ = Stress, MPa (psi)

Figure 66
 Payload Plate Analysis



FLEXURAL MODULUS:

$$D = \frac{Et^3}{12(1-\nu^2)}$$



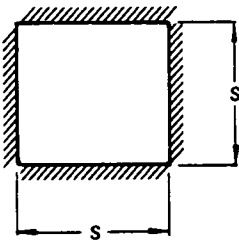
$$D = \frac{Et^3}{12(1-\nu^2)} + \frac{E'I'}{S}$$

or, if $E = E'$

$$D = E \left[\frac{t^3}{12(1-\nu^2)} + \frac{I'}{S} \right]$$

$$D = \frac{E}{12} \left\{ \frac{t^3}{(1-\nu^2)} + \frac{bh[h^2 + 3(t+h)^2]}{S} \right\}$$

FACE SHEET



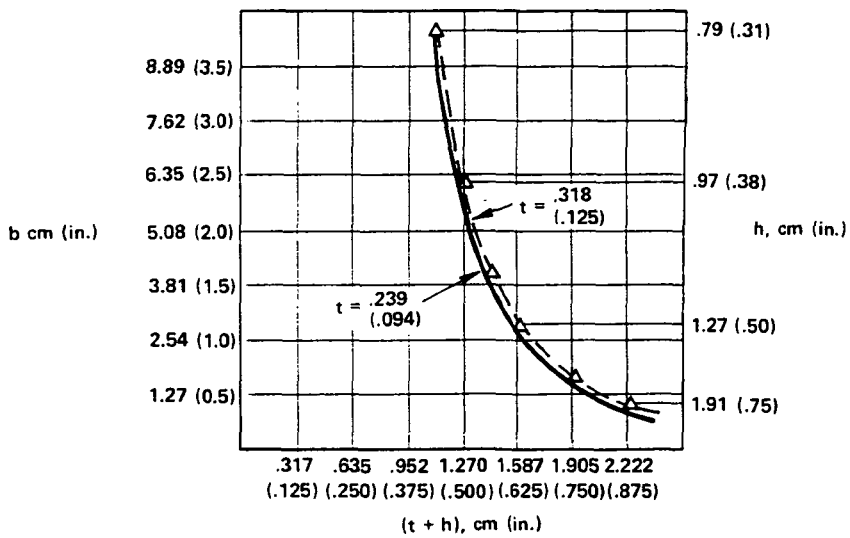
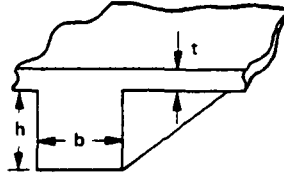
$$\sigma_{\max} = \frac{kws^2}{t^2} ; \quad y_{\max} = \frac{k_1ws^4}{Et^3}$$

$$S = 15.24 \text{ cm (6 in.)}$$

t	.160cm (.063 in.)	.239cm (.094 in.)	.318cm (.125 in.)
σ_{\max}	91MPa (13186. psi)	41MPa (5923. psi)	23MPa (3349. psi)
y_{\max}	.086cm (0.034 in.)	.025cm (0.010 in.)	.010cm (0.004 in.)

- b = Rib Width, cm (in.)
- D = Plate Flexural Rigidity, Ncm (lb-in.)
- E = Young's Modulus of Plate, GPa (psi)
- E' = Young's Modulus of Rib, GPa (psi)
- h = Rib Thickness, cm (in.)
- I' = Area Moment of Inertia of Rib, cm^4 (in^4)
- k = Stress Correction Factor
- k_1 = Deflection Correction Factor
- S = Rib Spacing, cm (in.)
- t = Plate Thickness, cm (in.)
- w = Distributed Load, GPa (psi)
- y = Deflection, cm (in.)
- ν = Poisson's Ratio
- σ = Stress, MPa (psi)

Figure 67
Reinforced Plate Analysis



- b = Rib Width, cm (in.)
- D = Plate Flexural Rigidity, Ncm (lb-in.)
- E = Young's Modulus of Plate, GPa (psi)
- E = Young's Modulus of Rib, GPa (psi)
- h = Rib Thickness, cm (in.)
- I = Area Moment of Inertia of Rib, cm⁴ (in⁴)
- k = Stress Correction Factor
- k₁ = Deflection Correction Factor
- S = Rib Spacing, cm (in.)
- t = Plate Thickness, cm (in.)
- w = Distributed Load, GPa (psi)
- y = Deflection, cm (in.)
- ν = Poisson's Ratio
- σ = Stress, MPa (psi)

Figure 68
Ribs

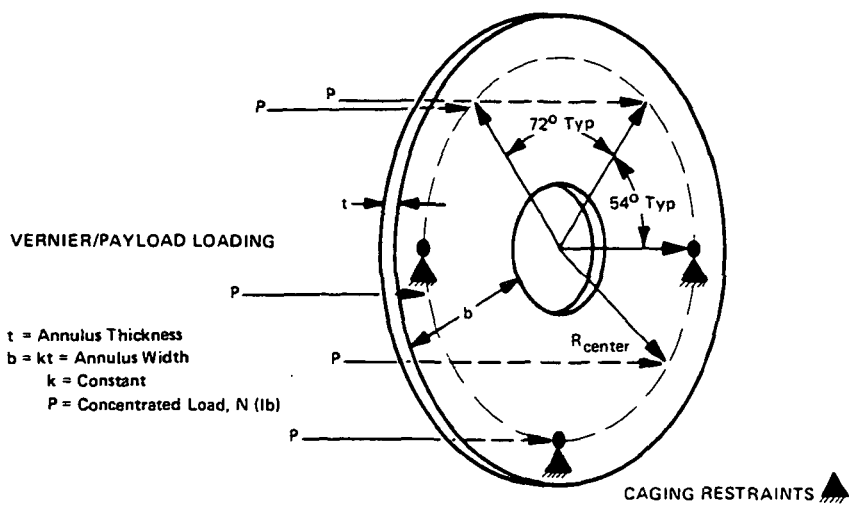


Figure 69a
Caging Annulus

R_{center} = Nominal Caging/Vernier Latch Centerline = 28 cm (11 in.)

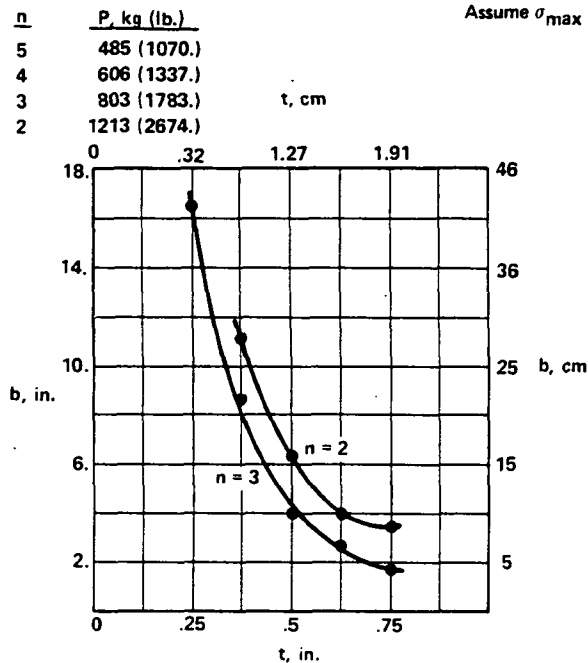
P_{total} = (Vernier + P/L) X $g_{\text{max design}}$

$$= \left[\frac{P/L}{R} + P/L \text{ Plate} + \text{Sus Vernier} \right] \times 6.5 = 2426 \text{ kg (5348 lb.) nominal}$$

$$\sigma_{\text{max}} = \frac{6PR_{\text{CK}}}{kt^3} ; K = \text{constant} = f\left(\frac{EI}{GJ}, \theta\right)$$

$P = P_{\text{total}} \div n$; n = number of effective clamps

Assume $\sigma_{\text{max}} = \frac{\sigma_{\text{yield}}}{4}$; to minimize horizontal deflection



b = WIDTH OF ANNULUS, cm (in.)

E = YOUNG'S MODULUS, GPa (psi)

G = SHEAR MODULUS, GPa (psi)

I = AREA MOMENT OF INERTIA, cm^4 (in^4)

J = AREA POLAR MOMENT OF INERTIA, cm^4 (in^4)

k = PROPORTIONALITY FACTOR BETWEEN THICKNESS AND WIDTH OF ANNULUS

K = CORRECTION FACTOR, AS DEFINED ABOVE

P = CONCENTRATED LOAD, N (lb)

R = CLAMP CENTERLINE RADIUS, cm (in.)

t = ANNULUS THICKNESS, cm (in.)

θ = HALF ANGLE OF UNSUPPORTED SEGMENT, DEG

σ = STRESS, MPa (psi)

Figure 69b
Caging Annulus

TABLE 22
PAYLOAD/VERNIER PLATES VS SUPPORTED PAYLOAD
CASE 3 STRESS AND DEFLECTION

Percent P/L	MPa	max (psi)	mm	y max (in.)
0	3.1	(445)	0.18	(0.007)
10	5.6	(805)	0.33	(0.013)
20	8.0	(1165)	0.46	(0.018)
30	10.5	(1525)	0.61	(0.024)
40	13.0	(1885)	0.76	(0.030)
50	15.5	(2246)	0.89	(0.035)
60	18.0	(2606)	1.04	(0.041)
70	20.5	(2966)	1.17	(0.046)
80	22.9	(3326)	1.32	(0.052)
90	25.4	(3686)	1.47	(0.058)
100	27.9	(4046)	1.60	(0.063)

4.2.2.2 Dynamic Environments

Dynamic environments usually constitute the most severe design environments because structural resonances within the specified frequency range create large effective loading.

The dynamic environments to which the ASPS will be exposed are the liftoff random vibration shown in Figure 70, the aeronoise random vibration in Figure 71. These levels were based upon Figures A-3 and A-4 of Reference 4. The sinusoidal vibration which is shown in Table 23, and the acoustic noise which is not shown are from Reference 3. The model used to analyze the effects of these environments on the ASPS is shown in Figure 72.

For the random vibration spectrums, the peak deflections and loads were calculated under the following assumptions:

- 1) Transmissibility (Q) of structural resonances is 10.
- 2) The payload mass of 600 kg is equally carried by payload cg clamps and the ASPS caging assemblies.
- 3) Latches and mounting structure below the latches or mounting/jettison assembly are rigid.

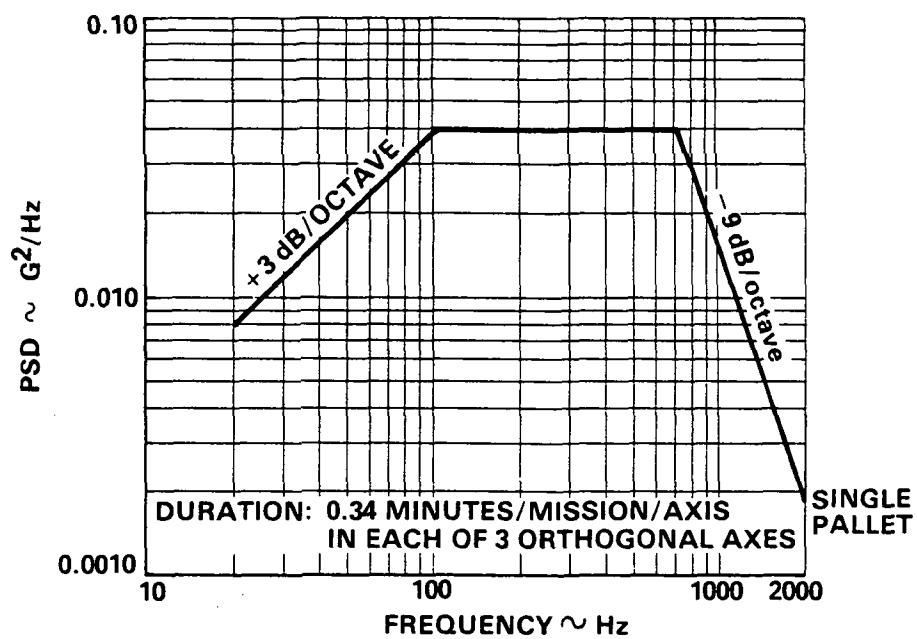


Figure 70
Liftoff Random Vibration Spectrums Input to
Pallet Mounted Equipment

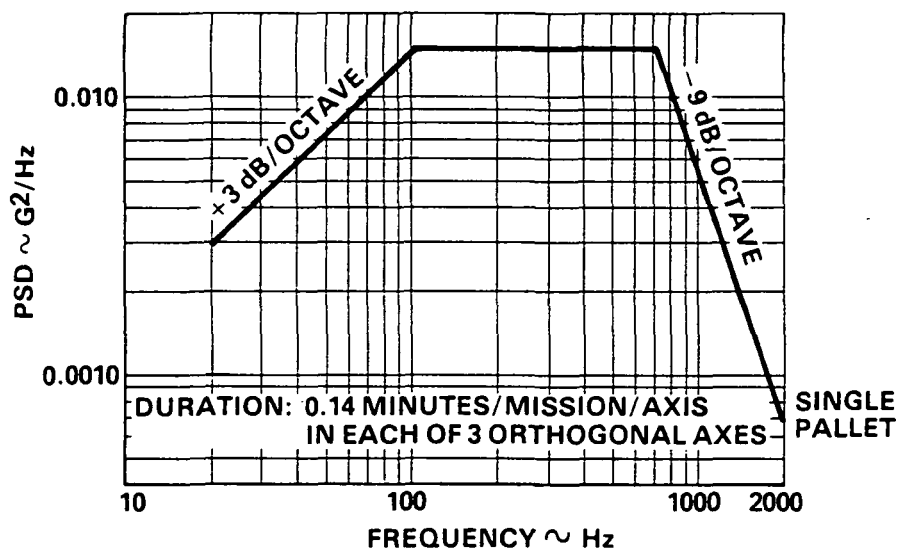


Figure 71
Aeronoise Random Vibration Spectrums Input to
Pallet Mounted Equipment

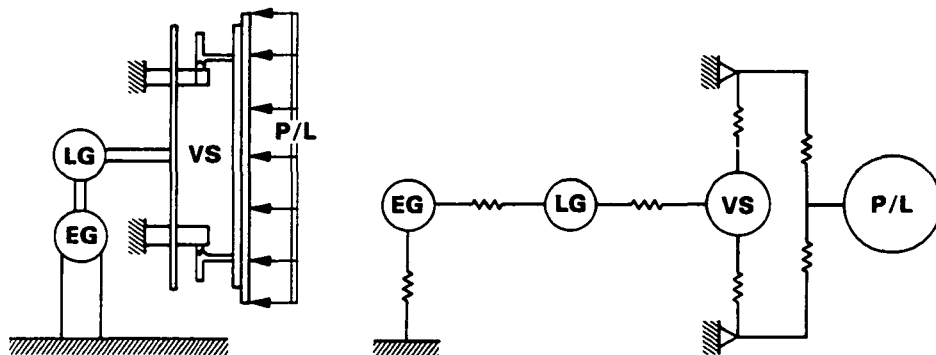


Figure 72
Environmental Model

TABLE 23
SINUSOIDAL VIBRATION

Frequency Range:	5 to 35 Hz
Level:	$\pm .25$ g 0 to peak
Sweep Rate:	1 oct/min (1 sweep only up and down)
Axes:	3 principal axes

Table 24 presents the response of the payload/vernier plate combination to the liftoff random vibration spectrum of Figure 70 and also includes the Margin of Safety (MS) values for the four loading configurations.

The aeronoise random vibration of Figure 71 was not analyzed because it is considered to be of minor consequence in comparison to the liftoff random vibration spectrum.

The sinusoidal vibration specification shown in Table 23, is much less severe than that of the random environment. Also, none of the ASPS structure has resonant frequencies in the range specified by this requirement. Therefore, the maximum load imposed would be .25 g maximum.

The maximum intensity of the acoustic environment corresponds to a loading of only .36 kPa (.052 psi). Over the entire area of the payload plate, this pressure contributes only 274.4N (61.7 lb) force which is small in comparison to the random vibration spectrums and even after inclusion of the frequency and transmissibility effects is substantially below the effects of the liftoff random spectrum.

TABLE 24
PAYLOAD/VERNIER PLATES - LIFTOFF RANDOM RESPONSE

Case	1	2	3	4
f_n , Hz	82.5	166.3	42.5	220.2
G, eqv	19.62	30.68	10.11	35.29
Y, eqv, mm (in.)	0.71 (0.028)	0.28 (0.011)	1.40 (0.055)	0.18 (0.007)
σ , eqv, MPa (psi)	21.1 (3057)	19.9 (2892)	24.1 (3493)	29.0 (4200)
MS	10.4	11.1	9.0	7.3

f_n = natural frequency, Hz

G = force of gravity proportionality factor

MS = margin of safety

Y = deflection, mm (in.)

σ = stress, MPa (psi)

SECTION 5.0

ELECTRONICS DESIGN

Electronics design has addressed two distinct areas: payload support functions and ASPS control functions. The need for special consideration of payload support functions was a direct result of the noncontacting magnetic suspension of the payload. Techniques for transferring power and data to a levitated moving payload had to be considered.

5.1 PAYLOAD DATA SUPPORT

In itself, the requirement for a noncontacting communication link does not bring new or exotic technology to mind. In fact, the use of simple RF telemetry was one of the techniques traded off. But given the inconvenience of mounting antenna hardware, and considering the mission dependant data requirements, the complex electronics needed, and the desire to avoid EMI, other methods became more attractive. The requirements for the payload data link included the transmission of multiple digital signals in both directions across a gap to a moving payload with six degrees of freedom. A maximum data rate of 5 MBPS was desired, and time integrity of the signals was to be maintained. The time integrity requirements, being inconsistent with multiplexing techniques, necessitated parallel data channels.

The techniques considered included variations of capacitive coupling, RF telemetry, inductive coupling (rotary transformer), beam optics, fiber optics, and flexible cables. The method selected utilizes a unique system of coaxial beam optics as described below.

5.1.1 ASPS Optical Data Coupler

Figure 73 shows a conceptual outline of the optical data coupler. Note that there are three concentric channels with the beams of the outer two channels folded back on themselves to reduce axial length. Each channel consists of one or more Gallium Arsinide Infrared LEDs with integral collimating lenses shining across the gap into an isolating lens which has a PIN photodiode detector centered in its focal plane. Such an arrangement is by nature isolated from radial translation and roll. Refer to Figure 74 in the calculation of spot size. From basic trigonometry and geometric optics, one can write the relationships of equations (11) through (13).

$$\frac{1}{S_2 + D} + \frac{1}{I} = \frac{1}{F_2} \quad (11)$$

$$(S_2 + D) \tan \theta = I \tan \phi \quad (12)$$

$$d_S = 2 (I - F_2) \tan \phi \quad (13)$$

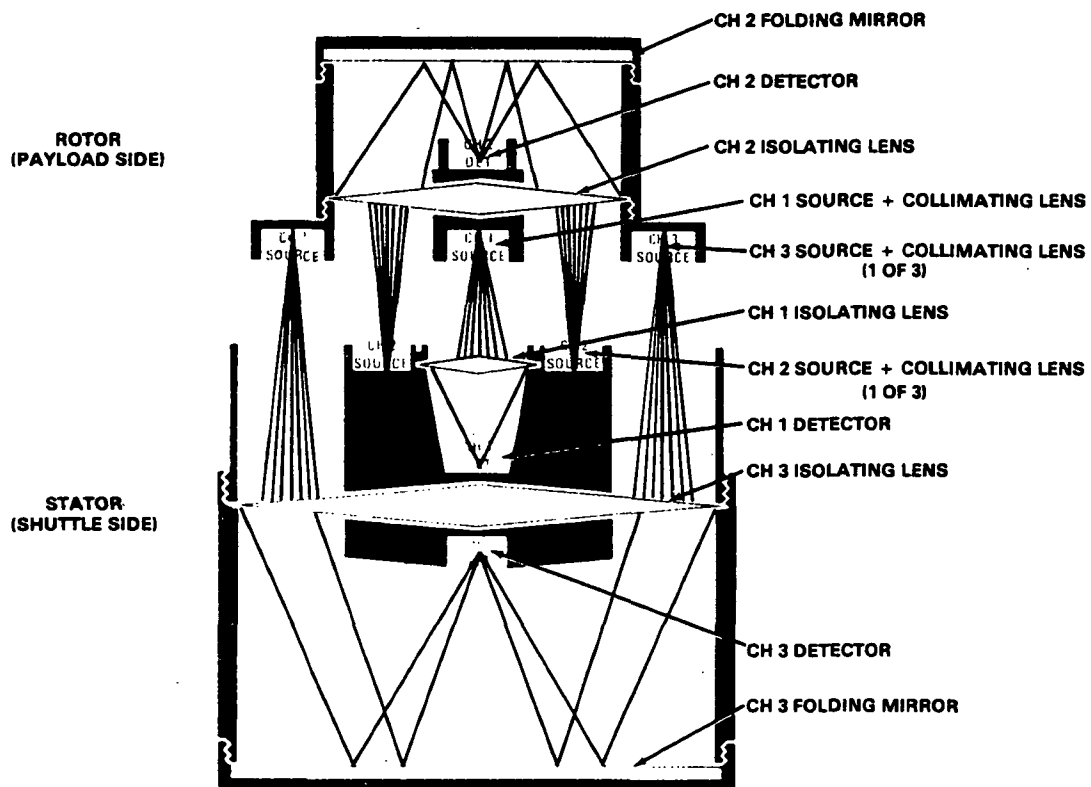


Figure 73
ASPS Optical Data Coupler

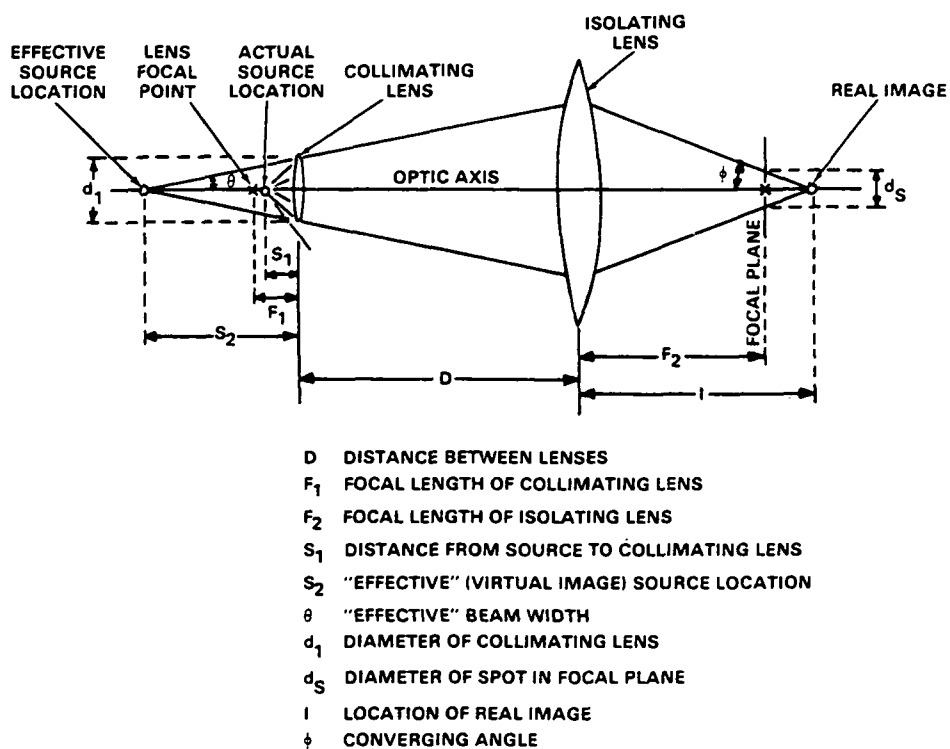


Figure 74
 Variable Definitions in Spot Size Calculation

Solving these for the spot size d_s , one obtains Equation (14).

$$d_s = 2F_2 \tan \theta \quad (14)$$

Note that the spot size is not a function of D , the axial translation, thus showing axial isolation. Writing down Equations (15) and (16), one can solve for d_s entirely in terms of mechanical parameters Equation (17).

$$\frac{1}{S_2} = \frac{1}{S_1} - \frac{1}{F_1} \quad (15)$$

$$\tan \theta = \frac{d_1}{2S_2} \quad (16)$$

$$d_s = d_1 F_2 \left(\frac{1}{S_1} - \frac{1}{F_1} \right) \quad (17)$$

Note that one can control spot size by varying the relationship between S_1 and F_1 , or the distance of the source from the collimating lens. Pointing isolation can be achieved by maintaining an adequate relationship between spot size, detector active area, and spot motion due to pointing. This motion can be calculated as follows: (See Figure 75)

Given an off-axis tilt of x degrees, one writes Equation (18).

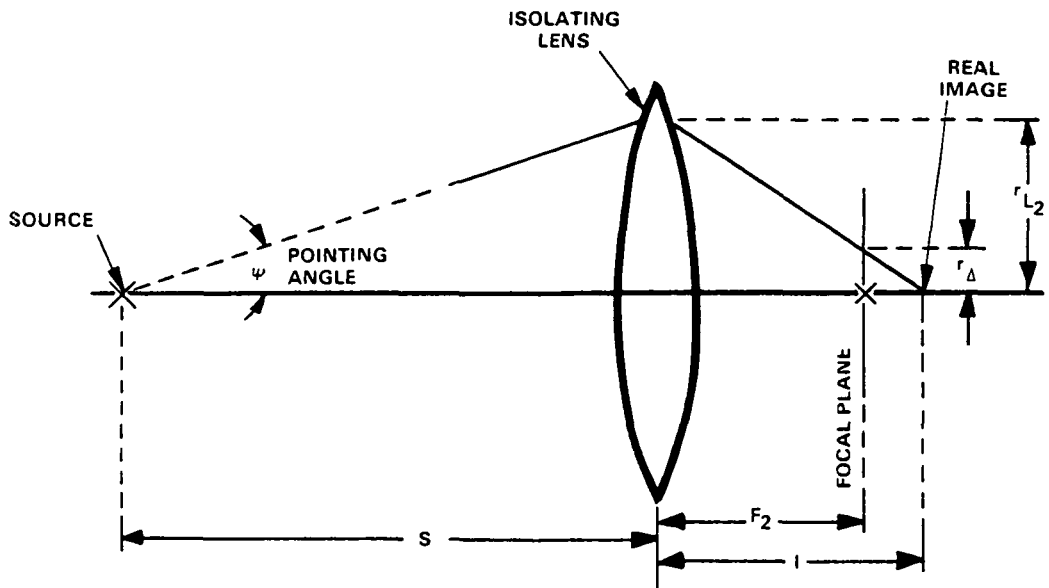
$$r_{L2} = S \tan x \quad (18)$$

Equation (19) follows from geometric optics and the spot motion r_Δ can then be solved,

$$\frac{1}{S} + \frac{1}{I} = \frac{1}{F_2} \quad (19)$$

$$r_\Delta = \frac{(I-F_2)}{I} r_{L2} = F_2 \tan x \quad (20)$$

Note that spot motion is influenced by the pointing angle and the isolating lens focal length, both of which are known. For pointing isolation, one simply sets the spot radius larger than the sum of the active area radius and r_Δ .



- S DISTANCE FROM SOURCE TO ISOLATING LENS
- I DISTANCE FROM IMAGE TO ISOLATING LENS
- F_2 FOCAL LENGTH OF LENS
- r_{L2} POINT AT WHICH BEAM STRIKES LENS
- r_{Δ} POINT AT WHICH BEAM STRIKES FOCAL PLANE
- ψ POINTING ANGLE

Figure 75
Variable Definitions in Spot Motion Calculations

The light beams are pulse-modulated with the digital data. However, the optical coupler system requires that the data channels never go completely idle. This requirement is due to the method of detection, which involves capacitive coupling and Automatic Gain Control (AGC) as illustrated in Figure 76. The receiver is designed to compensate for a factor of 15 change in signal strength over temperature, roll angle, and life, but since an AGC is used, it could potentially detect noise if the input were idle. The capacitive coupling is used to remove dark current, a dc component with a strong temperature dependence.

5.1.2 Optical Coupler Services

Since the data handling requirements for the payload are mission dependent, and since only a limited number of channels are available through the coupler, it was decided to place a Remote Acquisition Unit (RAU) on the payload plate. This RAU will be connected to the Spacelab Experiment Data Bus using two channels of the coupler, thereby providing the experiment with command and low-rate data handling capability. The third optical coupler channel will provide a means whereby the experiment can transmit high-rate (5 MBPS) data to the shuttle High-Rate Multiplexer (HRM) for downlink.

5.1.3 Interfaces

To provide for payload data support, the following interfaces are provided:

- The ASPS Control Electronic Assembly (CEA) is connected directly to a Command and Data Management System (CDMS) interconnecting station accessing both primary and redundant data busses, but not the Universal Time Clock (UTC) bus.
- The CEA is connected to an HRM input capable of 5 MBPS for downlink of scientific data.
- A connector is located on the payload plate providing the command and reply lines to the RAU, and making available the 5 MBPS downlink to the HRM.

5.2 PAYLOAD POWER SUPPORT

A requirement also existed for providing the payload with up to 300 watts of power. This value was based on an earlier study of payload power requirements which indicated that 300 watts would accommodate over 90 percent of the payloads under 600 kg. Based on expected cycle requirements, a maximum of one hour was applied to the maximum load, resulting in a 300 W-hrs of energy storage requirement. Power transfer techniques not requiring storage, such as a rotary transformer, were considered but rejected due to excessive radial forces which interfere with the suspension dynamics.

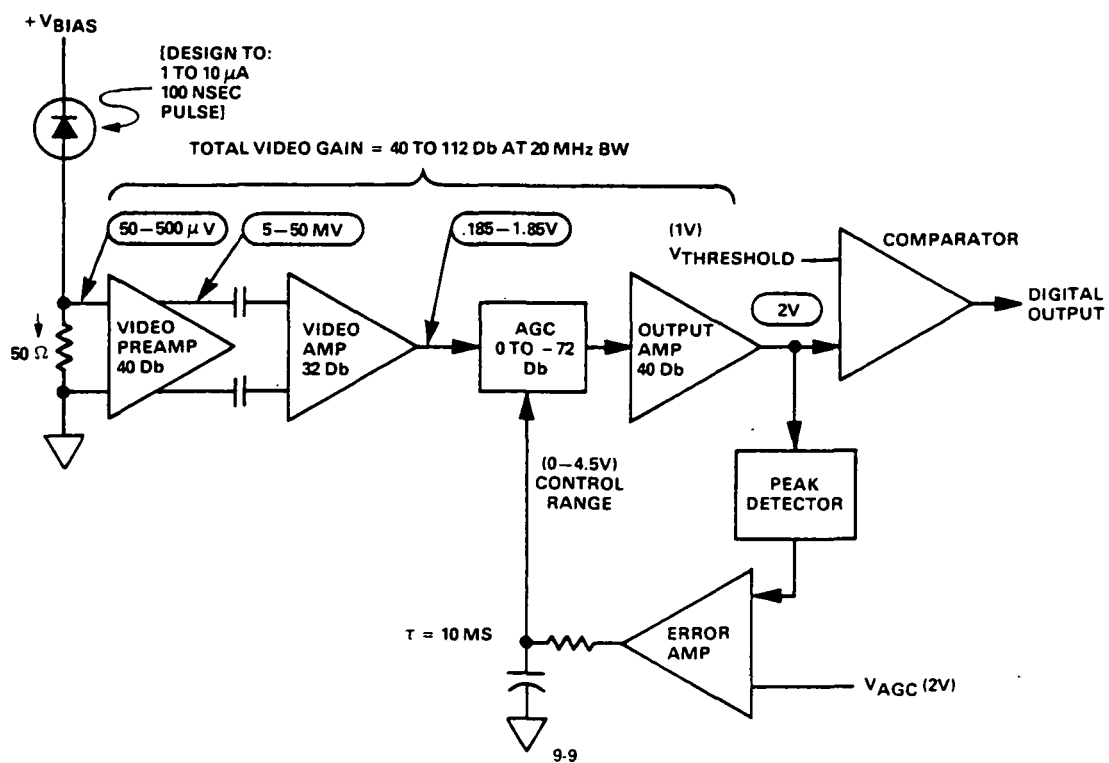


Figure 76
Beam Receiver Electronics

5.2.1 NASA Standard Nickel-Cadmium Spacecraft Cell

The selected energy storage medium is a nickel-cadmium secondary cell being developed by MSFC with a capacity of 20 Ampere-hours. Using these cells, a 28 ± 4 volt battery would thus have a nominal capacity of 560 watt-hours. This provides the required energy with only a 54 percent depth of discharge.

5.2.2 Battery Charging Considerations

Because it is desired to recharge the battery in one hour, a high charge rate must be employed. As shown in Figure 77, the fast charge characteristics of cell pressure and temperature are not constant, but rise sharply as overcharge is approached until the cell vents. Thus it is necessary to monitor the cell's entry into overcharge, and lower the charge rate before excessive pressure builds up. Battery voltage will be used as an indication of state of charge in order to reduce the charge rate from 20 A to 2 A before venting occurs.

5.2.3 Battery Temperature Considerations

The state of the art in nickel-cadmium technology imposes the most severe environmental constraint of any component of the ASPS. The worst-case operating temperature limits are 0 to 40°C, and the maximum storage limit is 50°C. The storage limit is the result of the use of nylon separators, and could be improved by the use of polypropylene. However, the operating limits are due to the battery's chemistry and cannot be improved substantially. As temperature increases, the cell's capacity and efficiency both begin to degrade, and a chemical self-discharge path becomes prominent. Furthermore, self-heating during charge compounds the problem by adding to the ambient. At low temperatures, it becomes increasingly difficult to charge the cell due to excessive pressure buildup resulting from inefficient recombination of gasses within the cell.

The presently projected operating temperature for the battery is 0 to 20°C, but the severity of the above considerations makes detailed thermal analysis and control essential.

5.2.4 Interfaces

A connector through the payload mounting plate will provide the experiment and the experiment RAU with battery power. The two may draw a maximum power of 300 watts, and a maximum energy of 300 watt-hours between battery charging cycles.

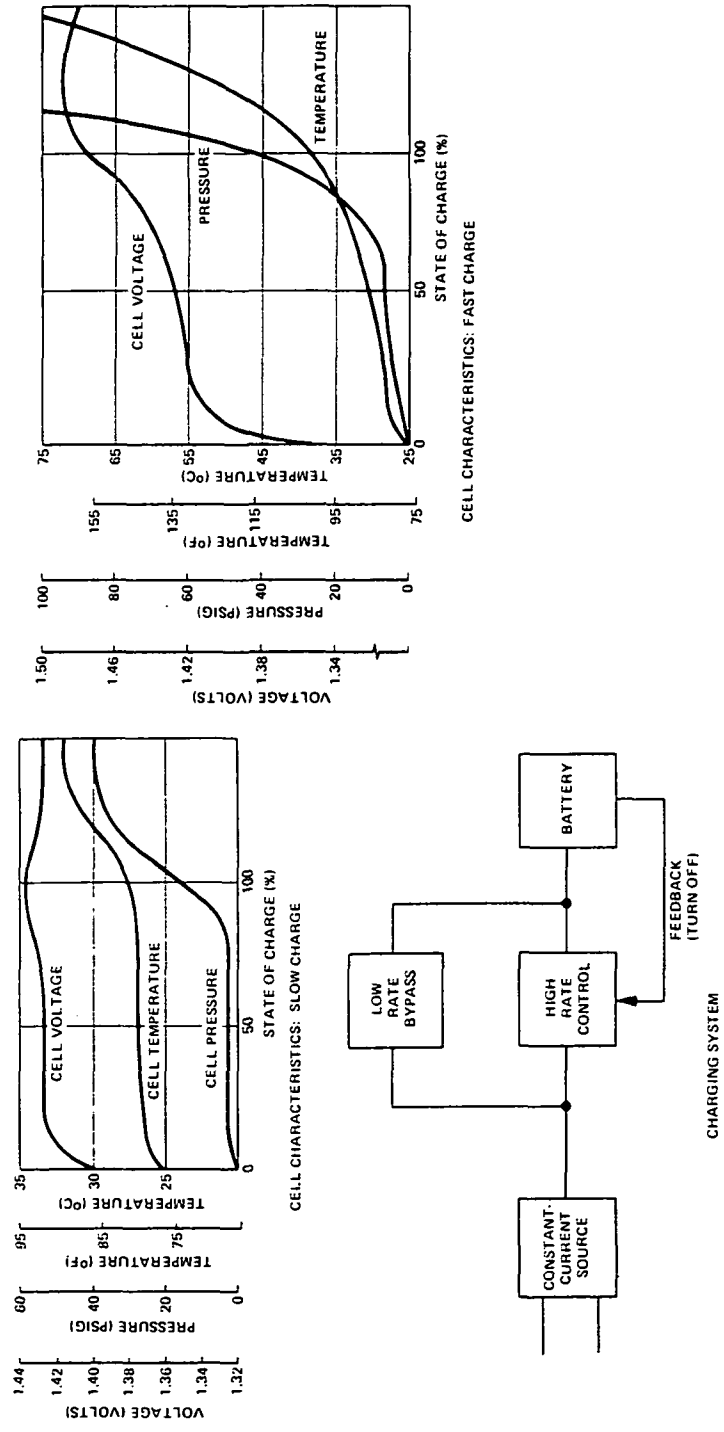


Figure 77
Battery Charging Characteristics

5.3 INFORMATION PANEL

The primary function of the ASPS Information Panel (Figure 78), as its name implies, is to display system mode, status, and warning indications. It is not intended as a port for manual control of the ASPS. During a typical mission in which no failures are encountered, the information panel remains passive and need not be referred to by the experimenter. However, if unsatisfactory system operation is noted, one can refer to the information panel to determine more precisely the nature of the problem. The current operating modes and bandwidths of each servo as well as many critical status and warning indications are given by the lights on the panel. Also given are the results of an "in-bounds" test on each pointing servo error signal which indicates whether the system is operating properly, as commanded.

If a system failure is discovered and it prevents the normal execution of the stow and latch sequence, a backup caging mode may be initiated from the panel to avoid the need for jettison. Discrete gimbal position information (CW or CCW of null) is provided by indicator lamps and the backup coil stepping sequence is accomplished by depressing the appropriate switch. Once the ASPS has been maneuvered to the caged position, pallet latches can be manually engaged and their operation confirmed.

Also included on the information panel is an indication of the rate of battery charge and voltage. Battery charge rate can be manually controlled and the automatic voltage cutoff circuit can be overridden in case of failure. The vernier latches can be engaged and released manually also.

5.4 CONTROL ELECTRONICS ASSEMBLY

The ASPS Control Electronics are contained within a package mounted on a pallet cold plate near the base of the Mounting and Jettison Assembly (MJA). This package includes the drive electronics for the coarse gimbals, MBAs, and roll motor, as well as all electronics necessary to determine from the proximity meters, resolvers, etc, the position of the payload in the coordinate system necessary to implement all control laws and CM offset correction. Also contained in the Control Electronics Assembly (CEA) are all interface electronics necessary to receive commands from and send data to an RAU, provide power conditioning and EMI filtering, and support payload electrical functions.

The modular packaging concept illustrated in Figures 79 through 81 will be used for the CEA. The power subassembly, located at the base of the package, contains power conditioning and EMI electronics. It is connected to the upper subassembly only through external connections, and is thus a detachable module permitting separate fabrication and test. The housing, mounted above it, contains slots for the electronics modules and the wiring harness which interconnects them. Inserted into the housing are 14 modules which consist of two facing printed wiring cards each. In the gimbal and roll driver modules, one printed wiring card is replaced by a metal card to provide better heat conduction to the housing walls. All power dissipation will be provided by heat conduction to the pallet cold plate upon which the assembly is mounted.

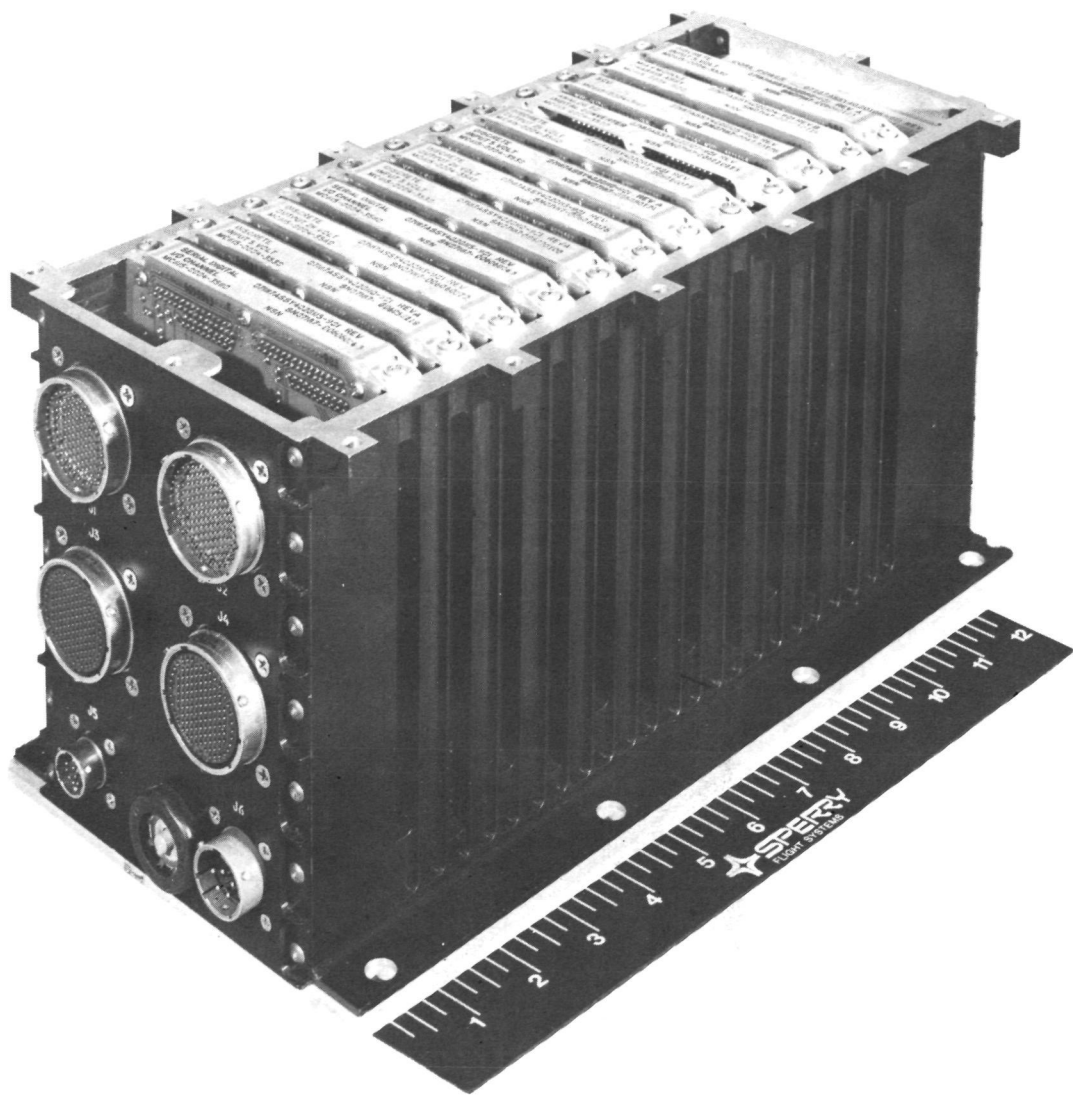


Figure 79
ASPS Control Electronics Assembly

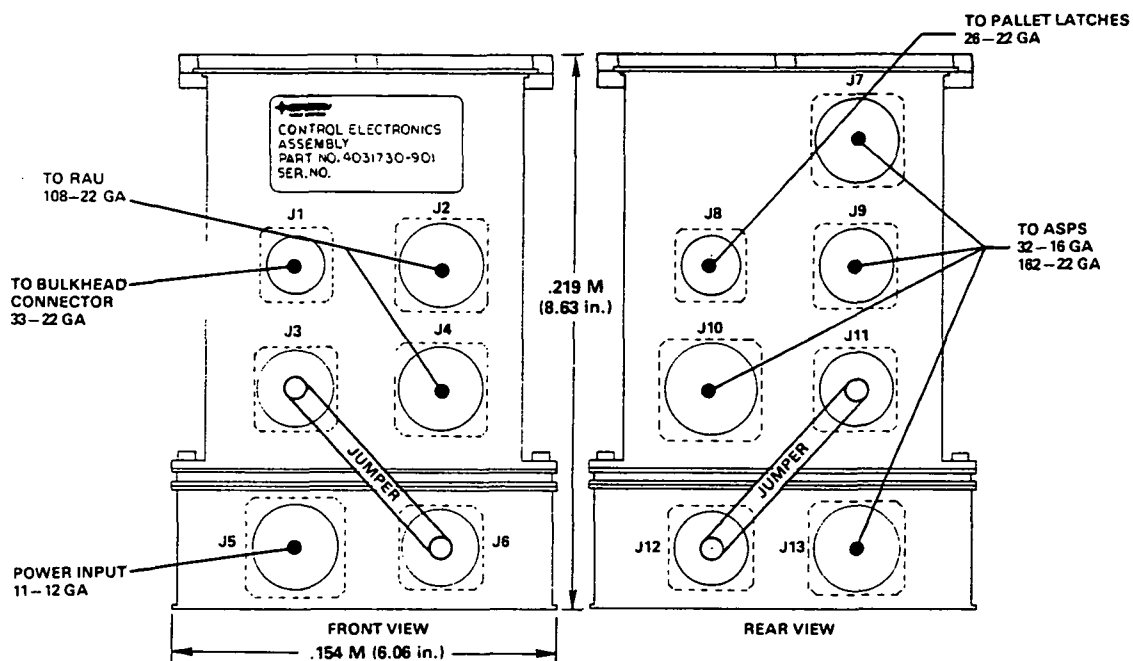


Figure 80
 ASPS Control Electronics Assembly Connectors

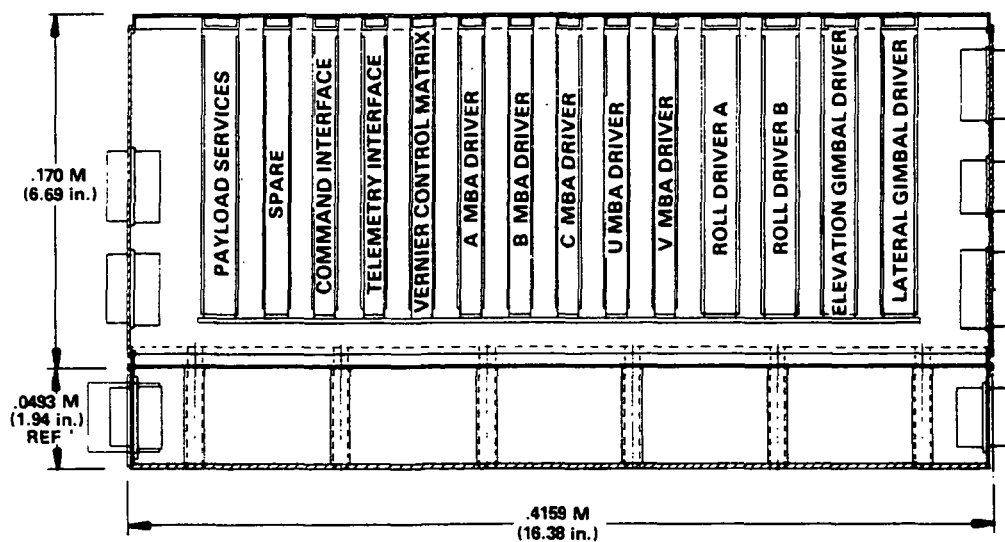


Figure 81
ASPS Control Electronics Assembly Side View

5.4.1 CDMS Interface

Figure 82 depicts the interfaces of the ASPS with the Orbiter/Spacelab, pallet, and payload. Control of the system begins with action on the part of the experimenter (user) at the Spacelab Data Display Unit (DDU) keyboard, communicating with his own software in the experiment computer. His software has access to Orbiter Attitude and ephemeris from the Orbiter General Purpose Computer (GPC), and can thus generate servo position commands to the ASPS. Those commands are transmitted through ASPS resident software in the experiment computer, through the CDMS bus to an RAU, and eventually arrive at the CEA. With pointing feedback obtained from the built-in ASPS sensors (resolvers and proximeters), the CEA can then point the ASPS in the desired direction with little load on the data bus. A second RAU, located on the payload plate and connected to the Spacelab Experiment Data Bus through the optical coupler provides a means for the user to communicate with his experiment via software, sending commands and retrieving low-rate data through the CDMS. If the experiment is equipped with its own pointing error sensor (star tracker, sun sensor, etc), the pointing error data for one or more axes can be sent to the CEA through the CDMS for use in the pointing control servos. Error signals, rate signals, and offset commands can be accepted in this mode. Although the use of externally supplied pointing feedback requires greater utilization of the data bus than when internal sensor feedback is used, the maximum bus utilization will still be less than 4.5 percent of its capability under worst-case conditions.

The CEA also interfaces to the ASPS Information Panel (Paragraph 5.3). This interface is a direct hardwire and provides for safety-related backup control of the ASPS.

5.4.2 Wiring Harness

Figure 83 depicts the wiring harness connections required to interface the CEA to the rest of the system. The CEA has connectors on both ends: the front comprising the shuttle interface and the back ASPS interface. The shuttle interface includes the hardwires to the information panel, data to the HRM, an interface to an RAU, and another to an Interconnect Station (I/S) stub for use by the experiment RAU, and finally power from an Electrical Power Distribution Box (EPDB). On the back of the CEA, one connector provides for all the pallet mounted latches, and four are connected directly to the MJA providing for all ASPS operations. The remaining connectors on each side provide for jumper cables to the CEA lower level, one on each side of the box.

Pyrotechnic initiation is provided for by an additional connector at the base of the MJA, the signals to which are provided by the mission integrator from an Orbiter subsystem and are not considered a part of the ASPS harness.

Above the MJA, the harness runs up through the gimbal flex capsules with branches for rotor and stator of each gimbal and the rest of the lines terminating in the Vernier Pointing Assembly (VPA).

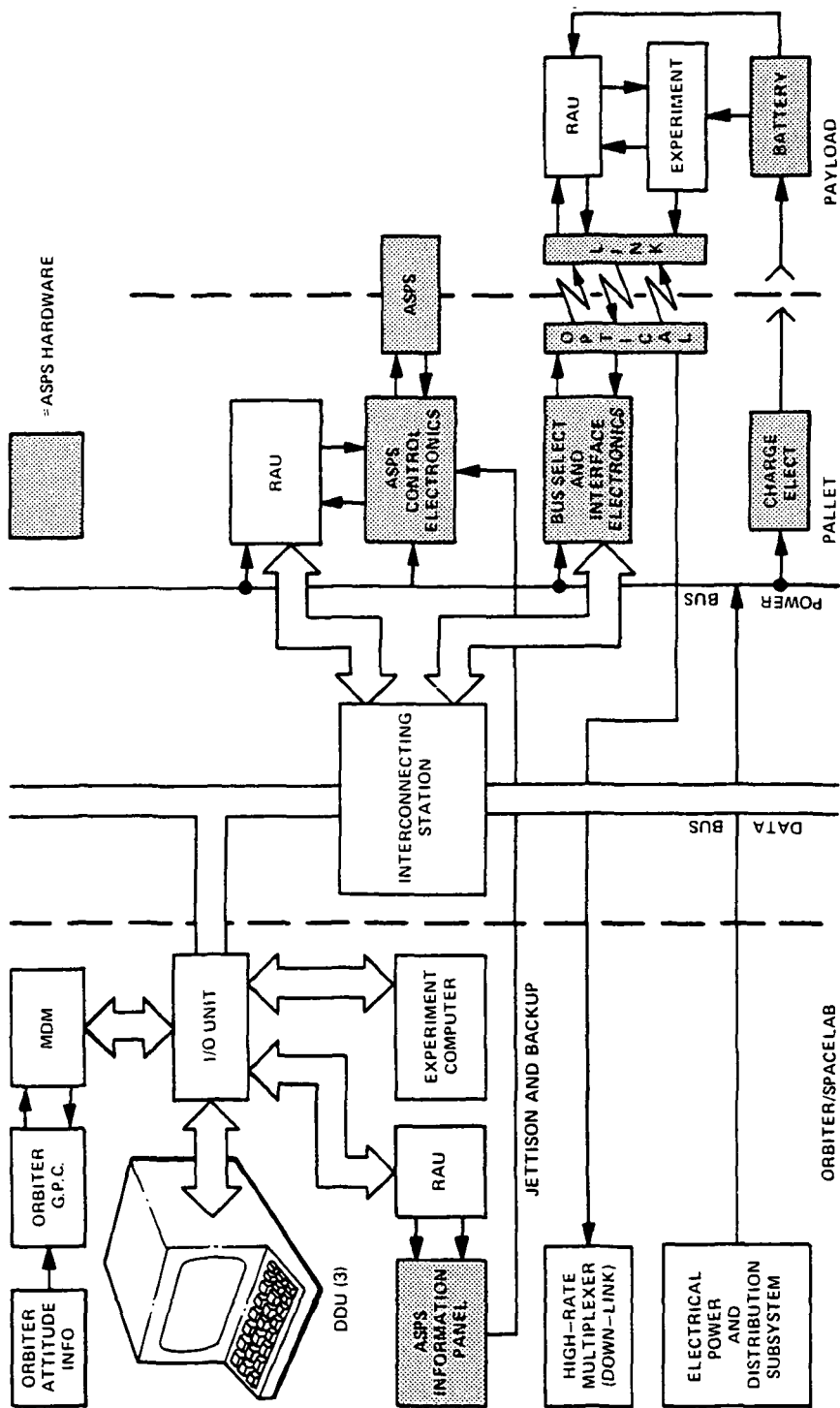


Figure 82
CDMS Interface

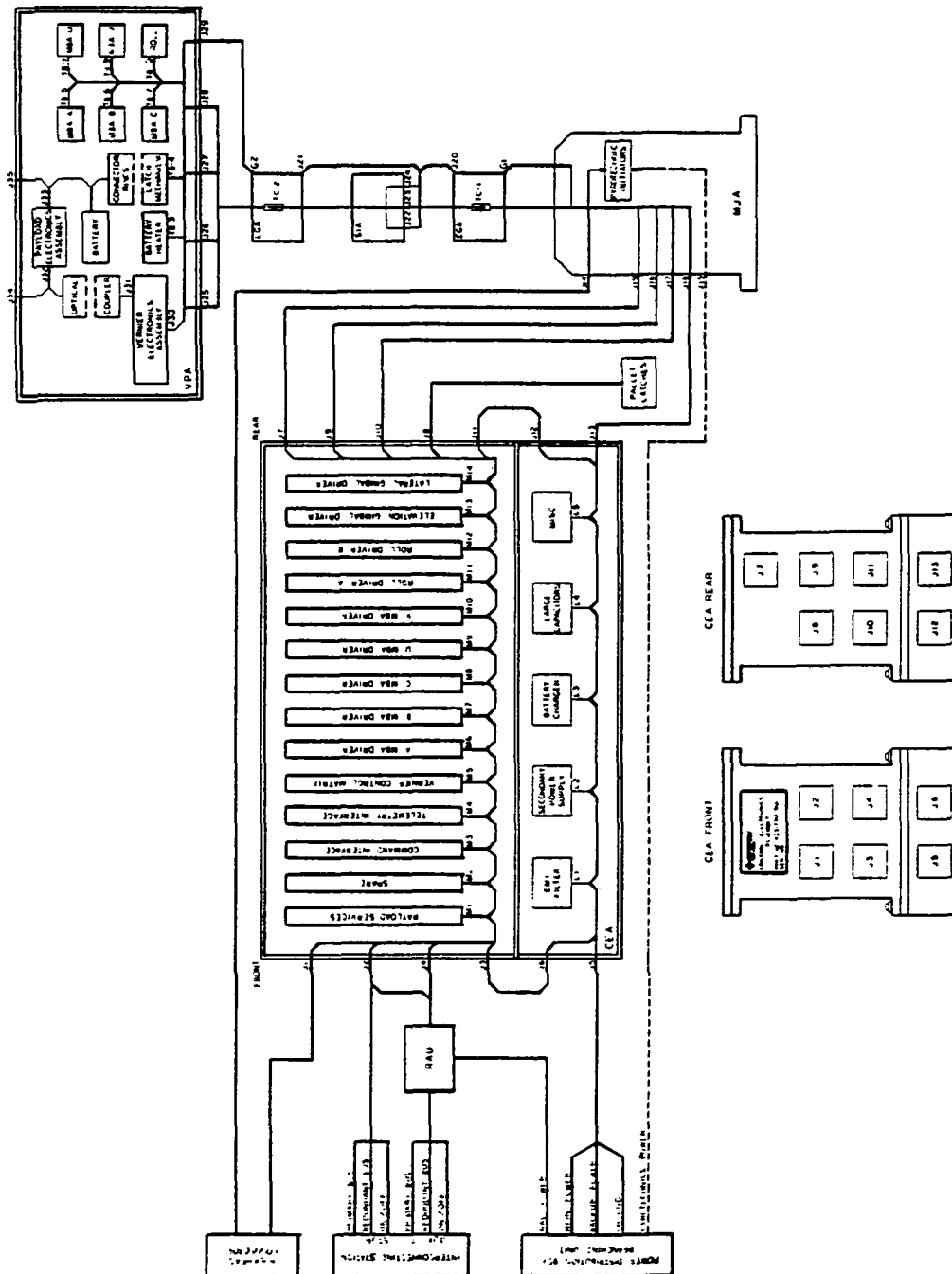


Figure 83
ASPS Wiring Harness Layout

5.4.3 Hybrids

The functions of power driver, modulator, and demodulator are repeated many times in the control electronics. Therefore, to conserve space, these functions are implemented using hybrid technology. These three hybrids (Figure 84) are presently under development by Sperry, and are at various stages of completion. The power hybrid (Figure 85) is the furthest along, with samples already under test. This hybrid, driven by a pulse-width modulator, constitutes one half of an H-bridge driver and is capable of switching 35 A. The modulator hybrid (Figure 86), and the demodulator hybrid (Figure 87) are a synchronous pair used for resolver drive and ac servo applications.

5.4.4 Modules

Inside the CEA, plug-in modules (Figure 88) provide for the functions of the ASPS. Some of the modules (MBA driver, gimbal driver) are identical and interchangeable. Each consists of two cards with a connector on each engaging the internal wiring harness. Interconnects between boards are accomplished through the connectors at the bottom of each module.

5.4.4.1 Coarse Gimbal Driver Module

Figure 89 shows the functions of the gimbal driver. Of particular interest is the internal/external feedback connection, gimbal rate override detection for rate limiting, and backup coil control.

5.4.4.2 Roll Driver Module A

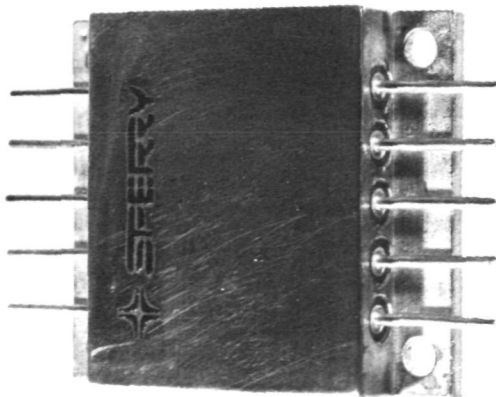
Figure 90 shows half of the roll servo. Module A drives the two "fixed" coils, which are modulated only by gap, and it contains the proximeter linearizing and averaging electronics necessary to generate the gap signal from the two proximeters surrounding the roll motor. Note also that the roll motor is an ac induction motor, requiring 200 Hz ac drive.

5.4.4.3 Roll Driver Module B

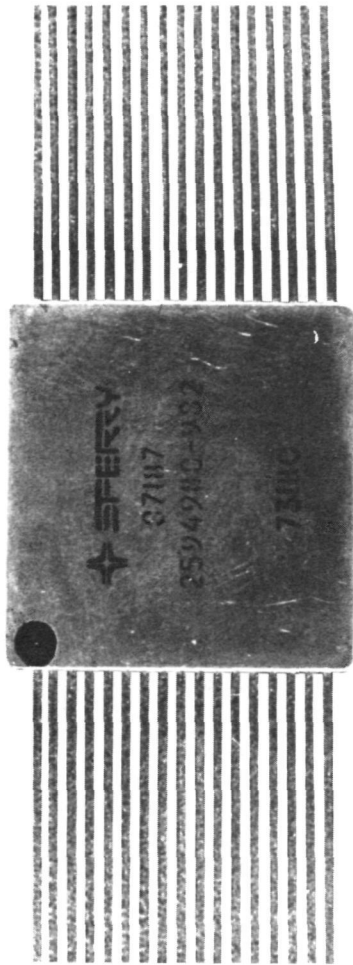
The other half of the roll function (Figure 91) includes the roll resolver driver with feedback mode selection, and the control coil drivers which are modulated by gap and torque command.

5.4.4.4 MBA Drive Module

The MBA Driver (Figure 92), provides much lower power output than the gimbal and roll drivers, but is functionally similar to both. The proximeter linearization electronics provides the gap signal which, along with force command, modulates the current drive about a bias current.



**HIGH POWER
BRIDGE DRIVER
HYBRID**



**SIGNAL
HYBRID**

Figure 84
ASPS Hybrid Packages

Figure 85
Power Driver Hybrid

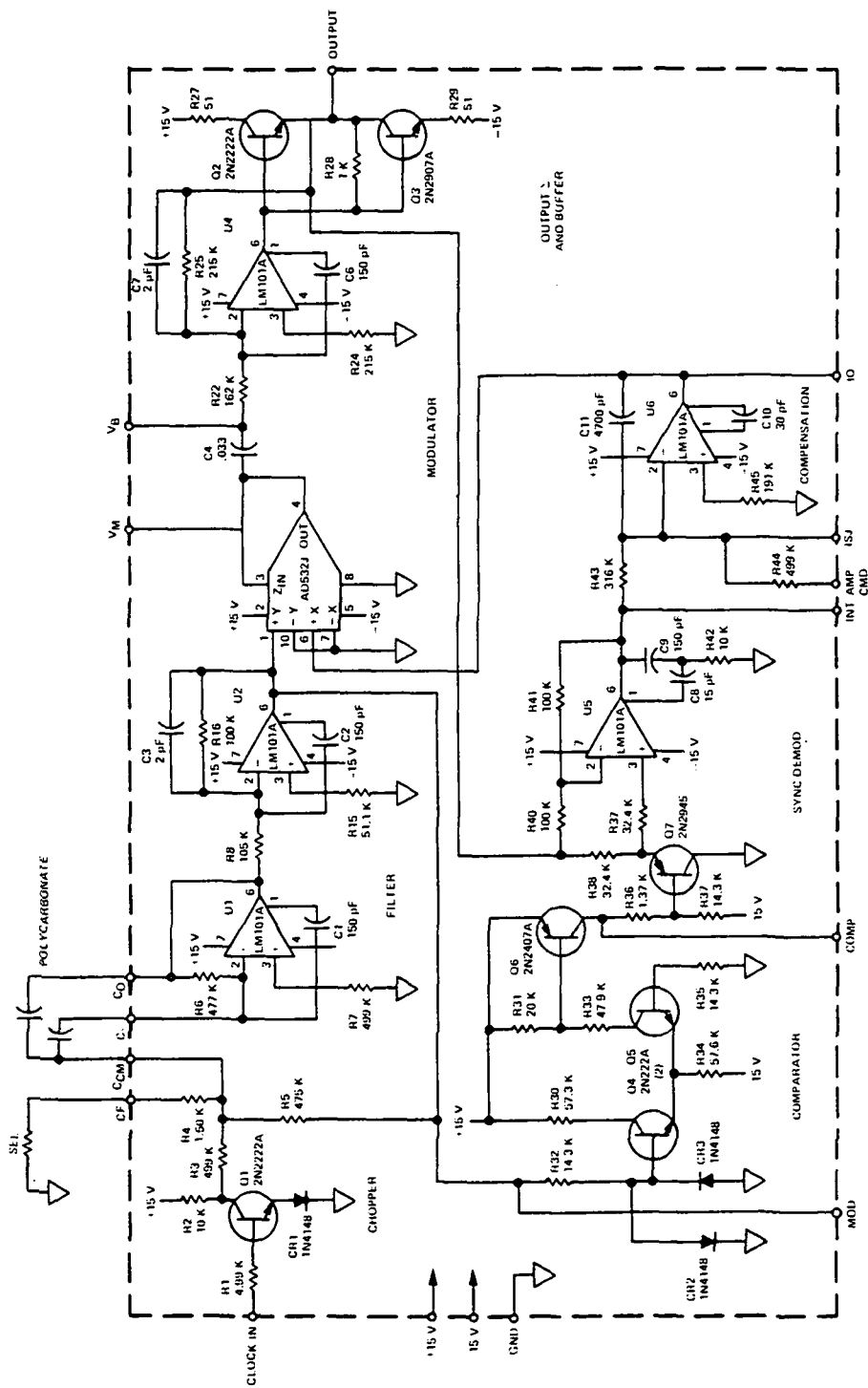


Figure 86
Modulator Hybrid

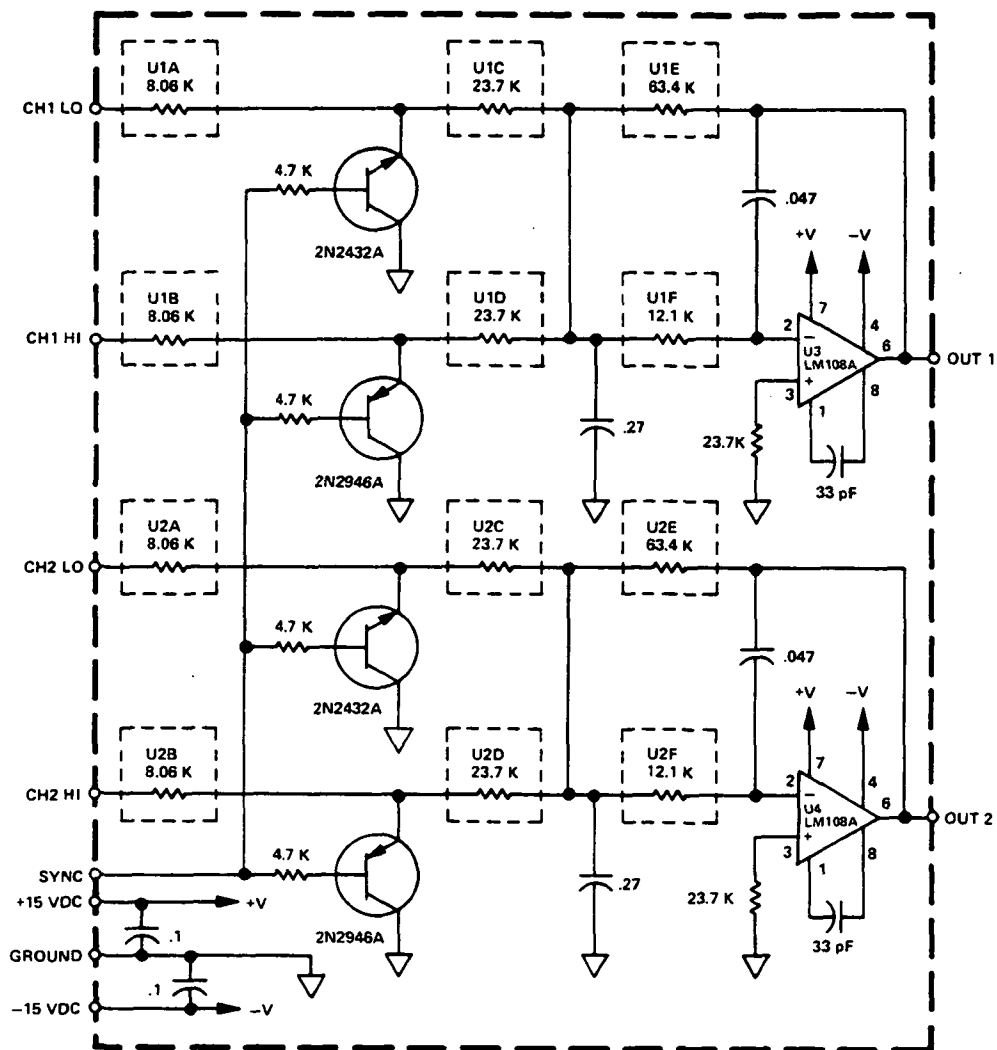


Figure 87
Dual Demodulator Hybrid

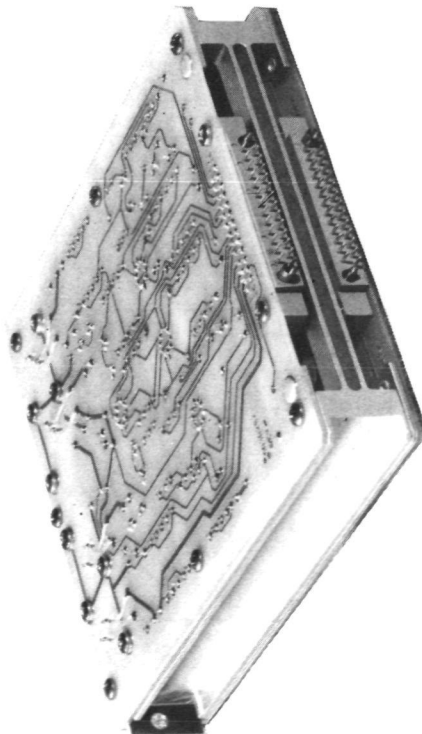
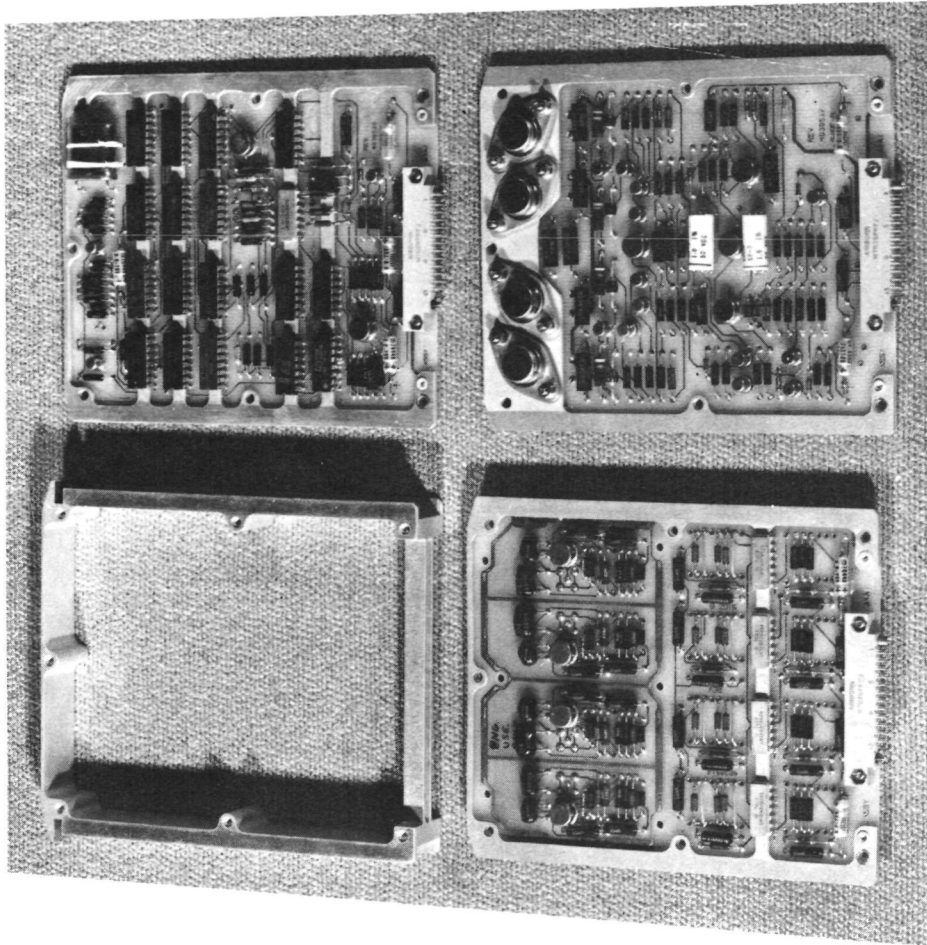
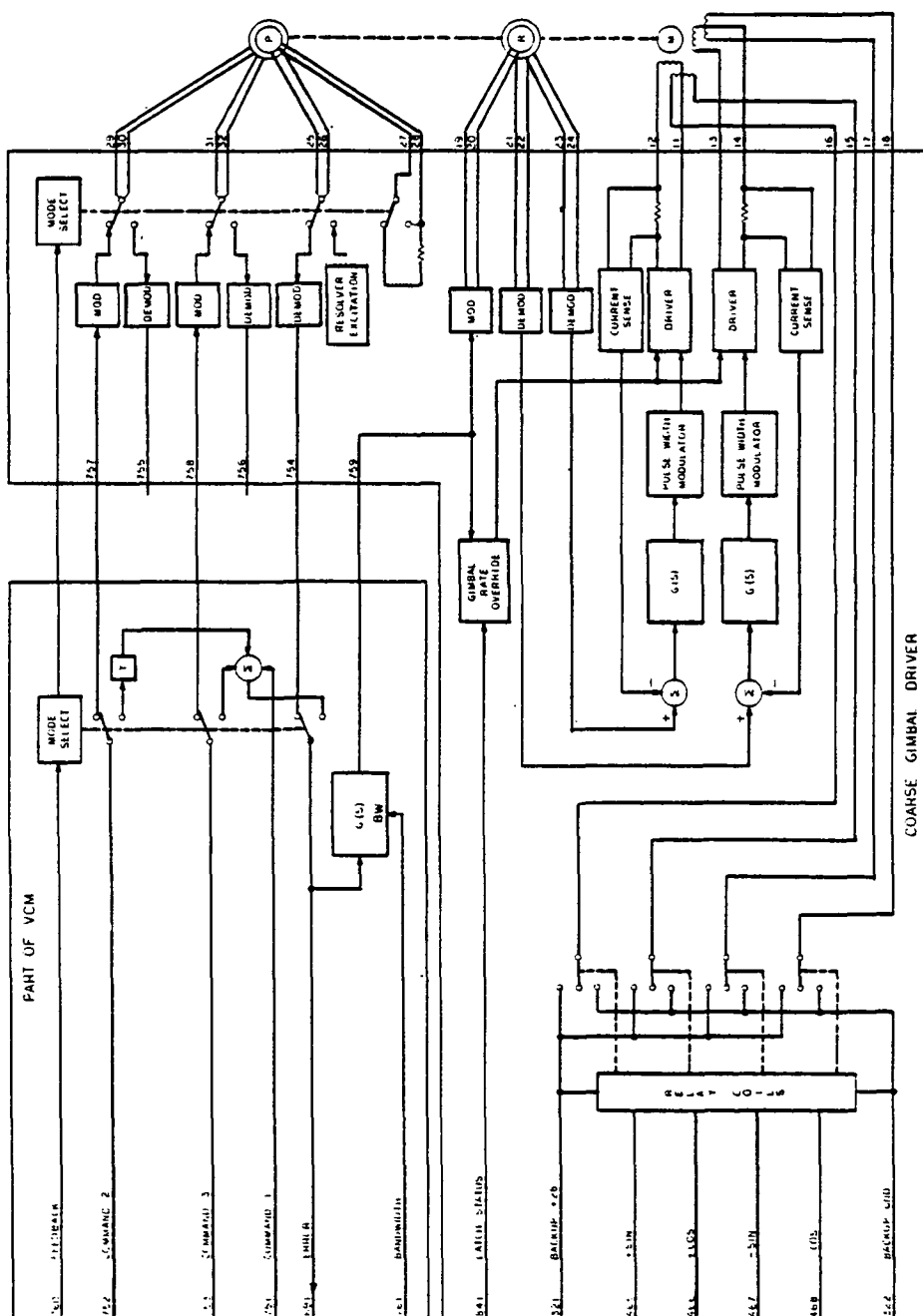
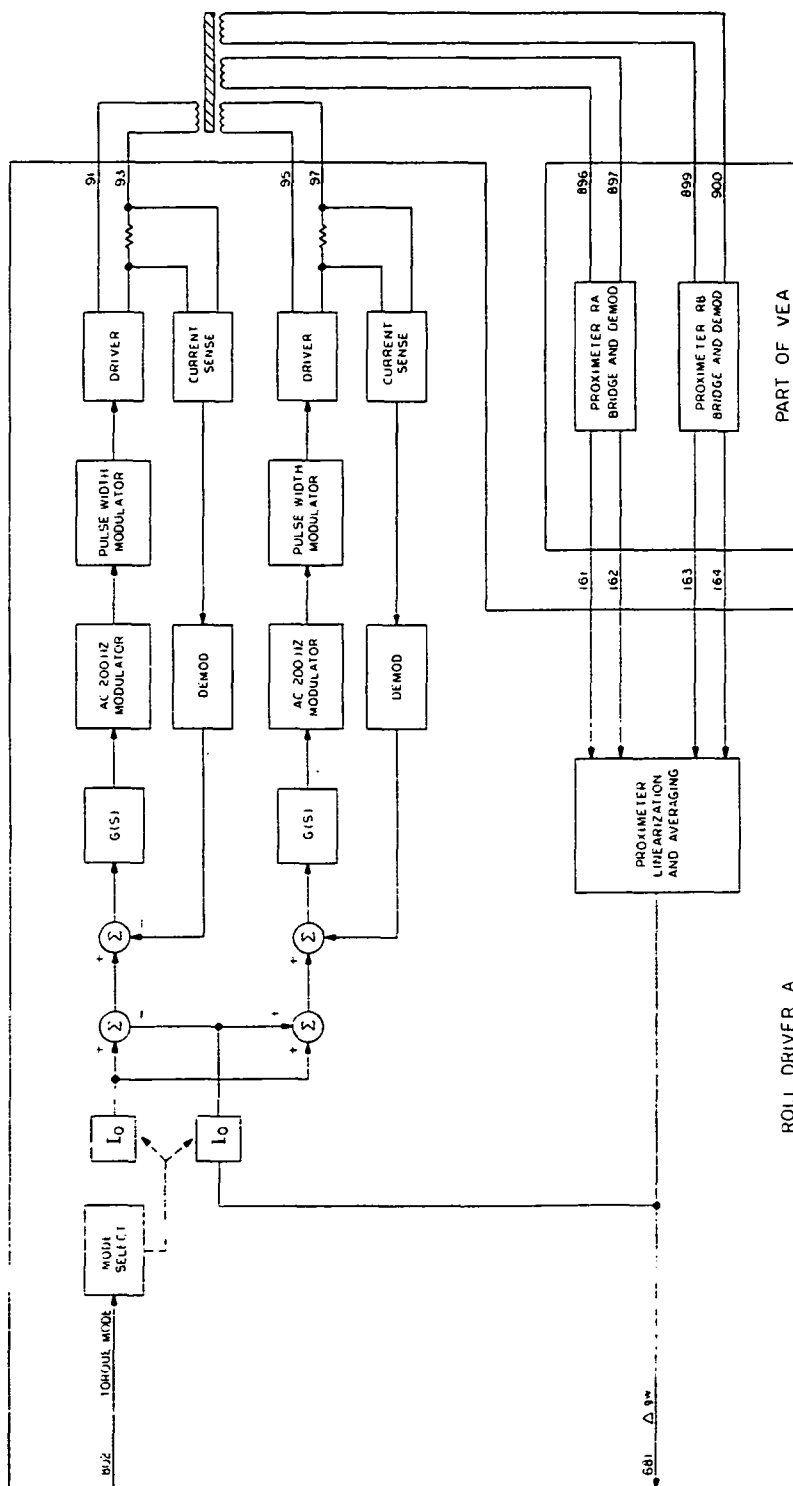


Figure 88
ASPS Control Electronics
Assembly Module and Cards





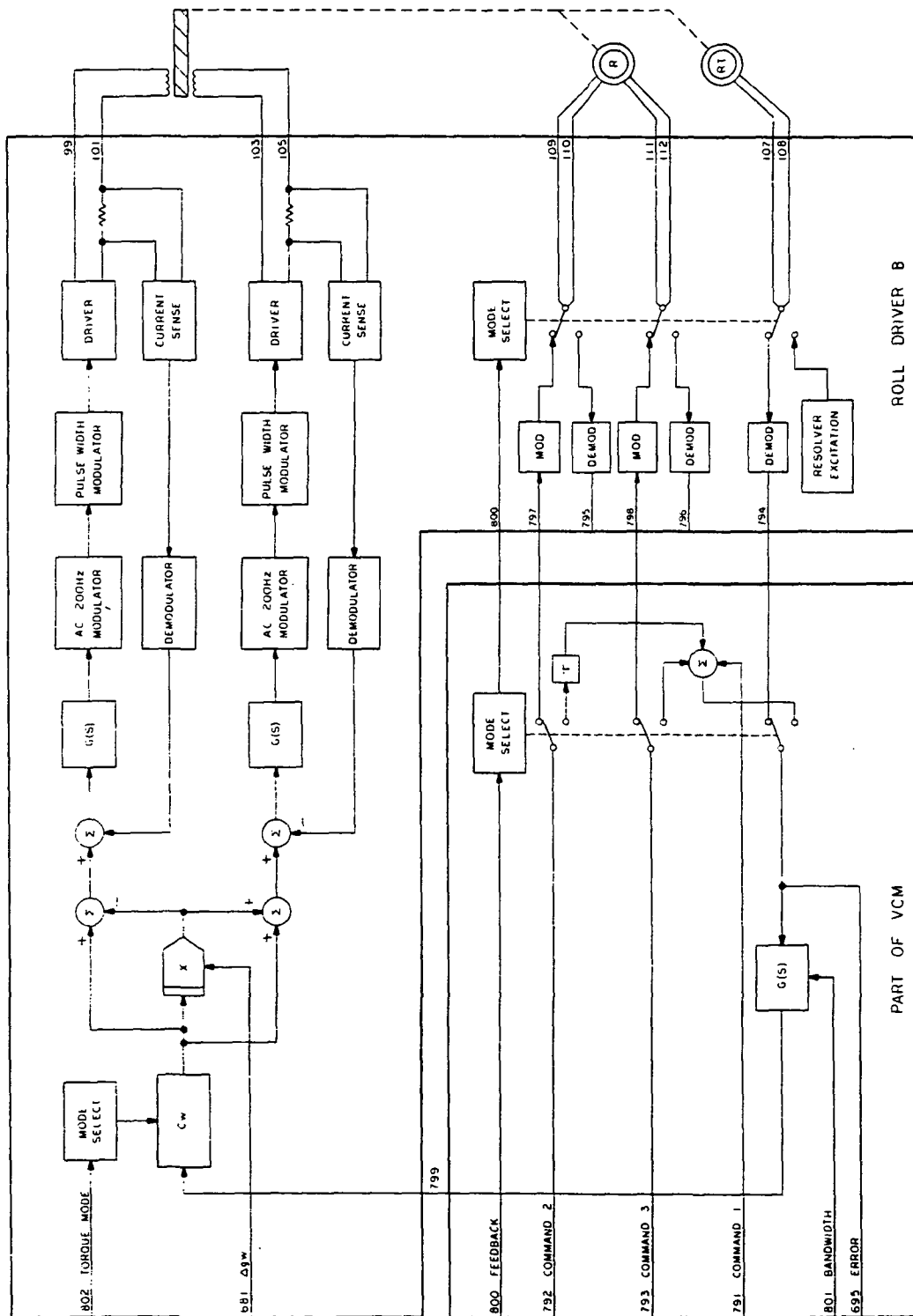


Figure 91
Roll Control Coil Drive Module (B)

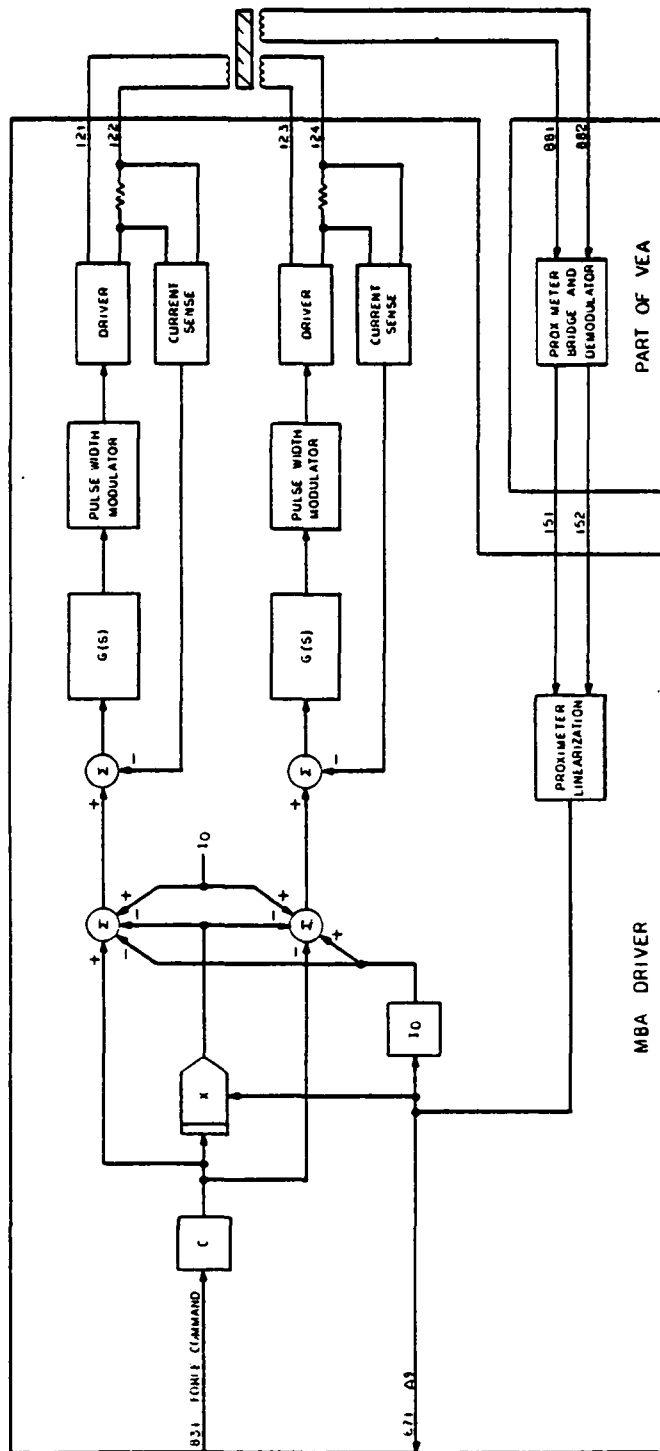


Figure 92
MBA Driver Module

5.4.4.5 Vernier Control Matrix Module (VCMM)

Figure 93 shows the contents of the VCMM. Note that some of these functions have already been portrayed on other diagrams for completeness. The reason they reside in this module is so all mission dependent parameters can be varied by changing only this one module. Functions not previously shown are variable transformations and cross-axis decoupling, as well as the pointing servo mode control.

5.4.4.6 Command Interface Module

Servo commands, both mode and value, are provided by serial burst from the RAU as shown in Figure 94. The servo mode control is buried in the unused bits in order that mode and value can be changed simultaneously. The serial command interface, shown in Figure 95, accomplishes this task.

5.4.4.7 Telemetry Interface Module

Figure 96 shows the functions of the telemetry module, which is responsible not only for a serial channel but some analog signals to the RAU as well. The serial channel includes 12-Bit converted analog signals and parallel digital status words as inputs.

5.4.4.8 Payload Services Module

This module (Figure 97) works in conjunction with the modules in the vernier electronics assembly (Paragraph 5.5) and payload electronics to provide for the operation of the optical coupler as well as experiment and payload RAU on/off and other service and backup functions. On/off switching of payload plate mounted electronics utilizes the relay switching shown in Figure 98.

5.5 VERNIER ELECTRONICS ASSEMBLY (VEA)

The VEA, shown in Figure 99, is a miniature version of the CEA in packaging design. This two-module unit is located in the VPA, under the roll motor, and contains the functions depicted in Figure 98. Impedance bridges and demods for the proximeters are located in the VEA to avoid including the gimbal twist capsules in the impedance bridge. Optical coupler electronics, which has a need to be close to the optical coupler, are also located in the VEA.

5.6 ASPS POWER AND ELECTRONICS WEIGHT

Figure 100 shows the primary contributors to the ASPS peak power. Of particular interest in this table is the roll motor drive which, due to the low power-factor of the load, dissipates more power within itself than it supplies to the load. Assuming a latched and powered down vernier assembly and minimal gimbal drive during battery charging, the peak power figure will not be exceeded during the recharge period.

The weight of the CEA is broken down in Figure 101.

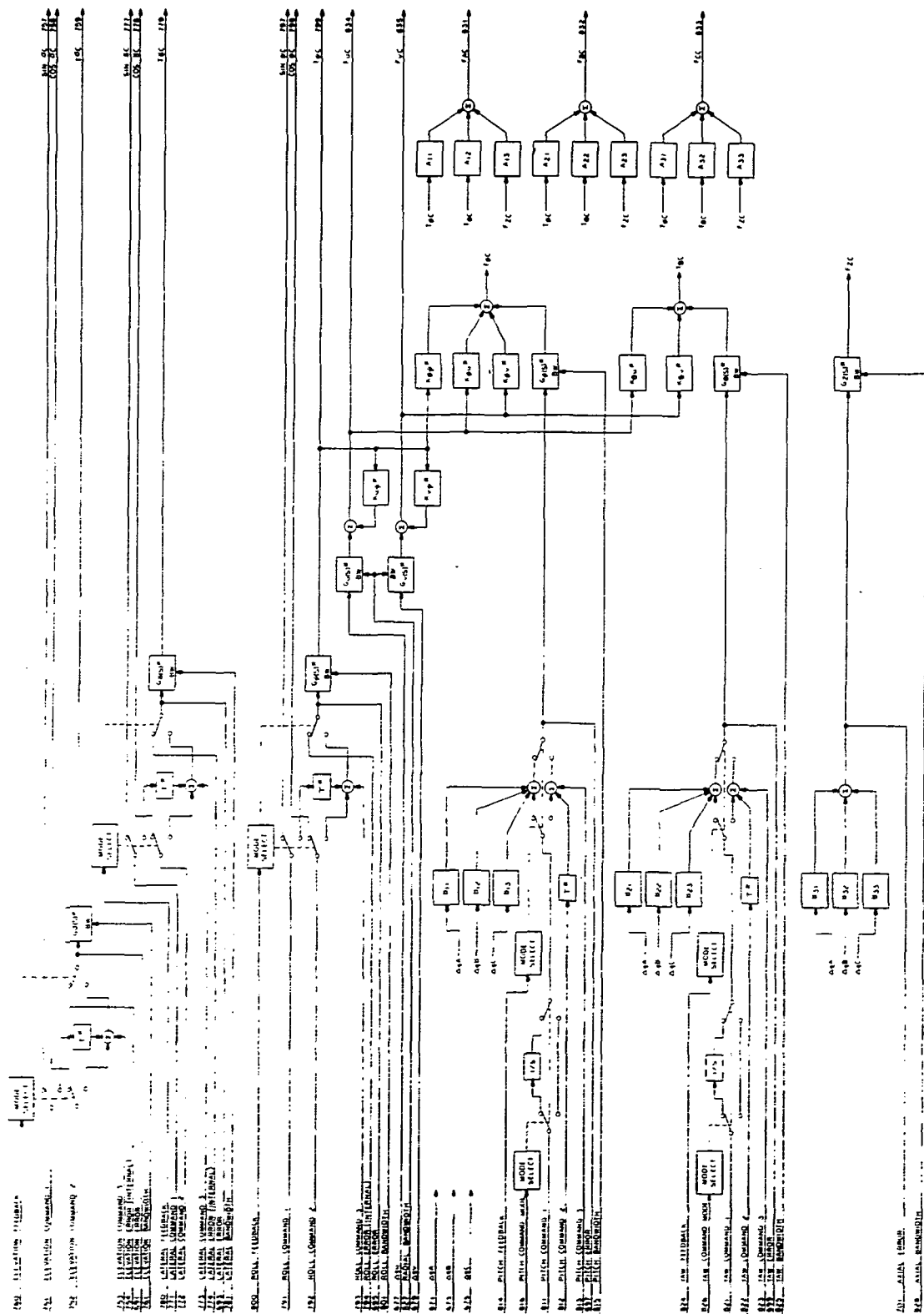


Figure 93
Vernier Control Matrix Module

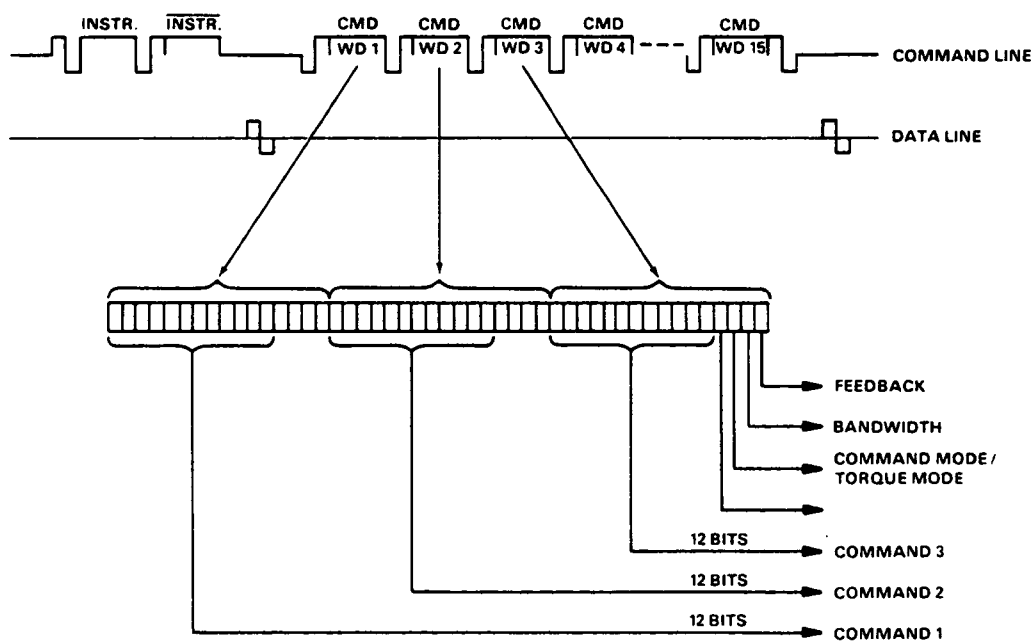


Figure 94
Serial Command Format

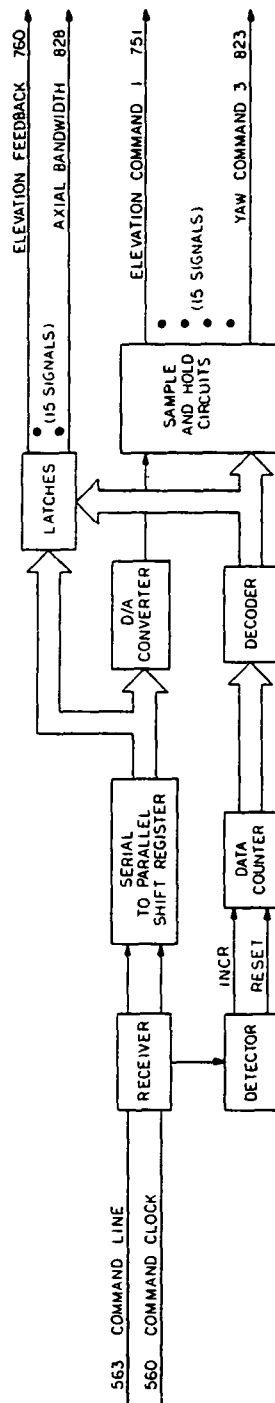


Figure 95
Command Interface Module

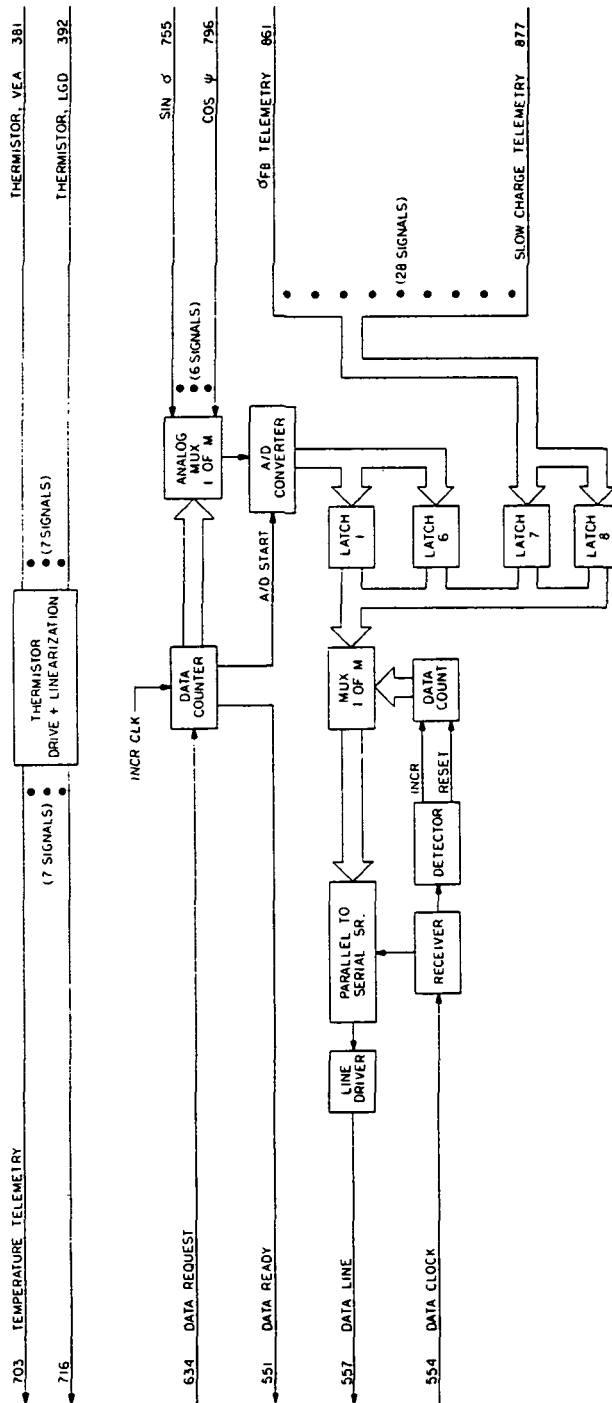


Figure 96
Telemetry Interface Module

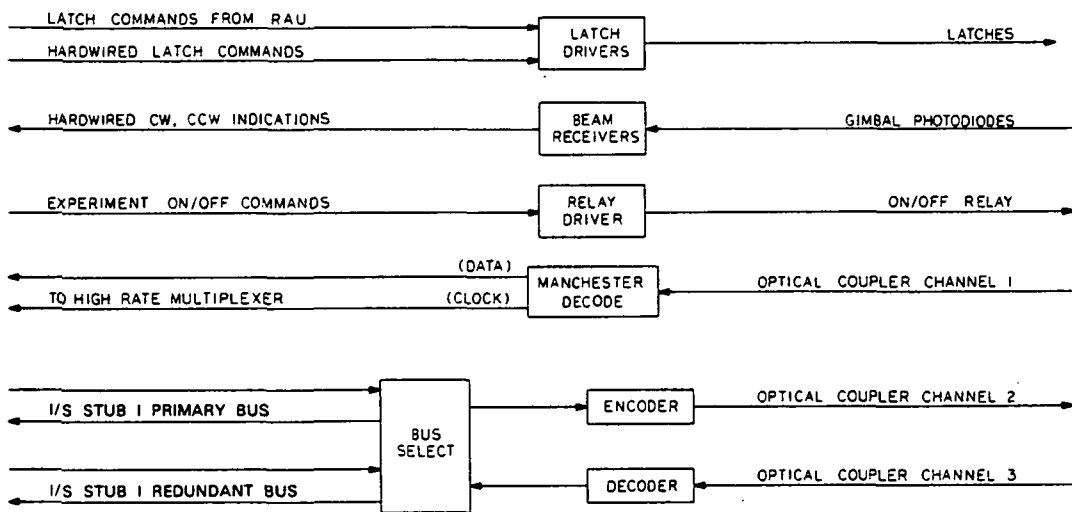


Figure 97
Payload Services Module

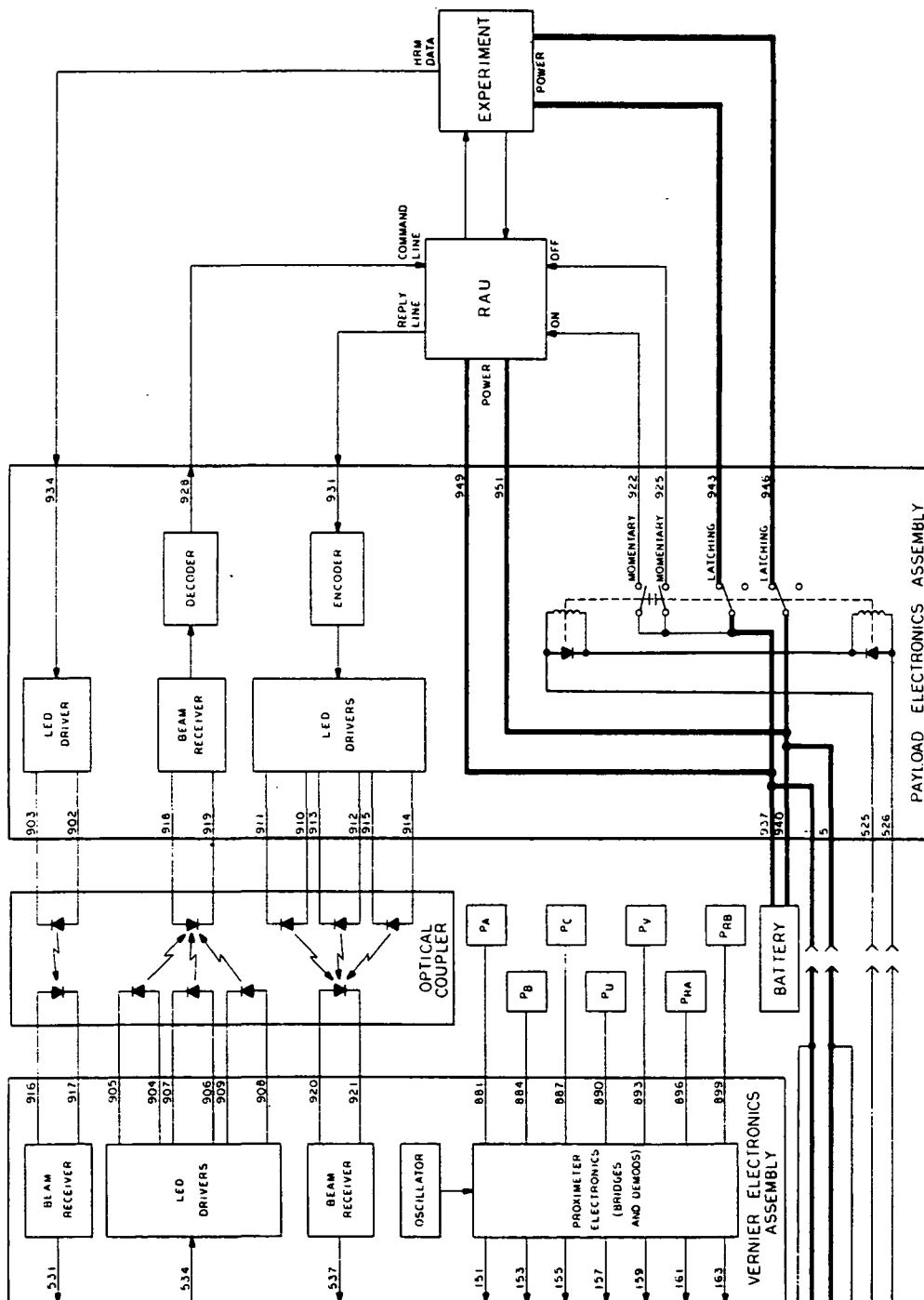


Figure 98
Vernier Assembly Electronics Modules

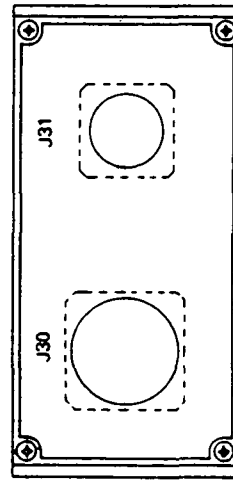
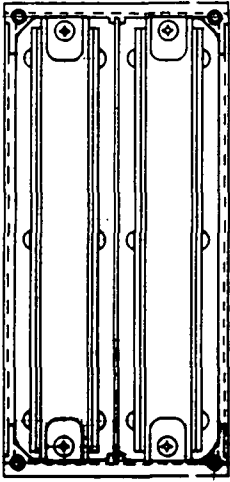
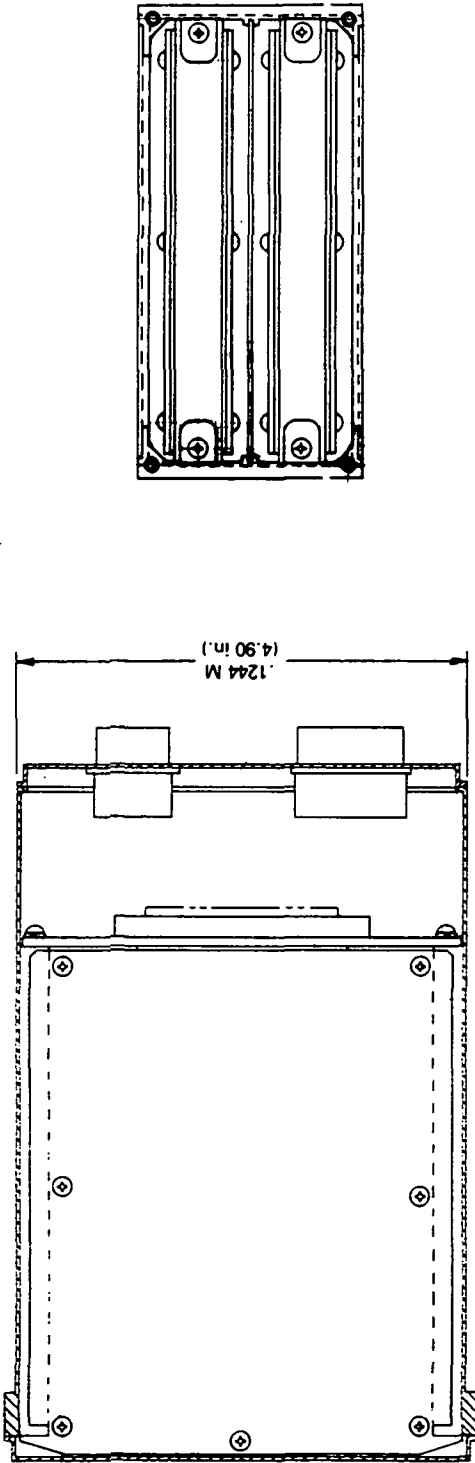


Figure 99
ASPS Vernier Electronics Assembly

DESCRIPTION	SECONDARY		PRIMARY			
	+15	+5	STANDBY		PEAK	
			DRIVER	LOAD	DRIVER	LOAD
ELEVATION GIMBAL	1.5				100.7	197.3
LATERAL GIMBAL	1.5				74.5	126.3
ROLL MOTOR	2.8		2.9	1.2	162.4	100.0
AXIAL MBA'S	4.8		11.7	15.6	21.6	93.0
RADIAL MBA'S	2.8		7.8	10.4	14.4	62.0
INTERFACE ELECTRONICS	3.1	3.5				
SUBTOTAL	20.0					
SECONDARY SUPPLY			5	20	5	20
SUBTOTALS			27.4	47.2	378.6	598.6
TOTALS			74.6		977.2	

Figure 100
ASPS Control Electronics Power Dissipation

<u>Component</u>	<u>Weight Kg (Lbs)</u>	<u>Qty</u>	<u>Total Weight Kg (Lbs)</u>
Top Cover	.204 (.45) X	1	.2041 (.45)
Rack Chassis	1.555 (3.43) X	1	1.555 (3.43)
Power Chassis	.866 (1.91) X	1	.866 (1.91)
Wire Harness and	1.542 (3.4) X	1	1.542 (3.4)
EMI Filter	2.476 (5.46) X	1	2.476 (5.46)
Secondary Supply	.680 (1.5) X	1	.680 (1.5)
Driver Module	.567 (1.25) X	4	2.268 (5.0)
Signal Module	.327 (.72) X	9	2.939 (6.48)
Total			12.531 (27.63)

Figure 101
ASPS Control Electronics Weight

Page Intentionally Left Blank

SECTION 6.0

ELECTROMAGNETIC COMPONENTS

6.1 INTRODUCTION

The electromagnetics components used within the ASPS are as follows:

Roll Axis:

- Torque Motor (1)
- Position Sensor (1)

Vernier:

- Axial Magnetic Bearing Assemblies (3)
- Radial Magnetic Bearing Assemblies (2)
- Translational Position Sensors (7)

Coarse Axes:

- Torque Motors (2)
- Position Sensors (4)

The roll axis and vernier components interface with the suspended rim which requires six degree-of-freedom for fine pointing and isolation from Shuttle disturbances. To provide the high degree of translational isolation required, large relative displacement must be accommodated across the vernier rotor and stator. Therefore, the electromagnetic components must be sized to provide the following operational gaps:

- ± 5.08 mm (.200 inch) radial
- ± 5.58 mm (.220 inch) axial
- $\pm .75$ degree tilt

The component designs also are intended to:

- provide unlimited roll axis freedom,
- use noncontacting elements throughout to maintain the complete mechanical isolation of the suspended element.

Other requirements which demanded special effort to ensure proper design achievement are:

- very low roll axis anomaly torques to maintain roll axis pointing stability,
- low leakage flux to prevent component interactions,
- complex force linearization and compensation in the vernier system to maintain the desired pointing stability of .01 arc second.

The coarse axis components contain no requirements unique to the ASPS, and state-of-the-art, conventional components are utilized.

The selection process and description of the final electromagnetic component designs are explained in the following paragraphs. In addition to selecting each component, the mechanical integration of the components into the ASPS was a prominent factor. A principal feature which evolved from the design effort was the plated, solid iron rotor used in conjunction with the roll axis torque motor, radial and axial magnetic bearings, and translational position sensors. The rotor, which can be fabricated from either 50 percent nickel-steel or from low carbon steel, is plated with .254 mm (.010 in.) copper on the radial sections to enhance the torque motor performance and then plated all over with .076 mm (.003 in.) nickel to enhance the translational position sensor performance. Although it was anticipated that these conductive platings would degrade the frequency response of the magnetic bearings, no degrading effects were recognized on the prototype test station fabricated.

6.2 ROLL AXIS TORQUE MOTOR

6.2.1 Requirements

The requirements for the roll axis torque motor are contained in Figure 102. A torque motor with a passive rotor is required. This motor must be capable of producing .68 N m (.5 ft-lb) of output torque while operating with a large, variable running clearance. Extremely low anomaly torques are required to maintain roll pointing stability, low leakage flux, and low extraneous radial forces are required to prevent coupling to other system components.

6.2.2 Candidates

The type of actuator concepts considered as candidates for the ASPS application operate on electromagnetic principles. These devices require simple electrical power, have proven reliability in space, and are simple and economical to construct. Figure 103 contains the family of electromagnetic actuators considered for this application. All operate with nonexcited rotors, are direct drive, and can readily be designed with segmented stators at large radii.

The important criteria in selecting the concept are as follows:

- Configuration coordination into the ASPS
- Force and flux coupling to other components
- Anomaly torque magnitudes

Figure 104 compares these criteria for the considered concepts. For the comparison it is assumed that the motor will be configured at a large diameter resulting in segmented stators. Two stators will therefore be used, mounted on the inner and outer radius of the rotor to eliminate the rotor/stator attractive forces at the rotor centered condition (first order forces). This results in large segments of the rotor without stator coverage.

PARAMETER	REQUIREMENTS
PEAK TORQUE MAX RATE	.677 NM (0.5 FT-LBS) 2 DEG/SEC
OPERATING CLEARANCE AXIAL RADIAL TRANSLATIONAL MOTIONS	7.49 MM (.295 IN.) 6.78 MM (.267 IN.) ±75% OF OPERATING CLEARANCES
POWER AT MAXIMUM TORQUE STAND BY POWER	100 WATTS MAXIMUM 5 WATTS MAXIMUM
MOTOR TORQUE CONSTANT SENSITIVITY TO TRANSLATIONAL MOTIONS	±30% MAXIMUM
COGGING TORQUE	$< 1.4 \times 10^{-4}$ NM (10^{-4} FT-LBS) o-pk AT $n > 65$ CYCLES/REV $< .0088/n$ NM (.0065/n FT-LBS) o-pk AT $n \leq 65$ CYCLES/REV
RIPPLE TORQUE	$< .02\%$ o-pk OF PEAK TORQUE AT $n > 65$ CYCLES/REV $< (1.3/n)$ o-pk OF PEAK TORQUE AT $n \leq 65$ CYCLES/REV ($n =$ CYCLES/REV)
HYSTERESIS	$< .014$ NM (.01 FT-LBS)
ROTOR	PASSIVE
RADIAL FORCES	< 0.89 N (0.2 LBS) FOR MOTIONS UP TO THE OPERATING CLEARANCES
LEAK FLUX	$< .1$ GAUSS AT 0.3 M (12 IN.) DISTANCE FROM THE UNIT
PEAK EXCITATION	±18.5 VDC

Figure 102
Roll Axis Torquer Requirements

CONSIDERED CONCEPTS:

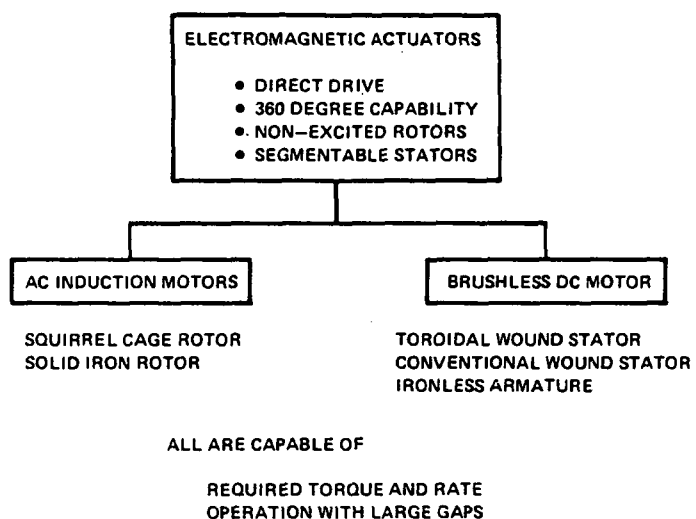


Figure 103
Roll Axis Torque Motor Candidates

ACTUATOR TYPE	RELATIVE FORCES		ANOMALY TORQUE		RELATIVE COMPLEXITY		LEAKAGE FLUX	
	1ST ORDER	2ND ORDER	RIPPLE	COGGING	STATOR	ROTOR	ROTOR	STATOR
AC INDUCTION MOTORS								
SQUIRREL CAGE ROTOR	NONE	1X	1%	1%	1X	2X (CAGE)	NONE	MEDIUM
SOLID IRON ROTOR	NONE	4X	<.03% ^①	<.03% ^①	1X	1X ^② (SOLID IRON)	NONE	MEDIUM
BRUSHLESS DC MOTORS ^③								
TOROIDAL WINDING	NONE	4X	2-4%	5-20%	1X	3X (100 MAGNETS)	HIGH	MEDIUM
CONVENTIONAL WINDING	NONE	4X	2-4%	5-20%	1X	3X (100 MAGNETS)	HIGH	MEDIUM
IRONLESS ARMATURE	NONE	NONE	2-4%	0	2X	4X (100 MAGNET & RETURN PATH)	LOW	LOW

① TESTED VALUE (LIMITED BY TEST EQUIPMENT)

② COMMON TO MAG BEARING

③ REQUIRES COMMUTATOR

Figure 104
Roll Axis Torquer Concept Comparison

6.2.2.1 AC Induction Motors

Two types of ac induction motors were considered:

- Squirrel cage rotor
- Solid iron rotor

Each operates on the basic induction motor principle that the flux wave generated in the stator, sets up circulating currents in the rotor which in turn generate a counter-flux field positionally lagging the stator-flux field and generating a torque. The squirrel cage rotor bounds the circulating currents within the conductor bars, utilizes low resistivity materials for the conductor bars, and presents a laminated iron surface at the operating gap interface. The solid iron rotor, usually used for simplicity in lieu of the squirrel cage, presents no bounds to the circulating currents and utilizes the resistivity of either the rotor iron or a rotor surface plating.

The solid iron rotor concept presents two unique features desirable for the ASPS application:

- A uniform operating surface is presented to the stator which theoretically eliminates all cogging and ripple anomaly torques except for those caused by the material nonhomogeneity.
- The rotor can be shared with the magnetic suspension.

The disadvantage of the solid iron rotor concept is that it is inherently less efficient, requiring higher stator weight, and flux levels resulting in higher radial forces.

The induction motors in comparison to the brushless dc motors:

- Have larger and heavier stators
- Have smaller anomaly torques
- Have less complex rotor construction
- Have passive rotors resulting in no rotor leakage flux

6.2.2.2 Brushless dc Motors

Three types of brushless dc motors were considered:

- Toroidal wound stator
- Conventional wound stator
- Ironless armature

Each operates on the basic dc motor principle, whereby the rotor field is established by permanent magnets, and multiple stator windings are excited at such time to generate a stator field (electrical) 90 degrees shifted from the rotor field. A commutation sensor is thus required to establish the proper

excitation period. The toroidal and conventional wound stators perform essentially identically, with the difference being the stator construction; the toroidal wound device does not use a conventional toothed stator lamination. The ironless armature concept has the rotor field return path, (normally the stator iron) integrated into the rotor body, and the stator windings (ironless) located in an air gap between the rotor magnets and return path.

The principle disadvantages of the brushless dc motors are:

- State-of-the-art ripple torque capability is approximately 2 to 4 percent.
- On those units with stator iron, very large cogging torques are possible when the rotor magnets pass the stator segment edges.
- The rotors are very complex, requiring approximately 100 magnets which have high-leakage flux about the complete rotor periphery.

The ironless armature concept, however, offers a feature highly desirable for the ASPS application and usually sought on all magnetic bearing supported systems. No radial forces are present between the rotor and stator and no cogging torques exist.

6.2.3 Concept Selection

The ac induction motor with the solid iron rotor is the concept selected for use in the ASPS. The reasons for selection were:

- The very low ripple and cogging torques are required to meet the roll pointing stability requirements.
- The simple rotor can be shared with the Magnetic Bearing Assembly (MBA) resulting in a simpler ASPS configuration.
- The absence of rotor leakage flux minimizes potential coupling problems to other components.
- The radial forces can be controlled with a bias field similar to that utilized for the MBA force linearization.
- The additional stator weight impact to the total ASPS system is minor as long as the stator can fit between the Axial Magnetic Bearing assemblies and does not exceed the axial or radial dimensions of the MBAs.

The final design is described in Figure 105.

PARAMETER	DESCRIPTION	
TYPE	AC INDUCTION MOTOR, SOLID IRON ROTOR WITH NICKEL AND COPPER PLATE	
CONFIGURATION	<ul style="list-style-type: none"> • TWO SEGMENTED STATORS • RADIAL MAGNETIC GAP OF 6.78 mm (0.267 IN.) • LOCATED FOR ZERO 1ST ORDER RADIAL FORCE • PASSIVE ROTOR • INTEGRAL GAP SENSORS • RADIAL FORCES ELECTRONICALLY COMPENSATED • TWO LEVEL EXCITATION 	
EXCITATION FREQUENCY	200 HERTZ	
POLES	48	
WEIGHT	9.1 Kg (20 LBS)	
PEAK TORQUE	LOW EXCITATION 0.027 NM (0.02 FT-LBS)	HIGH EXCITATION 0.677 NM (.05 FT-LBS)
PEAK POWER	<4 WATTS	<100 WATTS
STANDBY POWER	<2 WATTS	<50 WATTS
COGGING AND RIPPLE TORQUE	<.03% 0-PK	<.03% 0-PK
HYSTERESIS	NEGLIGIBLE	NEGLIGIBLE
RADIAL FORCES (COMPENSATED)	< .089 N (.02 LBS)	< 1.56 N (.35 LBS)*
LEAKAGE FLUX (AT 12 INCHES)	<.02 GAUSS	<0.1 GAUSS

*UNCOMPENSATED: 3.5 POUNDS/SEGMENT

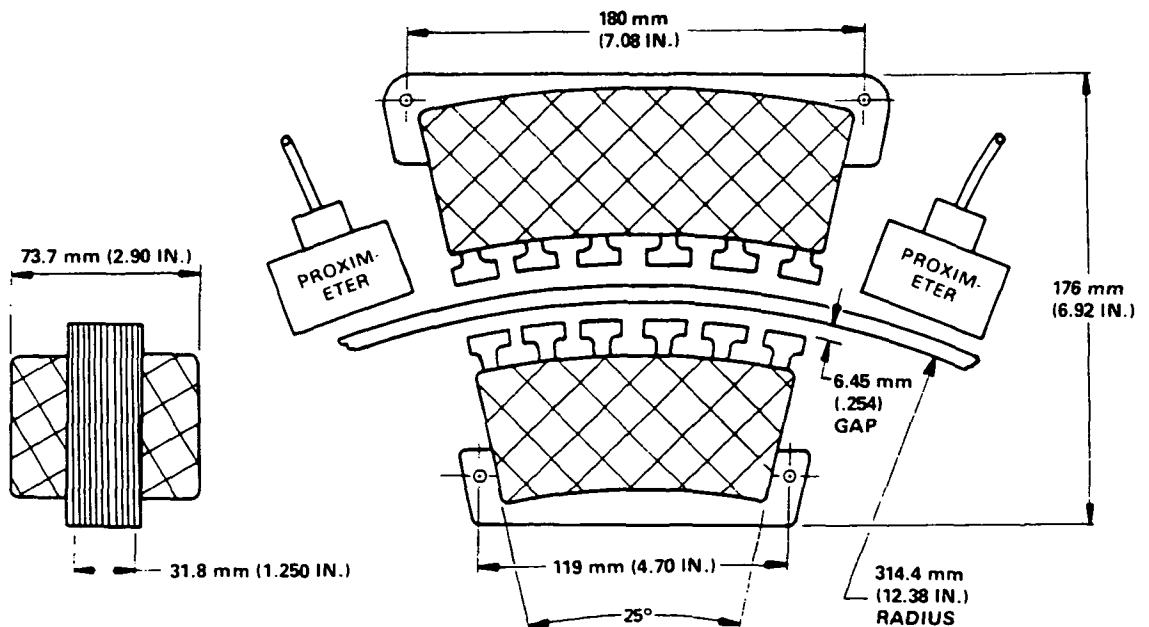


Figure 105
Roll Axis Torque Motor Design Description

6.2.4 Development Tests

To demonstrate that the anomaly torques on the ac Induction Motor - Plated Solid Iron Rotor concept were less than .05 percent of the desired torque level, a test on a smaller existing unit was performed. The test description and data are contained in Appendix D. No ripple or cogging was observed as measured to a resolution of .03 percent 0 to peak.

6.2.5 Design Notes and Trade-offs

6.2.5.1 Pole and Frequency Selection

Two of the basic parameters to be selected were the excitation frequency and the pole quantity. The torque output from an induction motor is directly related to the power dissipated in the rotor divided by the synchronous speed.

$$T = \frac{P_R}{\omega_s} \frac{P_R p}{120 f} \quad (11)$$

where

T = torque

ω_s = synchronous speed

P_R = power dissipated in the rotor

p = number of poles

f = excitation frequency

Because of problems meeting the input power specification, it is desirable to minimize the rotor power. To accomplish this, the pole quantity should be maximized and the frequency minimized. The pole quantity, selected as 48, is limited by the mechanical stability of the teeth where two teeth per pole are required and the teeth are very long and thin. The frequency selected, 200 hertz was a compromise from 60 hertz to minimize any vibrational effects due to feed-through of roll motor excitation frequency into the payload.

6.2.5.2 Power/Weight/Flux Level Trade-offs

The total input power consists primarily of the power dissipated in the rotor, and the stator winding heat (I^2R) losses. Since the power dissipated in the rotor is fixed by the frequency and pole quantity selection, the principle power/weight trade-off remaining is the I^2R losses. These are controlled by the stator cross-sectional area. In addition, the stator tangential length and rotor plating thickness determine the flux level required. The flux level determines the radial force and flux leakage magnitudes.

Since it seemed imprudent that the motor power should dictate the ASPS size, the largest available cross section capable of fitting into the ASPS design without impacting the ASPS outline was utilized to minimize input power. The rotor plating thickness was selected to be as thick as practical .254 mm (.010 in.), and the stator tangential length was selected to require an approximate .1 tesla flux level which yields reasonable force and flux leakage levels.

6.2.5.3 Equivalent Circuit

The calculated equivalent circuit per motor phase and method of calculating output torque and radial forces for each segment are shown in Figure 106 as follows:

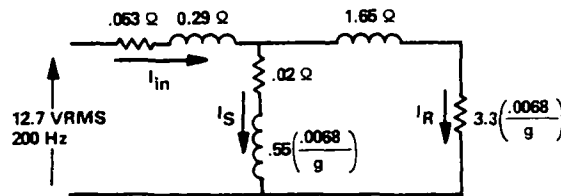


Figure 106
Equivalent Circuit per Phase

Output Torque (T) for each segment is:

$$T = \frac{2 I_{R1} I_{R2} (3.3)(.0068)(.019)}{g} = \frac{.00085 I_{R1} I_{R2}}{g}$$

where

T is in newton meter

I_{R1} , I_{R2} are phase currents in amps

g is air gap in meters

Radial Force (F) for each segment is:

$$F = \frac{1}{2} (I_{S1}^2 + I_{S2}^2) \frac{(.55)(.0068)}{g^2 2 \pi 200} = .0000015 \frac{I_{S1}^2 + I_{S2}^2}{g^2} \quad (13)$$

where

F is in newton

I_{S1} , I_{S2} are phase currents in amps

g is air gap in meters

6.2.5.4 Control Laws for Radial Force Compensation

The selected motor configuration has two segments, one inside the rotor and the other outside the rotor, mounted radially in-line. Each segment has two windings: fixed field and control field; all of which are represented by the equivalent circuit of 6.2.5.3. The following (Figure 107) sketch depicts the motor configuration:

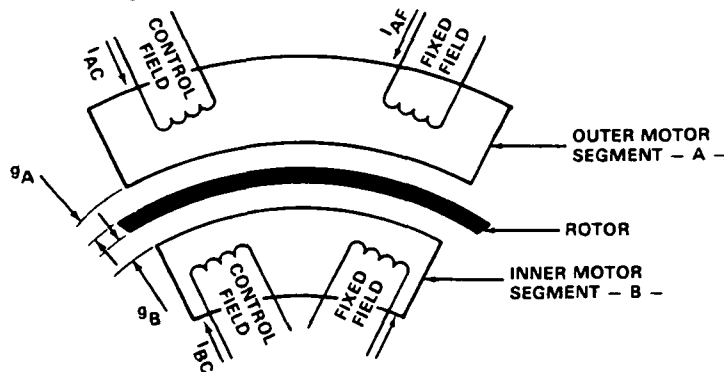


Figure 107
Motor Configuration

The objective of this configuration is to provide linear commandable output torque without radial force disturbances while the rotor position is allowed to vary. This is accomplished by causing the radial forces from the two segments to cancel while the output torques are additive by usage of control laws. The control laws establish a bias current (in the fixed field windings) and vary the excitation currents (to all windings) dependent upon the rotor position between the inner and outer motor segments.

The control laws are:

$$I_{AF} = \frac{I_{AFO} \ g_A}{g_0} \qquad I_{AC} = \frac{c \ T_C \ g_A}{g_0} \qquad (14)$$

$$I_{BF} = \frac{I_{BFO} \ g_B}{g_0} \qquad I_{BC} = \frac{c \ T_C \ g_B}{g_0}$$

where

g_A and g_B are the magnetic air gaps of the A and B segment respectively

g_0 is the magnetic air gap when the rotor is centered between the stators

$I_{AFO} = I_{BFO}$ are initializing or bias current determined such that at maximum torques command $I_{AF} = I_{AC}$ and $I_{BF} = I_{BC}$

T_C is the torque command input

c is the proportionality constant to arrange the torque command to the proper units.

The excitation control laws for the two-segment concept can now be applied to the torque and force formulas defined in Paragraph 6.2.5.3.

Defining

$$T = T_A + T_B$$

$$\text{and } F = F_A + F_B$$

with T and F the total torque and force respectively and the sub-letter designates the individual segments, and assuming that in Paragraph 6.2.5.3 equivalent circuit,

$$I_R \propto I_{iN} \text{ and } I_S \propto I_{iN} \quad (15)$$

Then the total torque from the segments is:

$$T = T_A + T_B = K_1 \left[\frac{I_{AFO}^2 c^2 T_C^2 g_A^2}{g_0^2 g_A} + \frac{I_{BFO}^2 c^2 T_C^2 g_B^2}{g_0^2 g_B} \right] \quad (16)$$

$$T = K_2 (g_A + g_B) T_C$$

However $g_A + g_B = \text{constant}$: therefore,

$$T = K_3 T_C \quad (\text{where } K_1, K_2 \text{ and } K_3 \text{ are proportionality constants})$$

The total radial force for the two segment configuration is:

$$F = F_A + F_B = K_4 \left[\frac{\frac{I_{AFO}^2 g_A^2}{g_0^2} + \frac{c^2 T_C^2 g_A^2}{g_0^2}}{g_A^2} - \frac{\frac{I_{BFO}^2 g_B^2}{g_0^2} + \frac{c^2 T_C^2 g_B^2}{g_0^2}}{g_B^2} \right] \quad (17)$$

$F = 0$ (where K_4 is a proportionality constant)

6.3 ROLL AXIS ANGULAR POSITION SENSOR

6.3.1 Requirements

The requirements for the roll axis angular sensor are contained in Table 25. A sensor, with a noncontacting rotor, capable of one arc minute accuracy, and one arc second resolution is required while operating with a large variable running clearance. Extremely low anomaly torque is required to maintain roll pointing stability; and low leakage flux and extraneous forces are required to prevent coupling to other system components.

6.3.2 Candidates

The following are the sensor concepts considered for the roll axis application:

- Resolver/Synchro
- Optical Encoder
- Inductosyn
- Xynetics Actuator/Sensor

All the concepts are capable of one arc minute accuracy and have unlimited rotation.

TABLE 25
ROLL AXIS ANGULAR SENSOR REQUIREMENTS

Parameter	Requirements
Operating Clearance	
Axial	7.49 mm (.295 in.)
Radial	6.78 mm (.267 in.)
Translational Motions	+75 Percent of operating clearances
Accuracy*	< 1 min (required only during $\pm .015$ translational motions or angular motions to $3/4$ degree)
Type	Absolute or incremental with initialization
Resolution	< 1 arc second
Radial Forces	< .45N (.1 LB) for motions up to the operating clearances
Rotational Forces	< 1.4×10^{-4} N m (10^{-4} FT LB) at 65 or more cycles/rev
	< $\frac{.0088}{nc}$ N m ($\frac{.0065}{nc}$ FT LB) at $nc \leq 65$ cycles/rev
Leakage Flux	< .1 gauss at .3 meters (12 in.) distance from unit
Mechanical Configuration	Noncontacting

*Component accuracy goal. System requirement is 6 arc minutes.

6.3.2.1 Resolver/Synchro

Resolvers and synchros are the most commonly used devices to convert angular position into electrical signals where high accuracy over large (> 30 degrees) ranges are required. Resolvers and synchros are motor-like components whose basic structure consists of a wound rotor and a wound stator, concentrically arranged to provide a variable mutual coupling between the windings of the two members. The principle difference between synchros and resolvers is the output winding. The synchro has three windings at 120 degrees space phasing, and the resolver two windings at 90 degrees space phasing. Schematic diagrams of both devices are shown in Figure 108.

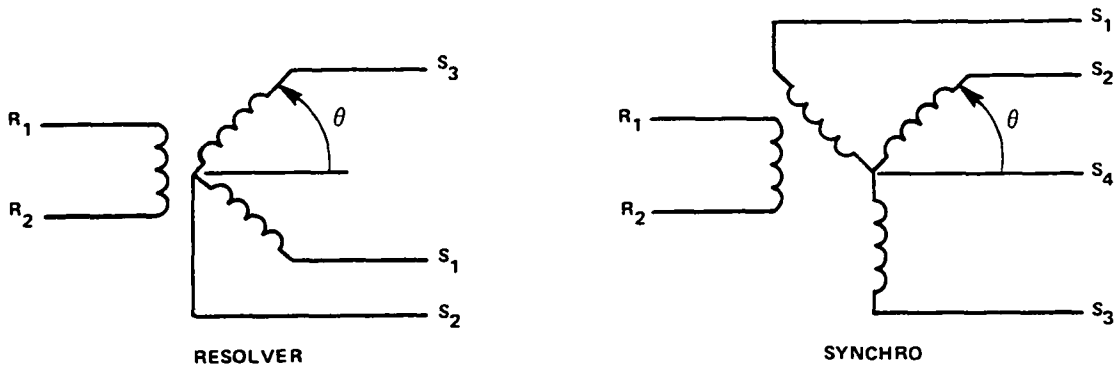


Figure 108
Resolver and Synchro Schematic Diagrams

The device functions essentially as follows:

Exciting the rotor establishes a two-pole magnetic field which couples with the stator. Since the stator windings are wound space-displaced, each winding provides an output voltage whose magnitude is related to the angle between the magnetic field established by the rotor and the respective stator winding.

$$\begin{aligned} V_{S3-S2} &= K V_{R1-R2} \sin \theta \\ V_{S1-S2} &= K V_{R1-R2} \sin (\theta - 90^\circ) = K V_{R1-R2} \cos \theta \end{aligned} \quad (18)$$

where

V_{R1-R2} is the rotor winding excitation

V_{S3-S2} is the stator sine winding output voltage

V_{S1-S2} is the stator cosine winding output voltage

K is the resolver transformation ratio

and the frequency of the output voltages are the same as the excitation frequency.

6.3.2.2 Optical Encoder

There are several different types of noncontacting shaft position encoders, however optical methods are the most advanced and therefore most applicable to the ASPS application. Figure 109 shows the basic elements of an optical encoder. They characteristically consist of a glass code wheel, a light source, optics to shape and direct the light through the code wheel, photocells to sense the light, and electronics to process the photocell information. Generally, the light sources, optics, and photocells are mounted on a stator, whereas the encoder hub and code wheel are part of a rotor shaft. If

the code wheel is in an angular position which permits light to pass through the optics and code wheel to a photocell, the photocell which is generated may be interpreted as a binary one output. Conversely, absence of light or photocell signal indicates binary zero. In some cases, as that illustrated in Figure 109, the photocell output is used directly as an analog signal. Each track has a separate photocell and the combination of one or zero outputs makes a coded binary word. Thus, if it is desired to resolve angular rotation into 1.32 arc minute increments, 14 rings or tracks of coded information would be required. The binary word represented by the combination of (14) one and zero photocell signals could define 214 bits or 16,384 unique angular directions or shaft positions.

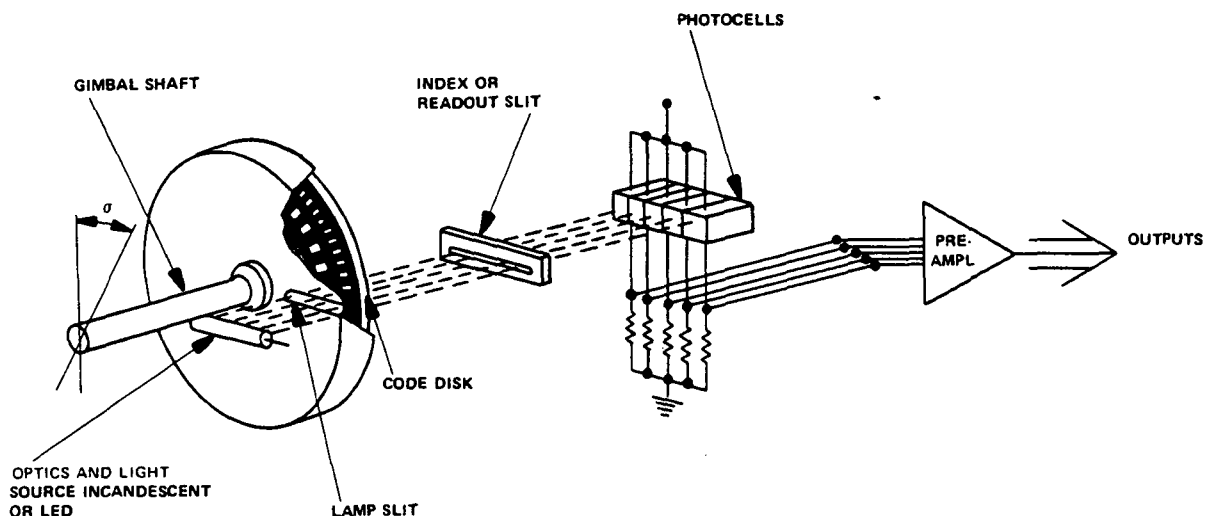


Figure 109
Basic System - Photoelectric Shaft Position Encoder

This basic technique is applicable to resolutions of 216 bits (19.8 arc second resolution) where the light wavelength (10 wavelengths of 9000 Å light) limits the ability to read the encoder. To obtain higher resolution, the highest resolution signal is used as a reference to electronically synthesize the higher resolution bits.

6.3.2.3 Inductosyn*

The operating principle of a rotary Inductosyn transducer is similar to that of an electrical resolver in that the output signal is a function of the position of the rotor winding relative to the two stator windings. The quantity that varies as a function of mechanical motion is the electromagnetic coupling between two conductor formations. In a resolver, these conductor formations are coils of wire, wound on suitable iron cores.

*Developed and Trademark Registered by Farrand Controls, Inc.

Inductosyn rotor and stator windings shown in Figure 110 are printed circuits on an insulated layer bonded to metallic plates and are in the form of hairpin turns. Inductosyn patterns may be printed on base materials such as steel, stainless steel, aluminum, beryllium, and titanium.

The rotor pattern is a hairpin winding consisting of an even number of series connected radial conductors. Each conductor is an electrical pole, and two poles define one cycle. For example, a pattern made of 360 poles is an 180 cycle device. This is often referred to as a 180-speed rotor, meaning that in association with the appropriate stator it provides 180 electrical cycles for 360 degrees of mechanical rotation. In this case, cycle length is 2 degrees.

The stator consists of two independent windings that are separated by a 90 degree space phase. The windings on the stator are arranged in groups to permit a one-quarter electrical cycle displacement of one set of windings with respect to the other. The coupling of the two windings to the rotor is in a sine and cosine relationship relative to the cycle length.

The stator sine and cosine voltage are

$$\begin{aligned}V_{\sin} &= K_S \sin N \sigma \\V_{\cos} &= K_C \cos N \sigma\end{aligned}\tag{19}$$

where

N = half the number of poles (electrical speed)

σ = shaft angle (radians)

The typical number of poles are 256, 360, 512, 720, 2000, and 2048. Output signals are the result of averaging over the total number of poles, thus averaging the effect of residual errors in individual conductor spacing and providing greater accuracy.

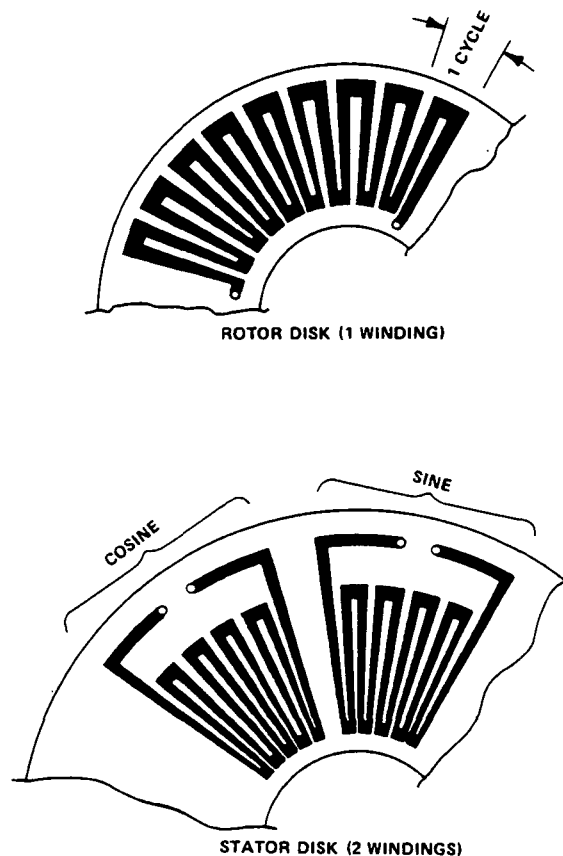


Figure 110
Rotary Inductosyn

Figure 111 illustrates how the output voltage is produced in the Inductosyn windings. The illustrations show schematic cross sections of single input and output windings. The direction of current flow on the input winding is \cdot out of the paper and \times into the paper. In A, the input is induced in the output winding, as shown by the positive peak of the coupling curve in C directly below the first turn of the output winding.

In B, the output winding has been displaced one-quarter electrical cycle to the right. In this position, the input conductors are midway between the output conductors. There are equally induced currents in opposite directions which cancel, and the resulting output current is zero, as shown by the intercept of the coupling curve in C.

A further one-quarter displacement of the output winding would give another maximum induced current in the opposite direction, as shown by the negative peak of the coupling curve in C.

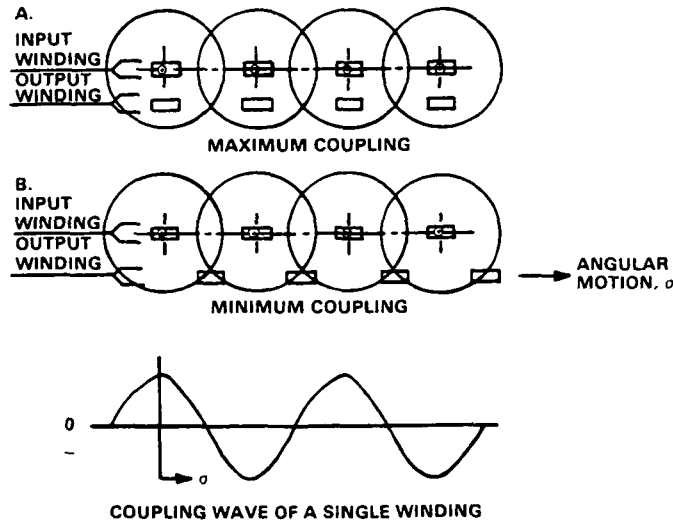


Figure 111
Production of Output Voltage

If the displacement, σ , is measured from the A position, the coupling curve shown represents the cosine output. A second winding displaced one-quarter cycle from the first is then the sine output.

In general, modulation of the amplitude of the induced output voltage will not be a pure sine or cosine function, but will be a periodic function with a period equal to double the input conductor or pole spacing. It may therefore be considered to be the sum of a sine (or cosine) curve plus a series of harmonics. With suitable design of conductor widths and spacing in the Inductosyn patterns, these harmonics are suppressed to less than .1 percent of the fundamental, and a nearly perfect sine wave coupling is achieved.

If the voltages equal to this particular pair of values are introduced into the two stator windings of a receiver, the output from the rotor will be a maximum when it is in the position corresponding to this vertical line, and will be a null at a point 90 degrees distant. The output from the rotor is also a sine curve. This is one form of the amplitude method of operating the

Inductosyn assembly, and may be used to reproduce a desired position from a control, to read out a position, or to follow another sine/cosine device.

The phase method can also be used to achieve the functions of control or readout. In one example of the phase method the two stator windings are energized by fixed equal amplitude voltages in time quadrature. The rotor output is then a constant amplitude signal having a time phase angle that changes linearly as a function of position. This signal can then be used to position the gimbal shaft in a phase locked loop.

6.3.2.4 Xynetics Actuator/Sensor

The Xynetics actuator/sensor is an actuator similar to a stepper motor whereby the position can be known by counting the actuation pulses. The rotor consists of a toothed structure of magnetic material where the tooth width is twice the position resolution. The stator consists of electromagnets, biased by permanent magnets, configured to step from one rotor tooth to the next by the minimum reluctance principle.

The important criteria in selecting the roll sensor are:

- configuration coordination into the ASPS
- operation capability with the required operating clearance and over the required motions.

Table 26 compares the concepts considered.

TABLE 26
ROLL AXIS SENSOR CANDIDATES
AND CONCEPT COMPARISON

Sensor Candidates	Resolution	Operating Clearance > 6.78 mm (.267 in.)	Functions Over Required Motions	Requires Rotor Power	Magnetic Leakage Radial Forces Rotational Forces
Resolver/ Synchro	< 1 Sec	Yes	Yes	Yes	Yes
Optical Encoder	≈ 1 Sec	Yes	No	No	No
Inductosyn	< 1 Sec	No: < .25 mm (.010 in.)	No	Yes	Minor
Xynetics Act/Sens	≈ 5 Sec	No; < .05 mm (.002 in.)	No	No	Yes
Requirement	< 1 Sec	Yes			

All are capable of 1 arc minute accuracy. Unlimited rotation.

The Xynetics actuator/sensor was considered primarily for the potential of eliminating a component by combining the roll actuator and sensor components. The concept, however, operates utilizing discrete features and to obtain the required resolution these features must be very small ($<.025\text{ mm}$) ($<.001\text{ in.}$). It is then impossible for it to discriminate these small features with a large rotor/stator operating clearance. The Inductosyn and the optical encoder also function by discrimination of small features. This prevents the Inductosyn from operating with the necessary rotor/stator operating clearance. The optical encoder is a special case since the light can be focused at a large distance from the source. This focus, however, cannot be maintained over the required rotor motions. In addition, the optical encoder has other special advantages in that the rotor is completely passive and no magnetic leakage flux or mechanical forces on the rotor exist.

The resolver/synchro, which operates on an area alignment concept, can be designed with very large rotor/stator operating clearance and will continue to function over the required rotor motions. Its undesirable aspects are that it requires power to the rotor and contains magnetic leakage flux and mechanical forces on the rotor.

6.3.3 Concept Selection

The resolver/synchro concept of which the resolver is applicable with a simpler readout, was selected for use in the ASPS. The reasons for selection were:

- The concept is completely operable and accurate over all the required rotor translations and rotations.
- The undesirable flux leakage and rotor mechanical forces can be controlled with low flux levels.
- Minimum development, risk, and cost.
- The pancake form is readily integrated into the ASPS.

The final design is described in Table 27 and Figure 112.

TABLE 27
ROLL AXIS ANGULAR SENSOR DESIGN DESCRIPTION

Parameter	Requirements
Type	Single speed, sine-cosine resolver
Operating Clearance	
Radial	8.89 mm (.350 in.)
Rotor Motions	
Axial	± 5.59 mm (.220 in.)
Radial	± 5.08 mm (.200 in.)
Angular	$\pm 3/4$ degree
Accuracy	
Resolver Transmitter(RX)	< 1 arc minute*
Resolver Control Transformer(RC)	< 1 arc minute* (Required only during $\pm .015$ translational motions or angular motions to $3/4$ degree)
Resolution	< 1 arc second
Weight	5.9 kg (13 LB)
Leakage Flux	$< .1$ gauss at .3 m (12 in.) from unit
Radial Forces	1.4×10^{-4} N m (10^{-4} FT-LB) > 65 cycles/revolutions
Rotational Forces	$< \frac{.0088}{N_c}$ N m ($\frac{.0065}{N_c}$ FT-LB) at N_c \leq cycles/revolution

*Component accuracy goal.

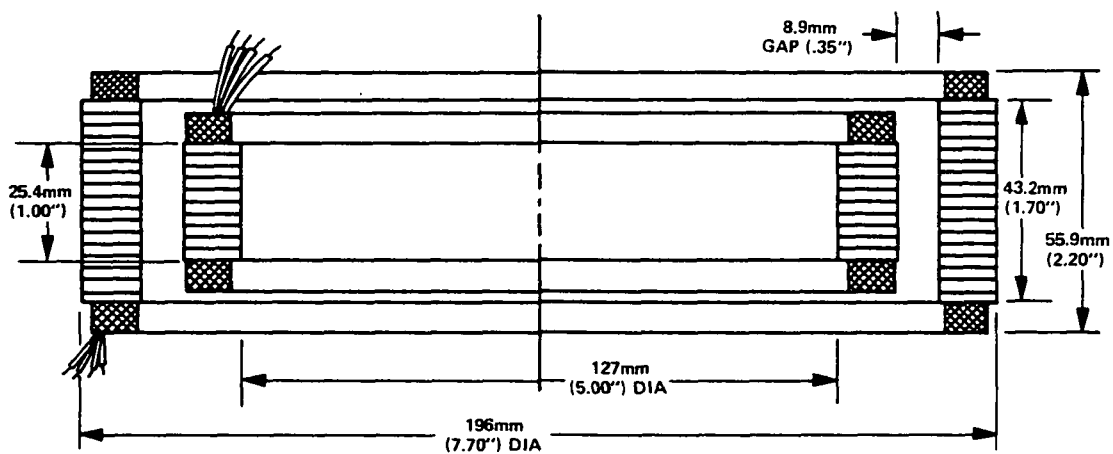


Figure 112
ASPS - Roll Axis Angular Sensor

6.3.4 Concept Application

Consequent to the selection of the resolver concept, two further application aspects were involved:

- The rotor will be powered through a rotary transformer.
- The resolver can be used in two modes - as a transmitter (RX) or as a control transformer (RC).

Independent methods to provide power to the resolver rotor were studied to maintain separation of the ASPS and payload functions. The best method obtained was the rotary transformer, and two vendors were found who have designed devices for similar usage in the past. The resultant rotary transformer design is described in Table 28.

Figure 113 illustrates the two performance modes and the rotary transformer application. In the transmitter (RX) mode, the resolver rotor is excited through the rotary transformer and the stator output signals are sine and cosine signals indicative of the rotor/stator angular position. In the control transformer (RC) mode, the excitation is sine and cosine signals indicative of a command angle to the resolver stator and the output is a signal through the rotary transformer proportional to the sine of the error angle.

6.3.5 Development Tests

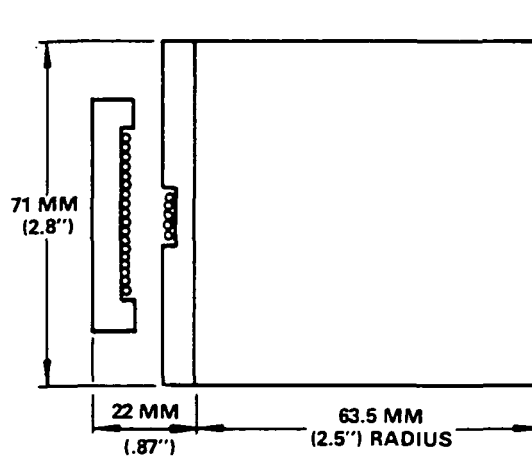
To confirm the resolver concept with the very large operating clearance, a model was fabricated and tested. To be consistent with the available schedule and funds, the model was fabricated on existing laminations, with a tooth combination not optimized for a highly accurate design. The important parameters to be verified by the model were:

- Transformation ratio and phase shift
- Accuracy and the error sensitivity over the specified rotor motions
- Radial and Rotational forces
- Leakage flux magnitude

The testing was performed by the vendor, Clifton, and was completed in two stages. First tests were performed at 200 hertz excitation frequency with the rotor quadrature winding shorted. Subsequently, it was recognized that better overall accuracy performance existed at 400 hertz and an open quadrature winding so additional tests were performed for that configuration. Tables 29 and 30 and Figure 114 describe the model and summarize the performance as measured during both series of tests. The rotor quadrature winding is a winding on the rotor placed 90 electrical degrees from the excitation winding, with the ends shorted internally. Its purpose is to attenuate rotor field position distortion caused by stator gap diameter out-of-roundness and thus improve the 2 cycle error characteristics.

TABLE 28
ROTARY TRANSFORMER DESCRIPTION

PARAMETER	DESCRIPTION	
TYPE	NON-CONTACTING, LOW POWER	
WEIGHT	2.7 Kg (6 POUNDS)	
	STATOR EXCITED	ROTOR EXCITED
EXCITATION	10 VOLTS 400 HERTZ	10 VOLTS 400 HERTZ
INPUT IMPEDANCE	> 50 OHMS	> 100 OHMS
OUTPUT IMPEDANCE	< 10 OHMS	< 200 OHMS
TRANSFORMATION RATIO	.7	.7
PHASE SHIFT	5 DEGREES	5 DEGREES



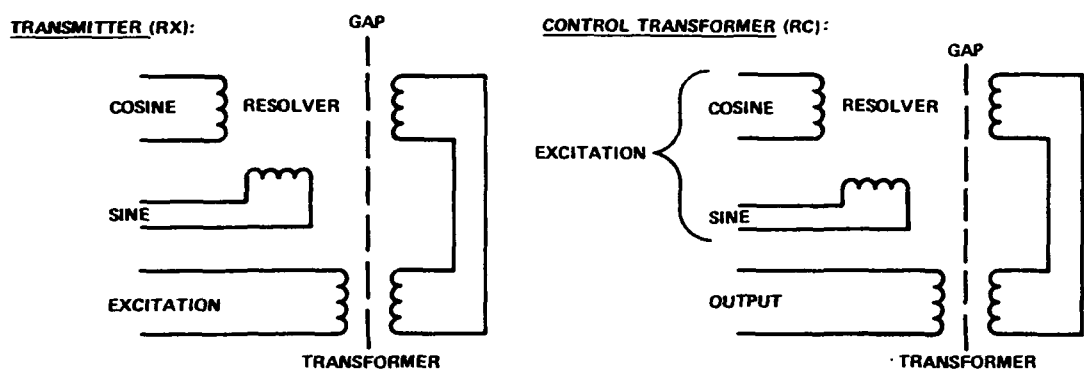


Figure 113
Use as a Transmitter and Control Transformer
with Rotary Transformer for Power Transfer

TABLE 29
ROLL AXIS ANGULAR SENSOR

Parameter	Dimension	
Rotor Inside Diameter	81.8mm (3.22 in.)	
Rotor Stack Height	25.4mm (1.00 in.)	
Rotor Overall Height	38.1mm (1.50 in.)	
Stator Outside Diameter	152.4mm (6.00 in.)	
Stator Stack Height	50.8mm (2.00 in.)	
Stator Overall Height	63.5mm (2.50 in.)	
Radial Gap (per side)	12.1mm (.476 in.)	
DC Resistance		
Rotor	15 ohms	
Stator	22 ohms	
Excitation (Rotor)	<u>7 volts, 2,000 Hz</u>	<u>7 volts, 400 Hz</u>
Input Current	.0375 A	.172 A
Input Power	.031 watts	.50 watts
Z _{RO}	22+j185 ohms	16.4+j37.0 ohms
Z _{SO}	35+j248 ohms	24.6+j49.6 ohms
Z _{SS}	40+j132 ohms	25.6+j26.4 ohms
Transformation Ratio	.7965	.7320
Phase Shift	5°29'	23°2'
Total Null Voltage	4.5 MeV	--
Accuracy	See Table	See Table
Radial Forces	.28 N (.062 LB)*	
Rotational Forces	<4.7 x 10 ⁻⁵ N m (3.5 x 10 ⁻⁵ FT-LB)*	
Leakage Flux	< .01 Gauss*	
Weight	2.77 kg (6.1 LB)	

*As overexcited to 41 volts, 1 A, 400 Hz.

TABLE 30
ROLL AXIS ANGULAR SENSOR
MODEL ACCURACY TEST DATA SUMMARY

Accuracy Test Data Summary				
Excitation Frequency	Quadrature Winding	Type of Calibration	Alignment Conditions	Maximum Errors (Arc Minutes)
2000 Hz	Shorted	Rotor Primary (RX)	Centered	+ .40, - .68
2000 Hz	Shorted	Rotor Primary (RX)	3/4° Angular tilt	+ .51, - .71
2000 Hz	Shorted	Rotor Primary (RX)	5.1mm (.20 in.) Radial Offset	+ .39, - 1.25
2000 Hz	Shorted	Rotor Primary (RX)	6.7 mm (.30 in.) Axial Offset	+ .15, - .90
2000 Hz	Shorted	Stator Primary (RC)	Centered	+ 4.9, - 7.4
400 Hz	Open	Rotor Primary (RX)	Centered	- .9, + 1.7
400 Hz	Open	Rotor Primary (RX)	.75° Angular Tilt	- .9, + 1.7
400 Hz	Open	Rotor Primary (RX)	5.1 mm (.20 in.) Radial Offset	- .4, + 3.2
400 Hz	Open	Rotor Primary (RX)	7.6 mm (.30 in.) Axial Offset	- 1.1, + .9
400 Hz	Open	Stator Primary (RC)	Centered	- 2.3, + 4.6
400 Hz	Open	Stator Primary (RC)	.75° Angular	- 1.8, + 4.4
400 Hz	Open	Stator Primary (RC)	5.1 mm (.20 in.) Radial Offset	- 2.8, + 4.0
400 Hz	Open	Stator Primary (RC)	7.6mm (.30 in.) Axial Offset	- 2.2, + 3.8

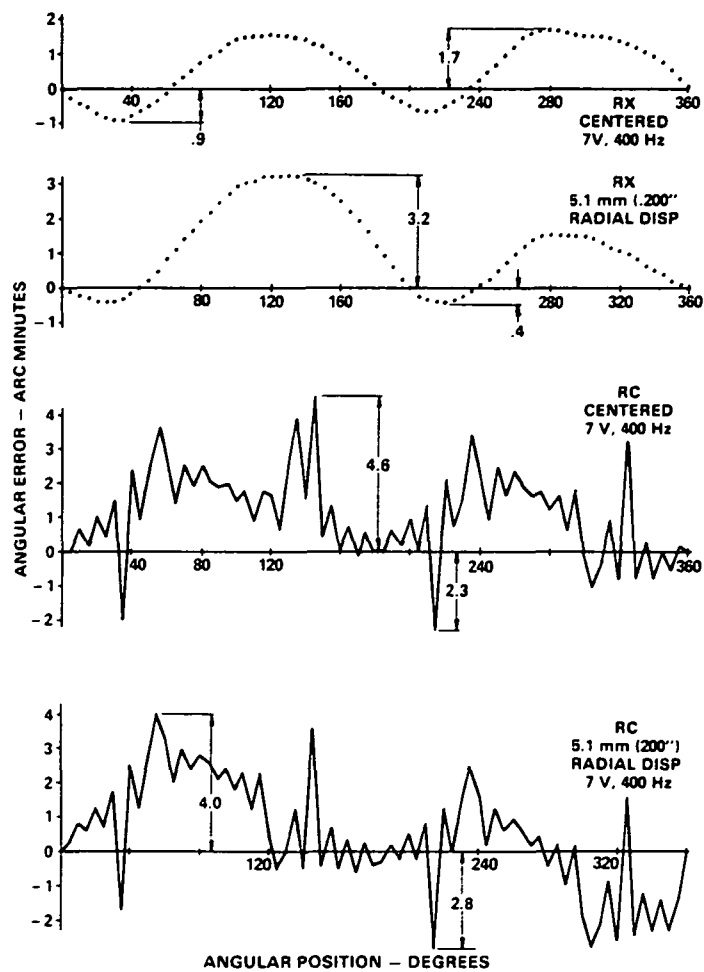


Figure 114
Roll Axis Angular Sensor Model Accuracy Test Data

Referring to Table 28, the unit was approximately three-quarter size with a larger than required air gap. No general performance problems exists, except for the phase shift at 400 hertz excitation where a marginal value of 23 degrees was measured. The final unit will be larger, however, and have a 8.9 mm (.35 in.) air gap which will improve the phase shift to approximately 10 degrees. The radial forces, rotational forces, and leakage flux were so low, the unit was over excited by a factor of 6 to obtain the measured values.

Referring to Table 30, the initial accuracy data obtained with a shorted quadrature winding at 2000 hertz is shown as better than .7 arc minute for RX performance, and 7.4 arc minutes for RC performance with little sensitivity to the ASPS rotor motions. Further testing indicated better accuracy performance was obtainable at 400 hertz with the quadrature winding open, the remaining data was obtained which shows errors of 1.7 arc minutes for RX performance and 4.6 arc minutes for RC performance.

Figure 114 is a plot of some of the 400 hertz data. The accuracy in the RX mode is primarily two cycles as expected for a unit with an open quadrature winding. The accuracy in the RC mode is encumbered by 36 and 4 cycle ripple caused by the nonoptimum lamination tooth combination. Discounting the ripple, the unit appears capable of 2 arc minutes performance with the rotor centered and 3 arc minutes performance over all the translations - consistent with the 6 arc minute system requirements.

Units to be procured for the ASPS hardware will contain optimum lamination teeth combinations and tighter tolerances to improve the performance to the 1 arc minute goal.

6.4 MAGNETIC BEARING ASSEMBLIES (MBA)

6.4.1 Requirements

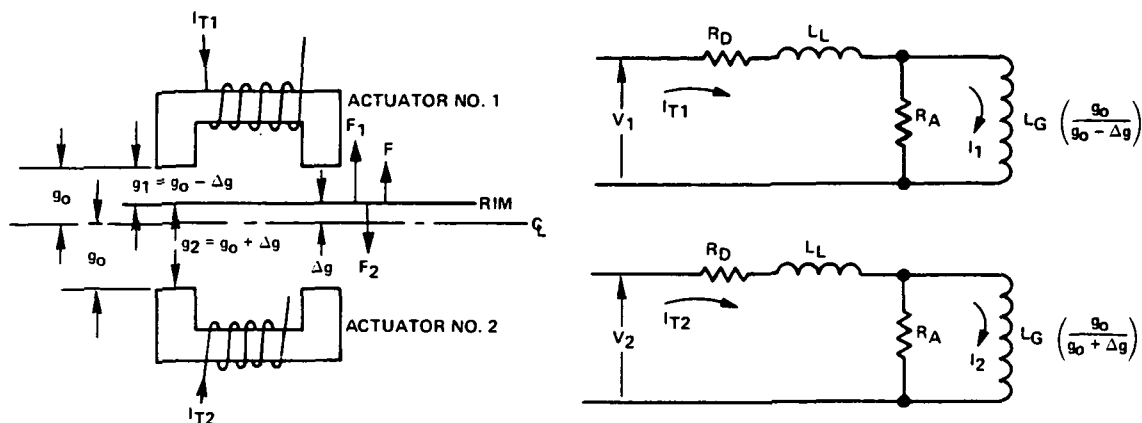
The requirements for the MBAs are contained in Table 31. Two electro-magnet solenoids with a common rotor, not using permanent magnets, are required. Three axial assemblies, each capable of $\pm 28.9\text{N}$ ($\pm 6.5\text{ lb}$) over $\pm 5.6\text{ mm}$ ($\pm .22\text{ in.}$) and two radial assemblies, each capable of $\pm 14.7\text{N}$ ($\pm 3.2\text{ lb}$) over $\pm 5.1\text{ mm}$ ($\pm .20\text{ in.}$) are used. They are operated with current excitation and control laws as shown in Figure 115. As explained in Section 2, these utilize a bias current (I_B) and air gap magnitude compensation to linearize the force characteristic to the form where

$$F = K I_C \text{ where } F \text{ is force}$$

I_C is control current

TABLE 31
MBA STATION REQUIREMENTS

Parameter	Requirements	
Configuration	Two linear solenoids with common rotor. No permanent magnets	
Peak Force per Station	Axial	Radial
Operating Range (From Centered Position)	+28.9N (6.5 LB _f) ±5.6 mm (.22 in.)	±14.2N (3.2 LB _f) ±5.1 mm (.20 in.)
Inductance Variation	< 20:1 over operating range	
Core Loss Resistance	> 10 times copper resistance	
Electrical Configuration	$I_{T1} = (I_B + I_C) \ g_1/g_0$ $I_{T2} = (I_B - I_C) \ g_2/g_0$ $F \propto I_C$	
Bias Current	$I_B = I_{C-MAX}$ For Minimum Peak Power (Symbols are defined in Figure 115)	
Scale Factor	BFSL $F/I_C = TBD \pm 5$ percent	
Linearity	< 1 percent full scale	
Power	< 5 watts standby < 33 watts worst case	



CURRENT CONTROL LAWS:

$$I_{T1} = (I_B + I_C) \frac{g_1}{g_0} \quad g_1 = g_0 - \Delta g \quad I_B = \text{BIAS CURRENT}$$

$$I_{T2} = (I_B - I_C) \frac{g_2}{g_0} \quad g_2 = g_0 + \Delta g \quad I_C = \text{CONTROL CURRENT}$$

FORCE LAW:

$$F = \frac{I_1^2}{2} \frac{d}{dg} \left[L_G \left(\frac{g_0}{a + bg_1} \right) \right] - \frac{I_2^2}{2} \frac{d}{dg} \left[L_G \left(\frac{g_0}{a + bg_2} \right) \right]$$

- g_0 = NOMINAL GAP (M)
- Δg = CHANGE IN GAP (M)
- 1, 2 = (SUBSCRIPTS) IDENTIFY PARAMETERS ASSOCIATED WITH COILS 1 AND 2
- F = FORCE (N)
- V = APPLIED COIL VOLTAGE (VOLTS)
- I_T = COIL CURRENT (AMPERES)
- I = MAGNETIZING CURRENT (AMPERES)
- L_G = MAGNETIZING INDUCTANCE (HENRIES)
- L_L = LEAKAGE INDUCTANCE (HENRIES)
- R_D = DC RESISTANCE (OHMS)
- R_A = AC RESISTANCE (OHMS)

Figure 115
Magnetic Suspension Station Control Law

6.4.2 Candidates

Three candidate configurations were considered as shown in Figure 116a and 116b; an open coil configuration, a partially closed coil or truncated cup core configuration, and a horse shoe configuration.

All the configurations could be designed to meet the force, range, and power requirements so the important criteria for selecting the concept are:

- compatibility with the translational position sensor
- flux leakage and/or coupling to other components
- minimum weight

The open coil configuration - conceived as a potential lower weight candidate, also appears that it will possess the highest flux leakage characteristic. Since the vernier assembly consists of many components, it was assumed the higher flux leakage would lead to component interaction problems and this configuration was therefore dropped from further consideration.

The truncated cup core and horseshoe configurations are each configured with more complete coil enclosures and will therefore provide less component interaction problems.

The truncated cup core and horseshoe configurations were modeled to determine whether either was advantageous with respect to leakage flux or power/weight capability. The test data summary is contained in the following chart:

Parameter	Units	Truncated Cup Core	Horseshoe
Weight	lb	7.15	7.86 (7.15)*
Power for 33.4N (7.5 lb)	watts	57.3	41.3 (49.9)*
Leakage Flux at 76 mm (3 inch)	gauss	20	16

COMPARISON OF HORSESHOE AND TRUNCATED CUP CORE CONCEPT MODELS

*Calculated for a constant weight comparison

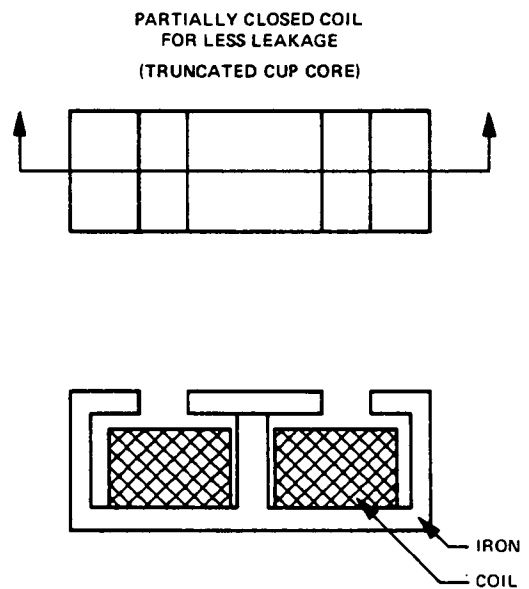
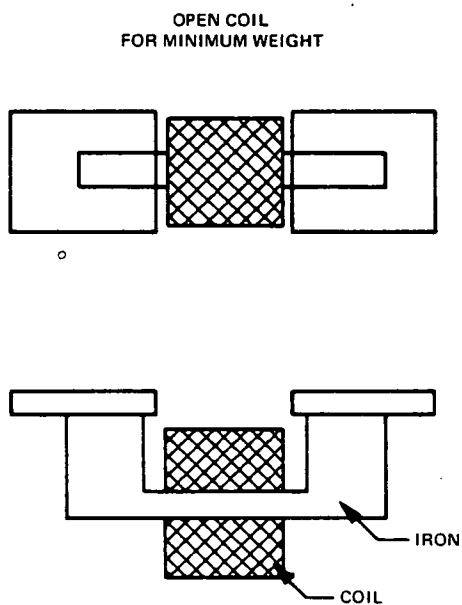


Figure 116a
MBA Configurations Considered

SELECTED:

- SAME LEAKAGE FLUX AS "TRUNCATED CUP CORE" CONFIGURATION
- EASY INTEGRATION WITH POSITION SENSOR
- SAME POWER/WEIGHT CAPABILITY AS OTHER CONFIGURATIONS

HORSESHOE

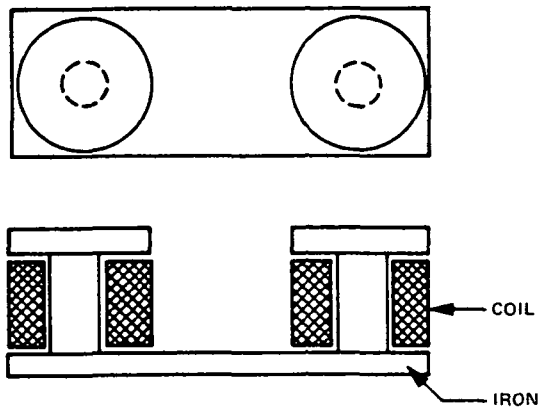


Figure 116b
MBA Configurations Considered

No obvious performance capability is shown for either concept. Although the horseshoe model was slightly heavier with less power dissipated, reshaping could be performed according to the following relationship:

$$\text{weight} \propto \frac{1}{\text{power}}$$

resulting in 49.9 watts losses at 31.8N (7.15 pounds), or 13 percent less losses than the truncated cup core concept. The leakage flux level of the horseshoe concept is also 20 percent less than the truncated cup core concept. Both of these differences are judged to be rather minor however, and the horseshoe concept was eventually selected because the two coil configuration allowed symmetrical placement of the translation position sensor within the bearing assembly into the space between the two coils.

6.4.3 Design Description

The electrical and mechanical descriptions of the MBA designs (radial and axial) are contained in Figures 117, 118, 119.

Both designs use solid iron stator configurations of 50 percent Ni-steel and a rotor material of low carbon steel (Note: a rotor material of 50 percent Ni-steel having better theoretical hysteresis performance, is considered as an option). Each assembly incorporates a translational position sensor in one actuator.

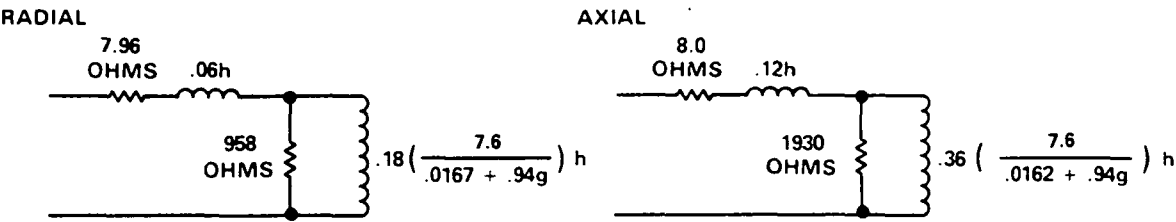
The radial design uses flat surfaces operating against the rotor radii. It was substantiated by analysis that no detrimental effects on linearity are introduced. The axial design uses flat surfaces against a flat rotor.

6.4.4 Model Tests

A station of the preliminary axial suspension design was fabricated for verification of the system concept and electronics design. Component tests to verify design calculations and to search for saturation and hysteresis effects were also performed and are reported here. (Systems test data are presented in Appendix C.)

The preliminary design utilized low carbon steel for both stator and rotor and yielded the force-gap-excitation characteristic of Figure 120. Two data anomalies exist: a hysteresis of seven percent, and a current square law nonconformity of seven percent caused by saturation of the stator piece connecting the two coil posts ("back iron"). The model was subsequently rebuilt with 50 percent Ni-steel in lieu of the low carbon steel, for the rotor and the stator, and with a thicker back iron. The data of Figure 121 was obtained with good hysteresis and current square law conformity. Recognizing the potential difficulty of obtaining a 50 percent Ni-steel rotor, the compromise case of 50 percent Ni-steel stators and low carbon steel rotor was also tested, and the data is shown in Figure 122; hysteresis of 2.5 percent existed.

1. EQUIVALENT CIRCUITS (EACH ACTUATOR)



2. OTHER PARAMETERS

	UNITS	RADIAL STATION	AXIAL STATION
FORCE CAPABILITY	NEWTONS (LBS)	± 14.2 (3.2)	± 28.9 (6.5)
RANGE	MILLIMETERS (IN.)	± 5.1 (.200)	± 5.6 (.220)
FORCE COEFFICIENT ($F = K \frac{i^2}{g^2}$)	$\frac{N \text{ MM}^2}{\text{AMP}^2} \left(\frac{LB \text{ IN.}^2}{\text{AMP}^2} \right)$	649 (.226)	1314 (.458)
BIAS CURRENT	AMPS	0.56	0.57
STANDBY POWER	WATTS	5.1	5.1
PEAK POWER	WATTS	27.1	29.7
CURRENT SQUARE LAW CONFORMITY	%	<1	<1
HYSTERESIS	%	<1	<1

Figure 117
Magnetic Bearing Assemblies Electrical Descriptions

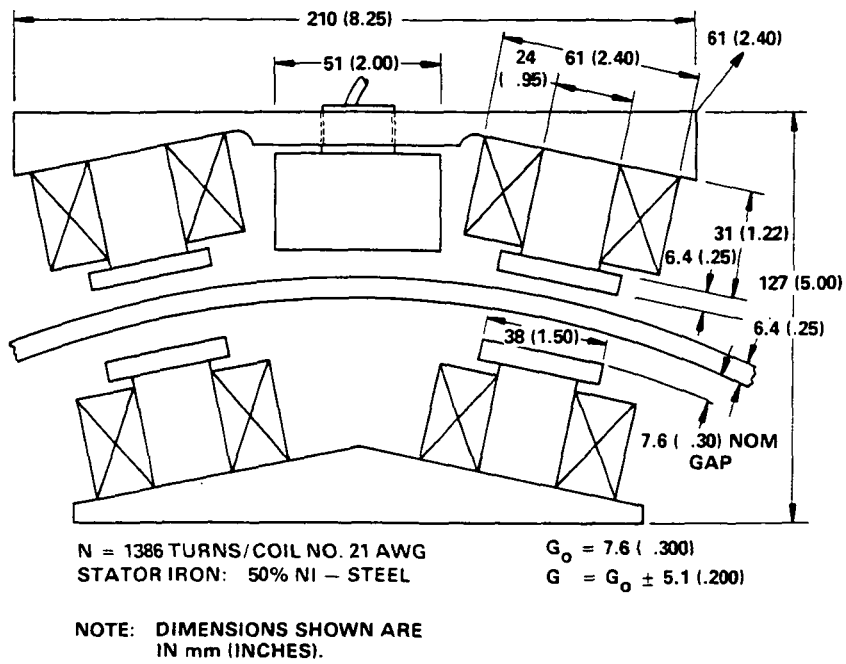


Figure 118
Radial Magnetic Bearing with Sensor
(Full Station)

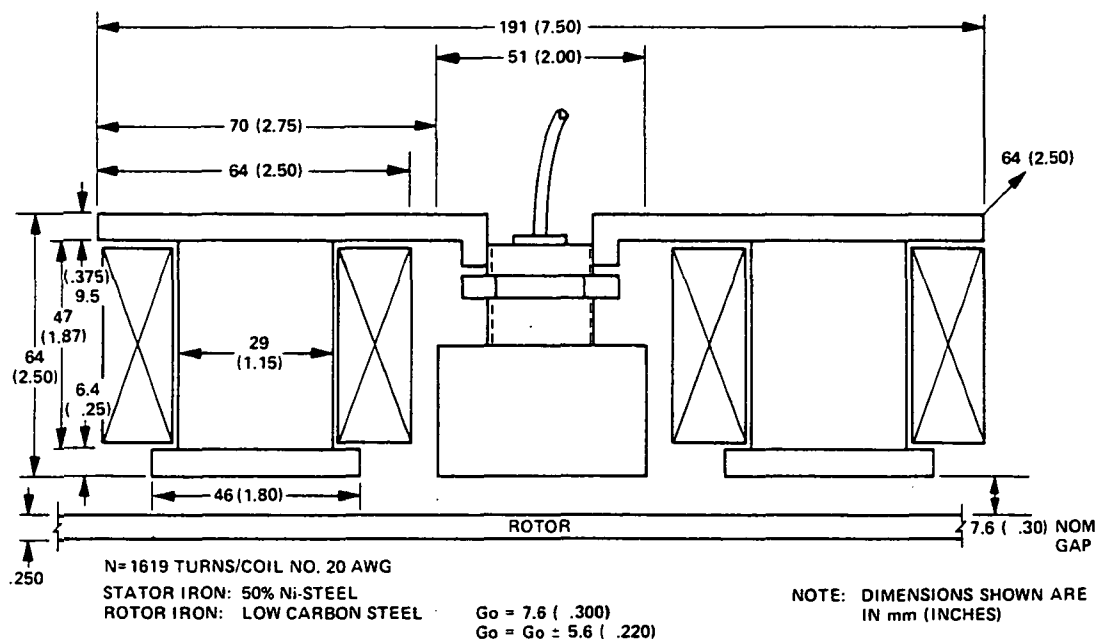
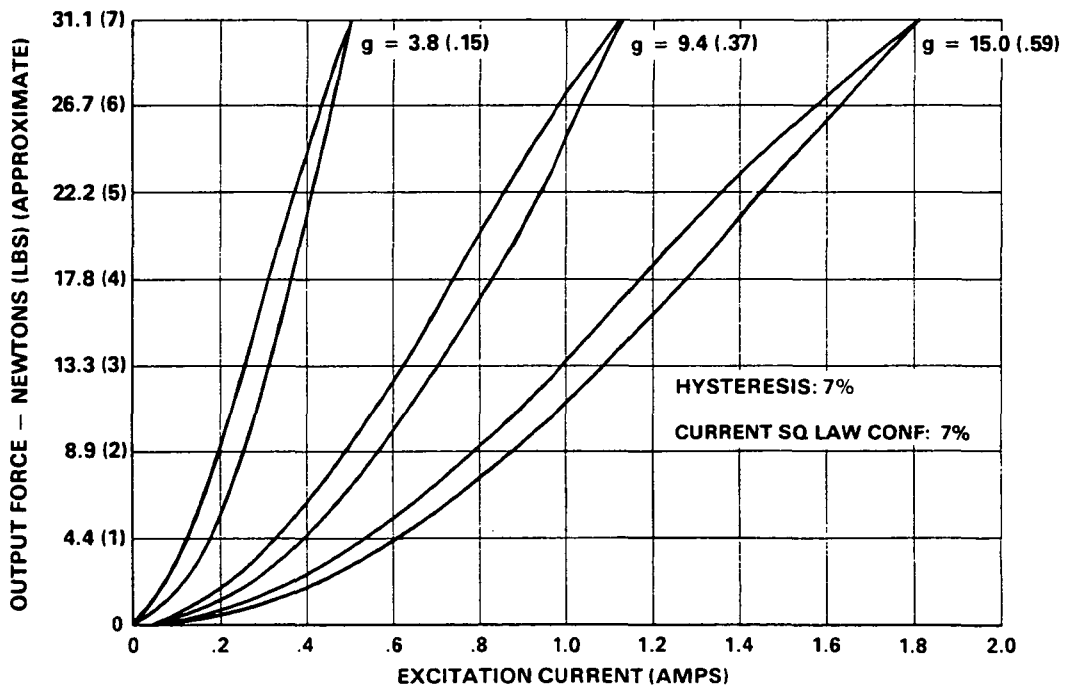
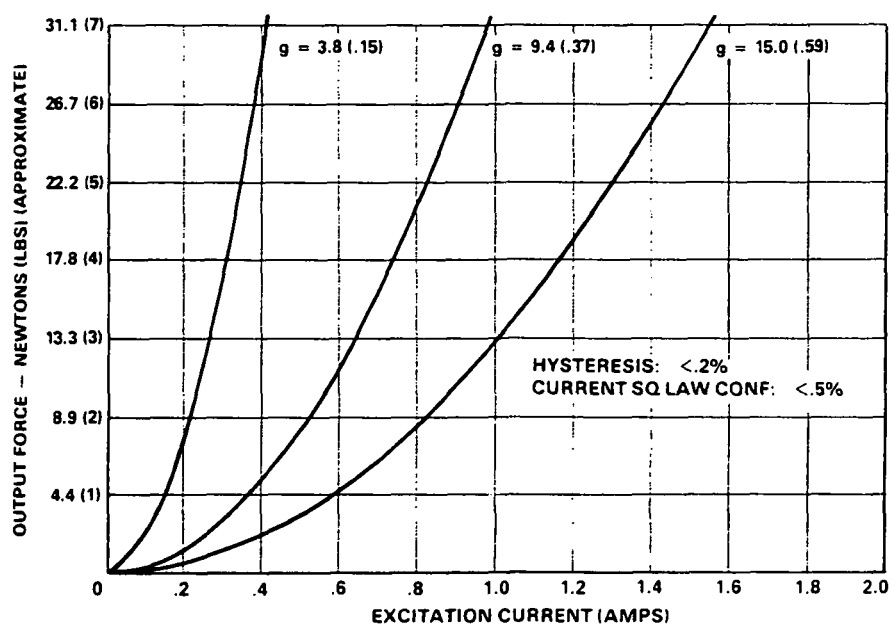


Figure 119
Axial MBA with Sensor
(Half Station)



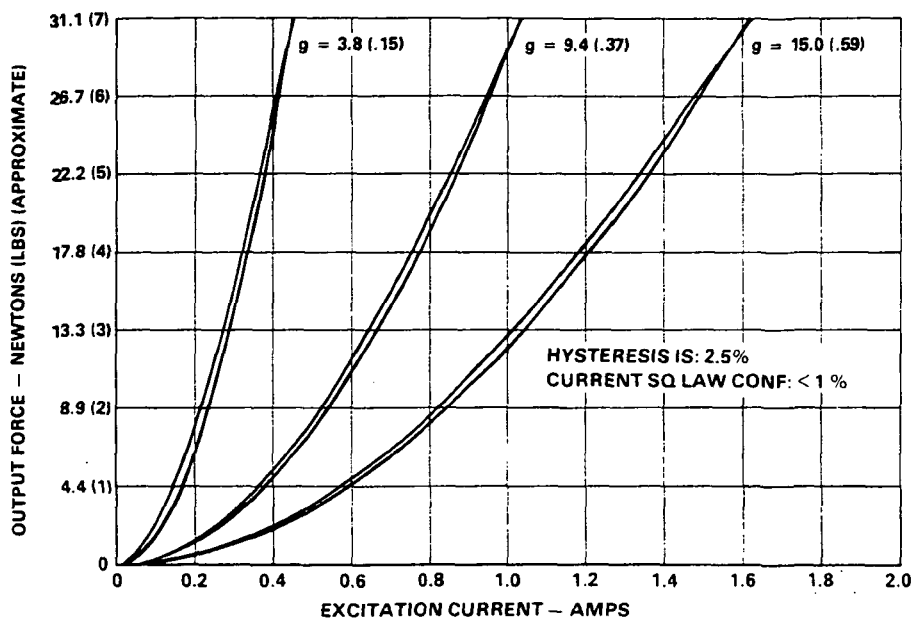
NOTE: g = MAGNETIC AIR GAP IN MM (INCHES)

Figure 120
MBA Model Test Data
Stator: Low Carbon Steel
Rotor : Low Carbon Steel



NOTE: g = MAGNETIC AIR GAP IN MM (INCHES)

Figure 121
MBA Model Test Data
Stator: 50% Ni-Steel
Rotor : 50% Ni-Steel



NOTE: g = MAGNETIC AIR GAP IN MM (INCHES)

Figure 122
MBA Model Test Data
Stator: 50% Ni-Steel
Rotor: Low Carbon Steel

A second configuration option related to hysteresis performance was also identified and explained in Figure 123a and 123b. Dependent upon the polarity connections of the two actuators comprising a magnetic bearing station, the rotor flux can be selected either aiding or bucking. When the rotor flux is aiding, consequent to the operational control law of a bias current with gap compensation, the rotor flux is independent of the force desired or gap existing. Since the flux does not change, no hysteresis should exist. When the rotor flux is bucking, no rotor flux exists in the presence of only bias currents (zero force command), and the rotor flux is proportional to the force command. Figure 123b compares the hysteresis for the two configuration options on a force comparison basis using a carbon steel rotor and 50 percent Ni-steel stators. The hysteresis is reduced approximately six to one in the rotor flux aiding configuration.

From this data, one can also presuppose a second kind of hysteresis. The hysteresis so far discussed occurs only because of changing flux magnitudes in the rotor material. Second variable is the rotor material changing as caused by a roll rotation of the rotor. In that case the flux varies from zero to the maximum level and a four percent hysteresis is expected similar to that measured during the flux bucking test presented in Figure 123b.

6.4.5 Rotor Material Options

Subsequent to the conclusion of the MBA model testing, the highest risk performance parameter recognized is the hysteresis caused by the rotor material. Figure 124 was therefore created to present the trade-offs of low carbon steel, a low cost material, versus 50 percent Ni-steel, a more sophisticated material with significantly lower theoretical hysteresis.

Since the ultimate performance desired is pointing stability, the materials should be compared at operating levels associated with the fine pointing mode. Typical fine pointing MBA force is .08 Newton, less than one percent hysteresis is required to achieve .01 arc second pointing stability. Tests performed in that range resulted in hysteresis measurements of five to seven percent independent of the rotor material, and attributed to the test fixture. Since fine pointing does not take place simultaneous with roll slewing, it was concluded that the dynamic hysteresis characteristics should not be a significant factor in the rotor material selection.

The trade-off therefore breaks down to

- a) the 50 percent Ni-steel costs significantly more - \$31K versus \$.5K for material only
- b) the 50 percent Ni-steel has much less material hysteresis

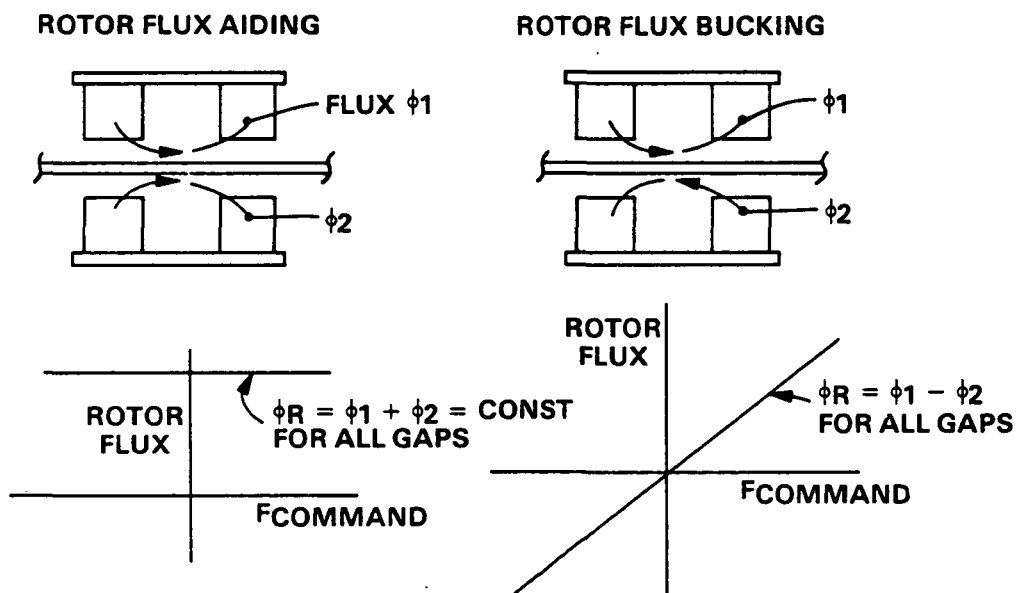


Figure 123a
Rotor Flux Options

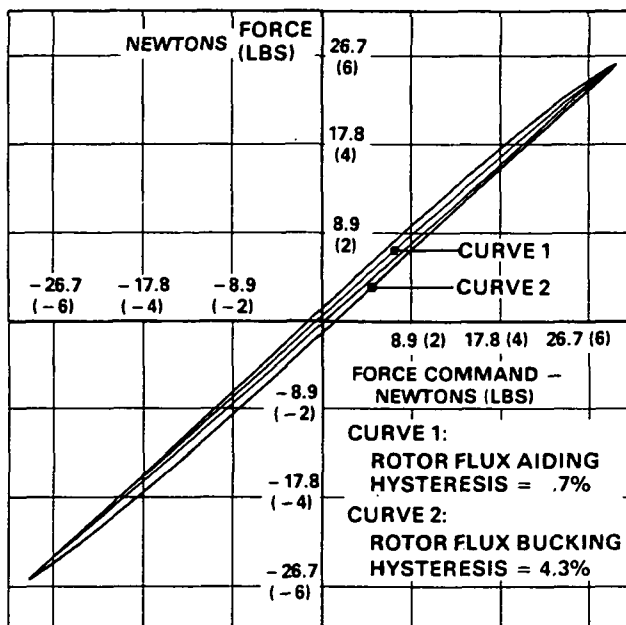


Figure 123b
 Hysteresis Versus Rotor Flux Polarities

	ROTOR MATERIALS	
	LOW CARBON STEEL	50% NI-STEEL
MATERIAL COST (MINIMUM ORDER)	\$5K	\$31K
SATURATION FLUX DENSITY	19K GAUSS	16K GAUSS
AVAILABILITY	2 WEEKS	12 WEEKS
HYSTERESIS OF ACTUATOR WITH CONSTANT ROTOR FLUX CONTROL LAW		
STATIC		
FOR $\pm 28.9\text{N}$ (6.5 LB)	.7% (TEST)	< .2% (TEST)
FOR $\pm 2.7\text{N}$ (.6 LB)	< 3.4% (TEST) *	< 5.3% (TEST) *
FOR $\pm .27\text{N}$ (.06 LB)	< 4.8% (TEST) *	< 6.6% (TEST) *
FOR $\pm .027\text{N}$ (.006 LB)	< 6.5% (TEST) *	< 5.9% (TEST) *
DYNAMIC (ROLL MOTIONS)	4% (PREDICTED)	< .2% (PREDICTED)

(TEST RESOLUTION .2%)
 HYSTERESIS REQUIRED TO BE
 < 1% IN THIS RANGE FOR .01 ARC
 SEC POINTING STABILITY
 VERNIER POINTING ASSUMES
 CONSTANT ROLL ANGLE

*ATTRIBUTED TO TEST FIXTURE

Figure 124
Rotor-Material Trade-off

6.5 POSITION SENSORS

6.5.1 Requirements

The requirements for the position sensors are as follows:

Range: Linear; ± 7.62 mm (.300 inch)

Accuracy: $\pm .076$ mm (.003 inch)

Bandwidth: 100 Hz minimum

Type: Adaptable to a large diameter annulus. No contact to the annulus.

6.5.2 Candidates

The initial criteria for selecting sensors is related to type. To be adaptable to the large diameter annulus and maintain the design intent of the application which requires no contact to the annulus, it is necessary that the sensor rotor be passive and not require any contacts. Three physical principles, as shown in Figure 125, are known which can be designed to satisfy these conditions: capacitive, inductive, and optical.

6.5.2.1 Optical Transducer

Two types of optical displacement transducers are recognized.

1. One type utilizes a fixed photoconductive potentiometer sensing element as depicted in Figure 126. It consists of a high-resistance potentiometer connected to the end terminals, low-resistance strips connected to the collector lead and photoconductive strips joining the low and high resistance elements. Light activates the photoconductive strips and electrically connects the collector to the respective positions of the high-resistance potentiometer. A displacement transducer arrangement is shown in Figure 127 whereby motion of the reflector causes motion of the light impingement on the potentiometer.

2. A second transducer type is a laser interferometer system shown in Figure 128. As the reflector on the to-be-measured object is displaced, an interference fringe is seen by the photodetector for each quarter of a laser wave length. The output of the photodetector is fed to a bidirectional counter which displays the fringe count or can be converted to a distance display.

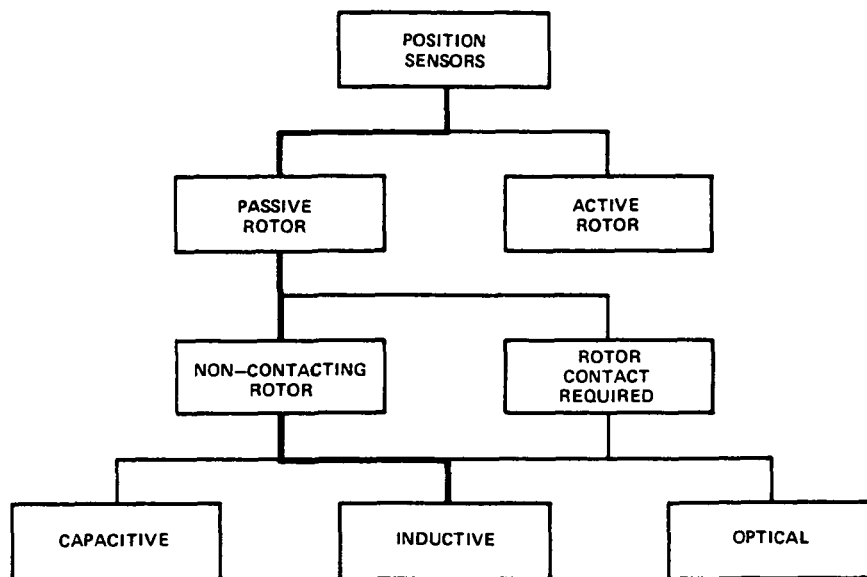


Figure 125
Position Sensor Classifications

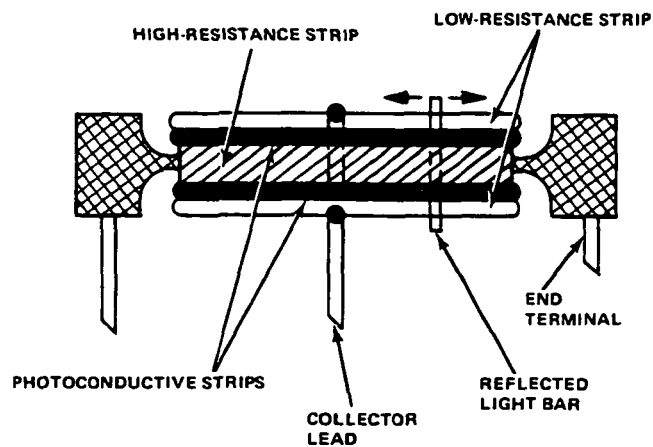


Figure 126
Photoconductive Potentiometer

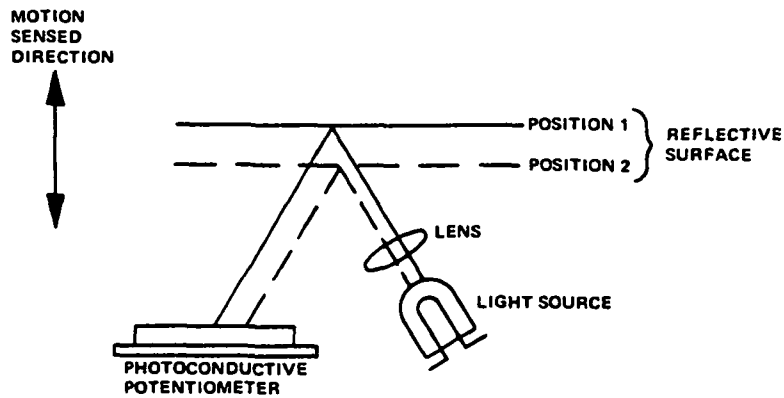


Figure 127
Photoconductive Potentiometer Transducer System

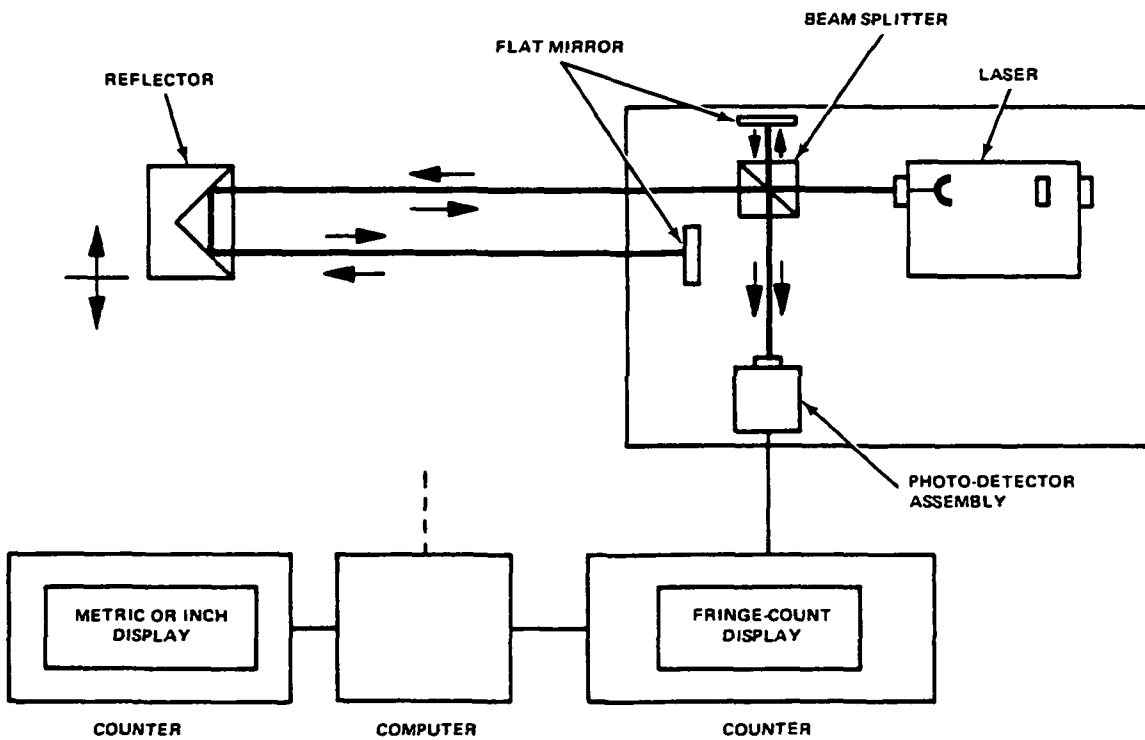


Figure 128
Laster Interferometer System

6.5.2.2 Capacitive Transducers

The capacitive transducer, Figure 129 consists of two stationary capacitor plates with an intermediate plate attached to the to-be-measured portion. This arrangement results in two capacitors which can be connected differentially so that, as shown in Figure 129, for an upward displacement, C1 will increase in capacitance and C2 will decrease in capacitance. Capacitive transducers are usually used for small range .122 to 2.54 mm applications. For longer range transducers, plate size to maintain adequate sensitivity becomes prohibitive.

6.5.2.3 Inductive Transducers

The inductive transducer consists of a coil of wire oriented so its induced field couples the surface to be measured. The coil impedance then becomes related to the position of the sensed surface. the surface to be sensed, or target area, may be either a conductor, whereby the device operates on the eddy current principle, or it may be ferromagnetic, which operates on the reluctance principle. Figure 130 shows an inductive transducer and a typical output conversion circuit.

Commercially available probes exist with ranges up to 63.5 mm (2.5 in.). The longer the range, however, the larger the probe face size.

6.5.3 Concept Selection

The inductive transducer has been selected for this application for the following reasons:

- The inductive sensor functions over an area, rather than a point or a line source, and thus averages out target surface anomalies and minimizes sensitivities to extraneous motions.
- The device integrates easily into the ASPS whereby identical sensors can be used for all sensing applications - radial MBA, axial MBA, roll motor control.
- Commercial devices, of relatively low cost and capable of meeting ASPS performance requirements exist, eliminating development cost and schedule risks.

The final design is described in Table 32 as operated from vendor supplied electronics.

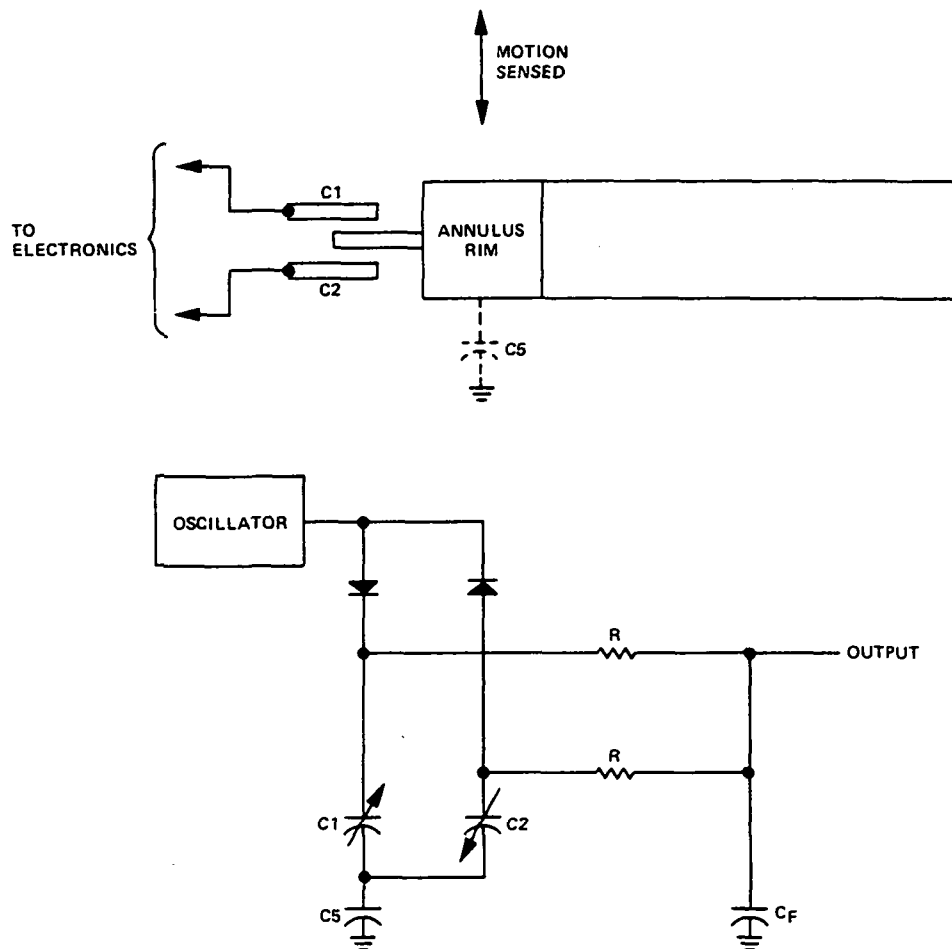


Figure 129
Differential Capacitor Transducer

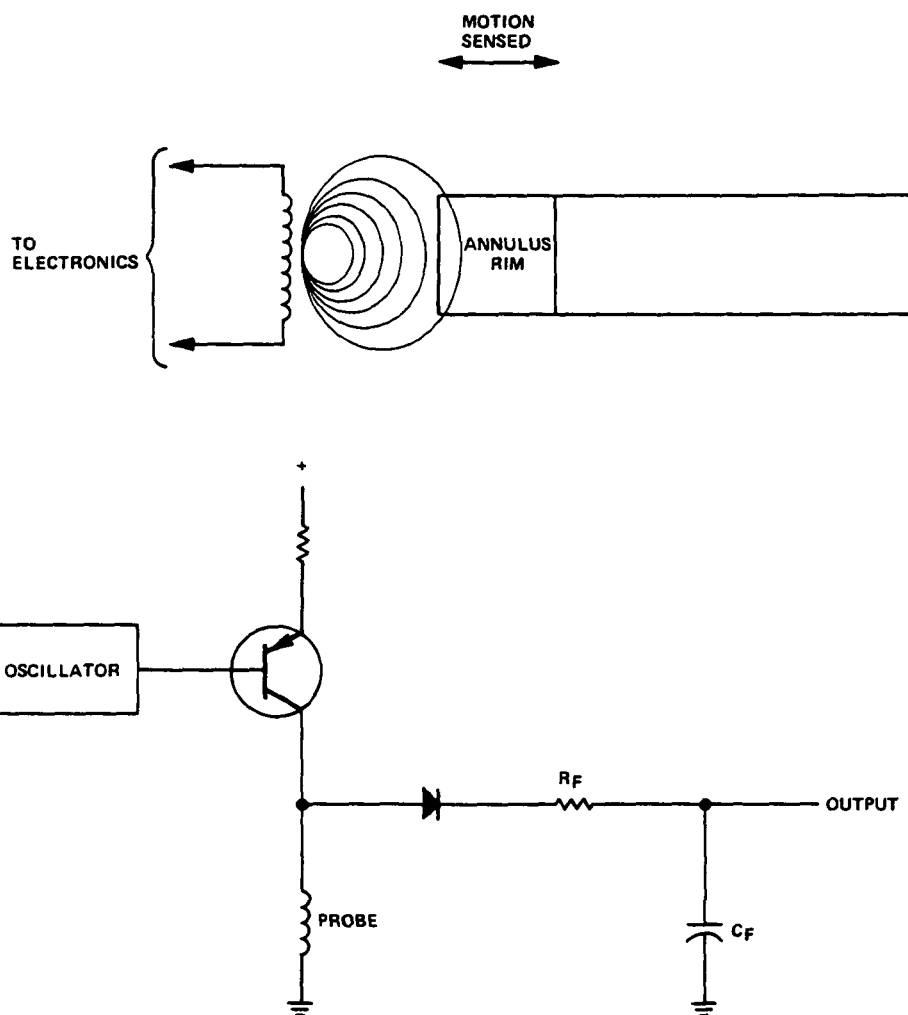
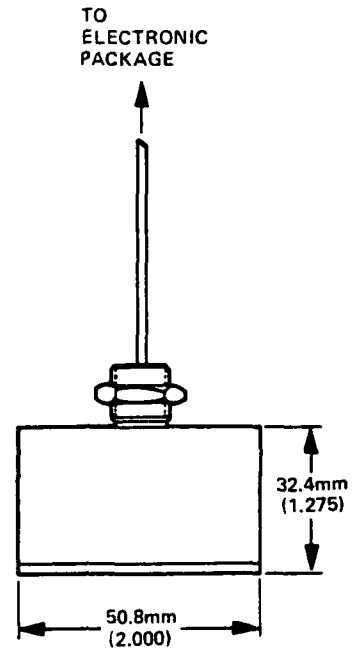


Figure 130
Inductive Transducer

TABLE 32
SELECTED SENSOR DESCRIPTION AND OUTLINE

PARAMETER	DESCRIPTION
RANGE:	25.4mm (1.01 IN)
LINEARITY:	<.2 PERCENT FULL SCALE
BANDWIDTH:	20 KHz
REPEATABILITY:	.05%
NOISE:	<.3 MILLIVOLTS
SENSITIVITY:	ADJUSTABLE UP TO .254V/M (10V/INCH)
OPERATING TEMP RANGE:	-55° C TO +75° C
INPUT POWER:	±12 VDC, 70 MA
SENSOR DIMENSIONS:	
OUTER DIAMETER:	50.8mm (2.000 IN.)
LENGTH:	32.4mm (1.274 IN.)
VENDOR:	KAMAN SCIENCES CORPORATION
TARGET MATERIAL:	NICKEL



6.5.4 Development Tests

In conjunction with the MBA model testing, a position sensor was necessary. Subsequent evaluation identified two sensing errors as shown in Figure 131. The top error curve is the calibration error when using the vendor supplied electronics. It essentially verifies .25 percent accuracy for a 25 mm (1.0 in.) range unit. The bottom error curve exists because the unit is integrated into the MBA and indicates an error exists related to the excitation current flowing in the magnetic bearing actuator. The dashed error curves are test data with no additional shielding around the position sensor. Additional shielding then reduced the error to that shown in the solid lines where at half force and half displacement, less than .025 mm (.001 in.) error exists. The shield used in these tests consisted of two concentric cylinders around the proximeter head. The inner cylinder was aluminum, .5 mm (.020 in.) thick and the outer cylinder was 80 percent Ni-steel, .6 mm (.024 in.) thick.

6.5.5 Design Notes and Trade-offs

6.5.5.1 Target Material and Size

Conductive targets tend to reduce the impedance of the transducer coil because eddy currents are set up in the target to oppose the field that created them. Conversely, targets of magnetic materials tend to increase the transducer coil impedance by presenting the field a low-reluctance path. The more conductive the target material, the more impedance is reduced; and the more permeable the target, the more the impedance is increased. Figure 132 shows relative output capability for various materials. The target for the position sensors will be the low-carbon-steel rotor shared by the MBAs and roll motor. To enhance position sensor performance, however, the rotor will be plated with .076 mm (.003 in.) thick nickel. The nickel plating enhances performance in two ways:

1. The relative output, as shown in Figure 132, doubles.
2. The low carbon steel is not as homogeneous as the nickel and would add an additional error as roll motions present a variable target.

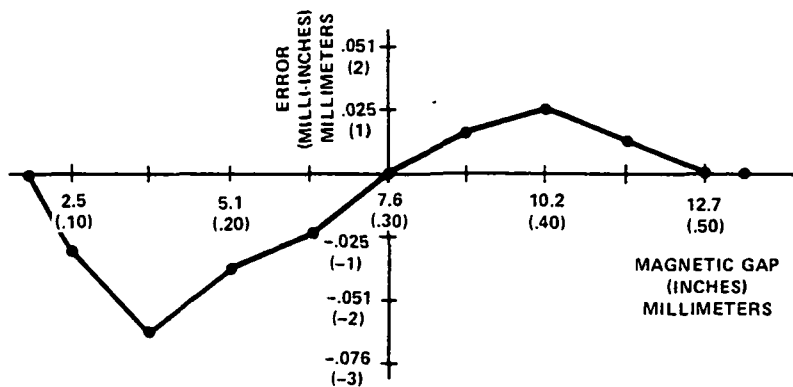
The target width is selected such that the transducer continues to be covered under conditions of maximum offset motion.

6.6 COARSE GIMBAL COMPONENTS

The coarse gimbals, to be controlled by position loops, each require an actuator (torque motor) and a position sensor. In addition, consequent to the selection of a brushless dc motor as the actuator, a commutation position sensor is also required.

Conventional, state-of-the-art components were desired.

CALIBRATION ERROR:



ERROR FROM MBA EXCITATION:

(ONLY OCCURS WITH EXCITATION THROUGH ONE ACTUATOR)

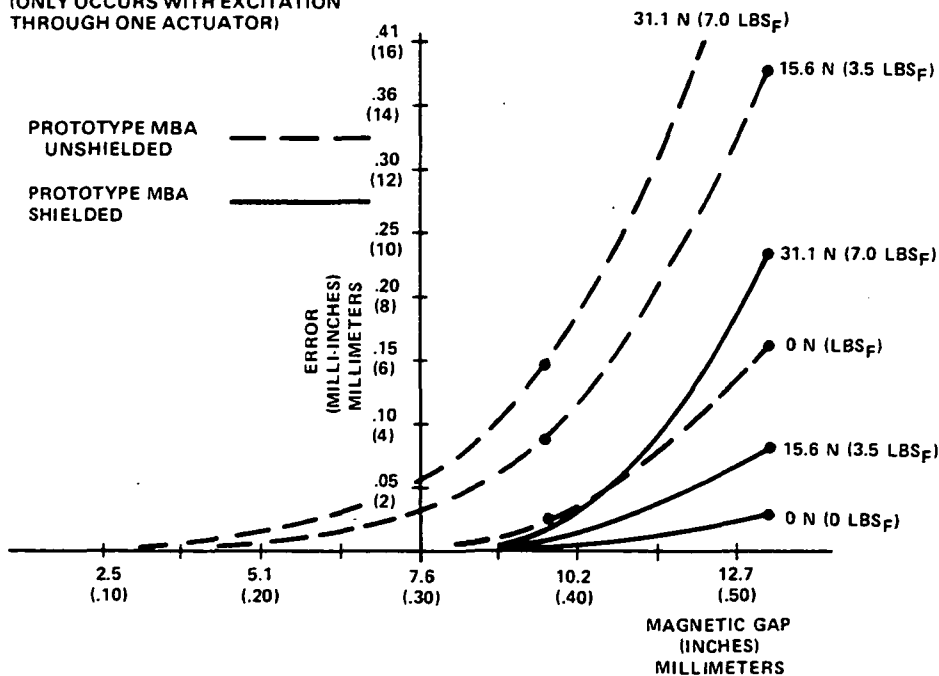


Figure 131
Position Sensor Errors

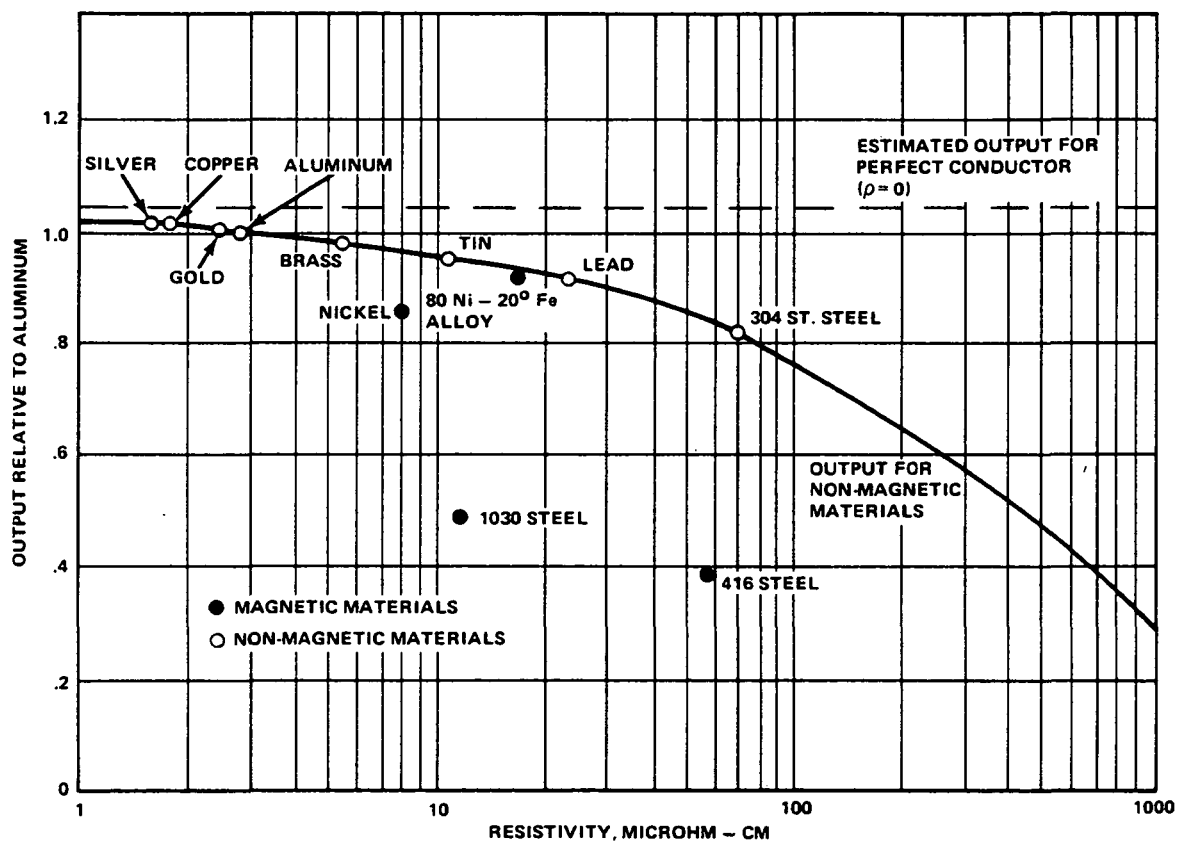


Figure 132
Relative Sensor Output Capability for
Various Rotor Materials

6.6.1 Torque Motor

The preliminary torque motor requirements are shown in Table 33. The principal requirement, peak torque, is determined by the experiment inertia and the gimbal acceleration desired. In addition, it was desirable to minimize the motor outer diameter and maximize the motor inner diameter. As the motor outer diameter increases, the ASPS overall height increases and the distance to the experiment center of gravity increases which results in a larger torque requirement. The motor inner diameter must be large enough to allow coaxial placement of the flex lead capsule.

TABLE 33
COARSE GIMBAL TORQUER PRELIMINARY REQUIREMENTS

Parameter	Requirements
Peak Torque	± 33.9 N m (25 FT-LB)
Max Rate	± 10 Deg/Sec
Angular Range	± 110 Degrees
Torque Ripple	< 5 percent
Anomaly Torques	< 1.35 N m (1 FT-LB)
Peak Power	< 200 watts

It was initially thought that a conventional brush-type dc motor would be adequate for the application. The performance was adequate and an off-the-shelf design would be the best economical choice. The large diameters of applicable off-the-shelf components, however, seriously impacted the ASPS system height and it was determined a special smaller diameter unit would be required at considerable higher cost. Brushless dc motors thus became cost competitive, and were therefore considered and eventually selected for the final design.

The brushless dc motor offers several advantages over the brush-type motor. These advantages are:

- No brushes: Brushes present a life limiting aspect inherently reducing the reliability. They also increase drag torques and degrade system resolution capability.

- Redundancy: The brushless dc motor offers a unique redundancy capability. Large motors of this type are usually wound with very few turns and multiple turns in hand as depicted in Figure 133. By separately terminating one of these conductors, an alternate excitation scheme is provided which can be utilized to allow manual torquing of the coarse axes in the event of other system failures.
- Failure Modes: Off-the-shelf brush motors, of this large size, do not have Samarium Cobalt magnets. The brushless dc motors can be designed with Samarium Cobalt rotor magnets eliminating demagnetization as a single point failure mode.

Table 34 summarizes the trade-offs for the final design selection. Compared are two off-the-shelf brush type designs, where the outer diameters were too large, and two brushless dc designs. One brushless dc design uses a non-optimized existing lamination and thus avoids a large nonrecurring cost while the other utilizes an optimum new lamination to show the penalty of using the existing lamination. The comparison is performed at approximately equal power dissipation for the required torque levels of 34 N m (25 ft-lb) for the elevation axis and 27 N m (20 ft-lb) for the lateral axis. Since it is expected that a special brush type design would cost approximately \$10K, usage of the brushless dc motor with the existing lamination is justified by the similar cost, lighter weight, and better performance. A penalty of 2.27 kg (5 pounds) is incurred for not optimizing the lamination. A further power/weight trade-off was then performed by varying the lamination stack length. The values in square brackets represent the final motor selection.

Table 35 describes the torque motor selected. Despite slightly different requirements for the lateral and elevation axes, identical units are planned to minimize cost and allow interchangeability.

6.6.2 Position Sensor and Commutation Sensor

The principle requirements of the position sensor are that it physically integrates into the gimbals easily, interfaces with the necessary electronics easily, and is accurate enough to provide state-of-the-art coarse positioning:

A single-speed resolver was selected for the following reasons:

- Proven reliability in space
- The pancake form is readily adaptable to the gimbal structures with a wide range of off-the-shelf sizes available.
- The single-speed analog signals are easily interfaced by electronics.
- State-of-the-art accuracy of one arc minute results in an adequate system accuracy of six arc minutes.
- The commutation sensor can be obtained on an identical lamination stack, enabling a balanced mechanical system design.

Tables 36 and 37 describe the selected position and commutation sensors.

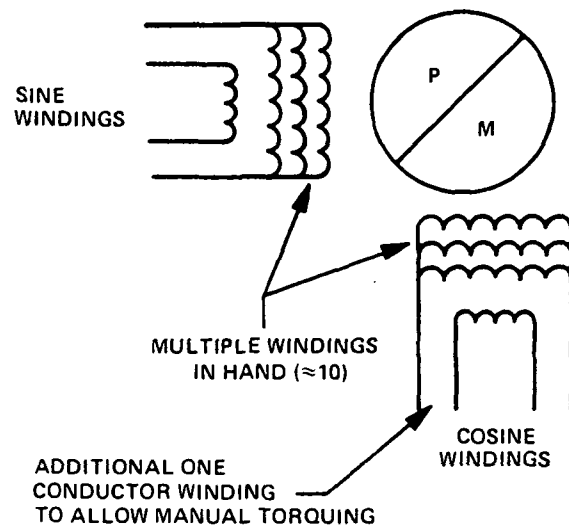


Figure 133
Coarse Torquer Redundancy

TABLE 34
COARSE TORQUER CANDIDATES

Parameter	Brush Type Designs		Brushless DC Design		Units
	No. 1	No. 2	Existing Lam	Optimum Design	
Outer Diameter	226 (8.9)	305 (23)	191 (7.5)	191 (7.5)	mm (inch)
Weight	11.3 (25)	7.7 (17)	9.3 (20.6)[11.3(25)]	15.4	KG (LBS)
Power for 27.1 N m (20 FT-LB)	150	144	146 [110]	146	watts
Power for 33.9 N m (25 FT-LB)	234	224	226 [169]	226	watts
Figure of Merit*	.065	.098	.082 [.078]	.107	$\frac{\text{Ft}}{\sqrt{\text{watt}}}$
Approximate Cost	5K ea	5K ea	10K ea	14K ea	Dollars
System Resolution Capability (Pulse Response)	85	85	99	99	Percent

*Figure of Merit = K_M/W

where $K_M = \text{Torque} / \sqrt{\text{Power}}$

(Ft-lb)/($\sqrt{\text{watt}}$)

and W = Weight (Lb)

↑
[SELECTED DESIGN]

- No Brushes
- Better System Performance
- Smaller Diameters

TABLE 35
COARSE GIMBAL TORQUER DESCRIPTION

PARAMETER	DESCRIPTION
TYPE	BRUSHLESS, DC, PERMANENT MAGNET, 2 PHASE, REDUNDANT
POLES	24
WEIGHT	11.3 Kg (25 LBS)
PEAK TORQUE	33.9 NM (25 FT-LBS)
MAXIMUM RATE	± 10 DEG/SEC
ANGULAR RANGE	± 360 DEGREES
POWER FOR PEAK TORQUE	200 WATTS MAXIMUM
PEAK EXCITATION	17 VOLTS PER PHASE
TORQUE SENSITIVITY	1.79 NM (1.32 FT-LBS)/PK AMPERE
DC RESISTANCE	0.55 OHMS/PHASE
WINDING INDUCTANCE	2.0 MILLIHENRIES/PHASE
RIPPLE TORQUE	<2.0% 0-PK
COGGING TORQUE	.18 NM (.12 FT LBS)
HYSTERESIS TORQUE	.88 NM (.65 FT LBS)
STATOR MATERIAL	VANADIUM PERMENDUR
ROTOR MATERIAL	SAMARIUM COBALT

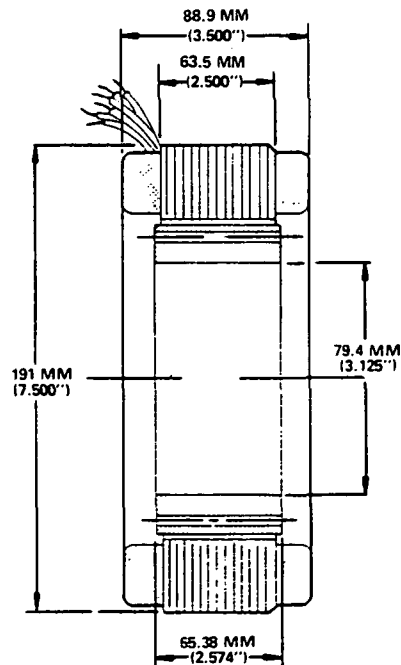


TABLE 36
COARSE GIMBAL POSITION RESOLVER

PARAMETER	REQUIREMENT
TYPE	SINGLE SPEED, SINE-COSINE RESOLVER (ROTOR & STATOR)
EXCITATION (ROTOR)	7 VOLTS (RMS), 2000 Hz
INPUT CURRENT	0.060 AMP MAX
INPUT POWER	0.040 WATT MAX
IMPEDANCES Z_{RO} Z_{SS}	120 OHMS MINIMUM 500 OHMS MAXIMUM
TRANSFORMATION RATIO	1.000
PHASE SHIFT	5 MAX DEGREES
ACCURACY RESOLVER TRANSMITTER(RX) RESOLVER CONTROL TRANSFORMER(RC)	1 ARC MINUTE, MAX 1 ARC MINUTE, MAX
WEIGHT	0.45 Kg (1.0LB), MAX

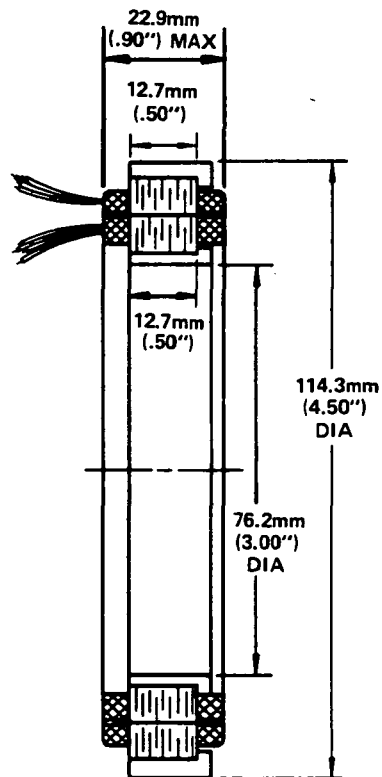
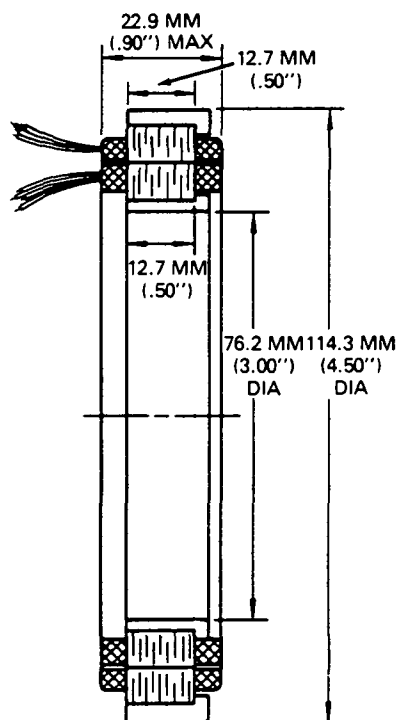


TABLE 37
COARSE GIMBAL COMMUTATING RESOLVER

PARAMETER	REQUIREMENT
TYPE	24 POLE (12 SPEED), SINE-COSINE RESOLVER
EXCITATION (ROTOR)	7 VOLTS (RMS), 2000 H _Z
INPUT CURRENT	0.060 AMP MAX
INPUT POWER	0.040 WATT MAX
IMPEDANCES Z_{RO} Z_{SS}	120 OHMS MINIMUM 500 OHMS MAXIMUM
TRANSFORMATION RATIO	0.250
PHASE SHIFT	10 MAX DEGREES
SINE AND COSINE WAVE SHAPE DISTORTION	2% MAX
WEIGHT	0.45 Kg (1.0 LB) MAX



Page Intentionally Left Blank

SECTION 7.0

ASPS THERMAL ANALYSIS

7.1 MODEL DESCRIPTION

A preliminary thermal analysis of the ASPS was performed to assess the severity of the in-orbit thermal control problem, and to evaluate the sensitivity of ASPS component temperatures to candidate thermal control system parameters such as heater power, surface properties, ambient temperature of surrounding structure, etc. While resulting temperatures are given for both hot and cold orbit conditions, it must be emphasized that these results are based on a very simplified model (15 modes), and that a much more detailed analysis is required to establish confidence in the required thermal control system.

The orbital conditions used were based on the worst-case environments of Orbital Flight Test Mission 4 (OFT-4). Hot and cold case extremes are as shown in Figure 134. The assumed ASPS orientation is straight "up" (pointing directly out of the payload bay). The model assumed Multilayer Insulation (MLI) covering of the ASPS in three sections. The nodes selected for the analysis are indicated in Figure 135 and defined below:

Node Number	Description
0	Pallet and pallet integration structure
1	Elevation gimbal bearings
2	Stator elements of elevation gimbal
3	Stator elements of lateral gimbal
4	Lateral gimbal bearings
5	Vernier base plate and vernier stator elements
6	Optical coupler housing and stator elements including rotary transformer
7	Batteries
8	Vernier rotor
9	Payload mounting plate
10	Payload
11	Outer layer of MLI covering elevation gimbal stator
12	Outer layer of MLI covering lateral gimbal stator
13	Outer layer of MLI cover vernier base plate
14	Deep space

(OFT-4)

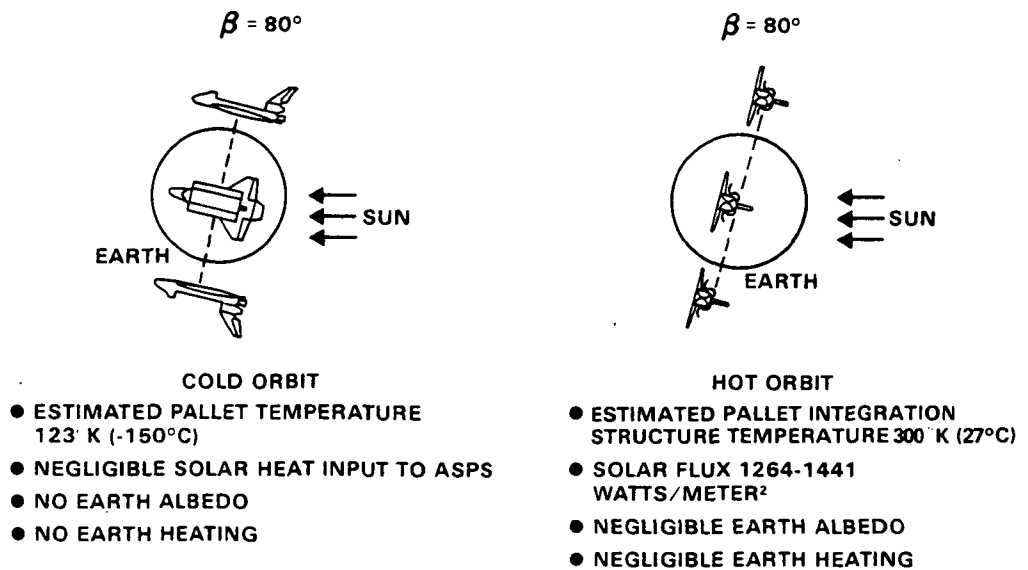


Figure 134
ASPS Orbital Thermal Environment

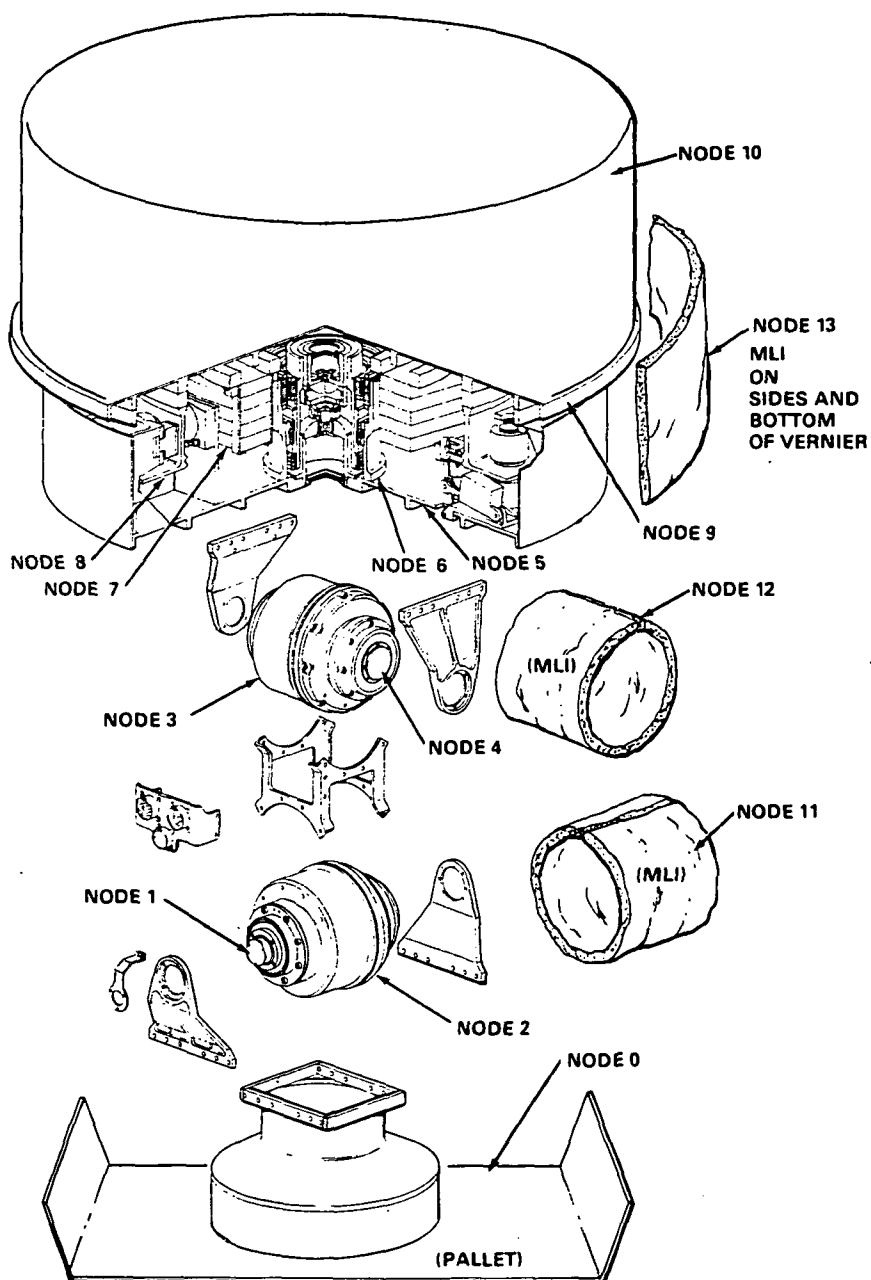


Figure 135
ASPS Thermal Mode Nodal Breakdown

The thermal model used is described by the set of differential equations:

$$C_i \frac{dT_i}{dt} = \sum_{j=0}^N \frac{1}{R_{ij}} (T_j - T_i) + \sum_{j=0}^N K_{ij} (T_j^4 - T_i^4) + P_i + S_i \quad (22)$$

where the subscripts i and j identify the nodes (between 0 and N) and

C_i = Thermal capacity of node i (watt-sec/degrees kelvin)

T_i = Temperature of node i (degrees kelvin)

t = Time (seconds)

R_{ij} = Thermal resistance between nodes i and j (K/Watt)

K_{ij} = Radiation constant between nodes i and j (Watts/K⁴)

P_i = Power dissipated in node i (Watts)

S_i = Solar input to node i (Watts)

N = Number of nodes = 14

7.2 MODEL PARAMETERS

Thermal capacities of the ASPS nodes were calculated from the weight and heat capacitance of the material corresponding to each node. The values of each of the 13 ASPS nodes are given in Table 38.

Thermal resistances between all of the contacting nodes were calculated from the cross-sectional area, mean path length, and conductivity of the material between nodes. Nominal values are listed in Table 39 for all contacting nodes.

The radiation constants between nodes were calculated from the grey body shape factors, radiation areas, and emissivities estimated for each surface. Nonzero nominal values are given in Table 40. Multilayer Insulation (MLI) was modeled as a separate node corresponding to the outermost blanket layer. The solar absorptivity (α_s) and emissivity of this surface were taken to be .15 and .73, respectively, which corresponds to the nominal characteristics of beta cloth. An equivalent resistance was calculated between the outer layer and the underlying structure which is representative of this type of material.

Internal power dissipation included in the model include that consumed by the magnetic bearings, the payload, and heater power. Gimbal torquer and roll motor power were neglected under the assumption of a low duty cycle for slewing. Table 41 contains the nominal values for the nodal power dissipation.

TABLE 38
NOMINAL THERMAL CAPACITANCES

Node Number, i	Thermal Capacity, C_i (Watt-Seconds/K)
1	167
2	11049
3	11049
4	167
5	13984
6	626
7	17430
8	13548
9	10436
10	23504
11	.79
12	.79
13	6.87

TABLE 39
NOMINAL THERMAL RESISTANCES

Conducting Nodes, i j	Resistance, R_{ij} (K/Watt)
0 to 1	7.36
1 to 2	2.87
2 to 11	776.
2 to 3	7.06
3 to 4	2.87
3 to 12	776.
4 to 5	.081
5 to 13	1.786
7 to 9	.057
8 to 9	.084
9 to 10	.005
5 to 6	.579

TABLE 40
NOMINAL RADIATION CONSTANTS

Radiating Nodes, i j	Radiation Constant, K _{ij} (Watts/K ⁴)
5 to 8	.36 x 10 ⁻¹⁰
5 to 9	4.52 x 10 ⁻¹⁰
6 to 7	.05 x 10 ⁻¹⁰
7 to 8	.19 x 10 ⁻¹⁰
10 to 14	5.63 x 10 ⁻⁸
11 to 14	.41 x 10 ⁻⁸
12 to 14	.41 x 10 ⁻⁸
13 to 14	3.64 x 10 ⁻⁸

Note: Emissivity of MLI assumed to be .73.

TABLE 41
INTERNAL POWER DISSIPATION

Heated Node, i	Power (Watts), P _i
5	40 (Operational) + Vernier Stator Heater Power 0 (Nonoperational)
10	59 (Operational) 0 (Nonoperational)
1, 2	Each receives one half elevation heater power
3, 4	Each receives one half lateral heater power
6	Optical coupler heater power
7	Battery heater power

Solar power input was calculated from the solar flux, area, view factor, and solar absorptivity of each surface. Table 42 lists the nominal values used.

Figure 136 portrays the topography of the thermal model used showing the heat paths connecting the various nodes. The jagged resistance symbols represent radiative paths while the usual electrical resistance symbol represents conductive heat transfer.

TABLE 42
SOLAR HEAT INPUT

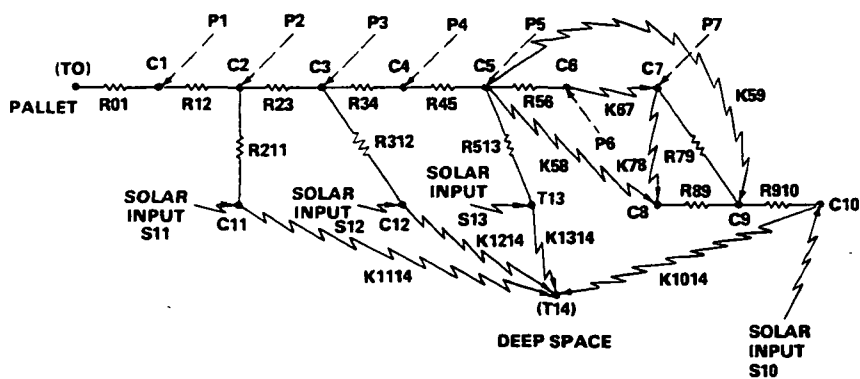
Illuminated Node, i	Solar Input Power (Watts), S_i
11	3.24
12	3.24
13	28.5
10	157.8

Note: Solar Absorptivity of MLI assumed to be .15.

The thermal model was simulated on both an analog computer and in a digital thermal analyzer program. Both programs produced steady state and transient results which agreed within 3°C. The analog computer was used for most of the analysis, however, because of its greater efficiency.

7.3 THERMAL CONTROL SYSTEM REQUIREMENTS AND APPROACH

The worst case OFT-4 orbital thermal environment can be divided into the hot and cold orbit cases shown in Figure 134. Due to the large β angle during the hot orbit, the ASPS is in full sunlight for the entire orbit. The estimated pallet integration structure temperature of 27°C and solar flux of up to 1441 W/m² both contribute to making this the hot case. The pallet integration structure surface temperature was calculated using the solar absorptivity and infrared emissivity of the pallets as supplied by Rockwell. A 25°C margin was added to account for heat entrapment due to pallet geometry and is included in the 27°C above. During the cold orbit, the ASPS points toward deep space for the entire orbit. The pallet integration structure temperature and radiation losses to deep space, require the use of heaters for this condition to maintain the allowable component temperatures given in Table 43. Cold case pallet temperature was assumed to be -150°C (123K) which is the worst case cold extreme defined for the pallet structure in Reference 3.



<u>NODE NUMBER</u>	<u>DESCRIPTION</u>
1	ELEVATION GIMBAL BEARINGS
2	ELEVATION GIMBAL
3	LATERAL GIMBAL STATOR
4	LATERAL GIMBAL BEARINGS
5	VERNIER BASE PLATE
6	OPTICAL COUPLER STATOR
7	BATTERIES
8	VERNIER ROTOR
9	PAYLOAD MOUNTING PLATE
10	PAYLOAD
11	ELEVATION GIMBAL MLI
12	LATERAL GIMBAL MLI
13	VERNIER MLI

Figure 136
ASPS Thermal Model

TABLE 43
ASPS COMPONENT TEMPERATURE LIMITS

Component	Operating Temperature Limits	Storage Temperature Limits
Gimbals Includes Electromagnetic Components	-29°C to 71°C	-40°C to 74°C
Gimbal Bearings	-17°C to 200°C	-17°C to 200°C
Optical Coupler	-10°C to 60°C	-65°C to 125°C
Batteries	0°C to 40°C	0°C to 40°C
Magnetic Bearings	-45°C to 80°C	-150°C to 100°C

Thermal isolation of the suspended components from the gimbal and vernier structure results from the small radiation heat transfer between fixed and suspended components. Although the batteries have been isolated from the non-suspended vernier components by wrapping them with aluminum foil, no attempt was made to isolate the batteries from the payload mounting plate. A good heat transfer path to the payload mounting plate is necessary as heat from the batteries must be dissipated during charging.

Since the payload was assumed in this analysis to completely cover the payload mounting plate, heat from the batteries is conducted into the experiment where it is radiated out from the experiment side walls. If the payload does not actually cover the entire payload plate, battery heat may be radiated from the uncovered portion of the payload mounting plate. The control of heat transfer into (or from) the experiment, may then be limited by utilizing thermal insulators between the experiment and payload mounting plate.

7.4 SIMULATION RESULTS

Predicted temperatures for hot orbit conditions were generated using both the digital and analog computer simulations. All exposed ASPS surfaces were exposed to the maximum solar flux to simulate direct sunlight and reflected sunlight from the pallet. The steady-state nodal temperatures from the simulations are listed in Figure 137. Because of the long duration of the hot orbit (26 hours), steady-state temperatures were achieved. Agreement between the two simulations is within 3°C. The thermal isolation of the floating components from the vernier and gimbal assemblies is apparent by the temperature differences. Component temperature levels controlled by the use of the Multilayer Insulation (MLI) are within desired limits. Nominal conditions for the hot orbit temperatures listed in Figure 137 are defined by Tables 38, 39, 40, 41 (with operational power and heaters off), 42 and a pallet integration structure temperature of 27 degrees C.

NODE DESCRIPTION	TEMPERATURE FROM	TEMPERATURE FROM
	ANALOG SIMULATION	DIGITAL SIMULATION
	(°C)	(°C)
ELEVATION GIMBAL BEARINGS	39	37
ELEVATION GIMBAL ASSEMBLY	43	41
LATERAL GIMBAL BEARINGS	54	51
LATERAL GIMBAL ASSEMBLY	59	56
VERNIER	59	56
OPTICAL COUPLER	59	56
BATTERIES	21	20
ROTOR	21	21
PAYLOAD MOUNTING PLATE	21	20
PAYLOAD	21	20

Figure 137
Hot Orbit Predicted Temperatures

Power flow in the model is listed in Figure 138 and is useful in understanding the temperature distributions. The total 258 watts of power input to the ASPS is distributed between several locations. Radiation heat losses from the vernier account for 30 of the 40 watts generated by the magnetic bearings. The radiation losses from the payload node account for the 159 watts absorbed by that node, the 29 watts of payload power dissipation, and the remaining 10 watts from the magnetic bearings.

Hot orbit component temperatures were found to be sensitive to pallet temperature, payload parameters, and vernier insulation thickness. Pallet temperature changes affect the temperature of the nonsuspended components as shown in Figure 139. The largest temperature changes are noticed in the elevation gimbal which is closest to the pallet.

Multilayer Insulation (MLI) is used to control the heat transfer to and from the payload node. The thermal properties of this material are characterized by the solar absorptivity (α_s) and infrared emissivity (ϵ) of its outermost layer. Nominal values for these constants are $\alpha_s = .15$, $\epsilon = .73$ which corresponds to beta cloth. The ratio of solar absorptivity to infrared emissivity has a large effect on the suspended portion of the ASPS shown by the payload assembly temperature curve in Figure 140. Increasing the (α_s/ϵ) ratio from its nominal value of .205 causes the payload node to absorb more energy from the sun and thus increases its temperature. Nonsuspended components are only slightly affected.

Increasing the payload area allows the payload power dissipation to occur over a larger area thus reducing the suspended component temperatures as shown by the payload assembly temperature curve in Figure 141. The nominal area corresponds to the circular area of the payload facing away from the vernier assembly and having a diameter of .93 m.

Changes in vernier base plate MLI insulation thickness affect the heat transfer to space from the vernier and thus affect the unsuspended component temperatures, as shown in Figure 142.

Temperatures for cold orbit conditions are maintained using both gimbal bearing heaters and the battery heaters. Nominal conditions are the same as for the hot case, except there is no solar flux on any surfaces and the pallet integration temperature is 120K. For the case in which the ASPS is operational (actuators powered), the predicted temperatures are listed in Figure 143. Maintaining these temperatures requires average heater powers of 25 watts for the elevation gimbal bearings, 10 watts for the lateral gimbal bearings, and 100 watts for the battery heaters. With the ASPS not operating (actuators unpowered), average heater powers are raised to 25 watts for the lateral gimbal bearing heaters, and 160 watts for the battery heaters. Predicted temperatures for the nonoperating case are listed in Figure 144 for both simulations. Component temperatures are seen to be operating within their storage temperature limits as desired. Power flows for both operating and nonoperating conditions are listed in Figure 145. It can be seen that the heater powers must be increased for the nonoperational condition to compensate for the power dissipation of the payload and magnetic bearings which are no longer present.

HEAT SOURCE	INPUT POWER (WATTS)	HEAT SINK	OUTPUT POWER (WATTS)
MAGNETIC BEARING POWER DISSIPATION	40	HEAT CONDUCTION TO PALLET	2
PAYLOAD POWER DISSIPATION	59	RADIATION HEAT LOSSES FROM GIMBALS	<1
SOLAR HEATING	159	RADIATION HEAT LOSSES FROM VERNIER	30
		RADIATION HEAT LOSSES FROM PAYLOAD	226
TOTALS	<u>258</u>	TOTAL	<u>258</u>

Figure 138
Hot Orbit Energy Balance

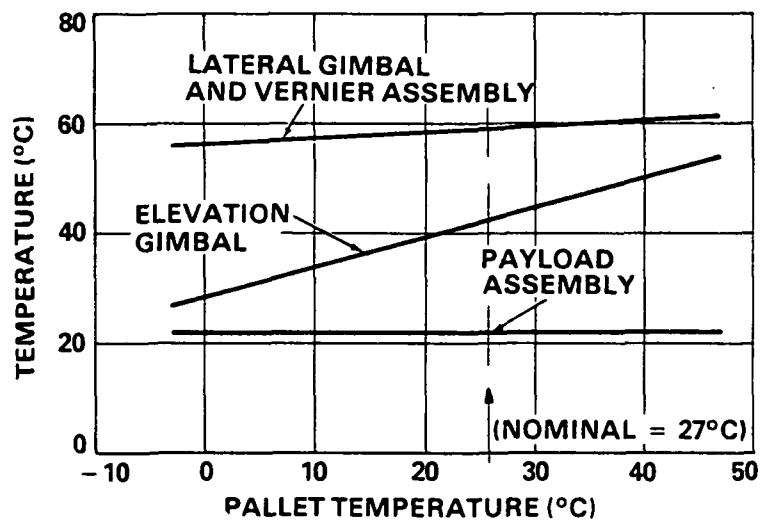


Figure 139
Effect of Pallet Temperature on Hot Orbit Temperatures

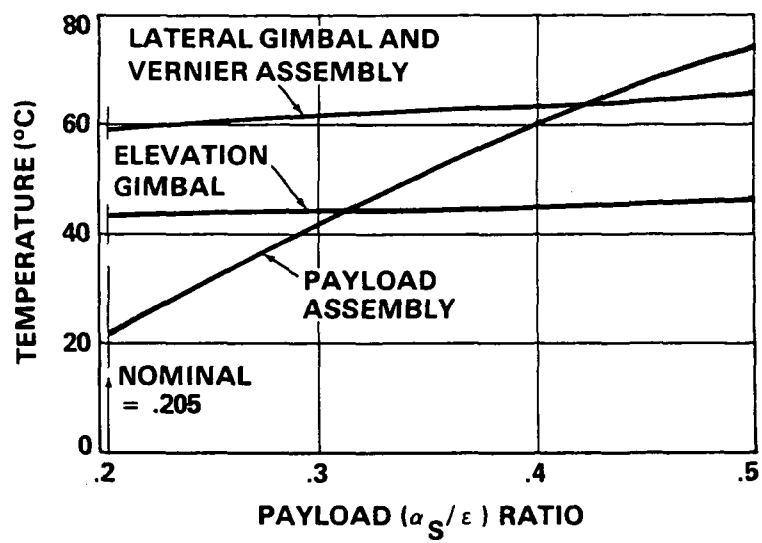


Figure 140
Effect of Payload (α_s/ϵ) Ratio on
Hot Orbit Temperatures

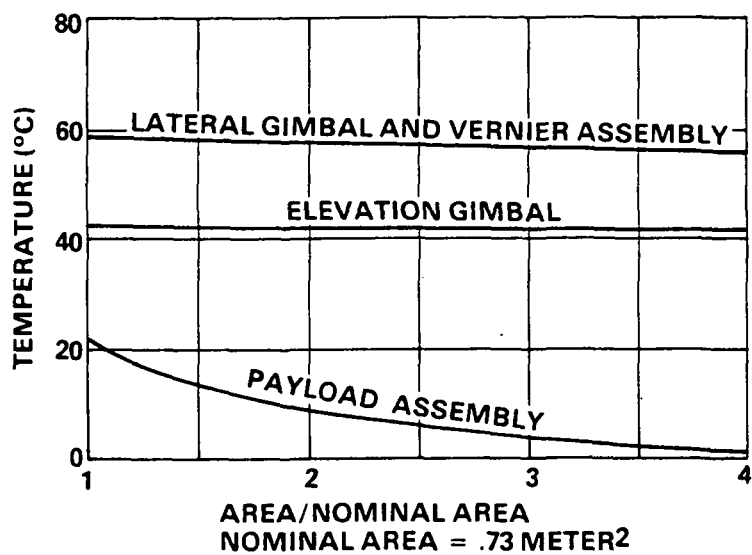


Figure 141
Effect of Payload Area on Hot Orbit Temperatures

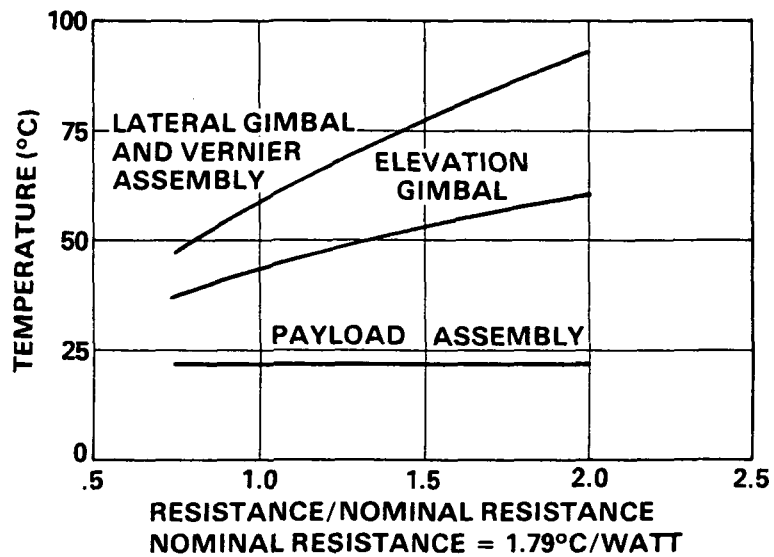


Figure 142
Effect of Vernier Base Plate MLI Insulation
on Hot Orbit Temperatures

NODE DESCRIPTION	TEMPERATURE FROM	TEMPERATURE FROM
	ANALOG SIMULATION	DIGITAL SIMULATION
	(°C)	(°C)
ELEVATION GIMBAL BEARINGS	28	29
ELEVATION GIMBAL ASSEMBLY	27	27
LATERAL GIMBAL BEARINGS	24	25
LATERAL GIMBAL ASSEMBLY	-5	-5
VERNIER	-6	-5
OPTICAL COUPLER	-5	-5
BATTERIES	7	4
ROTOR	2	-1
PAYLOAD MOUNTING PLATE	1	-2
PAYLOAD	1	-2

Figure 143
Cold Orbit Predicted Temperatures
ASPS Operational

NODE DESCRIPTION	TEMPERATURE FROM ANALOG SIMULATION	TEMPERATURE FROM DIGITAL SIMULATION
	(°C)	(°C)
ELEVATION GIMBAL BEARINGS	25	26
ELEVATION GIMBAL ASSEMBLY	22	23
LATERAL GIMBAL BEARINGS	16	17
LATERAL GIMBAL ASSEMBLY	-58	-57
VERNIER	-60	-59
OPTICAL COUPLER	-58	-59
BATTERIES	8	5
ROTOR	-1	-4
PAYLOAD MOUNTING PLATE	-1	-4
PAYLOAD	-2	-4

Figure 144
Cold Orbit Predicted Temperatures
ASPS Nonoperational

ASPS OPERATIONAL				ASPS NONOPERATIONAL			
HEAT SOURCE	INPUT POWER (WATTS)	HEAT SINK	OUTPUT POWER (WATTS)	HEAT SOURCE	INPUT POWER (WATTS)	HEAT SINK	OUTPUT POWER (WATTS)
ELEVATION GIMBAL BEARING HEATERS	25	HEAT CONDUCTION TO PALLET	23	ELEVATION GIMBAL BEARING HEATERS	25	HEAT CONDUCTION TO PALLET	24
LATERAL GIMBAL BEARING HEATERS	10	RADIATION HEAT LOSSES FROM GIMBALS	1	LATERAL GIMBAL BEARING HEATERS	25	RADIATION HEAT LOSSES FROM GIMBALS	1
BATTERY HEATERS	100	RADIATION HEAT LOSSES FROM VERNIER	42	BATTERY HEATERS	160	RADIATION HEAT LOSSES FROM VERNIER	28
MAGNETIC BEARING POWER DISSIPATION	40	RADIATION HEAT LOSSES FROM PAYLOAD	168			RADIATION HEAT LOSSES FROM PAYLOAD	157
PAYLOAD POWER DISSIPATION	59						
TOTAL	234	TOTAL	234	TOTAL	210	TOTAL	210

Figure 145
Cold Orbit Energy Balance

The temperatures during the worst-case heater condition, in which the ASPS is not operating, were found to be sensitive to the same parameters which affected the hot orbit temperatures. Effects of pallet temperature changes, shown in Figure 146, illustrate the gimbal temperature dependence on pallet temperature.

Heat transfer to space from the payload increases with increases in payload emissivity with a corresponding decrease in battery and payload temperatures, as shown in Figure 147.

Similarly, increases in payload area allows larger amounts of power to be radiated to space with corresponding decreases in battery and payload temperatures; see Figure 148.

Vernier insulation thickness, shown in Figure 149, reduces the heat transfer to space from the vernier assembly thus increasing the gimbal bearing temperatures.

7.5 CONCLUSIONS

Component temperatures from the hot and cold orbit analyses showed satisfactory operation of the thermal control system. The placement of the multi-layer insulation over the exposed ASPS surfaces and payload, in addition to the thermal isolation of the suspended components, provided acceptable temperatures during hot orbit conditions. Cold orbit temperature control was accomplished by using gimbal bearing heaters, battery heaters, plus the insulation properties of the MLI. The energy balance for the hot orbit condition showed that the payload heat transfer to space consisted of the power the payload had absorbed from the sun and the internal power dissipated by the payload electronics. Heat transfer from ASPS components to the payload was found to be very small (10 watts).

Changes in payload configuration from the OFT-4 payload should necessitate only small changes in the thermal control system. The thermal control system performance depends on the payload successfully radiating to space the solar energy it has absorbed and the power it has dissipated. Power generated from the ASPS magnetic bearings and heat dissipation necessary during battery charging, requires the availability of some reasonable area of the payload mounting plate to radiate heat to space if conduction through the experiment is to be avoided.

As further definition of critical parameters such as pallet temperature and payload configuration is generated, thermal analysis of the ASPS will continue. A more detailed model is in progress which will take into account pallet radiation heat transfer to the ASPS, entry, and post landing conditions. A larger number of nodes will be used to predict temperature distribution across critical components.

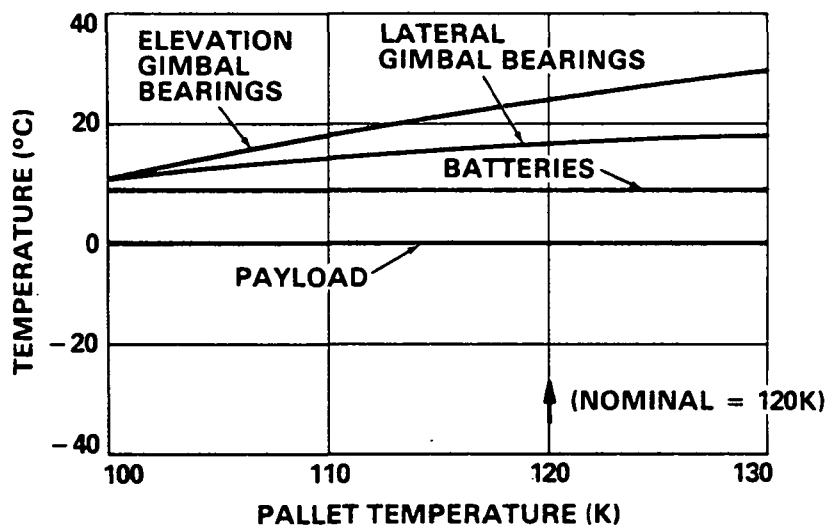


Figure 146
Effect of Pallet Temperature on Cold Orbit Temperatures
(ASPS Nonoperating)

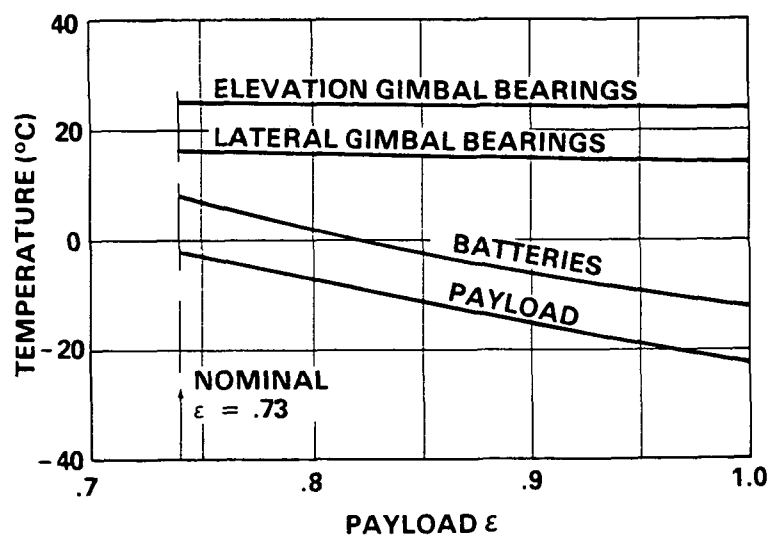


Figure 147
Effect of Payload Emissivity ϵ on Cold Orbit Temperatures
(Nonoperational)

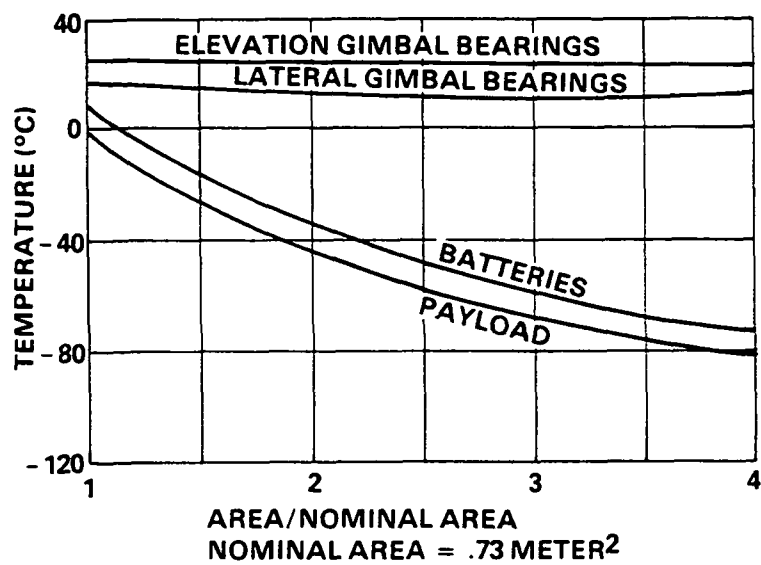


Figure 148
Effect of Payload Area on Cold Orbit Temperatures
(Nonoperational)

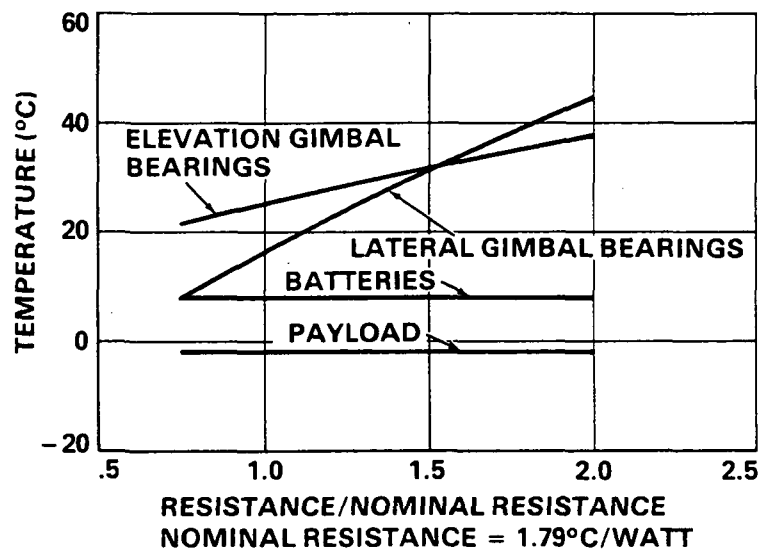


Figure 149
Effect of Vernier Base Plate MLI
Insulation on Cold Orbit Temperatures
(Nonoperational)

APPENDIX A

ASPS LINEAR SYSTEM MODEL

A simplified linear model of the ASPS has been developed for stability analysis, preliminary sizing, and control system synthesis. Figure 150 illustrates the linear system model which consists of: the shuttle, a single coarse gimbal, and the magnetically suspended payload. All motions are constrained in the plane of the diagram and a stiff rectilinear compliance is modeled at the coarse gimbal pivot. A description of coordinates and system variables follows.

ASPS Linear System Model

Description of Coordinates and System Variables.

$X_C, Z_C, X_E, Z_E, X_T, Z_T$ - Inertial translational coordinates of the shuttle, gimbal, and payload respectively - meters.

RCG - Vector, in shuttle coordinates, from the shuttle Center of Mass (CM) to the gimbal point - meters. RCGX = X component of RCG, etc.

RCJ - Vector, in shuttle coordinates, from the shuttle CM to the point of application of an external disturbance - meters.

ZEV - Distance from the CM of the combined gimbal and vernier stator to the payload attach point - meters.

ZGE - Distance from gimbal pivot to CM of combined gimbal and vernier stator mass - meters.

ZVT - Distance from the payload attach point to the payload CM - meters.

σ_0 - Coarse gimbal attitude - radians.

σ - Incremental coarse gimbal attitude - radians.

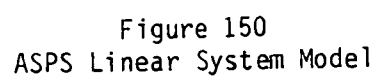
θ_C - Shuttle attitude - radians.

θ_t - Payload attitude - radians.

F_j - External disturbance force - newtons.

F_x, F_z - Interaction forces at gimbal - newtons.

F_A, F_R - Axial and radial interaction forces at gimbal/payload interface - newtons



T_α - Gimbal torque - newton meter

T_V - Magnetic bearing torque at gimbal/payload interface - newton meter

M_C, M_E, M_T - Mass of shuttle, gimbal, payload respectively - kilogram

I_C, I_E, I_T - Inertia of shuttle, gimbal, payload respectively - Kilogram
meter²

K_B - Gimbal stiffness - Newton per meter

Double dots over a quantity denotes the second derivative with respect to time of that quantity.

The equations of motion for each of the three bodies are:

Shuttle Dynamics

$$\left. \begin{aligned} M_C \ddot{X}_C &= -F_X \cos \sigma_0 - F_Z \sin \sigma_0 \\ M_C \ddot{Z}_C &= -F_Z \cos \sigma_0 + F_X \sin \sigma_0 + F_j \\ I_C \ddot{\theta}_C &= -T_\sigma + RCGX (F_Z \cos \sigma_0 - F_X \sin \sigma_0 \\ &\quad - RCGZ (F_X \cos \sigma_0 + F_Z \sin \sigma_0) - RCJX (F_{jZ}) \end{aligned} \right\} (A1)$$

Gimbal Dynamics

$$\left. \begin{aligned} M_E \ddot{X}_E &= F_X + F_R \\ M_E \ddot{Z}_E &= F_Z + F_A \\ I_E \ddot{\sigma} &= T_V + T_\sigma + Z_{EV} F_R - Z_{GE} F_X \end{aligned} \right\} (A2)$$

Gimbal Constraint Forces

$$\left. \begin{aligned} F_X &= (X_C \cos \sigma_0 - Z_C \sin \sigma_0 - X_E + Z_{GE} \sigma \\ &\quad + Z_{CG} \theta_C \cos \sigma_0 + X_{CG} \theta_C \sin \sigma_0) K_B \\ F_Z &= (Z_C \cos \sigma_0 + X_C \sin \sigma_0 - Z_E + Z_{CG} \sin \sigma_0 \\ &\quad + X_{CG} \theta_C \cos \sigma_0) K_B \end{aligned} \right\} (A3)$$

Gimbal Torquer

$$T_{\sigma} = G_{\sigma}(s) (\theta_C - \sigma) \quad (A4)$$

Payload Dynamics

$$\left. \begin{aligned} M_T \ddot{X}_T &= -F_R \\ M_T \ddot{Z}_T &= -F_A \\ I_T \ddot{\theta}_T &= -T_V + Z_{VT} F_R \end{aligned} \right\} (A5)$$

MBA Control

$$\left. \begin{aligned} F_A &= G_A(s) (Z_T - Z_E) \\ F_R &= G_R(s) (X_T - Z_{VT} \theta - X_E - Z_{EV} \sigma) \\ T_V &= -G_{\theta}(s) \theta_E + \hat{Z}_{VT} F_R \end{aligned} \right\} (A6)$$

NOTE: $\hat{}$ indicates a measured or estimated quantity.

G_{σ} , G_R , G_A , G_{θ} represent controller transfer functions. In this study, G_{σ} , G_R , G_A represent lead/lag servos with the form

$$G(s) = K \frac{(T_1 s + 1)}{(T_2 s + 1)} \quad (A7)$$

Three types of pointing servos have been evaluated in this study for $G_{\theta}(s)$. They are lead/lag compensation (as above), proportional plus rate feedback and proportional plus rate plus integral of error feedback.

An analog block diagram of the ASPS Linear System Model equations is shown in Figure 151. The model has been analyzed via a linear control system analysis program to obtain system roots, frequency responses, stability margins, and to perform various preliminary trade-off studies discussed in Paragraph 2.1 of this report.

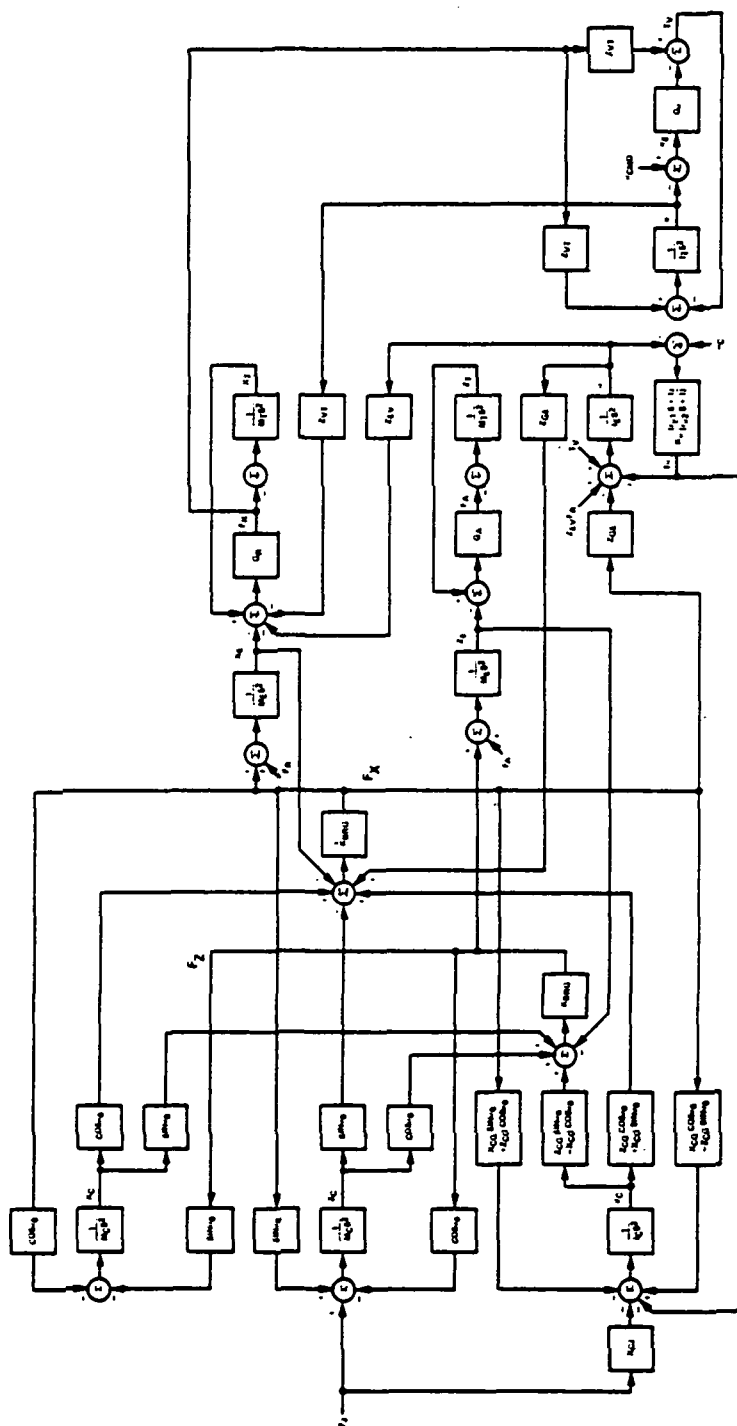


Figure 151
ASPS Linear System Model Block Diagram

Page Intentionally Left Blank

APPENDIX B

ASPS DIGITAL SYSTEM SIMULATION

The digital ASPS simulation utilized in this study has been adapted from one developed by Mr. C. Woolley of Langley Research Center. The simulation computes full six degree of freedom dynamics of the Shuttle with two offset gimbals and a magnetically suspended payload with six degrees of freedom. It also includes: nonlinear magnetic bearing models, gimbal friction, gimbal-payload cable dynamics, and a full payload CM decoupling law.

Figure 152 illustrates the simulation configuration, coordinate systems, and various pertinent dimensions. Also shown, is the MBA and roll motor mounting configuration viewed looking down at the lateral gimbal plate. A mathematical description of the simulation is included below.

LIST OF SYMBOLS IN ASPS SIMULATION

general units - length - meter, mass - kilogram, force - newton, torque - newton meter, inertia - kilogram meter², angle - radian

ACCD	Shuttle euler angle rate
ATT	Payload euler angle
ATTD	Payload euler angle rates
CABK	Cable translation stiffness newtons/meter
CABT	Cable torsional stiffness newton meters/radian
CK	Constant $g^2/4KI_0$ amp/newton
CON3	Constant K/g^2 newtons/amp ²
CON6	Constant K/g^2 newtons/amp ²
CXROC	-RBT(1)
CYROX	-RBT(2) CM decoupling circuit parameters (nominal values indicated)
CZROC	-RBT(3)
DLG	MBA gap
DLGD	MBA gap rate
ELECMD	Elevation gimbal command
ELERR	Elevation gimbal error
FA	Magnetic actuator output forces
FAC	Magnetic actuator force commands
FAP	Intermediate magnetic actuator force commands
FB	Magnetic actuator output forces

LIST OF SYMBOLS IN ASPS SIMULATION (cont)

FBC	Magnetic actuator force commands
FBP	Intermediate magnetic actuator force commands
FBT	MBA force applied to payload in payload coordinates
FC	Magnetic actuator output forces
FCAB	Cable Force
FCCC	Magnetic actuator force commands
FCMD	MBA force command
FCP	Intermediate magnetic actuator force commands
FOUT	MBA output forces
FU	Magnetic actuator output forces
FUC	Magnetic actuator force commands
FV	Magnetic actuator output forces
FVC	MBA force in Shuttle coordinates
FVCC	Magnetic actuator force commands
FVE	MBA force at elevation gimbal center
FVL	MBA force applied to payload at bearing center in lateral gimbal coordinates
FW	Magnetic actuator output forces
FWC	Magnetic actuator force commands
FWP	Intermediate magnetic actuator force commands
GAPK	Magnetic gap coefficient 1/meters
GAPKM	Estimated magnetic gap coefficient 1/meters
HCC	Shuttle angular momentum
HCCD	Shuttle angular momentum derivative
HEE	Elevation gimbal angular momentum
HLL	Lateral gimbal angular momentum
HTT	Payload angular momentum
HTTD	Payload momentum derivative
I1	Coil 1 current amp
I1D	Coil 1 current derivative amp/sec
I2	Coil 2 current amp
I2D	Coil 2 current derivative amp/sec
IC	Inertia of Shuttle augmented with gimbals

LIST OF SYMBOLS IN ASPS SIMULATION (cont)

ICI	Current command, coil 1 amp
IC2	Current command, coil 2 amp
IE	Inertia of elevation gimbal
IL	Inertia of lateral gimbal
IO	Bias current amps
IT	Inertia of payload IT is also redefined to JT
ITC	IT(1,1)
JCEL	5 x 5 matrix relating Shuttle and gimbal angular rates to angular momentum
KF1MAX	Elevation gimbal friction stiffness coefficient
KF2MAX	Lateral gimbal friction stiffness coefficient
KIA	Current loop integral gain, coil 1 volt/amp
KIB	Current loop integral gain, coil 2 volt/amp sec
KP	Pointing servo position gain N m/RAD
KP1	Elevation gimbal servo gain N m/RAD
KP2	Lateral gimbal servo gain N m/RAD
KPA	Current loop proportional gain, coil 1 volt/amp
KPB	Current loop proportional gain, coil 2 volt/amp sec
KPRL	Roll servo position gain N m/RAD
KPT	Centering servo gain N m/RAD
KR	Pointing servo rate gain N mSEC/RAD
KROL	Roll servo rate gain N mSEC/RAD
LATCMD	Lateral gimbal command
LERR	Lateral gimbal error
LG	Coil 1 coupling inductance henrys
LG2	Coil 2 coupling inductance henrys
LL1	Coil 1 leakage inductance henrys
LL2	Coil 2 leakage inductance henrys
LPHI	Lateral vernier servo command
LPSI	Roll servo command
LTHE	Pitch vernier servo command

LIST OF SYMBOLS IN ASPS SIMULATION (cont)

LU	Radial servo commands
LV	Radial servo commands
LZ	Axial servo command
	Magnetic Actuator Nomenclature
MC	Mass Shuttle
MCEL	$MC + ML + ME$
ME	Mass elevation gimbal
MEL	$ME + ML$
ML	Mass lateral gimbal
MT	Mass payload
MTL	MT
NCEL	$1/MCEL$
NT	$1/MT$
PHCMD	Lateral vernier pointing command
PHERR	Lateral vernier pointing error
PHTR	Relative angle between payload and lateral gimbal about lateral gimbal x axis
PSICMD	Roll vernier pointing command
PSIERR	Roll vernier pointing error
PX	Equivalent proximeter gaps and gap rates in lateral gimbal coordinates
PXDT	Equivalent proximeter gaps and gap rates in lateral gimbal coordinates
PY	Equivalent proximeter gaps and gap rates in lateral gimbal coordinates
PYDT	Equivalent proximeter gaps and gap rates in lateral gimbal coordinates
PZ	Equivalent proximeter gaps and gap rates in lateral gimbal coordinates
PZDT	Equivalent proximeter gaps and gap rates in lateral gimbal coordinates
RBT	Vector from payload CM to payload base
RCI	Shuttle inertial displacement
RCID	Shuttle velocity in inertial coordinates
RD	Coil dc resistance ohms
RGC	Vector from Shuttle CM to Elevation gimbal point

LIST OF SYMBOLS IN ASPS SIMULATION (cont)

RHOL	Roll servo damping coefficient
RHOR	Pointing servo damping coefficient
RQV	Effective radius of actuator system on lateral gimbal
RQVC	RQV
RTI	Initial displacement of payload CM
RTID	Initial velocity of payload CM
RUB	Effective radius of actuator system on payload
RUQ	Magnetic bearing gap
RUQO	Magnetic bearing gap rate
RVG	Vector from lateral gimbal point to payload base attach point
T1E	Elevation gimbal servo lead time constant seconds
T2E	Elevation gimbal servo lag time constant seconds
T1L	Lateral gimbal servo lead time constant seconds
T2L	Lateral gimbal servo lag time constant seconds
T1T	Centering servo lead time constant seconds
T2T	Centering servo lag time constant seconds
TBT	MBA Torque in payload coordinates
TCAB	Cable torque
TCCT	Total torque applied to shuttle in Shuttle coordinates
TEE	Elevation gimbal torquer output
TF1MAX	Elevation gimbal friction breakaway torque
TF2MAX	Lateral gimbal friction breakaway torque
TGC	MBA torque in Shuttle coordinates
TGE	MBA torque at elevation gimbal
TGL	MBA torque applied to payload at center of lateral gimbal in lateral gimbal coordinates
THCMD	Pitch vernier pointing command
THERR	Pitch vernier pointing error
THTR	Relative angle between payload and lateral gimbal about lateral gimbal y axis
TLL	Lateral gimbal torquer output
TVL	MBA torque applied to payload in lateral gimbal coordinates
V1	Coil 1 voltage volts

LIST OF SYMBOLS IN ASPS SIMULATION (cont)

V2	Coil 2 voltage	volts
V1MX	Voltage amplifier limit coil 1	volt
V2MX	Voltage amplifier limit coil 2	volts
VA3	Shuttle velocity at magnetic bearing locations in lateral gimbal	coordinates
VB3	Shuttle velocity at magnetic bearing locations in lateral gimbal	coordinates
VBT	Payload velocity at MBA interface in payload	coordinates
VC3	Shuttle velocity at magnetic bearing locations in lateral gimbal	coordinates
VCC	Shuttle velocity in Shuttle	coordinates
VCCD	Shuttle acceleration in Shuttle	coordinates
VGC	Shuttle velocity at elevation gimbal point in Shuttle	coordinates
VGE	Shuttle velocity at elevation gimbal in elevation gimbal	coordinates
VGL	Shuttle velocity at lateral gimbal in lateral gimbal	coordinates
VTTD	Payload acceleration in telescope	coordinates
VU1	Shuttle velocity at magnetic bearing locations in lateral gimbal	coordinates
VU2	Shuttle velocity at magnetic bearing locations in lateral gimbal	coordinates
VUL	Payload velocity at MBA locations in lateral gimbal	coordinates
VUT	Payload velocity at MBA locations in payload	coordinates
VV1	Shuttle velocity at magnetic bearing locations in lateral gimbal	coordinates
VV2	Shuttle velocity at magnetic bearing locations in lateral gimbal	coordinates
VVL	Shuttle velocity at lateral gimbal/MBA Interface center in lateral	gimbal coordinates
WCC	Shuttle angular rate	
WEE	Elevation gimbal angular rate	
WLL	Lateral gimbal angular rate	
WNR	Pointing servo bandwidth	RAD/SEC
WNRL	Roll servo bandwidth	RAD/SEC
WTT	Payload angular rates	

ASPS DIGITAL SYSTEM SIMULATION

100 START ITERATIVE LOOP

COORDINATE SYSTEMS AND TRANSFORMATIONS

SYSTEM	FIXED IN	ORIGIN AT
I	INERTIAL	COINCIDES WITH C ORIGIN AT T (0)
C	CARRIER (SHUTTLE)	CM
T	TELESCOPE (PAYLOAD)	CM
E	ELEVATION GIMBAL	CM
L	LATERAL GIMBAL	CM

ANGLES

ACC 1 CARRIER EULER ANGLES
 2
 3 123 ROTATION ORDER

ATT 1 TELESCOPE EULER ANGLES
 2
 3

AEE (2) ELEVATION GIMBAL ANGLE

ALL (1) LATERAL GIMBAL ANGLE

TRANSFORMATIONS

|DIJ| TRANSFORMS FROM J TO I

$$|DCT| = |DCI| |DTI|^T, |DLT| = |DLC| |DCT|$$

DCI MATRIX

$$|DCI| = \begin{matrix} DCI(1,1) = \cos ACC(3) * \cos ACC(2) \\ DCI(1,2) = \cos ACC(3) * \sin ACC(2) * \sin ACC(1) + \sin ACC(3) * \cos ACC(1) \\ DCI(1,3) = -\cos ACC(3) * \sin ACC(2) * \cos ACC(1) + \sin ACC(3) * \sin ACC(1) \\ DCI(2,1) = -\sin ACC(3) * \cos ACC(2) \\ DCI(2,2) = -\sin ACC(3) * \sin ACC(2) * \sin ACC(1) + \cos ACC(3) * \cos ACC(1) \\ DCI(2,3) = \sin ACC(3) * \sin ACC(2) * \cos ACC(1) + \cos ACC(3) * \sin ACC(1) \\ DCI(3,1) = \sin ACC(2) \\ DCI(3,2) = -\cos ACC(2) * \sin ACC(1) \\ DCI(3,3) = \cos ACC(2) * \cos ACC(1) \end{matrix}$$

DTI MATRIX

$$|DTI| = \begin{matrix} DTI(1,1) = \cos ATT(3) * \cos ATT(2) \\ DTI(1,2) = \cos ATT(3) * \sin ATT(2) * \sin ATT(1) + \sin ATT(3) * \cos ATT(1) \\ DTI(1,3) = -\cos ATT(3) * \sin ATT(2) * \cos ATT(1) + \sin ATT(3) * \sin ATT(1) \\ DTI(2,1) = -\sin ATT(3) * \cos ATT(2) \\ DTI(2,2) = -\sin ATT(3) * \sin ATT(2) * \sin ATT(1) + \cos ATT(3) * \cos ATT(1) \\ DTI(2,3) = \sin ATT(3) * \sin ATT(2) * \cos ATT(1) + \cos ATT(3) * \sin ATT(1) \\ DTI(3,1) = \sin ATT(2) \\ DTI(3,2) = -\cos ATT(2) * \sin ATT(1) \\ DTI(3,3) = \cos ATT(2) * \cos ATT(1) \end{matrix}$$

```

DLC=DPHI * DTHE
DLC(1,1)= COSAEE(2)
DLC(1,2)= 0.
DLC(1,3)=-SINAEE(2)
DLC(2,1)= SINALL(1)*SINAEE(2)
DLC(2,2)= COSALL(1)
DLC(2,3)= SINALL(1)*COSAEE(2)
DLC(3,1)= COSALL(1)*SINAEE(2)
DLC(3,2)=-SINALL(1)
DLC(3,3)= COSALL(1)*COSAEE(2)

```

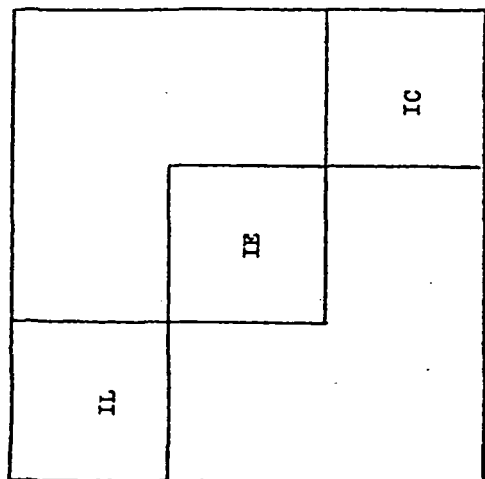
$$|DLC| = \begin{vmatrix} 1 & 0 & 0 \\ 0 & \text{COSALL}(1) & \text{SINALL}(1) \\ 0 & -\text{SINALL}(1) & \text{COSALL}(1) \end{vmatrix}$$

$$|DEC| = \begin{vmatrix} \text{COSAEE}(2) & 0 & -\text{SINAEE}(2) \\ 0 & 1 & 0 \\ \text{SINAEE}(2) & 0 & \text{COSAEE}(2) \end{vmatrix}$$

COMPUTE
JCEL

SL = SINALL(1)
 CL = COSALL(1)
 SE = SINAEE(2)
 CE = COSAEE(2)

COMPUTE JCEL



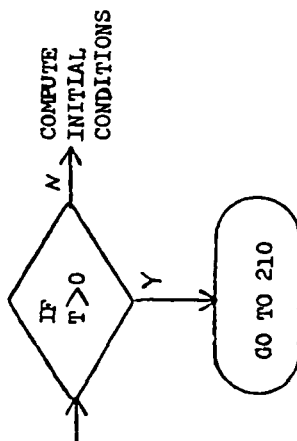
A^T
 5 x 9

J
 9 x 9

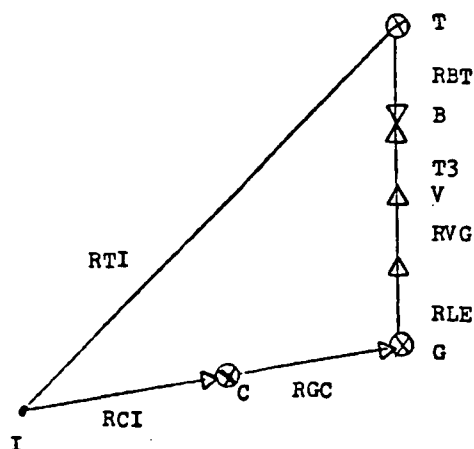
A
 9 x 5

$JCEL$ 5 x 5

1	0	0	0	0	0
0	CL	SLSE	0	SLCE	
0	-SL	CLSE	0	CLCE	
0	0	CE	0	-SE	
0	1	0	0	0	
0	0	SE	0	CE	
0	0	1	0	0	
0	0	0	1	0	
0	0	0	0	0	1



COMPUTE INITIAL CONDITIONS



INITIAL INERTIAL POS. OF TELESCOPE = \overline{RTI}

$$\overline{RTI} = [\overline{DCI}]^T ([\overline{DLC}]^T (\overline{RVG} - \overline{RBT} + [\overline{DLE}] \overline{RLE}) + \overline{RGC}) + \overline{RCI}$$

BASEPLATE TO TELESCOPE BASE GAP = $\overline{T3}$

$$\overline{T3} = [\overline{DLC}] ([\overline{DCI}] (\overline{RTI} - \overline{RCI}) - \overline{RGC}) + [\overline{DLT}] \overline{RBT} - \overline{RVG} - [\overline{DLE}] \overline{RLE}$$

BEARING GAPS, ASSUME T PARALLEL TO L

AXIAL GAPS AT A, B, C

$$RUQ(3,1) = TEMP3(3)$$

$$RUQ(3,2) = TEMP3(3)$$

$$RUQ(3,3) = TEMP3(3)$$

$$TEMP3 = \overline{T3}$$

X-Y RADIAL GAPS AT U V

$$RUQ(1,4) = TEMP3(1)$$

$$RUQ(2,4) = TEMP3(2)$$

$$RUQ(1,5) = TEMP3(1)$$

$$RUQ(2,5) = TEMP3(2)$$

INITIAL LATERAL GIMBAL RATES \overline{WLL}_{IC}

$$\overline{WLL}_{IC} = |DLT| \overline{WTT}_{IC}$$

INITIAL ELEVATION GIMBAL RATES \overline{WEE}_{IC}

$$WEE(2)_{IC} = COSALL(1) WLL(2) - SINALL(1) WLL(3)$$

$$WEE(1)_{IC} = WLL(1) , WEE(3)_{IC} = WLL(3)$$

CARRIER INITIAL MOMENTUM

$$\begin{pmatrix} HLL(1) \\ HEE(2) \\ HCC(1) \\ HCC(2) \\ HCC(3) \end{pmatrix} = |JCEL| \begin{pmatrix} WLL(1) \\ WEE(2) \\ WCC(1) \\ WCC(2) \\ WCC(3) \end{pmatrix}$$

TELESCOPE INITIAL MOMENTUM

$$\overline{HTT} = |IT| \overline{WTT}$$

GO TO 210

SHUTTLE KINEMATICS

210

CARRIER BODY RATES

$$\begin{pmatrix} WLL(1) \\ WEE(2) \\ WCC(1) \\ WCC(2) \\ WCC(3) \end{pmatrix} = |JCEL|^{-1} \begin{pmatrix} HLL(1) \\ HEE(2) \\ HCC(1) \\ HCC(2) \\ HCC(3) \end{pmatrix}$$

CARRIER EULER RATES

$$\dot{ACC}(1) = \frac{COSACC(3)WCC(1) - SINACC(3)WCC(2)}{COSACC(2)}$$

$$\dot{ACC}(2) = SINACC(3)WCC(1) + COSACC(3)WCC(2)$$

$$\dot{ACC}(3) = SINACC(2)ACC(1) + WCC(3)$$

CARRIER VELOCITY IN INERTIAL COORD.

$$\dot{RCI} = |PCI|^T \overline{VCC}$$

NOTE: $\overline{VCC}(0) = 0$

CARRIER VELOCITY AT ELEV GIMBAL CTR.

$$\overline{VGC} = \overline{VCC} + \overline{WCC} \times \overline{RCG}$$

ELEV. GIMBAL
KINEMATICS

ELEVATION GIMBAL KINEMATICS

ELEVATION GIMBAL BODY RATES

$$WEE(1) = \text{COSAE}(2)WCC(1) - \text{SINAE}(2)WCC(3)$$

$$WEE(3) = \text{SINAE}(2)WCC(1) + \text{COSAE}(2)WCC(3)$$

ELEVATION GIMBAL RATE

$$\dot{AEE}(2) = WEE(2) - WCC(2)$$

VEL. OF ELEV. GIMBAL IN ELEV. COORD.

$$\overline{VGE} = |\overline{DEC}| \overline{VGC}$$

VEL. OF LAT. GIMBAL CTR IN ELEV. COORD.

$$\overline{VGE} = \overline{VCE} + \overline{W}_{CC} \times \overline{RLE}$$

LATERAL GIMBAL KINEMATICS

LATERAL GIMBAL BODY RATES

$$WLL(2) = \text{COSALL}(1)WEE(2) + \text{SINALL}(1)WEE(3)$$

$$WLL(3) = \text{SINALL}(1)WEE(2) + \text{COSALL}(1)WEE(3)$$

LATERAL GIMBAL RATE

$$\dot{ALL}(1) = WLL(1) - WEE(1)$$

VEL. OF LAT. GIMBAL CTR IN LAT. COORD.

$$\overline{VGL} = |\overline{DLE}| \overline{VGE}$$

VEL. OF BEARING CTR. IN LAT. COORD.

$$\overline{VVL} = \overline{VGL} + \overline{W}_{LL} \times \overline{RVG}$$

VEL. OF BEARING STATIONS IN LAT. COORD.

$$VA3 = VVL(3) - RQV WLL(2)$$

$$VB3 = VVL(3) + .5 RQV WLL(2) + \frac{\sqrt{3}}{2} RQV WLL(1)$$

$$VC3 = VVL(3) + .5 RQV WLL(2) - \frac{\sqrt{3}}{2} RQV WLL(1)$$

$$VU1 = VVL(1) - \frac{RQV WLL(3)}{\sqrt{2}}$$

$$VU2 = WL(2) + \frac{RGV}{\sqrt{2}} WLL(3)$$

$$VV1 = VWL(1) + \frac{RGV}{\sqrt{2}} WLL(3)$$

$$VV2 = VWL(2) + \frac{RGV}{\sqrt{2}} WLL(3)$$

TELESCOPE KINEMATICS

TELESCOPE BODY RATES

$$\overline{WTT} = |IT|^{-1} \overline{HTT}$$

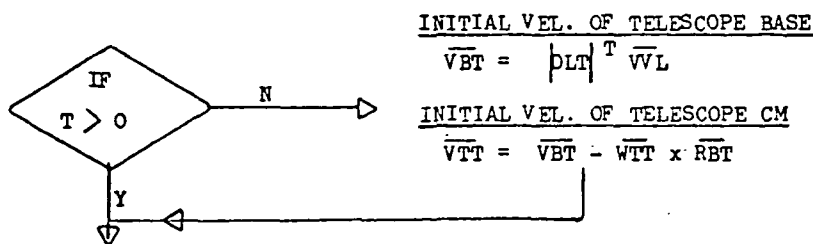
NOTE: $|IT|^{-1}$ IS A CONSTANT MATRIX

TELESCOPE EULER RATES

$$\dot{ATT}(1) = \frac{\cos ATT(3) \dot{WTT}(1)}{\cos ATT(2)} - \frac{\sin ATT(3) \dot{WTT}(2)}{\cos ATT(2)}$$

$$\dot{ATT}(2) = \sin ATT(3) \dot{WTT}(1) + \cos ATT(3) \dot{WTT}(2)$$

$$\dot{ATT}(3) = -\sin ATT(2) \dot{ATT}(1) + \dot{WTT}(3)$$



TELESCOPE VEL. IN INERTIAL COORD.

$$\dot{RTI} = |PTI|^T \dot{VTT}$$

TELESCOPE VEL. AT BEARING CTR.

$$\overline{VBT} = \overline{VTT} + \overline{WTT} \times \overline{RBT}$$

TELESCOPE VELOCITY AT BEARING STATIONS

AXIAL STATION A

$$VUT(1,1)=VBT(1)$$

$$VUT(2,1)=VBT(2)+RUB*WTT(3) \quad ALF = \frac{\sqrt{3}}{2}$$

$$VUT(3,1)=VBT(3)-RUB*WTT(2)$$

AXIAL STATION B

$$VUT(1,2)=VBT(1)-ALF*RUB*WTT(3) \quad BET = \sqrt{2}$$

$$VUT(2,2)=VBT(2)-.5*RUB*WTT(3)$$

$$VUT(3,2)=VBT(3)+.5*RUB*WTT(2)+ALF*RUB*WTT(1)$$

AXIAL STATION C

$$VUT(1,3)=VBT(1)+ALF*RUB*WTT(3)$$

$$VUT(2,3)=VBT(2)-.5*RUB*WTT(3)$$

$$VUT(3,3)=VBT(3)+.5*RUB*WTT(2)-ALF*RUB*WTT(1)$$

RADIAL STATION U

$$VUT(1,4)=VBT(1)-RUB*WTT(3)/BET$$

$$VUT(2,4)=VBT(2)+RUB*WTT(3)/BET$$

$$VUT(3,4)=VBT(3)-RUB*WTT(2)/BET+RUB*WTT(1)/BET$$

RADIAL STATION V

$$VUT(1,5)=VBT(1)+RUB*WTT(3)/BET$$

$$VUT(2,5)=VBT(2)+RUB*WTT(3)/BET$$

$$VUT(3,5)=VBT(3)-RUB*WTT(2)/BET-RUB*WTT(1)/BET$$

TRANSFORM INTO LAT. COORD.

$$\overline{VUL} = |DLT| \overline{VUT}$$

BEARING GAP RELATIVE MOTION

AXIAL GAP RATES AT A,B&C

$$RUGD(3,1)=VUL(3,1)-VA3$$

$$RUGD(3,2)=VUL(3,2)-VB3$$

$$RUGD(3,3)=VUL(3,3)-VC3$$

RADIAL GAP RATES AT U&V

$$RUGD(1,4)=VUL(1,4)-VU1$$

$$RUGD(2,4)=VUL(2,4)-VU2$$

$$RUGD(1,5)=VUL(1,5)-VV1$$

$$RUGD(2,5)=VUL(2,5)-VV2$$

AVERAGE BEARING GAPS AND GAP RATES
 $PX = (RUQ(1,4) + RUQ(1,5)) / 2.$
 $PY = (RUQ(2,4) + RUQ(2,5)) / 2.$
 $PZ = (RUQ(3,1) + RUQ(3,2) + RUQ(3,3)) / 3.$
 $PXDT = (RUQD(1,4) + RUQD(1,5)) / 2.$
 $PYDT = (RUQD(2,4) + RUQD(2,5)) / 2.$
 $PZDT = (RUQD(3,1) + RUQD(3,2) + RUQD(3,3)) / 3.$
 LAMBDAS
 $LU = KPT * (YLU + T1T * YLUD)$
 $YLU = ((PX + PY) / BET - YLU) / T2T$
 $LV = KPT * (YLV + T1T * YLVD)$
 $YLVD = ((PX - PY) / BET - YLV) / T2T$
 $LZ = KPT * (YLZ + T1T * YLZD) * MTC$
 $YLZD = (PZ / 1. - YLZ) / T2T$
 PHCMD = 0.00
 $PHERR = -ATT(1) + PHCMD$
 $LPHI = KP * (-PHERR) + KR * WTT(1)$
 THCMD = .523600
 $THERR = -ATT(2) + THCMD$
 $LTHE = KP * (-THERR) + KR * WTT(2)$
 PSICMD = 0.
 $PSIERR = PSICMD - ATT(3)$
 $LPSI = KPRL * (-PSIERR) + KR * WTT(3)$
 $FWP = -LPSI / (RUB + CXROC)$
 $FWC = FWP * MTC * (LU * (CYROC - CXROC) + LV * (CYROC + CXROC))$
 $/(BET * (RUB + CXROC))$
 $FAP = -LPHI + CZROC * MTC * LU / BET - CZROC * MTC * LV / BET - CYROC * LZ$
 $FBP = -LTHE - CZROC * MTC * LU / BET - CZROC * MTC * LV / BET + CXROC * LZ$
 $FCP = -LZ$
 ACTUATOR FORCE COMMANDS
 $FAC = -2. * FBP / (3. * RQVC) + FCP / 3.$
 $FBC = GAM * FAP / (3. * RQVC) + FBP / (3. * RQVC) + FCP / 3.$
 $FCCC = -GAM * FAP / (3. * RQVC) + FBP / (3. * RQVC) + FCP / 3.$
 $FUC = MTC * LU + FWC / BET$
 $FVCC = -MTC * LV - FWC / BET$

NOTE:

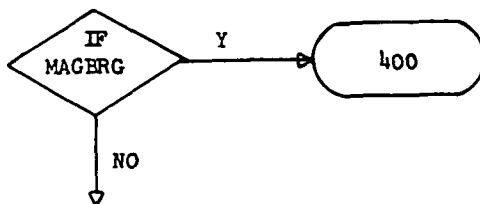
Proximeter readings are derived along x - y coordinates for convenience. In actual case, they're derived in U - V coordinates.

CENTERING SERVOS

VERNIER POINTING SERVOS

ROLL SERVO

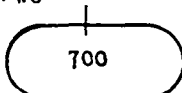
CONTROL AND
DECOUPLING
LAW



IDEAL BEARINGS

FA=FAC
 FB=FBC
 FC=FCCC
 FU=FUC
 FV=FVCC
 FW=FWC

MAG BEARING FORCES
 APPLIED TO TELESCOPE



400

NON LINEAR MAGNETIC ACTUATOR MODEL

```

SETUP ,INPUTS TO MAGNETIC ACTUATOR DO LOOP **
FCMD(1)=FAC
FCMD(2)=FBC
FCMD(3)=FCCC
FCMD(4)=FUC
FCMD(5)=FVCC
DLG(1)=RUQ(3,1)
DLG(2)=RUQ(3,2)
DLG(3)=RUQ(3,3)
DLG(4)=(RUQ(1,4)+RUQ(2,4))/BET
DLG(5)=(RUQ(1,5)-RUQ(2,5))/BET
DO 811 I=1,5
  DLGM(I)=DLG(I)
DLGD(1)=RUQD(3,1)
DLGD(2)=RUQD(3,2)
DLGD(3)=RUQD(3,3)
DLGD(4)=(RUQD(1,4)+RUQD(2,4))/BET
DLGD(5)=(RUQD(1,5)-RUQD(2,5))/BET
INITIALIZATION OF MBA S **
IF(TIME.GT.0.) GO TO 885
DO 810 I=1,5
  IC1(I)=(1.-GAPKM(I)*DLGM(I))*IO(I)
  IC2(I)=(1.+GAPKM(I)*DLGM(I))*IO(I)
  I1D(I)=0.
  I2D(I)=0.
  V1P(I)=RD(I)*IC1(I)
  V2P(I)=RD2(I)*IC2(I)
  I1(I)=IC1(I)
  I2(I)=IC2(I)
  V1PD(I)=0.
  V2PD(I)=0.
  I1DD(I)=0.
  I2DD(I)=0.
  CONTINUE
  CONTINUE
END OF INITIALIZATION **
DO 890 I=1,5
  IC1(I)=IO(I)+CK(I)*FCMD(I)-GAPKM(I)*DLGM(I)*CK(I)+FCMD(I)-GAP
  IKM(I)*DLGM(I)*IO(I)
  IE1(I)=50.*(IC1(I)-I1(I))
  IF(IE1(I).GT.15.) IE1(I)=15.
  IF(IE1(I).LT.-15.) IE1(I)=-15.
  V1PD(I)=KIA(I)*IE1(I)/50.
  V1(I)=V1P(I)+KPA(I)*IE1(I)/50.
  IF(V1(I).GT.V1MX(I)) V1(I)=V1MX(I)
  IF(V1(I).LT.-V1MX(I)) V1(I)=-V1MX(I)
  CON1(I)=(1.-GAPK(I)*DLG(I))
  CON2(I)=CON1(I)*CON1(I)
  I1D(I)=(V1(I)-RD(I)*I1(I)-(GAPK(I)*LG(I)*DLGD(I)*I1(I))
  /CON2(I))/(LL1(I)+LG(I)/CON1(I))

```

MAG ACTUATOR CONT.

```

FOUT1(I)=I1(I)*I1(I)*CON3(I)/CON2(I)
IC2(I)=IO(I)-CK(I)*FCMD(I)-GAPKM(I)*DLGM(I)*
CK(I)*FCMD(I)+GAPKM(I)*DLGM(I)*IO(I)
IE2(I)=50.*(TC2(I)-I2(I))
IF(IE2(I).GT.15.) IE2(I)=15.
IF(IE2(I).LT.-15.) IE2(I)=-15.
V2PD(I)=KIB(I)*IE2(I)/50.
V2(I)=V2P(I)+KPB(I)*IE2(I)/50.
IF(V2(I).GT.V2MX(I)) V2(I)=V2MX(I)
IF(V2(I).LT.-V2MX(I)) V2(I)=-V2MX(I)
CON4(I)=(1.+GAPK(I)*DLG(I))
CON5(I)=CON4(I)*CON4(I)
I2D(I)=(V2(I)-RD2(I)*I2(I)+(GAPK(I)*LG2(I)*DLGD(I)*I2(I))
/CON5(I))/(LL12(I)+LG2(I)/CON4(I))
FOUT2(I)=I2(I)*I2(I)*CON6(I)/CON5(I)
FTOT(I)=FOUT1(I)-FOUT2(I)

```

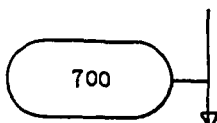
CONTINUE

RELABEL ACTUATOR FORCE OUTPUTS **

```

FA=FOT(1)
FB=FOT(2)
FC=FOT(3)
FU=FOT(4)
FV=FOT(5)
FW=FWC

```



COMPUTE ROLL GIMBAL ANGLE **

```

SROLR=DLT(2,1)
CROLR=DLT(1,1)
ROLR=ATAN2(SROLR,CROLR)

```

CABLE DYNAMICS **

IF(CABLE) GO TO 604

```

FCABX=0.
FCABY=0.
FCABZ=0.
TCABX=0.
TCABY=0.
TCABZ=0.

```

GO TO 675

CONTINUE

```

FCABX=-CABKX*PX
FCABY=-CABKY*PY
FCABZ=-CABKZ*PZ
TCABX=-CABTX*PHTR
TCABY=-CABTY*THTR
TCABZ=-CABTZ*ROLR
CONTINUE

```

LATERAL GIMBAL DYNAMICS

BEARING FORCES AT BEARING CNTR IN LATERAL COORDS

```

FVL(1)=(FU+FV)/BET+FCABX
FVL(2)=(FU-FV)/BET-FW+FCABY
FVL(3)=FA+FB+FC+FCABZ

```


BEARING TORQUES AT BEARING CNTR IN LATERAL COORDS

TVL(1)=ALF*RQV*(FB-FC)+TCABX
TVL(2)=RQV/2.*(FB+FC)-RQV*FA+TCABY
TVL(3)=FW*RUB+TCABZ

BEARING TORQUE AT CTR. OF LAT. GIMBAL IN LAT. COORD.

$$\overline{TGL} = \overline{TVL} + \overline{RVG} \times \overline{FVL}$$

RELATIVE \angle 'S PHTR + THTR BETWEEN TELESCOPE AND LAT. GIMBAL

$$PHTR = \sqrt{3} \ (RUQ(3,2) - RUQ(3,3)) / (3 \ RQVC)$$

$$THTR = (RUQ(3,2) + RUQ(3,3) - 2RUQ(3,1)) / (3 \ RQVC)$$

LATERAL GIMBAL SERVO WITH FRICTION MODEL

IF(TF2.GT. TF2MAX) TF2= TF2MAX
IF(TF2.LT.-TF2MAX) TF2=-TF2MAX
LATCMD=0.00
LERR=LATCMD-ALL(1)
TLL(1)=KP2*(YLL+T1L*YLLD)
YLLD=(LERR-YLL)/T2L
IF(GIMBFR) TLL(1)=TLL(1)-TF2

TOTAL LATERAL GIMBAL TORQUE

$$\overline{TLLT}(1) = \overline{TLL}(1) - \overline{TGL}(1)$$

LATERAL GIMBAL MOMENTUM DERIVATIVE

$$\dot{HLL}(1) = TLLT - WLL(2) \ HLL(3) + WLL(3) \ HLL(2)$$

WHERE

$$HLL(2) = IL(1,2) \ WLL(1) + IL(2,2) \ WLL(2) + IL(2,3) \ WLL(3)$$

$$HLL(3) = IL(1,3) \ WLL(1) + IL(2,3) \ WLL(2) + IL(3,3) \ WLL(3)$$

ELEVATION GIMBAL DYNAMICS

BEARING FORCE IN ELEV. COORD.

$$\overline{FVE} = \left| DLE \right|^T \overline{FVL}$$

BEARING TORQUES IN ELEV. COORD.

$$\overline{TGE} = \left| DLE \right|^T \begin{pmatrix} \overline{TLL}(1) \\ \overline{TGL}(2) \\ \overline{TGL}(3) \end{pmatrix} + \overline{RLE} \times \overline{FVE}$$

ELEVATION GIMBAL SERVO WITH FRICTION MODEL

```

IF(TF1.GT. TF1MAX) TF1= TF1MAX
IF(TF1.LT.-TF1MAX) TF1=-TF1MAX
ELECMD=.5236D0
ELERR=ELECMD-AEE(2)
TEE(2)=KP1*(YEE+T1E*YEED)
YEED=(ELERR-YEE)/T2E
IF(GIMBFR) TEE(2)=TEE(2)-TF1

```

TOTAL ELEV. GIMBAL TORQUE

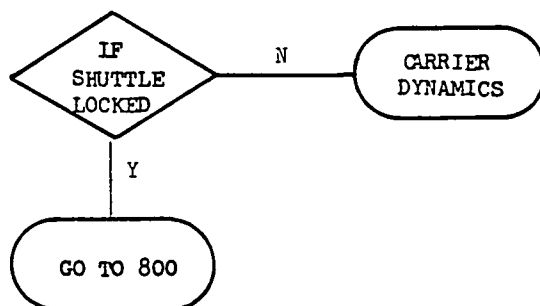
```
TEET(2) = TEE(2) - TGE(2)
```

ELEVATION GIMBAL MOMENTUM DERIVATIVE

```

HEE(1) = IE(1,1)WEE(1) + IE(1,2)WEE(2) + IE(1,3)WEE(3) + HLL(1)
TEMP = SINALL(1)HLL(2) + COSALL(1)HLL(3)
HEE(3) = IE(1,3)WEE(1) + IE(2,3)WEE(2) + IE(3,3)WEE(3) + TEMP
HEE(2) = WEE(1)HEE(3) - WEE(3)HEE(1) + TEET(2)

```



CARRIER DYNAMICS

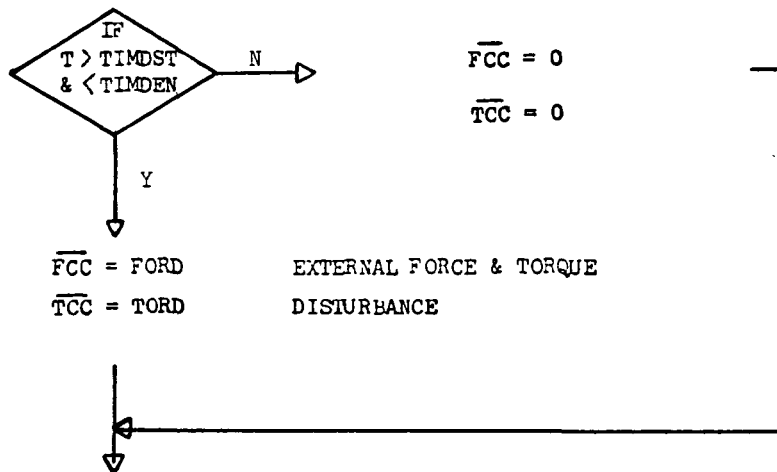
BEARING FORCE IN CARRIER COORD

$$\overline{FVC} = \overline{peq}^T \overline{FVE}$$

BEARING TORQUES IN CARRIER COORD

$$\overline{TGC} = \overline{peq}^T \begin{pmatrix} TGE(1) \\ TEE(2) \\ TGE(3) \end{pmatrix}$$

DISTURBANCE CONTROL



CARRIER VEL. DERIVATIVES

$$\dot{\overline{VCC}} = \frac{1}{MCEL} (\overline{FCC} - \overline{FVC})$$

TOTAL CARRIER TORQUE

$$\overline{TCCT} = \overline{TCC} - \overline{TGC} - \overline{RGC} \times \overline{FVC}$$

CARRIER MOMENTUM DERIVATIVES

$$\overline{HCC} = \overline{TCCT} - \overline{WCC} \times \overline{HCC}$$

800

TELESCOPE DYNAMICS

BEARING FORCES ON TELESCOPE

$$\overline{FBT} = |\overline{DLT}|^T \overline{FVL}$$

BEARING TORQUES ON TELESCOPE

$$\overline{TBT} = |\overline{DLT}|^T \overline{TVL}$$

TELESCOPE VELOCITY DERIVATIVES

$$\dot{\overline{VTT}} = \frac{1}{MT} \overline{FBT}$$

TOTAL TELESCOPE TORQUE

$$\overline{TTTT} = \overline{TBT} + \overline{RBT} \times \overline{FBT}$$

TELESCOPE MOMENTUM DERIVATIVES

$$\dot{\overline{\text{HTT}}} = \overline{\text{TTTT}} - \overline{\text{WTT}} \times \overline{\text{HTT}}$$

PRINT OUTPUT



INTEGRATION

INTEGRATION

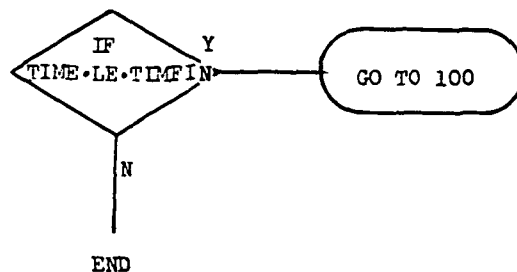
```
HCC(1)=HCC(1)+HCCD(1)*TIMED
HCC(2)=HCC(2)+HCCD(2)*TIMED
HCC(3)=HCC(3)+HCCD(3)*TIMED
ACC(1)=ACC(1)+ACCD(1)*TIMED
ACC(2)=ACC(2)+ACCD(2)*TIMED
ACC(3)=ACC(3)+ACCD(3)*TIMED
HLL(1)=HLL(1)+HLLD(1)*TIMED
ALL(1)=ALL(1)+ALLD(1)*TIMED
TF2=TF2+KF2MAX*ALLD(1)*TIMED
HEE(2)=HEE(2)+HEED(2)*TIMED
AEE(2)=AEE(2)+AEED(2)*TIMED
TF1=TF1+KF1MAX*AEED(2)*TIMED
HTT(1)=HTT(1)+HTTD(1)*TIMED
HTT(2)=HTT(2)+HTTD(2)*TIMED
HTT(3)=HTT(3)+HTTD(3)*TIMED
ATT(1)=ATT(1)+ATTD(1)*TIMED
ATT(2)=ATT(2)+ATTD(2)*TIMED
ATT(3)=ATT(3)+ATTD(3)*TIMED
RTI(1)=RTI(1)+RTID(1)*TIMED
RTI(2)=RTI(2)+RTID(2)*TIMED
RTI(3)=RTI(3)+RTID(3)*TIMED
RCI(1)=RCI(1)+RCID(1)*TIMED
RCI(2)=RCI(2)+RCID(2)*TIMED
RCI(3)=RCI(3)+RCID(3)*TIMED
RUQ(3,1)=RUQ(3,1)+RUQD(3,1)*TIMED
RUQ(3,2)=RUQ(3,2)+RUQD(3,2)*TIMED
RUQ(3,3)=RUQ(3,3)+RUQD(3,3)*TIMED
RUQ(1,4)=RUQ(1,4)+RUQD(1,4)*TIMED
RUQ(2,4)=RUQ(2,4)+RUQD(2,4)*TIMED
RUQ(1,5)=RUQ(1,5)+RUQD(1,5)*TIMED
RUQ(2,5)=RUQ(2,5)+RUQD(2,5)*TIMED
VTT(1)=VTT(1)+VTTD(1)*TIMED
VTT(2)=VTT(2)+VTTD(2)*TIMED
VTT(3)=VTT(3)+VTTD(3)*TIMED
VCC(1)=VCC(1)+VCCD(1)*TIMED
VCC(2)=VCC(2)+VCCD(2)*TIMED
VCC(3)=VCC(3)+VCCD(3)*TIMED
YLU=YLU+YLU*TIMED
YLV=YL*YLV*TIMED
YLZ=YLZ+YLZ*TIMED
```

```

YLL=YLL+YLLD*TIMED
YEE=YEE+YEED*TIMED
IF(MAGBRG) GOTO 900
GOTO 910
900 CONTINUE
**INTEGRATION OF ACTUATOR VARIABLES **
DO 891 I=1,5
V1P(I)=V1P(I)+(V1PD(I)+V1PDD(I))*0.5*TIMED
V2P(I)=V2P(I)+(V2PD(I)+V2PDD(I))*0.5*TIMED
IF(V1P(I).GT.20.) V1P(I)=20.
IF(V1P(I).LT.-20.) V1P(I)=-20.
IF(V2P(I).GT.20.) V2P(I)=20.
IF(V2P(I).LT.-20.) V2P(I)=-20.
I1(I)=I1(I)+(I1D(I)+I1DD(I))*0.5*TIMED
I2(I)=I2(I)+(I2D(I)+I2DD(I))*0.5*TIMED
V1PDD(I)=V1PD(I)
V2PDD(I)=V2PD(I)
I1DD(I)=I1D(I)
I2DD(I)=I2D(I)

```

TIME = TIME + TIMED



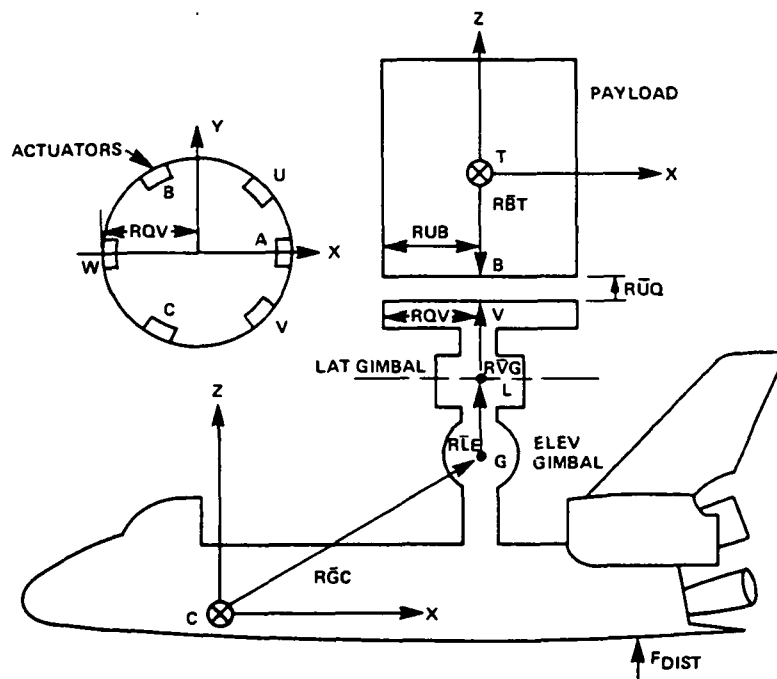


Figure 152
ASPS Digital System Simulation

Page Intentionally Left Blank

APPENDIX C

MAGNETIC ACTUATOR LINEAR AND NONLINEAR DYNAMIC MODELS AND PROTOTYPE TEST RESULTS

This appendix presents the MBA design calculations and equivalent circuit. Nonlinear and linear dynamic models are derived from the equivalent circuit, a prototype actuator was tested and the data is compared to the dynamic models. Breadboard electronics were fabricated and tested with the prototype actuator to verify the linearization and compensation system.

The design parameters of the magnetic bearing required for dynamic modeling and electronic compensation design are:

- the force, current, air gap relationship
- the ac equivalent circuit

Several sources exist to cause deviations from the idealized force, current, air gap relationship whereby

$$F = K I^2 / g^2 \quad F = \text{force} \quad (C1)$$

I = excitation current

g = air gap

One source is stator or rotor iron permeability changes over the operating flux range which causes deviations in the current squared relationship. These can be caused either by saturation at high flux levels or by use of materials with low initial permeability. In good design practice, however, high initial permeability materials are selected and cross sections are designed to inhibit saturation such that the current square law applies.

Two sources exist to cause deviations from the inverse gap square law:

1. Some of the permeance leakage terms are not inversely related to gap, thus their derivative is not inversely related to gap squared.
2. The permeance of the iron is significant, therefore for air gap changes, the magnetomotive force (mmf) distribution between the gap and iron permeance changes.

The second effect is most predominant; however, knowing it exists, compensation is readily available.

The ac equivalent circuit is shown in Figure 153. It consists of

R_D : winding dc resistance

L_1 : leaking inductance

R_A : AC resistance (allotment for ac iron losses)

L_2 : circuit inductance presented as a complex inverse gap relationship indicative of the significant permeance effect.

The force, current, gap relationship for any frequency can then be obtained from the equivalent circuit using the relationship

$$(C2) \quad F = \frac{1}{2} I^2 \frac{dL_2}{dg}$$

where I is the current through the L_2 branch.

The calculation consists of correlation of these equivalent circuit parameters to the mechanical dimensions and material properties. This process starts with the assumption of an equivalent magnetic circuit shown in simplified analog form in Figure 154. Assuming a complete set of actuator dimensions, the respective permeances of the magnetic circuit are calculated for each of three gap conditions; nominal, maximum, and minimum. The equivalent circuit parameters are then calculated as follows:

1. R_D is calculated from the coil dimensions and an assumed wire size. At the conclusion of the calculations, if the input voltage is improper, this parameter is iterated and the entire calculation is repeated.
2. The leakage inductance LL is

$$LL = N^2 P_\ell \quad (C3)$$

where N is the number of turns in the stator winding and P_ℓ is the leakage path permeance.

3. For each nominal, minimum, and maximum air gap, the circuit inductance (L_2) terms are calculated by

$$L_2 = L_G \frac{g_0}{a + bg} \quad (C4)$$

where L_G is the circuit inductance at nominal air gap.

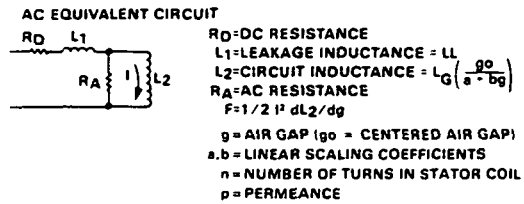


Figure 153
Magnetic Bearing Assembly Design Calculations

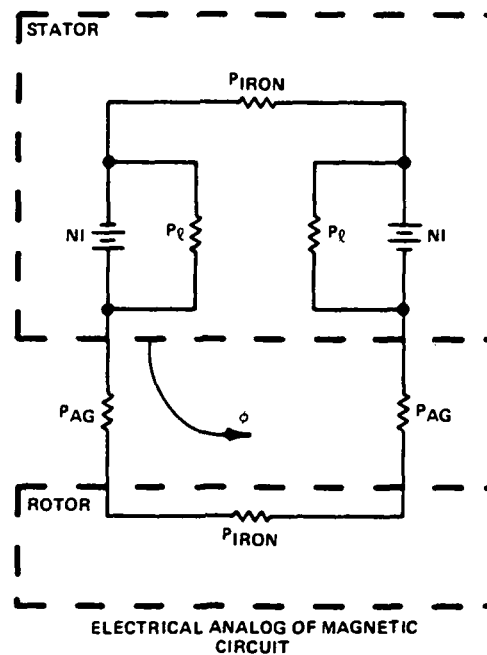


Figure 154
Electrical Analog of Magnetic Circuit

4. A simplified R_A is calculated from

$$R_A = \frac{12}{t^2} \frac{\rho}{\mu} L(\text{iron}) \quad (C5)$$

where ρ is iron resistivity

μ is iron permeability

t is iron thickness

$L(\text{iron})$ is inductance contribution of the iron presence

A summary of the calculation results for the MBA model fabricated is shown in Figure 155. Shown are the ac equivalent circuit for each actuator and several parameters at the nominal and gap travel limits.

Note that the sealing coefficients, a and b , may be approximated by $a \approx 0$, $b \approx 1$. If this substitution is made, the loop equations can be written which describe the dynamics associated with a single-magnetic bearing solenoid equivalent circuit, as shown in Figure 156. Note that two voltage components result from the time differentiation of

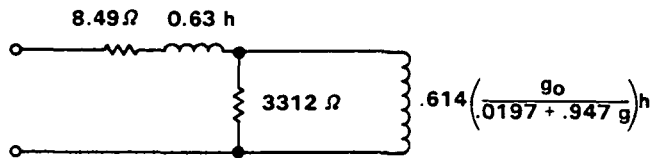
$$\left[\frac{L_G}{(1 - \xi \Delta g)} I_1 \right] \quad (C6)$$

The second term is known as the "speed voltage" and has a small effect on the ASPS. Differentiation of the coupling inductance with respect to position results in the force equation; the attractive force is proportional to current-squared and is inversely proportional to gap-squared. Electronic linearization and gap compensation, as described in Section 2, is based on this force relationship.

Overall dynamics of the compensated MBA is shown in block diagram form in Figure 157a and 157b. Both sides (coils) in the model are identical, except for the sign of the Δg coefficients. This sign change reflects the fact that rotor motion which increases the gap of one solenoid, decreases the gap of the other.

These nonlinear dynamics can be linearized for a small motion about a nominal gap offset, Δg_0 , and a nominal load force, F_0 , shown in Figures 158a and 158b. On a linearized basis, the inverse gap-square law becomes a linear positive feedback stiffness around the rigid body dynamics, and the multiplier used for gap compensation linearizes to a negative feedback stiffness equal to the positive bearing stiffness. The linearized model was used for low-level frequency response analysis of the MBA while the nonlinear model was simulated to predict transient and high-level frequency response performance.

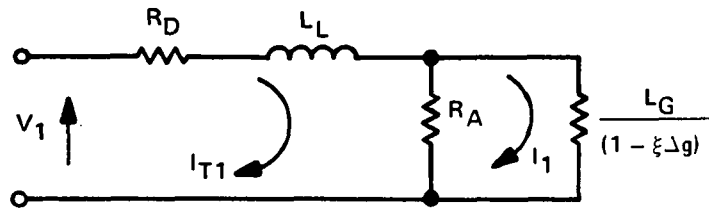
Figure 159 and 160 are photographs showing a prototype of the axial MBA which was built and tested to verify actuator sizing, the dynamic model, and the electronic compensation system. The bearing rotor was mounted to a force measurement system while the stator coils were connected to a freely moving mass as shown, or were rigidly fixed to the force fixture through a calibrated dividing head.



NOMINAL GAP (g_o) = 9.40 MM (.37 INCH)
 RANGE (Δg) = ($\pm .22$ INCH) ± 5.59 MM
 BIAS CURRENT = .483 AMPS
 AT 28.9 N (6.5 LBS_F)

	MINIMUM GAP	NOMINAL GAP	MAXIMUM GAP	UNITS
EXCITATION CURRENT	0.42	.967	1.51	AMPS
POWER	1.51	7.94	19.4	WATTS
INDUCTANCE	2.03	1.24	1.02	HENRIES

Figure 155
 Station Model Calculation Results



$$V_1 = R_D I_{T1} + L_L \dot{I}_{T1} + R_A (I_{T1} - I_1)$$

$$0 = R_A (I_{T1} - I_1) + \frac{L_G}{(1 - \xi \Delta g)} \dot{I}_1 + \xi (I_1) \frac{L_G}{(1 - \xi \Delta g)^2} \dot{\Delta g}_1$$

"SPEED VOLTAGE"

$$F_1 = \frac{I_1^2}{2} \frac{d}{dg} \left[\frac{L_G}{(1 - \xi \Delta g)} \right] = \frac{\xi L_G I_1^2}{2(1 - \xi \Delta g)^2} = \frac{K I_1^2}{g_0^2 (1 - \xi \Delta g)^2}$$

F_1 = DEVELOPED FORCE (N)

V_1 = APPLIED COIL VOLTAGE (VOLTS)

I_{T1} = TOTAL CURRENT THROUGH WINDING (AMPERES)

I_1 = CURRENT THROUGH CIRCUIT INDUCTANCE (AMPERES)

$$\xi \triangleq \frac{1}{g_0} \text{ (M}^{-1}\text{)}$$

$$K \triangleq \frac{\xi L_G g_0^2}{2} \text{ (N-M}^2\text{/AMP}^2\text{)}$$

Figure 156
Nonlinear Model Dynamics

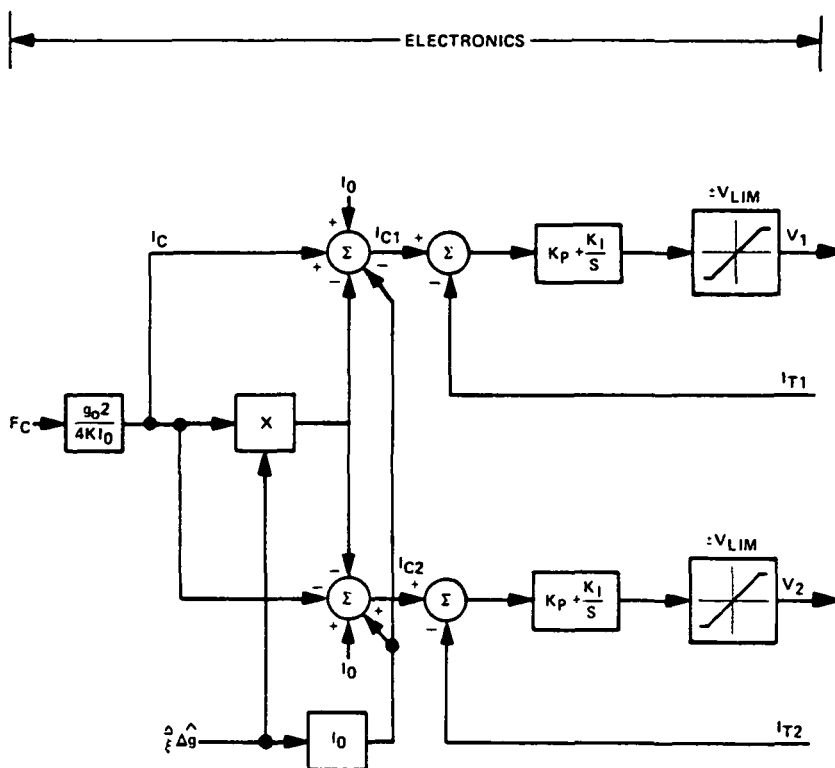


Figure 157a
Nonlinear Dynamic Model Magnetic Bearing Assembly

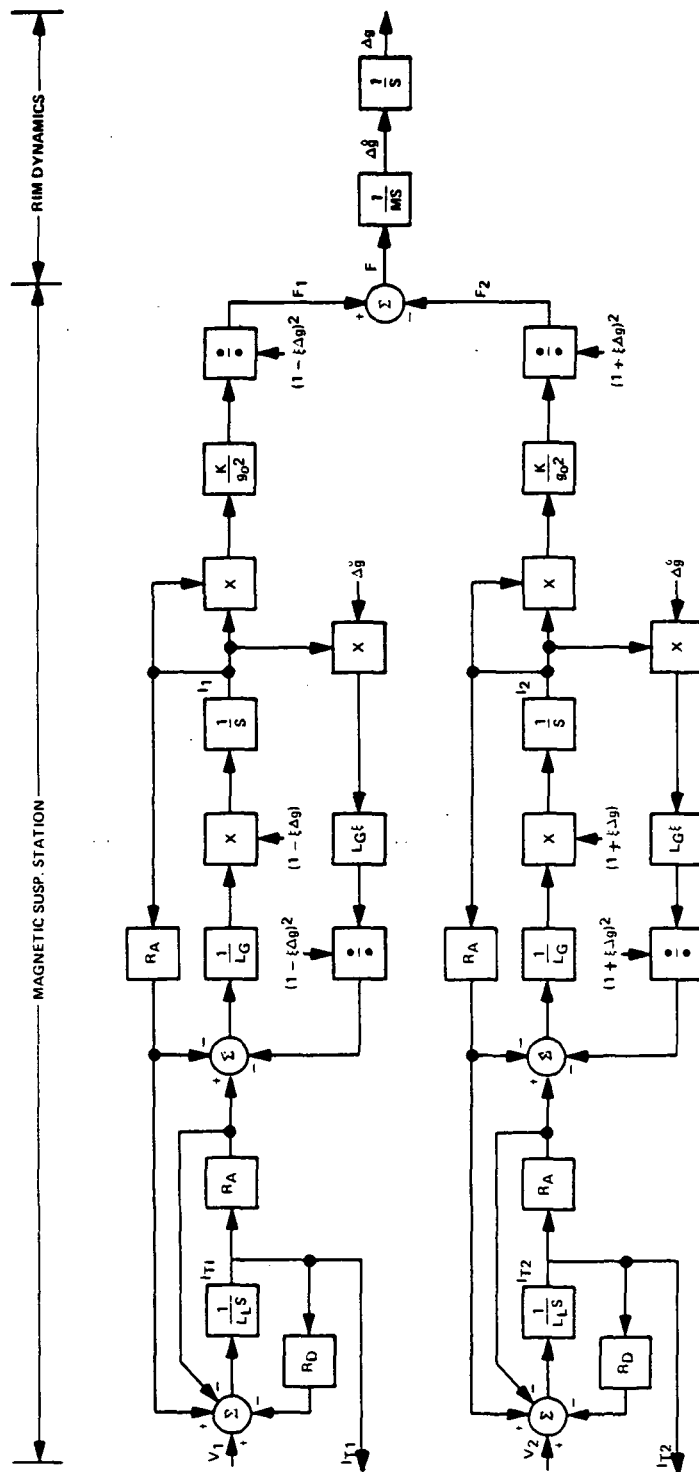
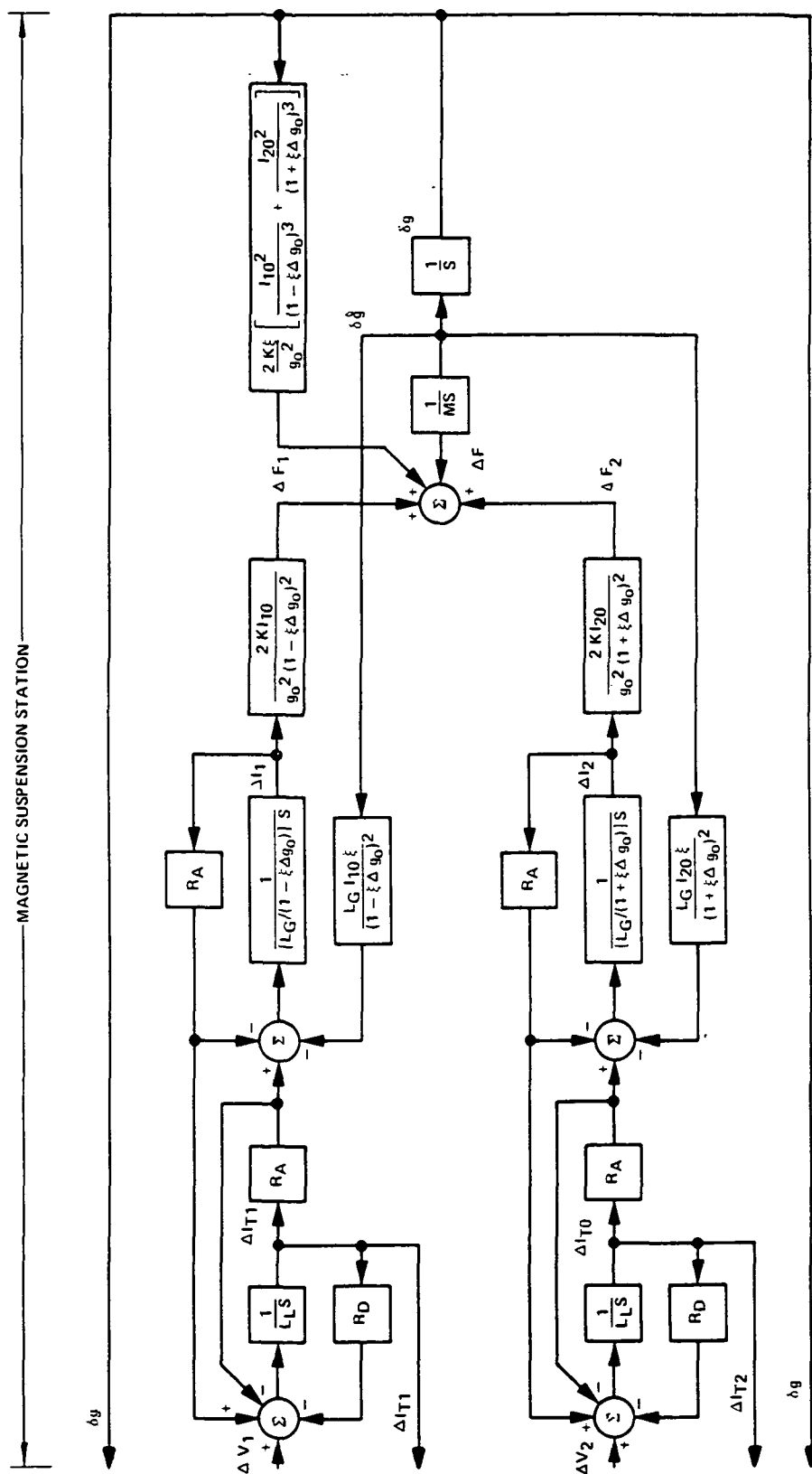


Figure 157b
Nonlinear Dynamic Model Magnetic Bearing Assembly



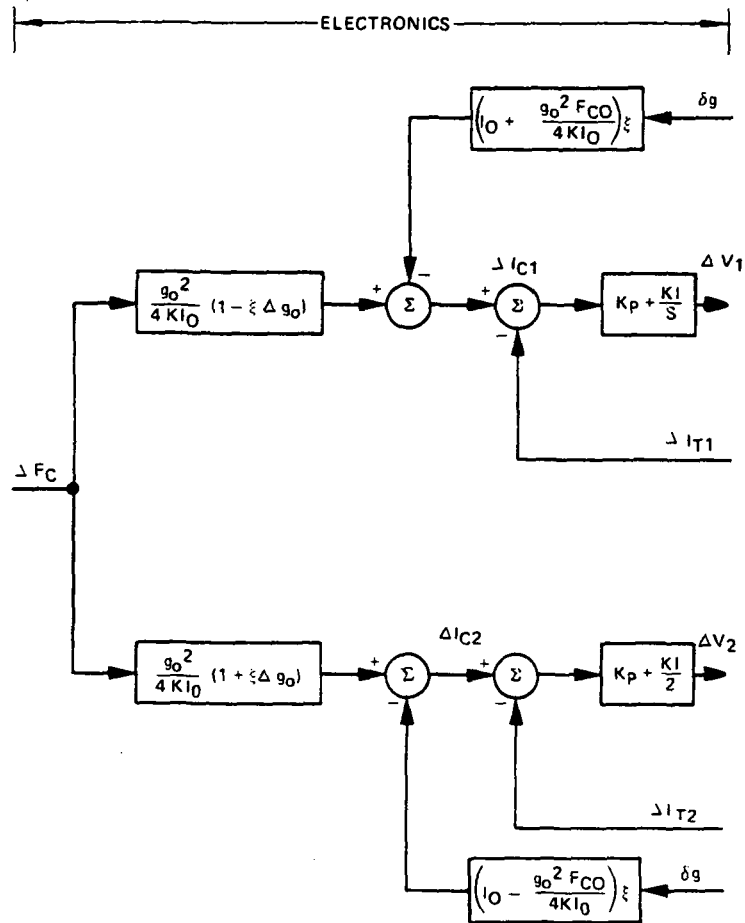


Figure 158b
Linearized Model Magnetic Suspension System

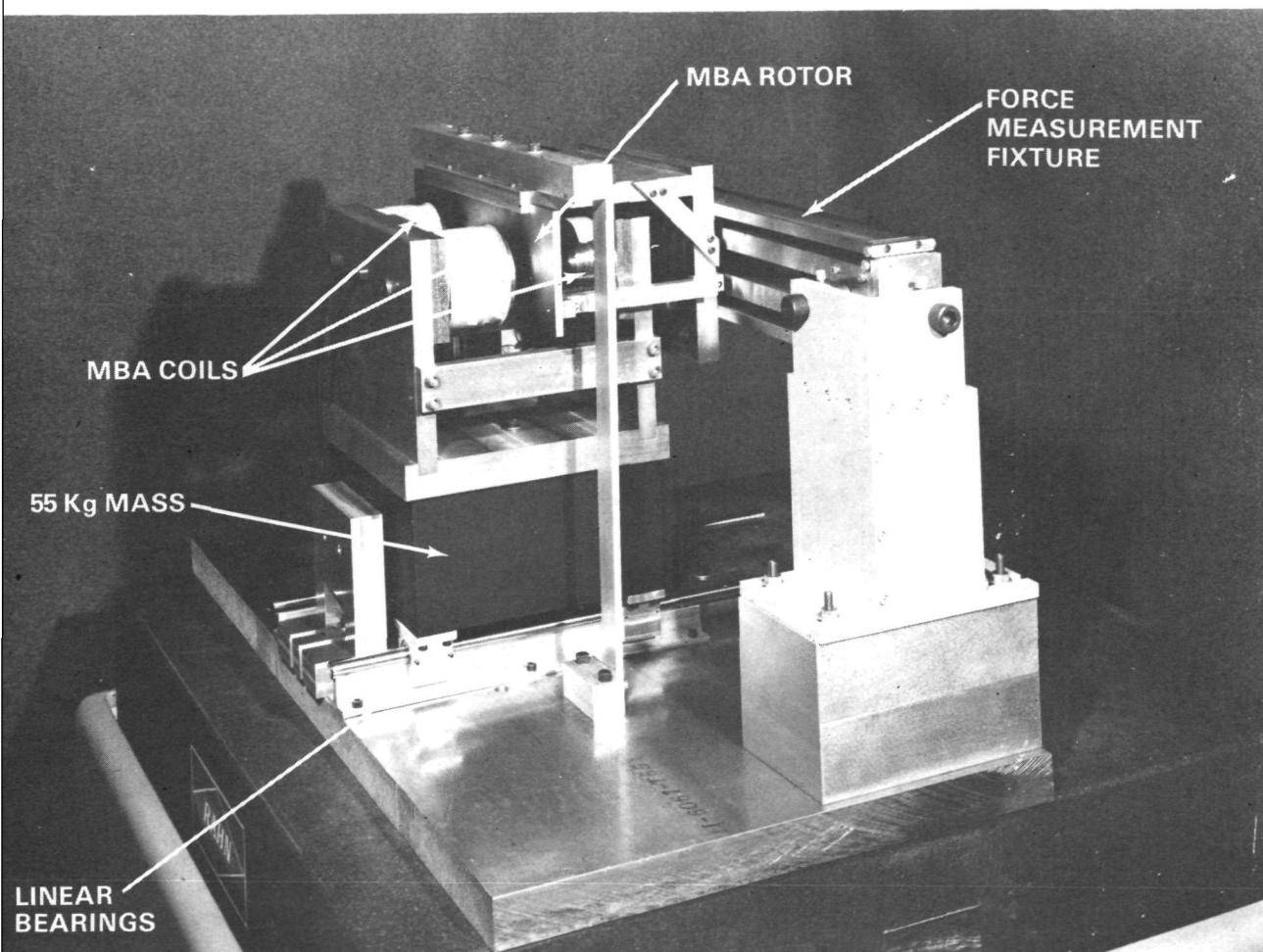


Figure 159
Prototype MBA Showing Test Mass

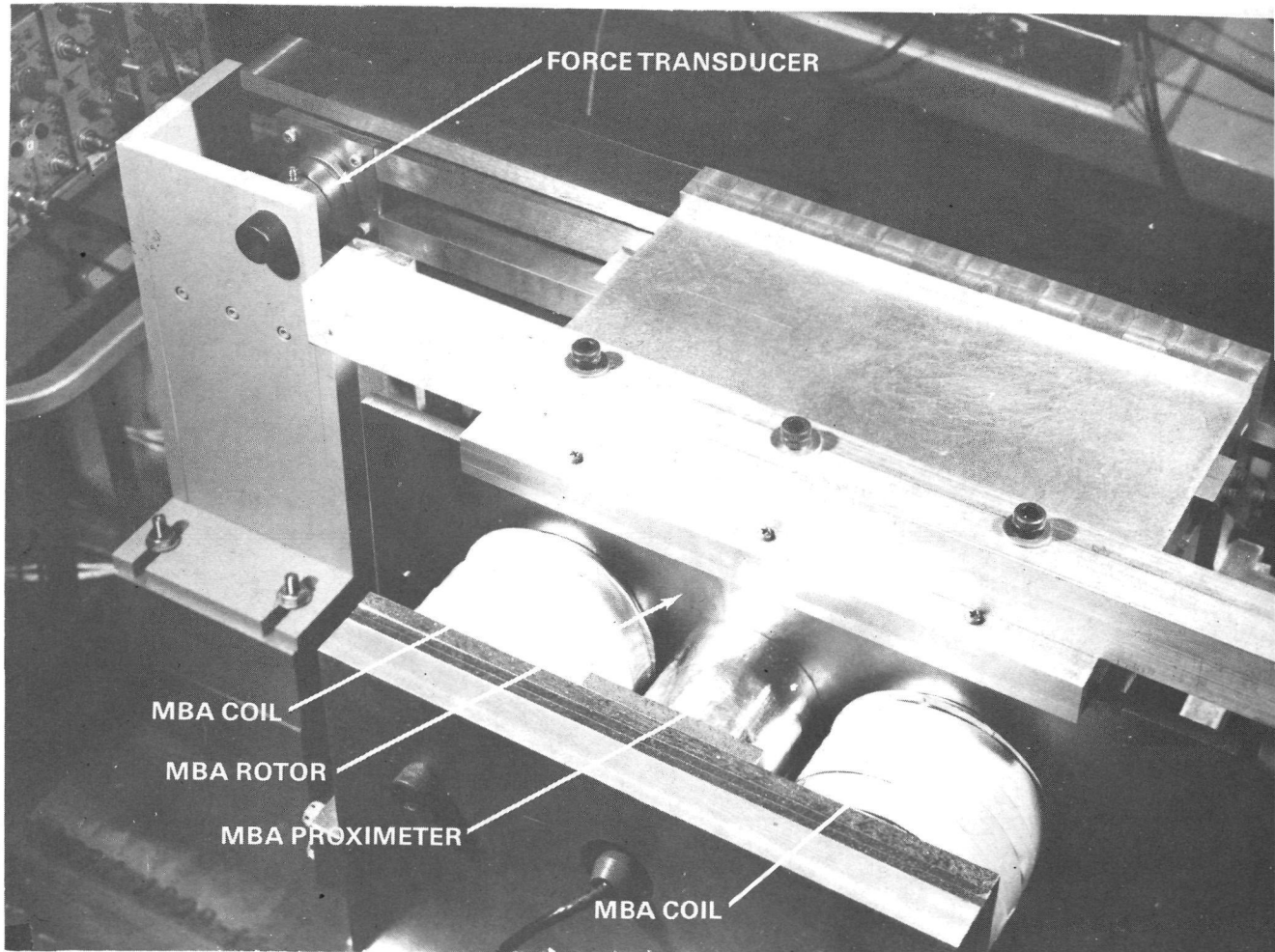


Figure 160
Prototype MBA Showing Proximeter

Determination of the force constant, K ; the gap coefficient, ξ , and the coupling inductance, L_G ; for the prototype bearing was made from analysis of static current-force-gap data as indicated in Figure 161 and 162. Both sides of the actuator produced identical square law current-force results. The data at nominal gap with an output of 4.45 N (1.0 lbf) was used to determine the force constant. The coupling inductance is not independent of the force constant, and is calculated directly from the same data. Parameter ξ , is used to account for the finite permeability in the iron. With no iron reluctance, it would equal simply $1/\mu_0 = 106.4 \text{ m}^{-1}$ (2.70 in⁻¹). The actual value on the prototype MBA was measured to be 101.6 m^{-1} (2.58 in⁻¹).

The leakage inductance and ac resistance affect the high-frequency input impedance of the actuator. If the ac resistance is assumed to be high in comparison to the dc resistance, and the gap fixed in its centered position, the input admittance transfer function can be calculated in terms of the equivalent circuit parameters. As listed on Figure 163, the dominant characteristic is a series R-L circuit comprised of the dc resistance and the total (leakage plus coupling) inductance. At higher frequency, a first order zero-pole pair occurs which is related to the ac resistance and the distribution of the inductance.

Input impedance measurements of the prototype MBA were made, and the phase angle data was used to calculate the ac resistance and leakage inductance. Figures 164 and 165 compare the hardware and model data at two gap locations. (Since the coupling inductance varies with the gap, both the high- and low-frequency impedance data change.) Good agreement is indicated.

Table 44 compares the theoretical and measured equivalent circuit values. Generally, good agreement exists except for leakage inductance. This is the most tenuous parameter to calculate or measure, and further modeling work is suggested in this area.

TABLE 44
COMPARISON OF THEORETICAL AND
MEASURED MODEL PARAMETERS

Parameter	Units	Theoretical	Measured
R_D	ohms	8.49	8.47
L_G	henry	.614	.640
ξ	m^{-1} (in ⁻¹)	100.8 (2.56)	101.6 (2.58)
R_A	ohm	3312	3417
L_L	henry	.63	.213

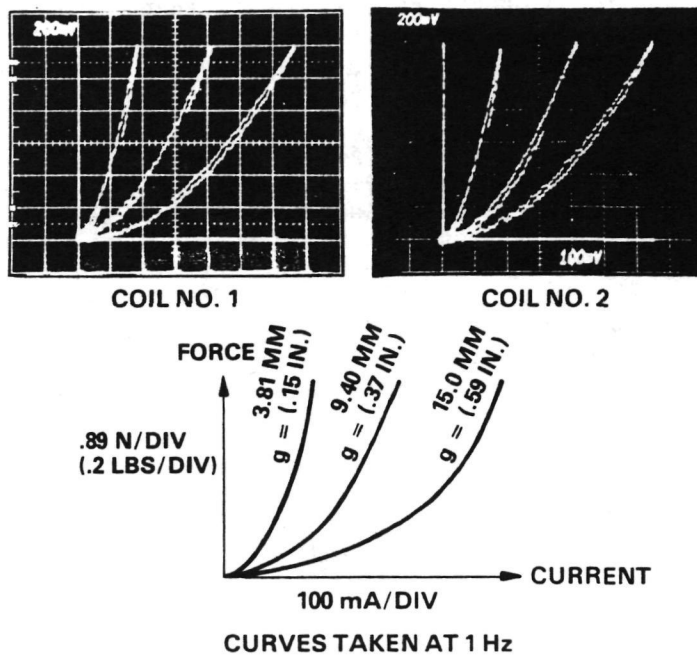


Figure 161
Coil Force Versus Current Characteristics

$$F = \frac{K I^2}{g_0^2 (1 - \xi \Delta g)^2}$$

WHEN $F = 1 \text{ LB}$

$\Delta g \text{ mm (IN.)}$	I
5.59 (.22)	.16
0 (0)	.37
-5.59 (-.22)	.58

USE $\Delta g = 0$ DATA TO DETERMINE K

$$K = \frac{F g_0^2}{I^2} = .00287 \frac{\text{NM}^2}{\text{AMP}^2}$$

$$\xi = \frac{1}{\Delta g} \left[1 - \frac{I}{g_0} \sqrt{\frac{K}{F}} \right] = 101.6 \text{ M}^{-1}$$

$$L_G = 2 \frac{K}{g_0^2} \frac{1}{(.2248 \text{ LBF/N}) (39.37 \text{ IN/M})} = .6398 \text{ HY.}$$

Figure 162
Determination of MBA Constants from Static Coil Measurements

FOR $R_A \gg R_D$

$$Y_{IN} = \frac{I_T}{V_1} = \frac{\left[\frac{L_G}{R_A} s + 1 \right]}{R_D \left[\left(\frac{L_L + L_G}{R_D} \right) s + 1 \right] \left[\frac{L_L L_G}{(L_L + L_G) R_A} s + 1 \right]}$$

SELECT L_L AND R_A TO MATCH PHASE DATA AT $\Delta g = 0$.

$R_A = 3417$ OHMS

$L_L = .2133$ HYS.

$R_D = 8.47$ OHMS (DIRECT MEASUREMENT)

$$Y_{IN} = \frac{\left[\frac{s}{2\pi f_1} + 1 \right]}{8.47 \left[\frac{s}{2\pi f_0} + 1 \right] \left[\frac{s}{2\pi f_2} + 1 \right]}$$

$\Delta g \text{ mm(IN.)}$	f_0 (Hz)	f_1 (Hz)	f_2 (Hz)
+5.59(+22)	2.17	1333	3882
(0)	1.58	850	3398
-5.59(-.22)	0.797	367	2917

WHERE Y_{IN} = LAPLACE TRANSFORMED INPUT ADMITTANCE OF COIL
(AMPS/VOLT)

f_0, f_1, f_2 = NATURAL FREQUENCIES OF TRANSFER FUNCTION
ROOTS (Hz)

Figure 163
Determination of MBA Constants from Coil
Input Impedance Measurements

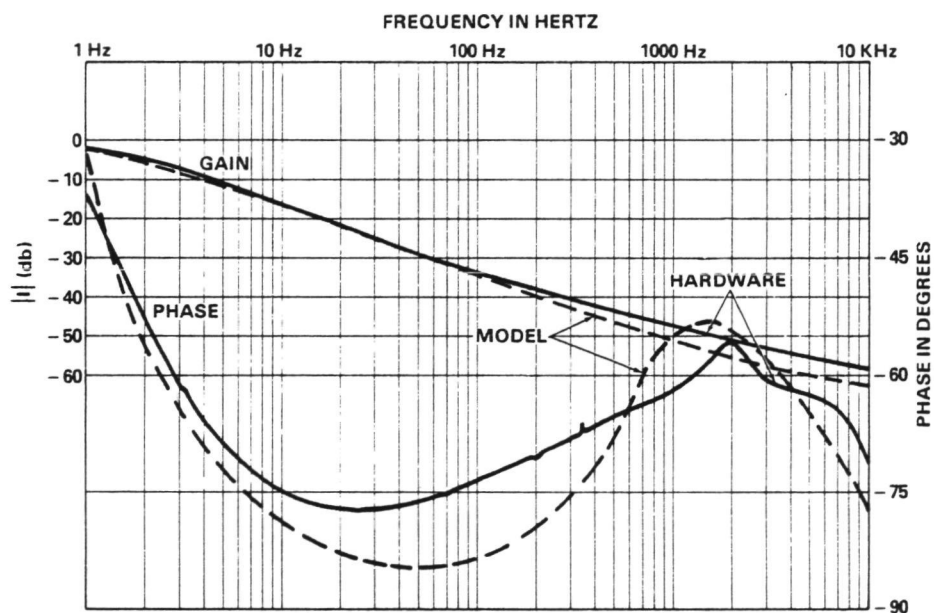


Figure 164
Coil Current/Voltage
Versus
Frequency, Gap = 9.40 mm (.37 inch)

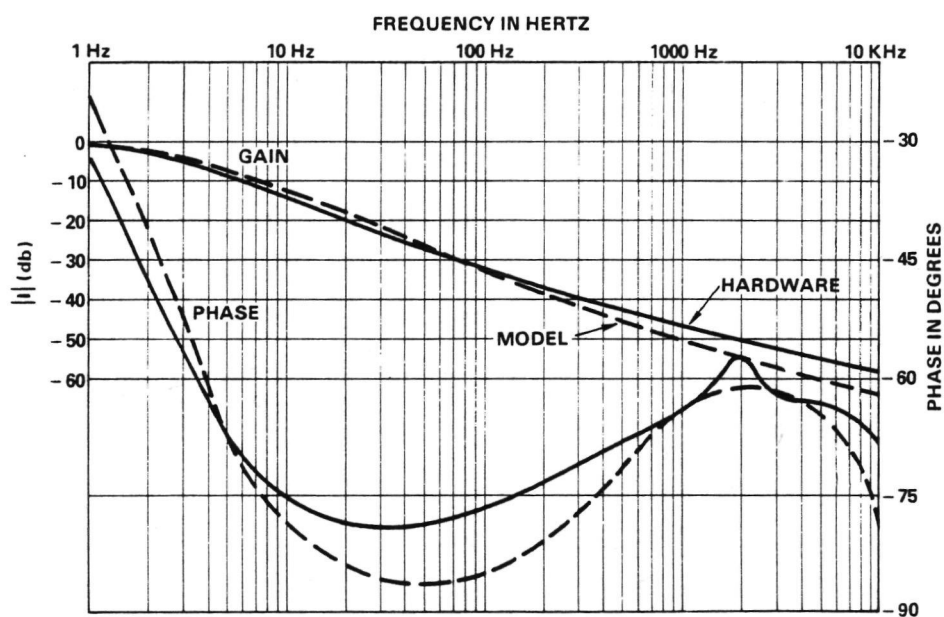


Figure 165
Coil Current/Voltage
Versus
Frequency, Gap = 15 mm (.59 inch)

Using breadboard electronics to provide current linearization and gap compensation, closed-loop system data were taken using the force measurement fixture. Figure 166 shows the high linearity of the actuator and the degree of gap compensation achieved. Better matching at high-force command could be achieved by adjusting the electronic gains and offsets used to provide the current and gap compensation, but the agreement at low-force commands was then worse. Since actuator linearity and gap compensation is most important during the vernier pointing mode where very low-force commands are required, the calibration shown was selected.

Figures 167 and 168 are closed-loop frequency responses of the hardware and model. The MBA test fixture contains structural modes above 70 Hz which results in the sharp peaks indicated. At large-force commands, (Figure 168), the voltage limit on the power driver creates a nonlinear roll-off due to $L \frac{dI}{dt} = V_{LIMIT}$. Note that the phase angle at low-frequency (e.g., 1 Hz) is not affected by this nonlinear roll-off.

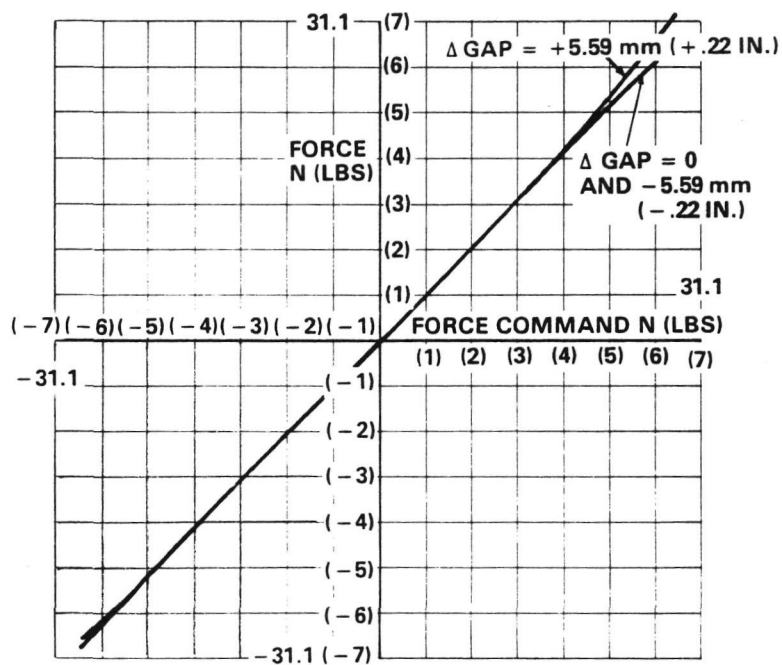


Figure 166
Prototype MBA Gap Compensation

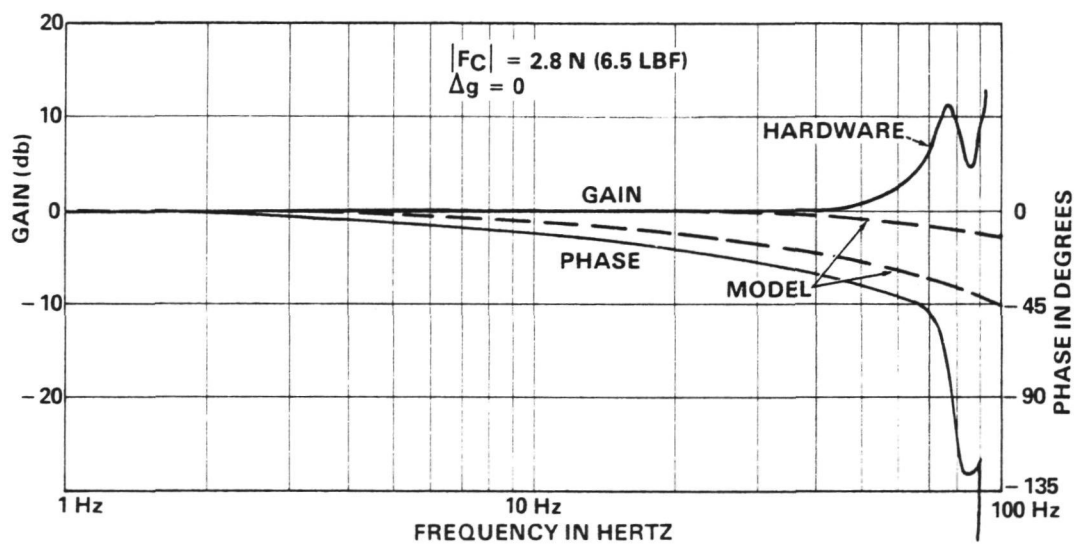


Figure 167
 Closed-Loop Frequency Response, F/F_C

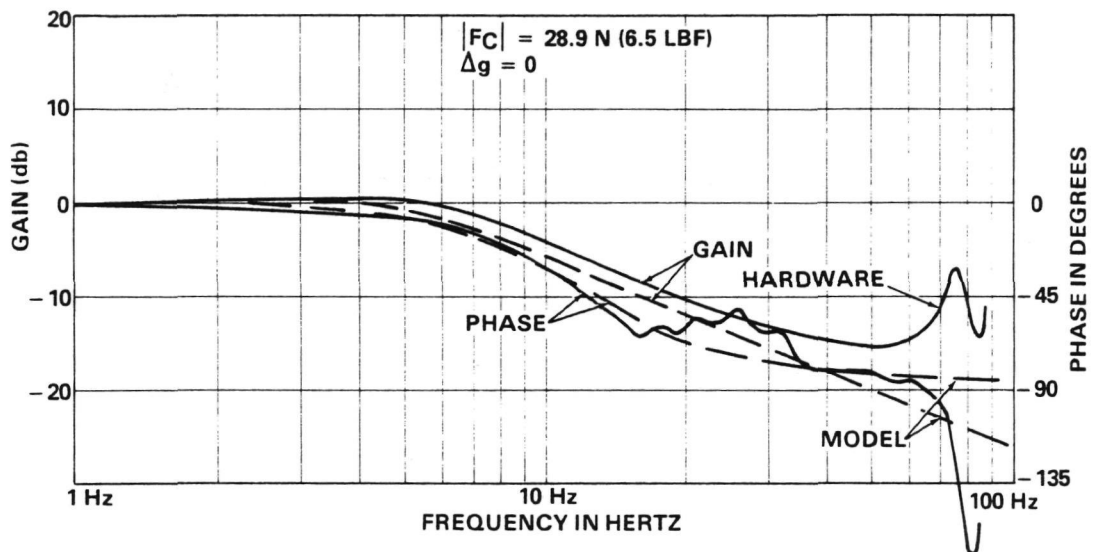


Figure 168
Closed-Loop Frequency Response, F/F_C

APPENDIX D

ROLL TORQUE MOTOR MODEL TEST REPORT

TEST: Cogging and Ripple Torque Measurement on an ac induction motor with a solid iron rotor.

DATE: 25 October 1976

Object

To demonstrate that the anomaly torques (cogging and ripple) of an ac induction motor with a solid iron rotor are less than .05 percent of the desired torque, which permits consideration of this device for use on the ASPS program.

Unit Tested

Stator - Two segmented stator Part No. 2501327 located 180 degrees apart.

Rotor - A copper plated, solid iron rotor, Part No. 255822 (tests were performed before and after removal of the copper plating).

Test Description

The torquer to be tested was mounted on a rotary platform on top of the air-bearing dynamometer, as depicted in Figure 169. Excitation was applied, as shown in Figure 170.

The air-bearing dynamometer consists of a gas supported member, stiffly supported in the translational axes and uninhibited rotationally (the sensing axis). A pick-off and actuator are mounted about the rotational axis and servo loop is closed between them making the actuator current proportional to the torque to hold the member rotationally at the pick-off null position. The rotor, of the torquer to be tested, is hard mounted to the gas supported member.

The rotary platform, to which the stator of the torquer to be tested is mounted, allows torque testing at various stator/rotor positions. It can be automatically driven through a motor/gear arrangement which allows a continuous plot to be obtained of torque versus relative rotor/stator position. During testing, a drive speed correspondent to 3.8 minutes/revolution was used.

Because the signal from the dynamometer electronics was noisy, with 60 Hz and 30 Hz, a 16 Hz low-pass filter was inserted between the recorder and dynamometer output. The low-pass filter is shown in Figure 171 and its frequency response is given in Figure 172. Since the filter characteristic is flat to 10 Hz, and the drive speed is 3.8 minutes per revolution, ripple and cogging data from 0 to 2280 cycle per revolution are obtained.

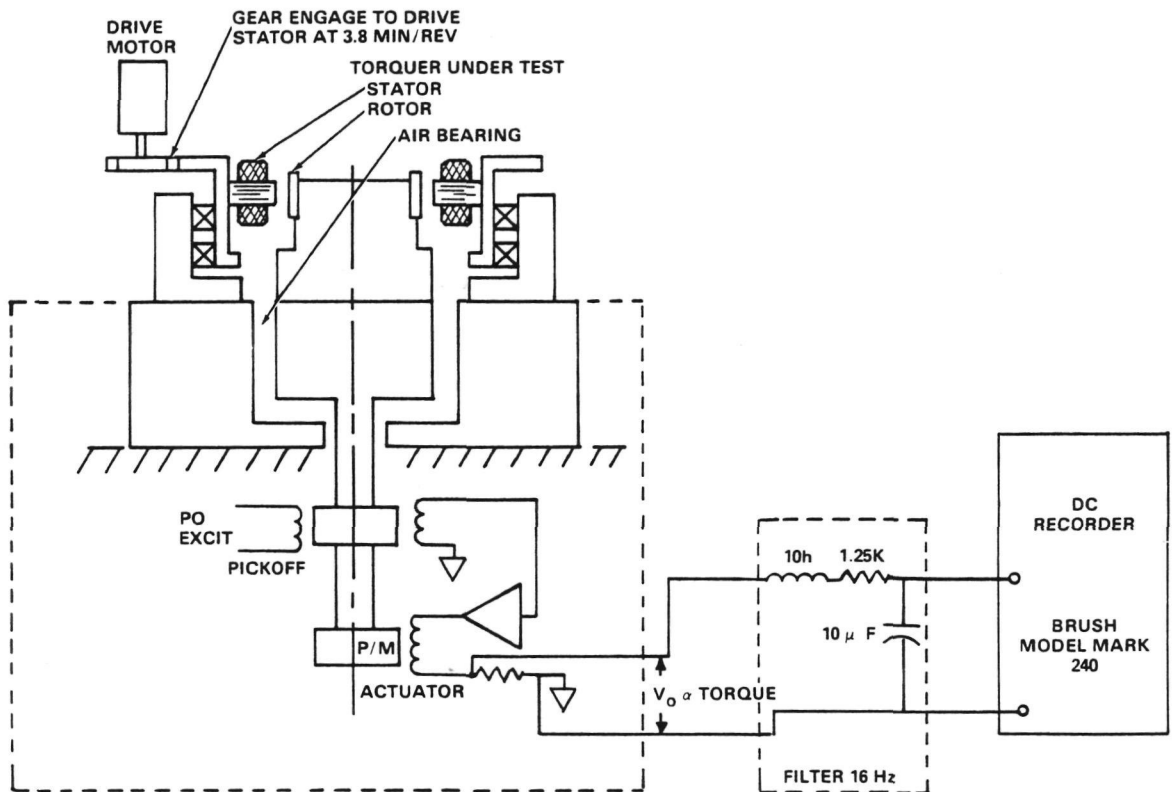


Figure 169
Mechanical Schematic of Roll Torque Motor Test Setup

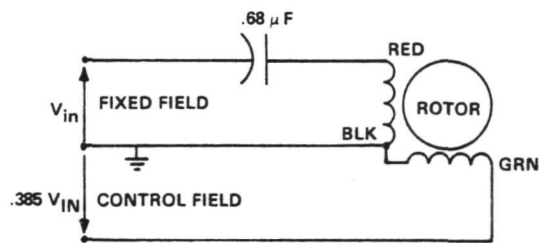


Figure 170
Torquer Excitation Schematic

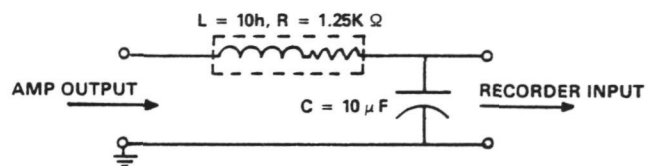


Figure 171
Low-Pass Filter

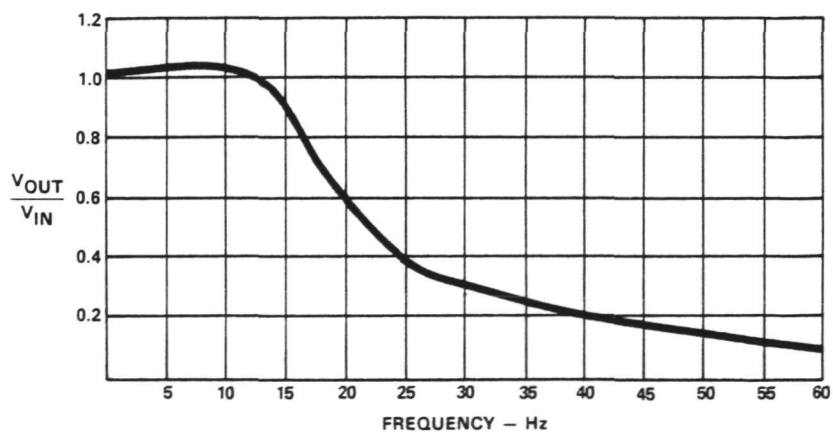


Figure 172
Low-Pass Filter-Response

Test Data

Chart 1 (Figure 173a) verifies the dynamometer torque stability. With no excitation to the torquer under test and no stator rotation, a noise free signal, observable to a resolution of .07 millivolts peak-to-peak exists.

Chart 2 (Figure 173a) verifies the stability of the dynamometer with the torquer excited. With 26 volts, 400 Hz excitation to the torquer and no stator rotation, a noise free signal observable to a resolution of .07 millivolts peak-to-peak from a basic signal of 70 mV existed. The slow drift in the torque level is due to increasing temperature caused by internal power losses.

Chart 3 (Figure 173a) is the ripple and cogging data for the solid iron, copper plated rotor. The line width has not changed, so the ripple and cogging are obviously less than .07 mV peak-to-peak or < .05 percent 0 to peak. The drift is a one cycle per revolution effect caused by misalignment of the radial centering force and the torque summing axis.

Charts 4 and 5 (Figure 173b) are similar to 2 and 3 except the torquer excitation was increased to 33 volts. This resulted in a higher torque level correspondent to a 106 mV offset and verifies ripple and cogging at < .03 percent 0 to peak.

Charts 6 (Figure 173b) and 7 (Figure 173C) are similar to 2 and 3 except the copper plating was removed from the rotor. Normal excitation (26 V) was used resulting in a torque level correspondent to a 31 mV offset. A definite ripple now exists of approximately .1 mV peak-to-peak or cogging and ripple of .16 percent 0 to peak.

Summary

Tests were performed to determine typical values for the cogging and ripple torque on an ac induction motor with a solid iron rotor. The results were as follows:

<u>Test Vehicle</u>	<u>Cogging and Ripple Torque Measured</u>
AC Induction Motor, Solid Iron Rotor	.16% 0-pk
AC Induction Motor Copper Plated Solid Iron Rotor	<*.03% 0-pk

*No cogging and ripple torque recognized to a threshold of .03 percent 0 to peak.

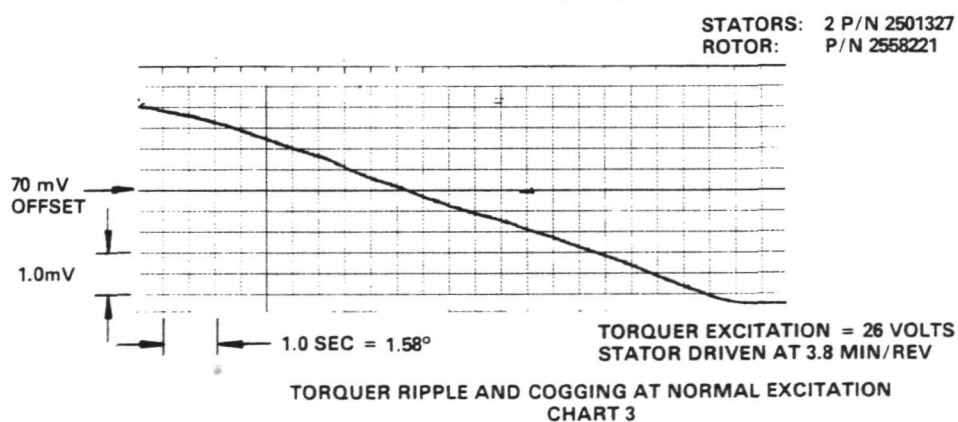
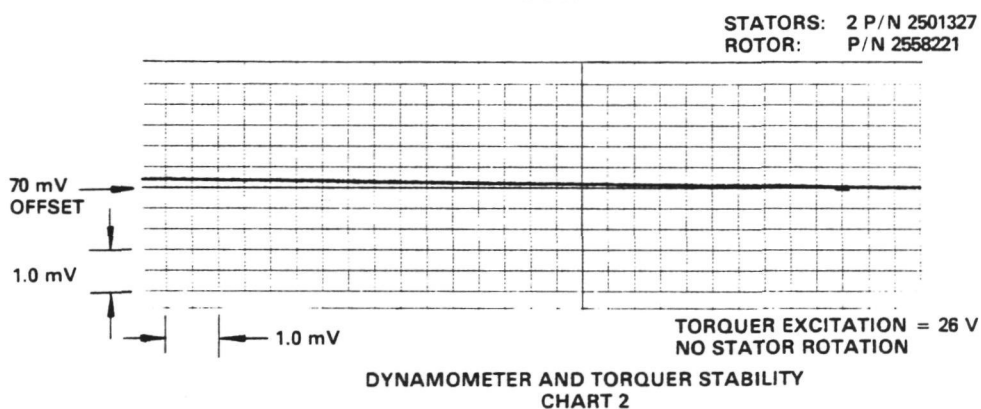
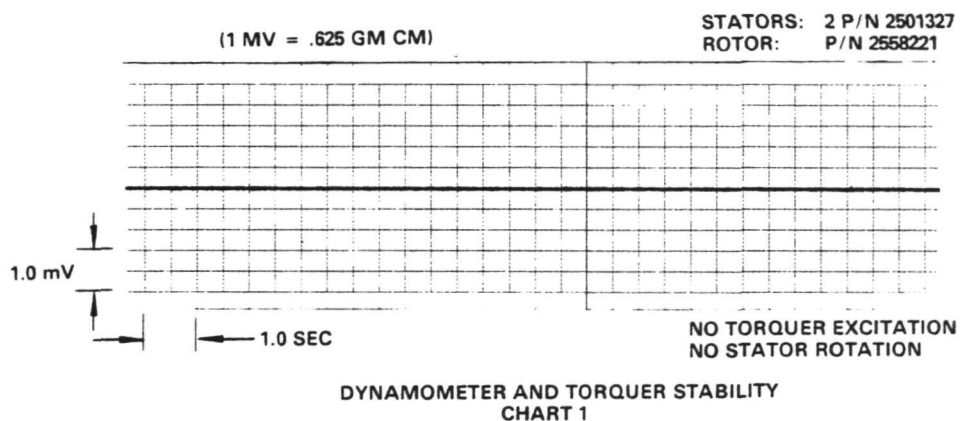


Figure 173a
Roll Motor Test
Charts 1, 2, and 3

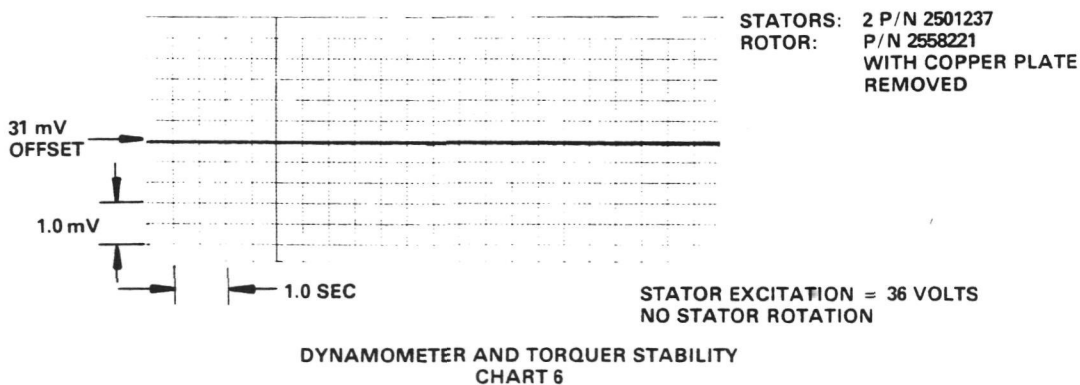
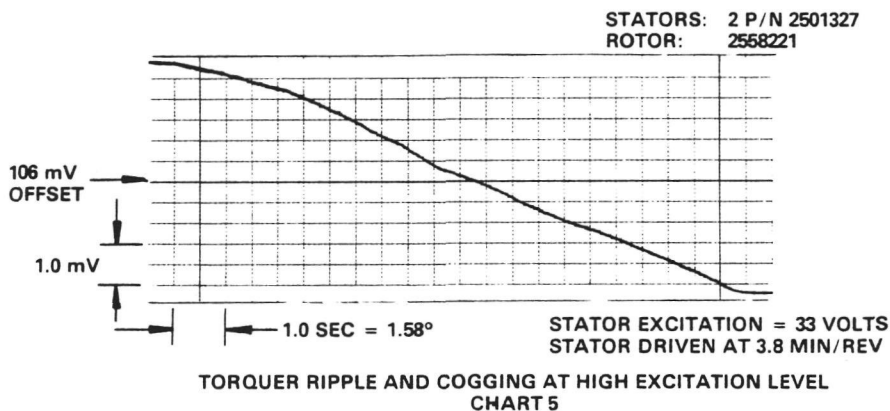
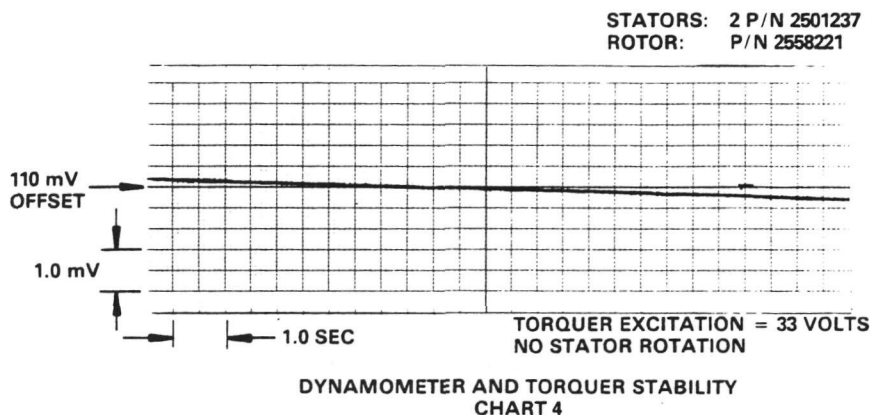


Figure 173b
 Roll Motor Test
 Charts 4, 5, and 6

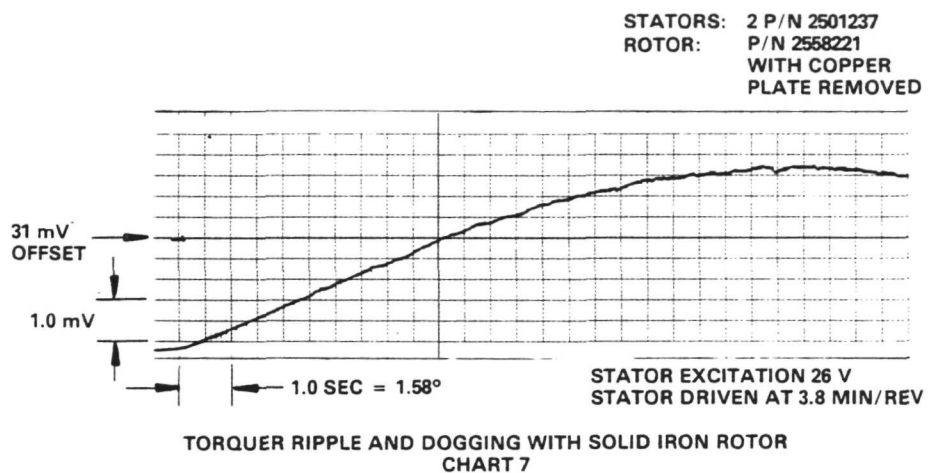


Figure 173c
 Roll Motor Test
 Chart 7

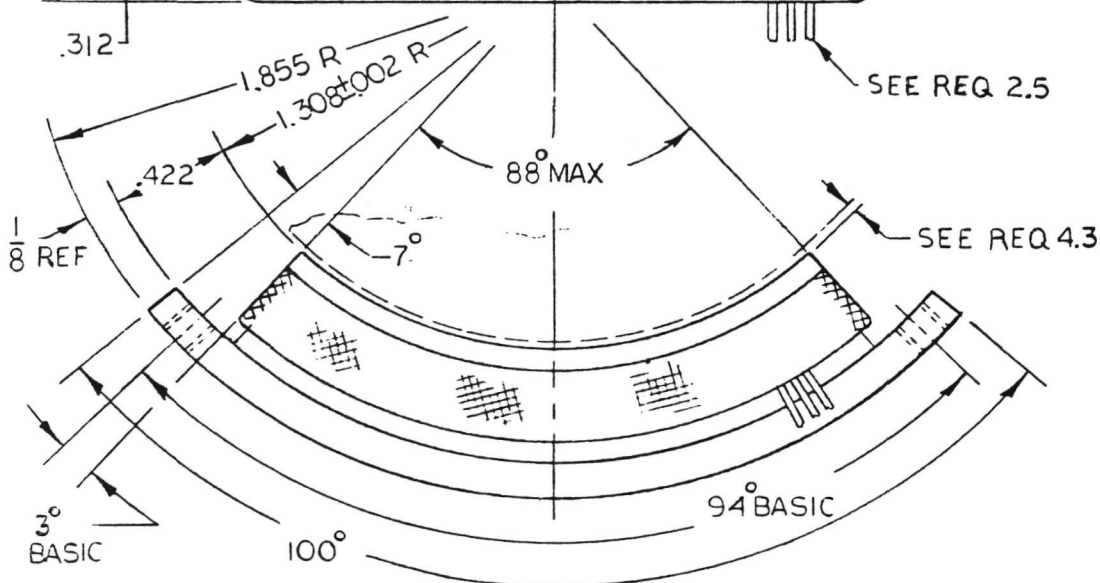
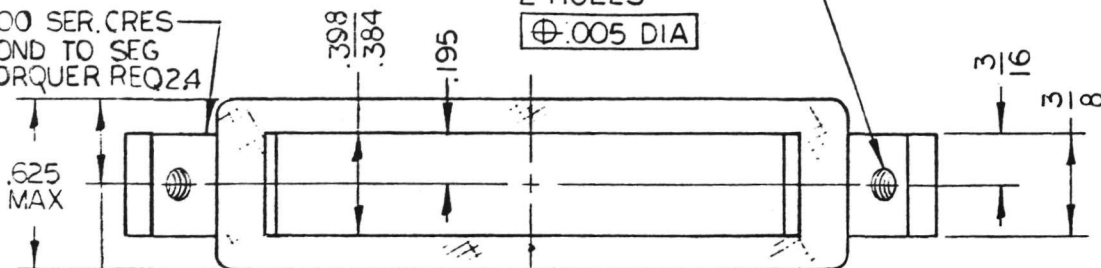
DWG NO. 2501327 SHEET 1 OF 6

APPLICATION		REVISIONS
NEXT ASSY	USED ON	FOR REVISION RECORD SEE LAST SHEET
	2593691	

300 SER. CRES.
BOND TO SEG
TORQUER REQ 2A

4-40 UNC-2B THRU
2 HOLES

$\varnothing .005$ DIA



◆ SPERRY ITEM CODES SEE EB699384

◆ SPERRY ITEM CODE								OPERATIONAL NOTE								A A A A A REV SHEET							
B	C	D	E	F	H	SPECIFICATION								11 10 9 8 7 6 5 4 3 2 1 SHEET INDEX									
11	21					CONTROL								SPERRY CLASS CODE									
						DRAWING								SHEET 5,6 MUST NOT BE SUPPLIED TO VENDORS									
UNLESS OTHERWISE SPECIFIED DIMENSIONS ARE IN INCHES TOLERANCES ON FRACTIONS DEC ANGLES $\pm 1/64$ $\pm .005$ $\pm 1^\circ$						CONTRACT								SPERRY RAND SPERRY FLIGHT SYSTEMS DIVISION PHOENIX, ARIZONA									
						DRAWN BY <i>C. L. L.</i> DATE <i>4 AUG 69</i>								TITLE SEGMENTED TORQUER STATOR									
						CHECKED BY <i>A. J. Rogers</i> DATE <i>15 JUL 69</i>								SIZE A CODE IDENT NO. 07187 DRAWING NO. 2501327 REV A									
SPERRY CLASS A						APPROVED FOR SPERRY <i>C. M. L.</i> DATE <i>15 JUL 69</i>																	
FIRST USED ON 2593691						APPROVED FOR								SCALE UNIT WT. 25 LB SHEET 1 OF 6									

FORM 1233-002AR3

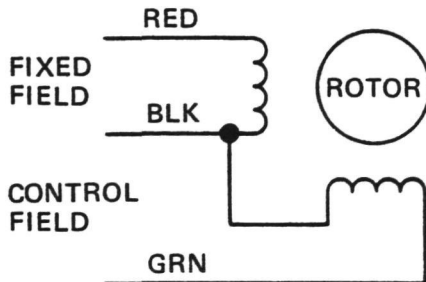
2501327-

DWG
NO.

2501327

SHEET

2



SCHEMATIC DIAGRAM

REQUIREMENTS: TWO PHASE SEGMENTED TORQUER STATOR

1. ELECTRICAL: (400 HERTZ) WHEN TESTED PER FIGURE 1.
 - 1.1 INTERMITTENT DUTY: THREE MINUTES EVERY 30 MINUTES
 - 1.1.1 FIXED FIELD:
 - 1.1.1.1 VOLTAGE: 26 VOLTS
 - 1.1.1.2 CURRENT: .12 AMPERE MAXIMUM
 - 1.1.1.3 POWER: 2.5 WATTS MAXIMUM
 - 1.1.2 CONTROL FIELD:
 - 1.1.2.1 VOLTAGE: 10 VOLTS
 - 1.1.2.2 CURRENT: .44 AMPERE MAXIMUM
 - 1.1.2.3 POWER: 2.2 WATTS MAXIMUM
 - 1.1.3 TORQUE OUTPUT: 25 GM-CM MINIMUM CW AND CCW
 - 1.2 CONTINUOUS DUTY:
 - 1.2.1 FIXED FIELD:
 - 1.2.1.1 VOLTAGE: 10 VOLTS
 - 1.2.1.2 CURRENT: .050 AMPERE MAXIMUM
 - 1.2.1.3 POWER: .40 WATT MAXIMUM

SPERRY SPEC REFERENCED

SIZE	CODE IDENT NO	DRAWING NO	REV
A	07187	2501327	A
SCALE	UNIT WT	SHEET	
		2	

FORM 1233-002CR3

1.2.2 CONTROL FIELD:

1.2.2.1 VOLTAGE: 3.85 VOLTS

1.2.2.2 CURRENT: .170 AMPERE MAXIMUM

1.2.2.3 POWER: .34 WATT MAXIMUM

1.2.3 TORQUE OUTPUT: 4 GM-CM MINIMUM CW AND CCW

1.3 DIRECTION OF ROTATION: CW ON ROTOR WHEN FACING LEAD EXIT ON STATOR WITH FIXED FIELD VOLTAGE LEADING CONTROL FIELD VOLTAGE BY 90 DEGREES.

1.4 DO RESISTANCE: (TEST PER SCHEMATIC)

1.4.1 FIXED FIELD: 210 OHMS ± 15 PERCENT

1.4.2 CONTROL FIELD: 8 OHMS ± 15 PERCENT

1.5 IMPEDANCE: (STALL)

1.5.1 FIXED FIELD: 300 (± 15 PERCENT) + J460 (± 15 PERCENT)

1.5.2 CONTROL FIELD: 12 (± 15 PERCENT) + J25 (± 15 PERCENT)

1.6 DIELECTRIC TEST: 500 VOLTS RMS, 60 HERTZ BETWEEN WINDINGS AND BETWEEN FIXED AND CONTROL WINDING AND LAMINATION STACK. THERE SHALL BE NO ARCING, BREAKDOWN OR ELECTRICAL DAMAGE.

1.7 INSULATION RESISTANCE: 500 VOLTS DC, 100 MEGOHMS BETWEEN ANY SET OF WINDINGS AND LAMINATION STACK.

2. MECHANICAL:

2.1 PART SHALL BE MARKED LEGIBLY AND PERMANENTLY WITH MANUFACTURER'S NAME OR SYMBOL AND PART NUMBER.

2.2 STATOR MOUNTING SURFACES AND DIAMETER TO BE FREE OF FINISHES.

2.3 WINDING TO BE IMPREGNATED WITH WESTINGHOUSE POLYESTER B-185 VARNISH OR EQUIVALENT.

2.4 MOUNTING BRACKET: TO BE BONDED TO LAMINATION STACK WITH B.F. GOODRICH CO'S A-1177 OR EQUIVALENT. CONTINUOUS FILLET TO BE PROVIDED HIGH TEMPERATURE CURE.

2.5 LEADS TO BE NO. 30 AWG STRANDED WIRE, TEFLON INSULATED, 12 INCHES LONG MINIMUM, STRIP 1/4 INCH APPROXIMATELY, COLOR CODED AS PER SCHEMATIC, EXIT AS SHOWN.

2.6 THERE SHALL BE NO PROTRUSIONS OF ANY KIND THAT COULD MOVE INTO THE AIRGAP OR BEYOND THE OUTLINE DIMENSIONS AND CAUSE FRICTION BETWEEN ROTATING PARTS.

SPERRY SPEC REFERENCED

SIZE	CODE IDENT NO	DRAWING NO	REV
A	07187	2501327	A
SCALE	UNIT WT	SHEET	

FORM 1237-100001

3. ENVIRONMENTAL: (PART SHALL BE CAPABLE OF MEETING THE ORIGINAL REQUIREMENTS WHEN TESTED PER SAE AS396)

3.1 AMBIENT TEMPERATURE RANGE: -65° TO $+125^{\circ}\text{C}$

3.2 VIBRATION: PARAGRAPH 7.6 EXCEPT 20 TO 500 HERTZ, 2G MAXIMUM ACCELERATION.

3.3 HUMIDITY: PARAGRAPH 7.5, 5 CYCLES

3.4 SHOCK: 30G, 11 MS TERMINAL PEAK SAWTOOTH

4. GENERAL:

4.1 ALL VALUES AT $25^{\circ} \pm 5^{\circ}\text{C}$ UNLESS OTHERWISE STATED.

4.2 MANUFACTURER'S RESPONSIBILITY: THERE WILL BE NO CHANGE IN THE DESIGN OF THE PART, IN THE MATERIALS AND PROCESSES IN ITS CONSTRUCTION, OR IN THE MANUFACTURER'S PART NUMBER AFTER THE FIRST ACCEPTABLE UNITS HAVE BEEN RECEIVED BY SPERRY UNLESS REQUESTED AND/OR APPROVED BY SPERRY IN WRITING.

4.3 ALL VALUES WHEN USING ROTOR, SPERRY PART NO. 2558221 USING AN AIR GAP OF $.006 \pm .002$ INCH AND CONNECTED PER SCHEMATIC DIAGRAM.

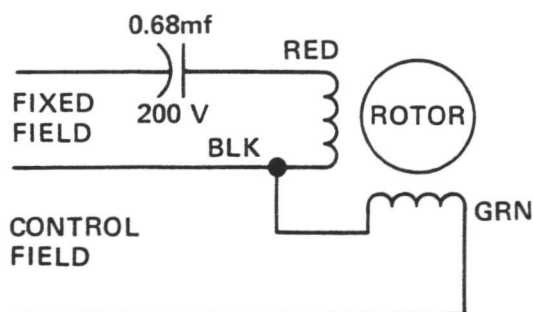


FIGURE I

SPERRY SPEC REFERENCED

SIZE	CODE IDENT NO	DRAWING NO	REV
A	07187	2501327	1
SCALE	UNIT WT	SHEET	

DWG
NO

2501327

SHEET

5

5. INSPECTION AND TESTS (BY SPERRY): 100 PERCENT 1.1.3, 1.2.3, 1.3, 1.4, 1.6, AND 1.7

SOURCES OF SUPPLY:

SPERRY RAND CORP (90012)
ELECTRO COMPONENTS PLANT
DURHAM, NORTH CAROLINA
PART NO. 2935024

SPERRY TO FURNISH VENDOR COPY OF DRAWING 1573-111.

PL-525-137

SPERRY SPEC REFERENCED

SIZE

CODE IDENT NO

DRAWING NO

REV

A

07187

2501327

SCALE

UNIT

SHEET

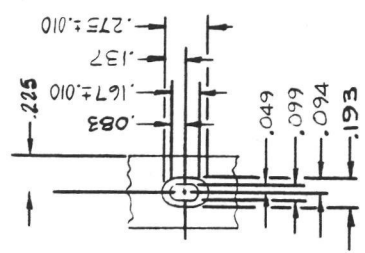
5

FORM 1235, OCT 1953

DWG NO. 2501327 SHEET 6

REVISIONS			
LTR	DESCRIPTION	DATE	APPROVED
A	SH1 WAS SH1 OF 5 SH2: REQ 1 WAS ---400 HZ. REQ 1.1.1.2 WAS 14 AMP MAX REQ 1.1.1.3 WAS 2.2 W MAX REQ 1.2.1.2 WAS .055 AMP MAX. REQ 1.2.1.3 WAS 40 W MAX. SH3 REQ 1.4 WAS D.C. RES. REQ 1.4.1 WAS $85\Omega \pm 15\%$ REQ 1.5 WAS (STALL) REQ 1.5.1 WAS $125(\pm 15\%) + J460(\pm 15\%)$. SH 4: REQ 4.3 WAS ---OF .005 IN. --- DIAG. ADDED FIG. 1. ADDED SH 6. 208305(M)	21 A.C. 69	

SIZE	CODE IDENT NO	DRAWING NO	REV
A	07187	2501327	A
SCALE	UNIT	WT	SHEET
			6



PARTIAL VIEW A-A

- NOTES:
1. DIMENSIONS APPLY WHEN PART IS ROUNDED.
 2. FINISH AS FOLLOWS:
 - 2.1 ACID COPPER PLATE 2.602 DIAMETER (OD) PER M690975 .0015 TO .0030 THICK.
 - 2.2 ACID COPPER PLATE 2.502 DIAMETER (I.D) PER M690975 .0010 TO .0028 THICK.
 3. THE WALL THICKNESS SHALL NOT VARY MORE THAN .001 TOTAL ALL AROUND.
 4. REMOVE BURRS AND SHARP EDGES.
 5. INTERPRET DRAWING IN ACCORDANCE WITH USA S1 Y14.5-1966.
 6. DO NOT APPLY PIECE MARK.
 7. DIMENSIONS, TOLERANCES AND SURFACE FINISH VALUES **APPLY** BEFORE THE APPLICATION OF THE FINISH.
 8. FINISH ALL OVER 125/.

[illegible]

APPENDIX E DESIGN ADDENDUM

This appendix contains the additional system design which was developed after the basic ASPS design contract was completed. The "delta" design consists of the addition of an attitude determination system utilizing the NASA Standard DRIRU-II and NASA Standard Spacecraft Computer NSSC-II. All mission dependent control laws are also included in NSSC-II as software.

E1 Attitude Determination System (ADS)

The ASPS ADS accepts the DRIRU-II $\Delta \theta$ pulse outputs and uses them as inputs to a third order quaternion integration algorithm to yield the ASPS payload attitude in a unit quaternion format. The unit quaternion defines the payload attitude as an Euler axis rotation from an inertial reference coordinate system. The unit quaternion elements relate to the magnitude of the Euler axis rotation and the direction cosines of the Euler axis relative to the inertial reference coordinate system as follows:

$$Q = \begin{bmatrix} q_0 \\ q_1 \\ q_2 \\ q_3 \end{bmatrix} = \begin{bmatrix} \cos (\phi/2) \\ \sin (\phi/2) \cos \alpha \\ \sin (\phi/2) \cos \beta \\ \sin (\phi/2) \cos \gamma \end{bmatrix} \quad (E1)$$

where ϕ is the magnitude of the Euler rotation and $\cos \alpha$, $\cos \beta$ and $\cos \gamma$ are the direction cosines of the Euler axis relative to the inertial reference coordinate system.

It can be shown that the rate of change of this quaternion is given by the first order differential equation

$$\dot{q} = \frac{1}{2} q \omega \quad (E2)$$

where $\omega = (0, \omega_1, \omega_2, \omega_3)$ is the quaternion composed of the angular rate

vector of the payload with respect to inertial space as expressed in the payload body axes coordinate system

ω_1 = payload X body axis
inertial rate

ω_2 = payload Y body axis
inertial rate

ω_3 = payload Z body axis
inertial rate

Body axis inertial
rates sensed by
the DRIRU-II

Equation (E2) can be written in terms of the four quaternion elements

$$\dot{q}_0 = 1/2 [\omega_1 q_1 - \omega_2 q_2 - \omega_3 q_3]$$

$$\dot{q}_1 = 1/2 [\omega_1 q_0 + \omega_3 q_2 - \omega_2 q_3]$$

$$\dot{q}_2 = 1/2 [\omega_2 q_0 - \omega_3 q_1 + \omega_1 q_2]$$

$$\dot{q}_3 = 1/2 [\omega_3 q_0 + \omega_2 q_1 - \omega_1 q_2]$$

} (E3)

Equation (E3) can be integrated by means of a difference equation obtained by a Taylor series expansion

$$q(t + \Delta t) = q(t) + \dot{q}(t) \Delta t + \ddot{q}(t) \frac{(\Delta t)^2}{2} + q(t) \frac{(\Delta t)^3}{6} + \dots \quad (E4)$$

It is assumed that the payload rates are constant over the integration intervals, Δt , so that Equation (E3) is time invariant over the interval. Substituting Equation (E3) into Equation (E4) yields the quaternion integration algorithms which are implemented in the NSSC-II digital computer. However, the algorithms will depend upon the number of terms used in the Taylor series expansion Equation (E4). The order of the quaternion integration algorithm refers to the order of the Taylor series expansion used to derive the algorithm, where the first order expansion uses the first two terms in Equation (E4), the second order expansion uses the first three terms in Equation (E4), etc.

Making the substitution of Equation (E3) into Equation (E4) for the first, second, third and fourth order Taylor series expansion yields the following quaternion integration algorithms

$$\begin{aligned}
 q_0(t + \Delta t) &= q_0(t) \left[1 - B^2 + \frac{B^4}{6} \right] - \frac{1}{2} - \frac{B^2}{6} C_0 \\
 q_1(t + \Delta t) &= q_1(t) \left[1 - B^2 + \frac{B^4}{6} \right] + \frac{1}{2} - \frac{B^2}{6} C_1 \\
 q_2(t + \Delta t) &= q_2(t) \left[1 - B^2 + \frac{B^4}{6} \right] + \frac{1}{2} - \frac{B^2}{6} C_2 \\
 q_3(t + \Delta t) &= q_3(t) \left[\underset{\substack{\uparrow \\ \text{1st}}}{1} - \underset{\substack{\uparrow \\ \text{2nd}}}{B^2} + \underset{\substack{\uparrow \\ \text{4th}}}{\frac{B^4}{6}} \right] + \frac{1}{2} - \frac{B^2}{6} C_3
 \end{aligned}
 \quad \left. \vphantom{\begin{aligned} q_0(t + \Delta t) \\ q_1(t + \Delta t) \\ q_2(t + \Delta t) \\ q_3(t + \Delta t) \end{aligned}} \right\} (E5)$$

where

$$\begin{aligned}
 B^2 &= [(\Delta\theta_X)^2 + (\Delta\theta_Y)^2 + (\Delta\theta_Z)^2] \\
 C_0 &= [q_1(t) \Delta\theta_X + q_2(t) \Delta\theta_Y + q_3(t) \Delta\theta_Z] \\
 C_1 &= [q_0(t) \Delta\theta_X + q_2(t) \Delta\theta_Z - q_3(t) \Delta\theta_Y] \\
 C_2 &= [q_0(t) \Delta\theta_Y - q_1(t) \Delta\theta_Z + q_3(t) \Delta\theta_X] \\
 C_3 &= [q_0(t) \Delta\theta_Z + q_1(t) \Delta\theta_Y - q_2(t) \Delta\theta_X]
 \end{aligned}
 \quad \left. \vphantom{\begin{aligned} C_0 \\ C_1 \\ C_2 \\ C_3 \end{aligned}} \right\} (E6)$$

and $\Delta\theta_X$, $\Delta\theta_Y$ and $\Delta\theta_Z$ are the DRIRU-II outputs for the X body axis, Y body axis and Z body axis, respectively, over the quaternion integration interval, Δt .

The first order algorithm corresponds to the two terms labeled "1st", the second order algorithm is the first order algorithm plus the term labeled "2nd", etc. Higher order quaternion integration algorithms could be derived which would add one additional term to each equation for each increasing order of the algorithm.

A quaternion integration computational error will exist during constant slewing which varies inversely with the order of the quaternion integration algorithm. This error will also be a function of the payload slew/track rate and the quaternion integral interval, Δt . Another computational error will

exist due to using a finite computer word length in the quaternion integration algorithm. These errors were investigated to determine the order of the quaternion integration algorithm required, the integration interval required and the necessity of using double precision arithmetic in the quaternion integration computation.

First consider the errors during constant slewing which result from truncating the Taylor series expansion of $q(t + \Delta t)$ in the derivation of the quaternion integration algorithm. The quaternion transformation errors may be evaluated using two sequential transformations. An arbitrary vector in the inertial reference axes can be exactly transferred to the payload body axes using the exact quaternion transformation over an angle $\theta \Delta t$. This payload body referenced vector can now be transferred back into the inertial reference axes using a transformation corresponding to the actual quaternion algorithm to be evaluated, which contains the exact incremental attitude change over a single integration interval $(\Delta \theta - \Delta t)$. The resultant error angle between the initial vector and the final vector will then represent the quaternion integration algorithm error over a single integration interval, Δt . Performing this calculation yields the expressions for the integration algorithm truncation errors shown in Table 45.

Another type of error exists which is called "degradation of unit length." It was previously noted that the quaternion which defines the payload attitude as an Euler axis rotation from an inertial reference coordinate system is a unit quaternion. Therefore, the quaternion elements must satisfy the constraint that the norm $\equiv 1$.

$$q_0^2 = q_1^2 + q_2^2 + q_3^2 \equiv 1 \quad (E7)$$

Note that this constraint holds for the quaternion elements in Equation (E1) since the sum of the squares of the direction cosines is identically one. The amount by which the sum of the squares of the four quaternion elements differs from unity is the degradation of unit length error. However, this error can be eliminated by constraining the sum of the square of the four quaternion elements to equal unity after each integration interval. This is accomplished by multiplying each quaternion element by the same correction factor necessary to achieve the constraint given in Equation (E7). This normalization is utilized on the ASPS ADS and hence the degradation of unit length error is eliminated.

TABLE 45
SUMMARY OF QUATERNION INTEGRATION ERROR EQUATIONS

Order of the Quaternion Integration Algorithm	Normalized Three Axis Angular Error $\theta / \theta_{S/T}$		
	Integration Algorithm Truncation	Computer Round-Off	
		Single Precision	Double Precision
1	$\frac{(\dot{\theta}_{S/T} \Delta t)^2}{12}$ 9.47	$\frac{16 (2^{-N})}{(\dot{\theta}_{S/T} \Delta t)}$ 3020	$\frac{16 (2^{-2N})}{(\dot{\theta}_{S/T} \Delta t)}$.0461
2	$\frac{(\dot{\theta}_{S/T} \Delta t)^2}{24}$ 4.74	$\frac{36 (2^{-N})}{(\dot{\theta}_{S/T} \Delta t)}$ 6800	$\frac{36 (2^{-2N})}{(\dot{\theta}_{S/T} \Delta t)}$.104
3	$\frac{(\dot{\theta}_{S/T} \Delta t)^2}{480}$ 1.04 x 10 ⁻⁴	$\frac{40 (2^{-N})}{(\dot{\theta}_{S/T} \Delta t)}$ 7550	$\frac{40 (2^{-2N})}{(\dot{\theta}_{S/T} \Delta t)}$.115
4	$\frac{(\dot{\theta}_{S/T} \Delta t)^2}{1920}$ 2.60 x 10 ⁻⁵	$\frac{44 (2^{-N})}{(\dot{\theta}_{S/T} \Delta t)}$ 8310	$\frac{44 (2^{-2N})}{(\dot{\theta}_{S/T} \Delta t)}$.127
<p>The numbers at the bottom of the boxes indicate the angular error in arc seconds for the following conditions:</p> <p>$\dot{\theta}_{S/T} = \pi/150$ rad/s $\Delta t = 1$ second</p> <p>$\theta_{S/T} = 72$ degrees $N = 16$ bits</p>			

The final quaternion integration computational error to be considered is the round-off error due to using a finite computer word length in the computation. The error in the product of two N bit words, truncated to an N bit word, will on the average be half of the least significant bit. Using fixed point arithmetic, one bit is used for the algebraic sign of the variable and (N-1) bits are used for the magnitude. Therefore, the average error in the product of two N bit words will be

$$E_{R1} = \frac{1}{2} \times \frac{1}{2^{N-1}} = 2^{-N} \quad (E8)$$

Using double precision arithmetic in the quaternion integration computation will give an average error in the product of two words which is

$$E_{R2} = \frac{1}{2} \times \frac{1}{2^{2N-1}} = 2^{-2N} \quad (E9)$$

Each of the four quaternion elements requires M multiplications for each integration step, where M is a function of the order of the quaternion integration algorithm. The value of M is 4, 9, 10 and 11 for the first, second, third and fourth order quaternion integration algorithms, respectively.

Each quaternion integration step could produce an error for each quaternion element which is $M \times 2^{-N}$ for single precision arithmetic and $M \times 2^{-2N}$ for double precision arithmetic. This is a worst case estimate because the error due to each multiplication is assumed to be in the same direction such that the total error is the algebraic sum of the individual multiplication round-off errors.

It can be shown that the maximum three axis error due to the quaternion integration round-off error is

$$\theta_e = 4 \times (\text{Error of each quaternion element})$$

Therefore the maximum three axis error over a single integration step due to quaternion integration round-off errors is

$$\theta = 4 \times M \times 2^{-N} \text{ for single precision arithmetic}$$

$$\theta = 4 \times M \times 2^{-2N} \text{ for double precision arithmetic}$$

These results are summarized for the first, second, third and fourth order quaternion integration algorithms in Table 45.

To select the order of the quaternion integration algorithm, select the integration cycle time and determine if double precision arithmetic is necessary; assume a maximum slew/track rate of 1.2 deg/sec since this is the maximum rate capability of the DRIRU-II and assume that the maximum allowable computational error is 1 arc second over a 1 minute time interval.

For

$$\dot{\theta} = 1.2 \text{ deg/s} = \pi/150 \text{ rad/s}$$

$$\theta = 1.2 \text{ deg/s} \times 60 \text{ sec} = 72 \text{ deg},$$

and assuming an integration cycle time (Δt) of 1 second and a 16-bit computer word length ($N = 16$) yields the errors shown at the bottom of the individual boxes in Table 45.

It should be noted that, for the assumed conditions, the third order quaternion integration algorithm yields a computational error which is more than four orders of magnitude less than the error obtained from a second order integration algorithm. However, the computational requirements of the third order algorithm are not significantly greater than those of the second order algorithm. Consequently, a third order quaternion algorithm was chosen.

It should also be noted that the quaternion integration round-off error is much greater than the 1 arc second allowed for single precision arithmetic. Therefore, double precision arithmetic was chosen for the quaternion integration algorithm computation.

It would be possible to select the quaternion integration time interval, Δt , such that the errors due to the third order integration algorithm truncation and the double precision computer round-off are equal. Referring to Table 45, this would require that

$$\frac{(\dot{\theta}_{S/T} \Delta t)^4}{480} = \frac{40 (2^{-2N})}{(\dot{\theta}_{S/T} \Delta t)} \quad (E10)$$

For $\dot{\theta}_{S/T} = \frac{\pi}{150} \text{ rad/s}$ (1.2 deg/s) and $N = 16$ bits, this yields an integration cycle time of 4 seconds. However, the expression for the error due to computer round off is a worst case estimate which assumes that the error due to the individual multiplications are all in the same direction. Consequently, the round-off error could be significantly less than predicted by the expression in Table 44. Therefore, a 1 second quaternion integration cycle time was selected.

The preceding analysis has assumed a constant slew/track rate over the quaternion integration interval, Δt . The ability of the third order quaternion integration algorithms performed with double precision arithmetic and an iteration cycle time of 1 second to perform an earth tracking mode was investigated. The analysis made the following simplifying assumptions.

- Spherical earth with 3960 mile radius
- Circular orbit with 200 mile altitude
- Track a target on earth in the orbit plane

These assumptions provide a peak track at nadir of 1.4 deg/sec. The error was determined for a 320 second time interval from nadir pointing which corresponds to a 21.12 degree orbit angle variation. The error was 2.4 arc second which is well within the goal of 1 arc second/minute.

The ASPS requires a fine pointing mode bandwidth of approximately 1 Hz. A 1 second quaternion integration cycle time is not compatible with this requirement if the payload attitude obtained via the quaternion integration of the DRIRU-II $\Delta\theta$ pulses is the only feedback. However, an approach was conceived which uses DRIRU-II $\Delta\theta$ pulses at a higher sample rate to provide an attitude error which is updated every 1 second by the quaternion integration derived error. Figure 174 shows a simplified single axis block diagram of this dual fast loop/slow loop attitude error generator.

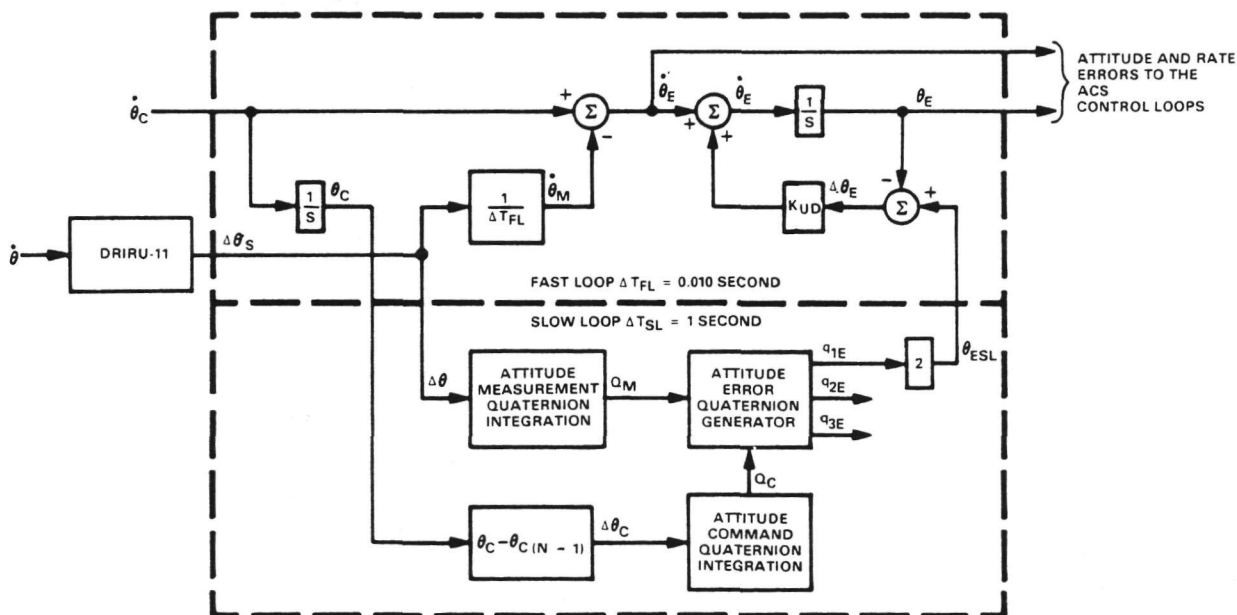


Figure 174
Fast Loop/Slow Loop Attitude Error Generator
Simplified Single Loop Block Diagram

Consider the fast loop without the slow loop update (let $K_{UD} = 0$). Then the fast loop simply takes the $\Delta\theta$ incremental attitude change over the fast loop cycle time and divides it by the fast loop cycle time to obtain an approximate value of the payload rate ($\dot{\theta}_m$) in Figure 174. This rate is subtracted from the commanded rate ($\dot{\theta}_c$) to obtain the rate error ($\dot{\theta}_e$) which is integrated to obtain the position error (θ_e). Note that the fast loop is essentially a rate control loop in which the feedback rate ($\dot{\theta}_m$) is actually a pseudo rate by virtue of the manner in which it is derived. Consequently, the fast loop will generate attitude errors due to the inaccuracy of the rate feedback, errors in the integration of the rate error and lack of an attitude sensor feedback. However, it will be adequate if it is "updated" periodically by the slow loop error which is accurately determined via quaternion integration of the rate command and the DRIRU-II $\Delta\theta$ pulse outputs.

The slow loop update of the fast loop could be performed by simply setting $\theta_e = \theta_{eSL}$ after each slow loop computation (see Figure 174). However, this would put a small transient into the ASPS ACS. Therefore, another update approach is implemented in which the attitude error θ_e is slaved to the slow loop attitude error through a closed loop. The time constant of the update loop is $1/K_{UP}$ seconds. The update loop

$$[(\Delta\theta_e = \theta_{eSL} - 0) \text{ and } K_{UP}] \quad (E11)$$

could be placed in either the fast loop or the slow loop. However, if it is placed in the slow loop, the slow loop sample period of 1 second will prevent using a loop time constant less than 1 second. Therefore, the update loop is closed in the fast loop. This allows the loop time constant to be much less than 1 second, which is the period between small step commands to the loop from θ_{eSL} .

E2 Command Generators/Processors

The ASPS software provides two command generators and one command processor. These are the maneuver command generator, the raster command generator and the manual pointing command processor.

The maneuver command generator is used to command the ASPS to make an Euler axis rotation from the present attitude to the desired (target) attitude in a minimum amount of time within the rate and acceleration limits which are imposed as constraints. It is assumed that jerk limiting is not required on the ASPS. The maneuver is accomplished in two steps. First, the maneuver command quaternion is computed. It is the quaternion which represents the error between the target attitude quaternion (Q_t) and the present attitude quaternion (Q_m). The calculations are referred to as the "Maneuver Command Quaternion Generator" in Figure 175.

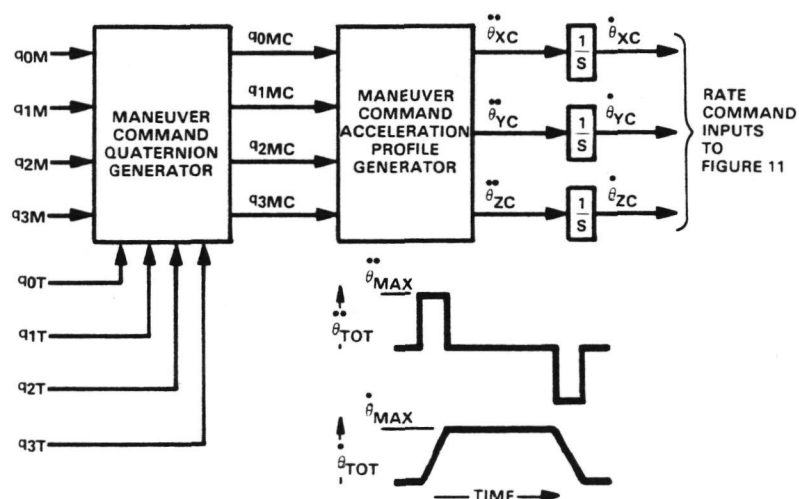


Figure 175
 Maneuver Command Generator Block Diagram
 and Maneuver Euler Axis Rotation Acceleration
 and Rate Profiles

Secondly, a maneuver acceleration profile is generated which incorporates both rate and acceleration limits on the command. The maneuver acceleration profile consists of a pulse of acceleration, a coast period and a pulse of deceleration. The acceleration pulse amplitude is made equal to the acceleration limit and the pulse width is calculated such that the area under the pulse equals the rate limit. This gives the acceleration and rate profiles shown in Figure 175. The calculations required to accomplish this are referred to as the "Maneuver Command Acceleration Profile Generator" in Figure 175.

Note that the command acceleration and rate profiles shown in Figure 175 are the Euler axis rotation acceleration and rate profiles. The commands to the three payload body axes are scaled down by the direction cosines of the Euler axis with respect to the payload body axes. Also, note that the calculations shown in Figure 175 are made only once at the start of the maneuver and the three body axis acceleration commands are integrated in the fast loop to yield the three body axis rate commands which serve as inputs to Figure 174.

There are a number of raster command generators which could be implemented. The one which has been initially implemented for the ASPS generates the search raster scan pattern shown in Figure 176. The raster scan pattern parameters d and e are input parameters, where d is an integer multiple of e . Therefore, the ratio d/e is the number of individual scan segments after the initial scan out to the corner of the search pattern.

The raster scan pattern command is obtained by generating a slew command for each individual scan segment of the scan pattern. These individual slew commands are generated in a manner similar to the slew command generator. They also incorporate acceleration and rate limits on the individual scans. Each raster scan segment command is automatically initiated at the end of the previous scan segment command.

The Manual Pointing Control (MPC) is a "joystick" which allows an experimenter to manually point the ASPS. The MPC outputs are rate limited in the MPC software. The manual pointing command processor accepts the MPC outputs and processes them to impose acceleration limits on the rate commands. The processor outputs become rate command inputs to Figure 174. A block diagram of the manual pointing command processor is presented in Figure 177. The pitch and yaw axes accelerations are reduced by the ratio of the individual axis rate to the total pitch/yaw rate to apportion the acceleration between the two axes. The acceleration limits are $216 \text{ arc seconds/s}^2$ in roll and $2000 \text{ arc seconds/s}^2$ total about any axis in the pitch/yaw plane.

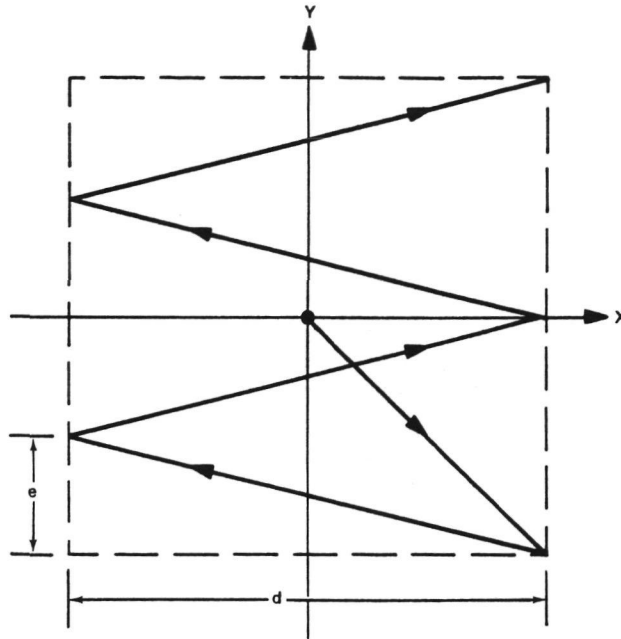


Figure 176
Search Raster Scan Pattern Command (Projection of Z
Pointing Axis Unit Vector on the Initial X-Y Plane)

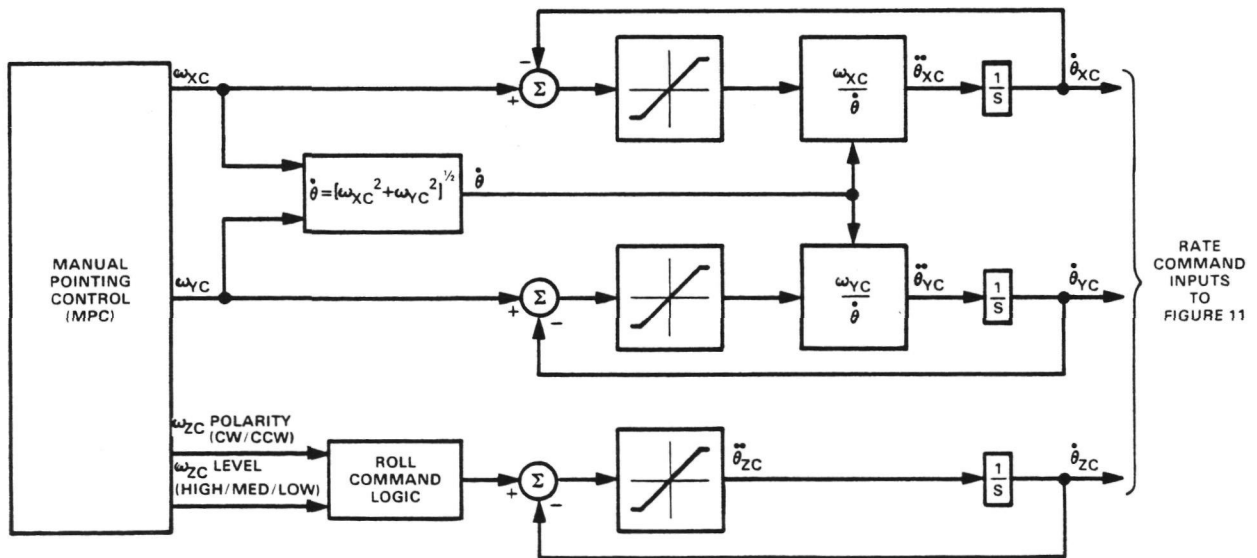


Figure 177
Manual Pointing Command Processor Block Diagram

E3 Digital Attitude Control System (ACS)

The ASPS digital ACS includes the following NSSC-II software functions:

- Variable Gimbal Position Command Rate Limiter
- Gimbal Control Laws
- Elevation Gimbal Inertia Compensation
- Vernier Pointing, Centering, and Roll Control Laws
- Transformation from Vernier Axial Gaps to Payload Plate Relative Errors
- Transformation from Pitch and Yaw Torque Commands and Z-Axis Force Command to Axial Actuator Force Commands
- CM Offset Decoupling

Each of these items has been discussed previously except the variable gimbal position command rate limiter. It provides the algorithms necessary to limit the rate-of-change of the gimbal position commands to ensure that the gimbals are never commanded to a rate such that a full deceleration torque from the gimbal torque motor cannot stop the gimbal prior to it hitting the gimbal stop. Thus the rate limit must decrease as the gimbal approaches the gimbal stop.

The digital implementation of the control laws, transformation matrices and CM offset decoupling is straightforward and needs no special attention with two exceptions:

- The 10 Hz digital control loops require special attention to the transport lags, computation iteration cycle time and the control law implementation to provide a digital control loop design with satisfactory dynamic response without requiring a very short computation iteration cycle time which would unnecessarily burden the NSSC-II computer utilization.
- The ASPS fine pointing mode control loop design must be given special attention to minimize the limit cycle which will exist due to the DRIRU-II $\Delta\theta$ pulse quantization and quantization of the vernier axial actuator force commands.

10 Hz Control Laws

The vernier pitch and yaw control loops have 10 Hz bandwidths in the slew mode to keep the payload plate centered in the gap, and the coarse gimbal control loops have 10 Hz bandwidths in the fine pointing mode to make the gimbals appear rigid to the payload. A digital simulation of a simplified single axis control loop was utilized to investigate the loop dynamic response as a function of the loop transport lag, computation iteration cycle time and the control law digital implementation. The control law is of the form

$$\frac{T_c}{\theta} = 1024 \times J \times \left(\frac{16}{s} + 1 \right) \frac{(s/16 + 1)}{(s/1000 + 1)} \quad (E10)$$

where J is the payload inertia. This yields an open loop transfer function whose asymptotic straight-line Bode gain approximation has a 0 dB crossover frequency of 64 rad/s.

The simulation was exercised for values of transport lag from 0 to 8 milliseconds, and values of the computation iteration intervals of 5, 10, and 20 milliseconds. Three different control law digital implementations: direct simulation with trapezoidal integration, direct simulation with Simpson's Rule integration, and a difference equation obtained via the Tustin transform were also exercised. The direct simulation refers to generating the control law by combining individual integrators as would be done on an analog computer simulations.

Table 46 summarizes the results obtained from the simulation. An acceptable loop dynamic response is achieved with a 10 millisecond computation iteration interval, a total loop transport lag of less than 6 milliseconds and a digital control law implemented with a difference equation obtained via the Tustin transform. Notice that acceptable response could also be obtained with a 20 millisecond computation iteration interval and a total loop transport lag of less than 2 milliseconds. The total loop transportation lag consists of the individual lags due to the A/D (feedback) interface, the control law computation time and the D/A (command) interface. The lag is minimized by giving priority to the transfer of the A/D feedback signals and the D/A command signals which are in the 10 Hz loops and the computations which generate the command as a function of the feedback. Computational efficiency of the NSSC-II would suffer if a software priority structure were used which guaranteed less than 2 millisecond transport lag for these loops, however. Therefore, the fast loop cycle time was set at 10 milliseconds which requires a 6 millisecond maximum lag.

Quantization and Scaling

Fine pointing stability of the ASPS will be limited by the DRIRU-II $\Delta\theta$ pulse quantization of .05 arc seconds. This may be reduced through the use of other sensors in addition to the DRIRU-II, such as a fine sun sensor, payload provided pointing error, etc. Even with an ideal set of inertial sensors, however, the quantization of the vernier axial force commands will create a small residual limit cycle.

TABLE 46
SUMMARY OF RESULTS OF ϵ 10 HZ DIGITAL
CONTROL LOOP SIMULATION

Control Law Implementation	Computation Iteration Interval (milliseconds)	Total Loop Transport Lag (milliseconds)	Response
Direct Simulation with Trapezoidal Integration	5	0	Very poorly damped
	10	0	Unstable
Direct Simulation with Simpson's Rule Integration	10	0	Poorly damped
	20	0	Unstable
Difference Equation via Tustin Transform	10	6	Satisfactory
	10	8	Poorly damped high frequency oscillation
	20	2	Satisfactory
	20	4	Poorly damped high frequency oscillation
	20	6	Unstable

The limit cycle resulting from the quantization of the vernier axial force commands will be proportional to the D/A converter granularity and inversely proportional to the payload inertia. A simulation of the fine pointing mode indicates that this limit cycle would have a 1.1 arc second peak-to-peak amplitude and a 4.5 second period for the smallest (50 kg-m^2) payload inertia, a 12 bit D/A converter and the axial force commands scaled to the maximum values of 34.3 Newtons. A scaling of 34.3 N is required to slew the maximum size payload of 600 kg mass, 500 kg-m^2 inertia at an acceleration of $2000 \text{ arc seconds/s}^2$. In the fine pointing mode, the peak force delivered by the axial actuators is less than .35 N. If the force commands are rescaled during fine pointing, the limit cycle amplitude will drop to .01 arc second peak-to-peak. Rescaling the force commands is easily achieved in ASPS by switching the bias currents used on the MBAs to a lower value. This has the advantage of reducing any residual force imbalances due to calibration errors, etc by the same ratio.

LIST OF REFERENCES

- ¹Anderson, W.W., and Groom, N.J., "The Annular Momentum Control Device (AMCD) and Potential Applications," NASA TN D-7866, 1975.
- ²Anderson, W.W., and Joshi, S.M., "The Annular Suspension and Pointing (ASP) System for Space Experiments and Predicting Pointing Accuracies," NASA TR R-448, 1975.
- ³"Spacelab Payload Accommodations Handbook," SLP2104 dated January 1977.
- ⁴Andrews, P.D. and Cormack, A., "Flight Experiment Definition of an Annular Suspension and Pointing System (ASPS)," Rockwell International Space Division, SD77-AP-0027, May 1977.

1. Report No. NASA CR-3343		2. Government Accession No.		3. Recipient's Catalog No.	
4. Title and Subtitle DESIGN OF THE ANNULAR SUSPENSION AND PAINTING SYSTEM (ASPS) (Including Design Addendum)				5. Report Date October 1980	
				6. Performing Organization Code	
7. Author(s) D. Cunningham, T. Gismondi, B. Hamilton, J. Kendig, J. Kiedrowski, A. Vroman, and G. Wilson				8. Performing Organization Report No.	
				10. Work Unit No.	
9. Performing Organization Name and Address Sperry Flight Systems P.O. Box 21111 Phoenix, Arizona 85036				11. Contract or Grant No. NAS1-14214	
				13. Type of Report and Period Covered Contractor Report	
12. Sponsoring Agency Name and Address National Aeronautics and Space Administration Washington, DC 20546				14. Sponsoring Agency Code	
15. Supplementary Notes Langley Technical Monitor: Claude R. Keckler Final Report					
16. Abstract The Annular Suspension and Pointing System is an experiment pointing mount designed for extremely precise 3-axis orientation of shuttle experiments. It utilizes actively controlled magnetic bearings to provide noncontacting vernier pointing and translational isolation of the experiment.					
17. Key Words (Suggested by Author(s)) Experiment Pointing Mount, Magnetic Suspension			18. Distribution Statement Unclassified - Unlimited		
			Subject Category 19		
19. Security Classif. (of this report) Unclassified		20. Security Classif. (of this page) Unclassified		21. No. of Pages 355	
				22. Price A16	

National Aeronautics and
Space Administration

Washington, D.C.
20546

Official Business

Penalty for Private Use, \$300

SPECIAL FOURTH CLASS MAIL
BOOK

Postage and Fees Paid
National Aeronautics and
Space Administration
NASA-451



NASA

POSTMASTER:

If Undeliverable (Section 1
Postal Manual) Do Not Re